



Durham E-Theses

A study of an axisymmetric wall jet with streamline curvature and its application to the coanda flare

Morrison, Jonathan Finlay

How to cite:

Morrison, Jonathan Finlay (1982) *A study of an axisymmetric wall jet with streamline curvature and its application to the coanda flare*, Durham theses, Durham University. Available at Durham E-Theses Online: <http://etheses.dur.ac.uk/7404/>

Use policy

The full-text may be used and/or reproduced, and given to third parties in any format or medium, without prior permission or charge, for personal research or study, educational, or not-for-profit purposes provided that:

- a full bibliographic reference is made to the original source
- a [link](#) is made to the metadata record in Durham E-Theses
- the full-text is not changed in any way

The full-text must not be sold in any format or medium without the formal permission of the copyright holders.

Please consult the [full Durham E-Theses policy](#) for further details.

Academic Support Office, Durham University, University Office, Old Elvet, Durham DH1 3HP
e-mail: e-theses.admin@dur.ac.uk Tel: +44 0191 334 6107
<http://etheses.dur.ac.uk>

A STUDY OF AN AXISYMMETRIC WALL JET
WITH STREAMLINE CURVATURE AND
ITS APPLICATION TO THE
COANDA FLARE

by

JONATHAN FINLAY MORRISON B.Sc. (Dunelm)

Department of Engineering
University of Durham

A thesis submitted for the degree of
Doctor of Philosophy of the University of Durham

JANUARY 1982

The copyright of this thesis rests with the author.
No quotation from it should be published without
his prior written consent and information derived
from it should be acknowledged.



The deeper we look into nature, the more we recognise that it is full of life, and the more profoundly we know that all life is a secret and that we are united with all life that is in nature. Man can no longer live his life for himself alone. We realise that all life is valuable and that we are united to all this life. From this knowledge comes our spiritual relationship to the universe.

Albert Schweitzer

Dedicated to my parents

A B S T R A C T

An effectively incompressible turbulent wall jet with streamwise and axisymmetric curvature has been studied as a simplification of the Coanda flare, in order to develop a calculation procedure for design purposes.

Measurements of Reynolds stresses show very high turbulence levels caused by the combined effects of streamline curvature and divergence, leading to increased entrainment and jet growth/velocity decay rates. Discrepancies in the data also indicate a significant presence of quasi-steady longitudinal vortices. In the vicinity of the sudden change from flow with streamwise wall curvature to that without, the whole layer shudders; the separate components of the Reynolds stress tensor, structural parameters and the mean flow all respond as a damped second order system.

Both the presence of two extra rates of strain which interact non-linearly and large history effects at sudden changes in surface curvature make large demands on any turbulence closure. Second order correlations do not show any degree of similarity when scaled relative to one another. A calculation method has been developed incorporating the calculation of the cross-stream pressure gradient in a plane or axisymmetric geometry. A simple mixing length model with empirical corrections for the large effects of streamline curvature and divergence has been used to close the solution. This is regarded as no more than a first step; the calculation method is suitable for extension to include a full Reynolds stress closure.

ACKNOWLEDGEMENTS

Inevitably in work of this nature, there are many people, too numerous to mention individually, to whom I am indebted.

However, I would like to express my gratitude to Dr. D. G. Gregory-Smith who set up the project and whose support and encouragement were invaluable throughout. I would also like to thank Dr. J. C. Boden and Dr. C. Titcombe of the B.P. Research Centre at Sunbury-on-Thames and Mr. R. E. Witheridge of Kaldair Limited for their help and advice, particularly during my stay at Sunbury whilst conducting the large-scale tests.

Thanks are due to Albert Harker and Les Fleet of the thermo-fluids laboratory and Trevor Nancarrow of the electrical laboratory. I am also grateful to the technicians of the central science site workshop who were concerned with the fabrication of the test rig and overcame the formidable problems encountered in the machining of the flare. The assistance of Mr. C. Campbell and the technicians of the Engineering Department workshop is also greatly appreciated.

I would also like to thank Dr. C. F. King for his advice concerning the hot-wire analysis, Dr. C. Preece for his help with the computing associated with the data analysis and Chris Plummer for her speedy and efficient typing.

I am indebted to the Science Research Council and the British Petroleum Company Limited for their financial support.

LIST OF CONTENTS

	Page
List of Contents	vi
List of Figures	xi
Principal Notation	xiv
 CHAPTER 1 - INTRODUCTION	 1
1.1 The Coanda Flare	1
1.2 The Coanda Effect - Streamline Curvature Induced by an Adjacent Boundary	3
1.3 Breakaway	4
 CHAPTER 2 - THEORETICAL BACKGROUND	 8
2.1 Introduction	8
2.1.1 The Generalised Equations of Motion	9
2.1.2 The Statistical Description of Turbulence	10
2.1.3 Homogeneity and Isotropy	13
2.2 Shear Layers	16
2.2.1 Reynolds Stresses	17
2.2.2 Transport Equations	17
2.2.3 Local Equilibrium and Self-Preservation	20
2.2.4 Turbulent Flow Near a Wall.	21
2.3 Classification of Shear Layers	22
2.3.1 Boundary Layer/Thin Shear Layer	23
2.3.2 Fairly Thin Shear Layer	25
2.4 Previous Work on Wall Jets	25
2.4.1 Turbulent Wall Jets on Flat Surfaces	26
2.4.2 Turbulent Wall Jets with Streamline Curvature	28
2.4.3 Axisymmetric Turbulent Wall Jets	30
2.5 The Effects of Extra Rates of Strain on Tubulent Flow	31
2.6 The Effects of Streamline Curvature on Turbulent Flow	32
2.6.1 Longitudinal Vortices	33
2.6.2 Unstably-Curved Wall Shear Layers	35
2.6.3 Stably-Curved Wall Shear Layers	41

2.7	The Effects of Streamline Divergence on Turbulent Flows	41
2.7.1	Relevance to the Present Work	41
2.7.2	Previous Work	42
2.8	Summary	44
CHAPTER 3 - APPARATUS AND EXPERIMENTAL PROCEDURE		46
3.1	Model Flare Tests	46
3.1.1	Flare and Plenum Chamber	46
3.1.2	Air Supply	47
3.1.3	Traverse Gear	49
3.1.4	Probes	49
3.1.5	Calibration Nozzle	51
3.1.6	Instrumentation	51
3.1.7	Plotting Routines	53
3.1.8	Traverses	54
3.2	Large Scale Tests	55
3.2.1	Flare and Air Supply	55
3.2.2	Traverses	56
CHAPTER 4 - HOT-WIRE ANALYSIS		62
4.1	Introduction	62
4.2	Linearization	64
4.2.1	Analogue Linearization	65
4.2.2	Effective Linearization - Taylor Expansion Method	65
4.2.3	Comparison of Linearization Techniques	65
4.3	Resolution of Effective Cooling Velocity	67
4.4	Remaining Sources of Error	69
4.4.1	Shear Effect on Wires	69
4.4.2	Wall Proximity	70
4.5	Analogue/Digital Data Analysis	70
4.6	Review of Signal Analyses	71
4.6.1	Conventional Method	71
4.6.2	Statistical Methods	72
4.6.3	Method of Acrivelellis (1977a,b & 1978a,b)	73

4.7	Selected Analysis	74
4.7.1	Recorded Data	74
4.7.2	Reduction of Effective Cooling Velocities to Total Velocity Components	74
4.7.3	Separation of Mean and R.M.S. Components	74
4.7.4	Solution for $y < 1.06$ mm	75
4.8	Assessment of the Analysis.	75
CHAPTER 5 - EXPERIMENTAL RESULTS		80
5.1	Establishment of Quasi-Two-Dimensional Conditions	80
5.2	Discharge Coefficient Data	80
5.3	Static Pressure Measurements	82
5.4	Mean Velocity Profile Data	83
5.5	Conventional Second Order Correlations	85
5.6	Structural Parameters	89
5.7	Results from Large Scale Tests	90
CHAPTER 6 - CALCULATION METHOD		115
6.1	Review of Available Methods	115
6.1.1	Integral Methods	115
6.1.2	Differential Methods	117
6.1.3	Outline of PS Method	121
6.2	Equations of Motion	123
6.2.1	Grid and Control Volume	123
6.2.2	Momentum Equations	123
6.2.3	Order of Magnitude Analysis of Terms	124
6.3	Solution of Parabolic Equations	127
6.3.1	Definition of Stream Function and Mass Flowrates	127
6.3.2	Transformation to (x, ω) Coordinates	128
6.3.3	The Finite Difference Grid and Equations	129
6.4	Extension of Method to Flows With Significant Cross- Stream Pressure Gradient - 'Partial-Parabolic' Pressure	130
6.4.1	Equations to be Solved	132
6.4.2	Algorithm Sequence	132

6.4.3	Initial Conditions	134
6.4.4	Pressure Calculation	135
6.4.5	Solution for \bar{V}	135
6.4.6	Extra Terms in the x-Component Mean Momentum Equation	136
6.4.7	Convergence Criterion and Stability	137
6.5	Additional Features	138
6.5.1	Geometry and Boundary Conditions	138
6.5.2	Modified Law of the Wall	138
6.5.3	Determination of U_m and $y_m/2$	139
6.6	Summary	139
CHAPTER 7 - TURBULENCE MODELLING		144
7.1	Review of Available Turbulence Models	145
7.1.1	Algebraic Specifications of Eddy Viscosity	145
7.1.2	Specification of Eddy Viscosity by Differential Equation	147
7.1.3	Reynolds Stress Models	149
7.1.4	Additional Models	152
7.2	Assessment of Models	153
7.3	Representation of Mixing Length in Calculation Method	155
7.4	Modelling of Streamline Curvature Effects	157
7.4.1	Mixing Length Corrections for the Effects of Streamline Curvature	157
7.4.2	Analysis for Mixing Length Correction Applicable to Flows with Large Curvature	160
7.5	Modelling Streamline Divergence Effects	164
7.6	Allowance for "History" Effects	165
7.7	Modelling of Combined Streamline Curvature and Divergence Effects	167
CHAPTER 8 - COMPUTER PROGRAM RESULTS		169
8.1	Cases I - \bar{V}	170
8.2	Cases \bar{VI} - \bar{VIII}	173
8.3	Discussion of Calculation Method	175
8.3.1	Node Distribution	175
8.3.2	Mean Velocity Profiles	176
8.3.3	The Pressure Calculation and Stability	177

CHAPTER 9 - DISCUSSIONS AND CONCLUSIONS	205
9.1 Comments on the Experimental Data	
9.2 Streamwise Curvature and Divergence Effects	
9.3 Assessment of the Turbulence Modelling Procedure	
9.4 Suggestions for Further Work	
9.5 Conclusions	
References	215
Appendix A - Three-Hole Probe Calibration and Corrections	230
Appendix B - Hot-Wire Analysis - Four Probe Orientations	232
Appendix C - Full Solution of Six Hot-Wire Response Equations	234
Appendix D - Simplified Hot-Wire Analysis for Near-Wall Regions	236
Appendix E - Equation of Motion	237
Appendix F - Reynolds Stress Transport Equations	241
Appendix G - Program Users Guide	245

LIST OF FIGURES

Fig. No.		Page
1.1	Basic principles and geometry of Coanda flare	6
1.2	Coordinate System	7
3.1	Basic elements of flare model	57
3.2	Distribution of surface pressure tappings	58
3.3	Schematic diagram of rig	59
3.4	Probe geometries	60
3.5	Velocity and pitch calibrations for 3-hole probe	61
4.1	CTA and CCA configurations	78
4.2	Linearization checks for $n = 0.33$	78
4.3	Definition of U_N , U_B and U_T	79
4.4	Hot-wire orientations	79
5.1	Discharge coefficient variation with pressure ratio and slot width	91
5.2	Reduced values of C_D	92
5.3	Wall pressure variation in streamwise direction	93
5.4	Case A: Static pressure profiles	94
5.5	Case A: $\bar{U} \ v \ y$ (hot-wire probe)	95
5.6	Case A: $\bar{U} \ v \ y$ (3-hole probe)	96
5.7	Case B: $\sqrt{\bar{U}^2 + \bar{V}^2} \ v \ y$ (3-hole probe)	97
5.8	Case A: Growth/velocity decay rate	98
5.9	Case B: Growth/velocity decay rate	99
5.10	Case A: $\bar{U}/\bar{U}_m \ v \ \xi$ (hot-wire probe) $\theta = 20^\circ - 75^\circ$ only	100
5.11	Case A: $\bar{U}/\bar{U}_m \ v \ \xi$ (hot-wire probe)	101
5.12	Case A: $\bar{U}/\bar{U}_m \ v \ \xi$ (3-hole probe)	102
5.13	Case B: Non-dimensional $\sqrt{\bar{U}^2 + \bar{V}^2} \ v \ \xi$ (3-hole probe)	103
5.14	Case A: $\bar{V}/\bar{U}_m \ v \ \xi$ (hot-wire probe)	104

5.15	x-component normal stress profiles	105
5.16	y-component normal stress profiles	106
5.17	Radial component normal stress profiles	107
5.18	Shear stress profiles	108
5.19	Structural parameter \overline{uv}/q^2	109
5.20	Structural parameter $R \overline{uv}$	110
5.21	Structural parameter $\overline{v^2}/\overline{u^2}$	111
5.22	Full scale tests: $\sqrt{\overline{u^2} + \overline{v^2}}$ v y	112
5.23	Full scale tests: non-dimensional $\sqrt{\overline{u^2} + \overline{v^2}}$ v y	113
5.24	Full scale tests: growth/velocity decay rate	114
6.1	Grid and control volume	141
6.2	Finite different grid	142
6.3	Control volumes for partial-parabolic procedure	143
7.1	Mixing length distributions	168
8.1	Case I: growth/velocity decay rate	179
8.2	Case I: wall shear stress	180
8.3	Case I: mean velocity profiles	181
8.4	Case I: shear stress profiles	182
8.5	Case II: growth velocity decay rate	183
8.6	Case II: wall shear stress	184
8.7	Case II: mean velocity profiles	185
8.8	Case II: shear stress profiles	186
8.9	Case III: growth/velocity decay rate	187
8.10	Case III: wall shear stress	188
8.11	Case III: mean velocity profiles	189
8.12	Case III: shear stress profiles	190
8.13	Case IV: growth/velocity decay rate	191
8.14	Case IV: mean velocity and shear stress profiles	192
8.15	Case V: growth/velocity decay rate	193
8.16	Case V: mean velocity/shear stress profiles	194

8.17	Case VI: growth/velocity decay rate	195
8.18	Case VI: wall shear stress	196
8.19	Case VI: mean velocity profiles \bar{U}/\bar{U}_m	197
8.20	Case VI: mean velocity profiles \bar{V}/\bar{U}_m	198
8.21	Case VI: shear stress profiles	199
8.22	Case VII: growth/velocity decay rate	200
8.23	Case VII: shear stress profiles	201
8.24:	Case VIII: growth/velocity decay rate	202
8.25	Comparison of entrainment rates	203
8.26	Wall pressure predictions.	204

PRINCIPAL NOTATION

a_1	\overline{uv}/q^2
C_f	skin friction coefficient = $\tau_w / \frac{1}{2} \rho \bar{U}_m^2$
D	diameter
d	diameter
e	general extra rate of strain
f	body force
H	shape parameter = δ^*/θ
h	= $1 + y/r$
K	= $\bar{U}/rh/\partial\bar{U}/\partial y$
k	turbulent kinetic energy = $\frac{1}{2} \overline{q^2} = \frac{1}{2} (\overline{u^2} + \overline{v^2} + \overline{w^2})$
k_1)) k_2)	constants in equation for hot-wire effective cooling velocity
L	integral length scale
L_ϵ	eddy dissipation length scale
ℓ	length or length scale of energy containing eddies
ℓ_o	mixing length
ℓ_C	mixing length with streamline curvature
ℓ_D	mixing length with streamline divergence
M	Mach number
\dot{m}_x	mass flow rates across line of constant x
\dot{m}_ω	mass flow rates across line of constant ω
\dot{m}_y	mass flow rates across line of constant y
Nu	Nusselt number
n	index or wave number
P	stagnation ^{pressure} or production rate of turb. kinetic energy
P_{ij}	production rate of stress tensor $\overline{u_i u_j}$
p	static pressure
p'	fluctuating component of static pressure

Re_p	slot Reynolds number = $\left\{ (P_o - P_{atm})rt/\rho v^2 \right\}^{\frac{1}{2}}$
Re_s	slot Reynolds number = $\bar{U}_s t/\nu$
Re_w	wire Reynolds number
R_{ij}	double velocity correlation function
\hat{R}_{ij}	normalised double velocity correlation function
R	axisymmetric radius of curvature
r	streamwise radius of curvature
Ri	Richardson number
s	distance interval
T	integral time scale or temperature
t	time or slot width
u_τ	$= \sqrt{\tau_w/\rho}$
\bar{U}	x-direction mean velocity
u	x-direction fluctuating velocity
\bar{V}	y-direction mean velocity
v	y-direction fluctuating velocity
\bar{W}	z-direction mean velocity
w	z-direction fluctuating velocity
x	streamwise coordinate along the or parallel to surface
x_o	distance of hypothetical origin upstream of slot
y	coordinate perpendicular to x-direction
z	circumferential direction

Greek Symbols

α	angle between axis of symmetry and tangent to surface or, angle between wire and x-direction
$\left. \begin{matrix} \alpha_1 \\ \alpha_2 \end{matrix} \right\}$	constants in streamline curvature correction to l_o
α_{20}	temperature coefficient of resistivity at 20° C

γ	ratio of specific heats
δ	shear layer thickness or kronecker delta
δ^*	displacement thickness
ϵ	turbulent energy dissipation rate
η	Kolmogorov length scale
θ	$\tan^{-1} \bar{V}/\bar{U}$ or momentum thickness
κ	law of wall constant
λ	mixing length constant
μ	viscosity
ν	kinematic viscosity
ν_T	turbulent shear stress
ξ	$y/y_{m/2}$
ρ	density
σ	mixing length constant for divergence correction
τ	shear stress or time interval
ν_E	Kolmogorov velocity scale
ψ	stream function
ω	$(\psi - \psi_I)/(\psi_E - \psi_I)$

Subscripts/Superscripts

amb/atm	ambient/atmospheric
B	bi-normal or bridge of anemometer
E	E boundary
eff	Effective
e/ ∞	free-stream
f	fluid
I	I boundary
i j k l	tensor components
L	linearized
m	maximum or mean
m/2	at $\bar{U}_{m/2}$

N	normal
n	exponent
s	slot
sup	supply
T	tangential
w	wire
xz	xz-plane
xy	xy-plane
X	grid position x
XM1	grid position one step upstream
XP1	grid position one step downstream
-	mean
'	differentiation with respect to length
$\vec{}$	vector

CHAPTER 1

INTRODUCTION

Flaring in the energy industry is a necessary consequence of having to safely dispose of tail gases produced in various industrial processes and also toxic gases which have to be completely burned. Coanda flares are in widespread use by British Petroleum at oil installations and also on off-shore production platforms in the North Sea, yet the design procedure is purely empirical.

Thus the motivation for the work reported here was to produce a computer model of the jet flow in order to aid the design and use of these flares. This necessitated an experimental study of the turbulence structure of the flow in order to provide data relevant to the further development of calculation methods for turbulent jet flows which have streamwise curvature and divergence of the mean flow streamlines.

1.1 THE COANDA FLARE

The basic principles and geometry of the Coanda flare are shown in Figure 1.1. The basic flare shape was designed at the B.P. Research Centre, Sunbury-on-Thames. A high pressure gas is forced from an annular slot at the base of the flare and follows the contour, entraining air as it goes. The entrainment rate is higher than that of the traditional pipe flare and so the gas burns with a turbulent pre-mixed flame usually giving completely oxidised combustion products. Thus pollution and radiation are reduced, the flame length is shorter, and in emergencies the flare is able to cope with the combustion of crude oil. Flame initiation does not occur until the widest part of the flare, i.e. the first quadrant of the flow is flame free. Thus a computer



prediction model without combustion features could still give a good indication of the jet characteristics in the region of flow where streamline curvature and divergence effects are most prominent. This region therefore plays the most important part in determining the flow structure.

It is necessary that the computer prediction model should be able to cope with a variable geometry and give satisfactory predictions of jet growth rate and turbulence levels. The main design criterion is that throughput and entrainment should be maximised using the simplest possible flare profile. The flare flow is described quantitatively by reference to Figure 1.2. Two-dimensional flow symmetry enforces the nominal identities:

$$\overline{W} = 0$$

$$\overline{UW} = 0$$

$$\overline{VW} = 0$$

where W is the circumferential component of velocity and the two double correlation terms involve the fluctuating component of W .

Wilkins et al (1977) provide a survey of various designs of flare in use. The commercially named Indair (Induced-air) flare has the same shape as that of Figure 1.1 but possess the added feature of an optional low-pressure supply which supplements the high-pressure supply by its introduction into the flame at the top of the flare. The involute of this shape (generated by a concave line rather than a convex one) has also been used successfully, mainly by using smaller individual flares but in a matrix with many others (Mardair - Marine-induced-air). This internal configuration produced lower noise and radiation levels and was primarily developed for use in the North Sea. It is not considered further as it has a substantially different flow structure.

1.2 THE COANDA EFFECT - STREAMLINE CURVATURE INDUCED BY AN ADJACENT BOUNDARY

The effect whereby a fluid attaches itself to an adjacent surface was first documented by Young (1800) as quoted by Wille and Fernholz (1956). Newman (1961) provides a reference to Reynolds (1870) who noted that a ball placed on top of a vertical axisymmetric jet of water remains in stable equilibrium. Likewise the flow of gas around the flare is stably adhered to the flare surface, the necessary centrifugal force being produced by the low-pressure region immediately adjacent to the surface. Coanda patented several devices for thrust augmentation on aircraft and it was through this work that his name became associated with the effect rather than the understanding of it. Consequently the term "Coanda effect" is often applied as a blanket expression to the phenomenon of a wall jet on a convex surface, without distinguishing certain important features. Wille and Fernholz (1956) distinguish two phenomena, one inviscid, the other a consequence of viscous interaction between the jet and the surrounding fluid. Bradshaw (1973) gives a detailed description where the term "Coanda effect" covers three phenomena:-

- (a) the tendency of a fluid to remain attached to a curved surface that is a simple consequence of the inviscid flow equations (for a liquid jet, surface tension promotes attachment);
- (b) the acceleration of the ambient fluid (entrainment) thereby causing a low-pressure region if the jet is adjacent to a wall - the jet 'sucks' itself onto the wall and this is a viscous phenomenon;
- (c) the effect of streamline curvature on a mixing layer which in this case causes a marked increase in growth rate of the jet.

Item (c) is the most important single effect of streamline curvature on a wall jet. It is important to distinguish the difference

between stably and unstably curved flows. According to the stability criterion of Rayleigh (1916), a fluid element in a curved flow whose angular momentum decreases with increasing distance from the centre of curvature is unstable. Radial displacement of the fluid element away from the centre of curvature places it in a region of lower angular momentum. Therefore, the local radial pressure gradient will be too small to contain the fluid element and so it will move further away from the centre of curvature. Thus unstably curved flows ($\partial(Ur)/\partial y$ negative) have increased turbulence levels and growth rates compared with the same uncurved flow. The converse argument holds for stably curved flows ($\partial(Ur)/\partial y$ positive) which show a reduction in turbulence activity. The convention implied above is that r is positive for convex curvature and negative for concave curvature.

A parallel and equally important phenomenon is the effect of divergence of the mean flow streamlines on the turbulence structure. Divergence here is meant as a collective term for flows with either diverging or converging mean flow streamlines. For a diverging flow (α positive in Figure 1.2), the turbulence is increased, thus increasing the jet entrainment rate and making $\partial U/\partial x$ more negative, consistent with the continuity equation. The converse is true for a converging flow. Bradshaw (1978) attributes increased mixing to the increase in vorticity along an axis perpendicular to the plane in which the cross section of a fluid element is decreased.

The combined effects of streamline curvature and divergence produced a highly turbulent flow for the region of interest $90^\circ > \alpha > 0$.

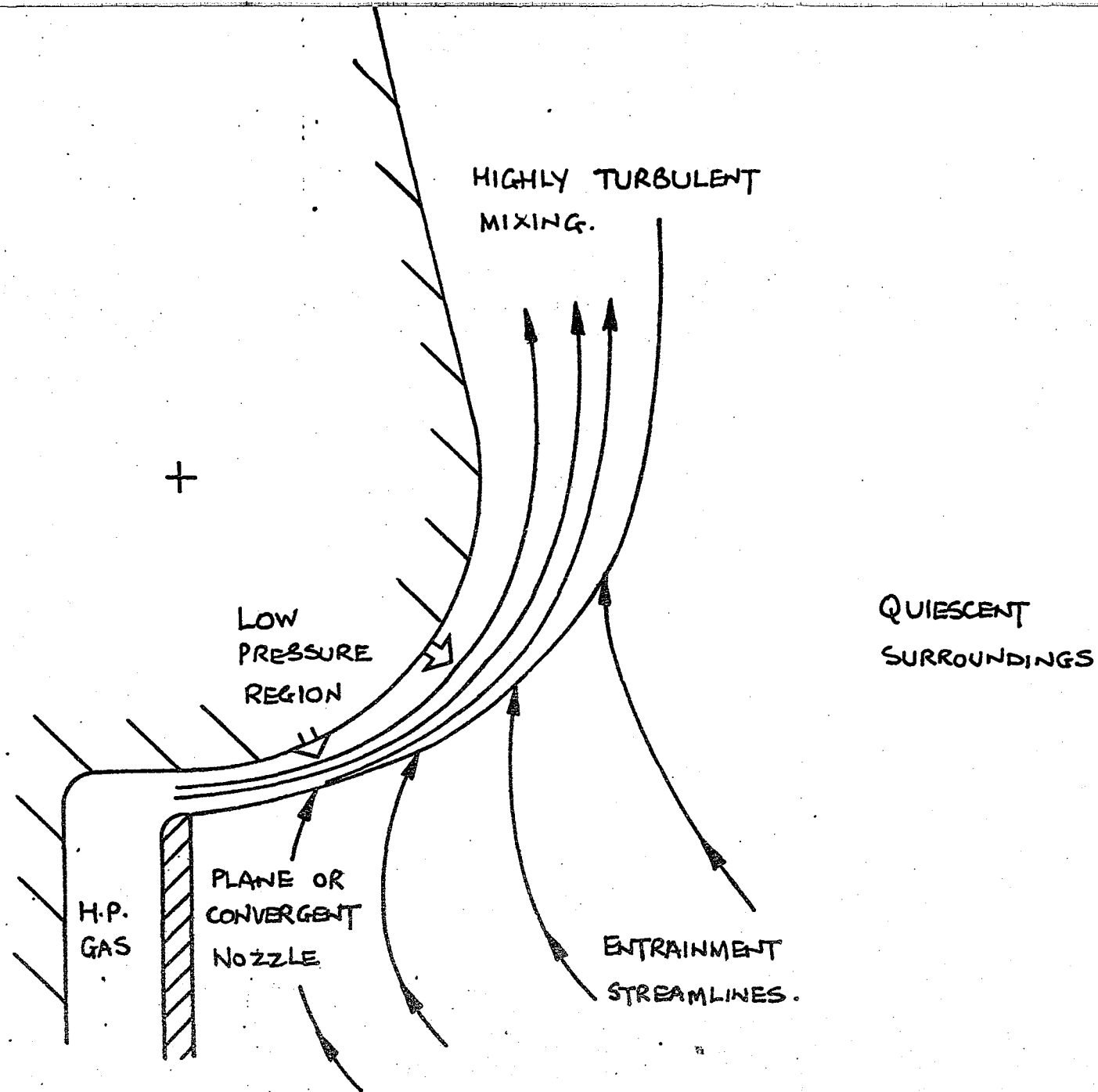
1.3 BREAKAWAY

This is a phenomenon where the flow separates from the flare

surface at or just downstream of the slot. It is likely to be a compressible flow effect, probably separation induced by shock waves, and therefore occurs under choked conditions. This investigation is concerned with the incompressible aspects of the flow structure and primarily the influence of the flare profile on the turbulence structure and the implications for the calculation method. Breakaway warrants an investigation of its own and is not considered further.

The work reported here falls naturally into two parts: chapters three, four and five describe the experimental work undertaken with a view to studying the turbulence structure of the jet; chapters six, seven and eight describe the development of a calculation method and recommendations for a suitable turbulence model. The remaining chapters describe the comparisons between the experimental results and the computer predictions.

FIG. 1.1 Basic
Principles and Geometry
of Coanda Flare



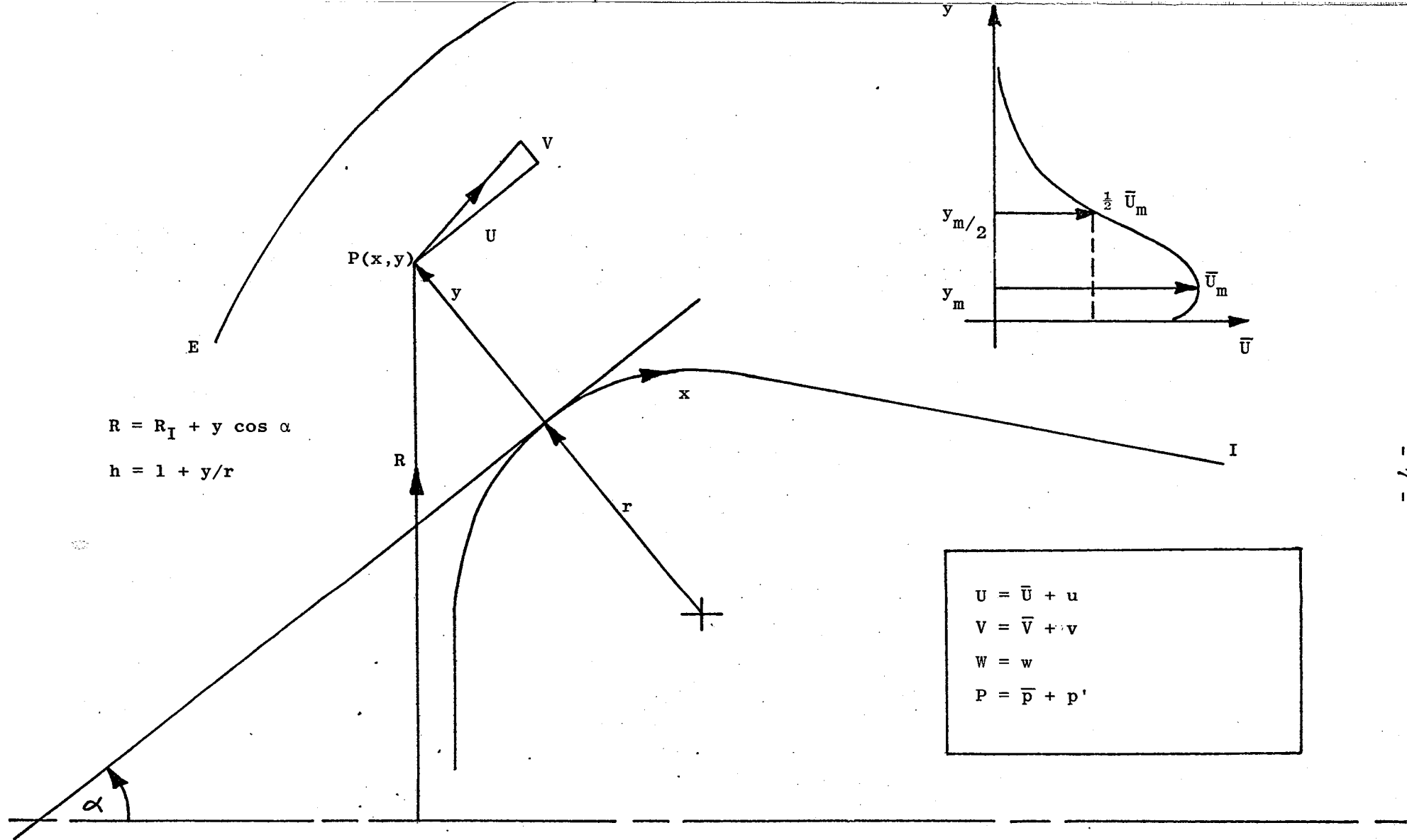


FIG. 1.2 Coordinate System (z is the circumferential coordinate)

CHAPTER 2

THEORETICAL BACKGROUND

Turbulent shear layers are only a small section of the enormous field of turbulent flows. They share the distinguishing characteristic that there is a substantial gradient of total pressure across their width. The study of shear layers is therefore important in order to be able to predict flows with practically important boundary conditions. Distorted shear layers provide a sub-class of flows which require even greater understanding of the physical processes involved. Therefore this chapter includes a brief summary of how turbulent flows are described. It also includes a review of previous work concerning wall jets and of more recent studies of the effects of streamline curvature and divergence on shear flow structure. The standard texts of Townsend (1976), Hinze (1975), Rotta (1962) and Bradshaw (1971, 1976a) provide a much more thorough treatment of turbulent shear flows.

2.1 INTRODUCTION

A complete mathematical description of turbulence necessarily involves statistical theory and is too complicated for engineering applications. Qualitative descriptions often use the concept of the eddy or vortex where random vortex stretching causes interaction between fluctuations of different sizes and orientation (expressed by the non-linearity of the equations of motion). Thus length scales and velocity or time scales range from typical values for the bulk flow down to the smallest motions, where this minimum is set by the viscous dissipation of energy. Energy enters the turbulence by interaction of the larger eddies with the mean flow field, without which the turbulence would decay. These larger eddies carry most of the turbulent kinetic energy and the transmission of this energy to smaller and smaller scales (the

energy cascade) is independent of viscosity except in the final stages. Transport equations are used to describe the life history of eddies or vortices, although for the sake of simplicity certain assumptions have to be made.

2.1.1 The Generalised Equations of Motion

All the equations in this chapter refer to constant property values of density, temperature and viscosity of a Newtonian fluid. The Navier-Stokes equation (momentum equation) can then be written in tensor notation as:-

$$\frac{\partial U_i}{\partial t} + U_\ell \frac{\partial U_i}{\partial x_\ell} = - \frac{1}{\rho} \frac{\partial p}{\partial x_i} + \nu \frac{\partial^2 U_i}{\partial x_\ell^2} + f_i \quad \dots (2.1)$$

where f_i represents the x_i -component of a body force such as gravity.

The continuity equation is:

$$\frac{\partial U_\ell}{\partial x_\ell} = 0 \quad \dots (2.2)$$

The "divergence" form of the left-hand side of the Navier-Stokes equation is obtained by adding U_i times the continuity equation to the left-hand side of equation (2.1) and becomes:

$$\frac{\partial U_i}{\partial t} + \frac{\partial (U_i U_\ell)}{\partial x_\ell}$$

Pressure fluctuations are always determined by the velocity field and can be calculated by taking the divergence of the Navier-Stokes equation (2.1) and using continuity to rearrange:

$$\frac{1}{\rho} \frac{\partial^2 p}{\partial x_i^2} = - \frac{\partial U_i}{\partial x_\ell} \frac{\partial U_\ell}{\partial x_i} = - \frac{\partial^2 (U_i U_\ell)}{\partial x_i \partial x_\ell} \quad \dots (2.3)$$

Equation (2.3) shows that pressure is not a locally defined quantity, but is an integral over the whole flow field; it is the Poisson equation for pressure. With the further restrictions that the flow is steady and two-dimensional, equations (2.1) to (2.3) reduce to equations (6.4) to (6.7). These equations are discussed more fully in Chapter 6.

Another important equation is that for the instantaneous rate of conversion of kinetic energy per unit volume to heat, viz:

$$E = \frac{1}{2} \nu \left(\frac{\partial U_i}{\partial x_j} + \frac{\partial U_j}{\partial x_i} \right)^2 \quad \dots (2.4)$$

which is important obviously in the smaller scales of motion. Its simplification is discussed in § 2.1.3.

2.1.2 The Statistical Description of Turbulence

In order to define a turbulent flow, it is necessary to specify a mean and fluctuating component for velocity vectors and the pressure field. Thus

$$U_i = \bar{U}_i + u_i \quad \text{and} \quad p_i = \bar{p}_i + p'_i$$

where \bar{p}'_i and $\bar{u}_i = 0$.

The eddy concept is used to describe typical flow patterns which contain a typical range of wavelengths of motion. The statistical mean most used to measure the spatial structure of turbulence is the double velocity correlation function:

$$R_{ij}(\underline{x}, \underline{s}, \tau) = \overline{u_i(\underline{x}, t) u_j(\underline{x} + \underline{s}, t + \tau)} \quad \dots (2.5)$$

where $u_i(\underline{x}, t)$ is a component of the instantaneous velocity fluctuation at position \underline{x} and time t . Underscores denote vector quantities.

Spatial correlations (or covariances) are used when $\tau = 0$, where R_{ij} is then a measure of the strength of eddies whose length in direction \underline{s}

is greater than s . Therefore the shape of the correlation function as s changes size gives some information about the eddy structure of the flow. Time correlations (autocorrelations) are also used when $s = 0$ and $i = j$. By definition $R_{ij} = 0$ as s or τ approaches infinity.

Taylor's hypothesis is an important experimental tool and proposes that if the mean velocity in the x -direction is very much greater than the turbulent fluctuations, then the changes in velocity pattern as it sweeps past a fixed point are negligible and therefore:

$$u_i(x, y, z, t + \tau) = u_i(x - \bar{U}\tau, y, z, t) \quad \dots (2.6)$$

Thus the longitudinal space correlation and time correlation are similarly related:

$$R_{ij}(x, -\bar{U}\tau, 0, 0) = R_{ij}(x, \tau) \quad \dots (2.7)$$

Correlations with separation in the direction of mean velocity are difficult to measure as an upstream probe will interfere with the one downstream. Therefore measurement of time correlations, and the use of Taylor's hypothesis is more accurate if a method of intrusive flow measurement is used.

The normalised form of the double correlation function:

$$\hat{R}_{ij}(x, s, t) = \frac{R_{ij}(x, s, t)}{R_{ij}(x, 0, 0)} \quad \dots (2.8)$$

is used for the measure of integral length and time scales, viz:

$$\begin{aligned} l_{ij}^L(x) &= \int_{-\infty}^{\infty} \hat{R}_{ij}(x, s, 0) ds \\ l_{ij}^T(x) &= \int_{-\infty}^{\infty} \hat{R}_{ij}(x, 0, t) dt \end{aligned} \quad \dots (2.9)$$

The most used of these is the longitudinal integral scale $L_L(x)$ which gives an indication of the mean eddy size in the longitudinal direction. Therefore it can be used as a typical length scale of the energy-containing eddies.

For convenience, the covariance $\overline{u_i(x) u_j(x+s)}$ is often replaced by its three-dimensional Fourier transform $\phi_{i,j}$ defined by:-

$$\overline{u_i(x) u_j(x+s)} = \int \phi_{ij}(n) \exp(i n s) dn \quad \dots(2.10)$$

where n is the wave number vector and $i = \sqrt{-1}$. ϕ_{ij} is then the three-dimensional wave number spectrum which has a distribution in "wave number space". Another form of $\phi(n)$ is:-

$$E(n) = \frac{1}{2} \int \phi(n) dA \quad \dots(2.11)$$

where δA is the elemental surface area of a surface bounding the wave number space. $E(n)$ represents the average density of turbulent energy in the wave number space at wave number n . However, one-dimensional spectra are used most as they provide the easiest means of physically interpreting the flow. Thus:

$$\phi_{ij}(n_1) = \frac{1}{2\pi} \int_{-\infty}^{\infty} \overline{u_i(x_1) u_j(x_1 + s_1)} \exp(-i n_1 s_1) ds_1 \quad \dots(2.12)$$

is the one-dimensional wave-number spectrum of $\overline{u_i u_j}$ for a wave-number component in the x_1 -direction. Frequency spectra can likewise be defined by the use of the Fourier transform of the autocorrelation.

The double velocity correlation or the wave number spectrum provide alternative ways of describing a turbulent flow. However,

this description is only complete if the probability distribution function for the velocity field is joint-normal, that is for each point in the flow field the probability of having a fluctuating component of velocity u is given by:

$$P(u) = \frac{1}{\sqrt{(2\pi u^2)}} \exp \left(-\frac{1}{2} u^2 / u^2 \right) \quad \dots (2.13)$$

A single-point distribution is practically of more use and in particular departures of the actual probability distribution function from the normal form give indications of the relative importance of higher order velocity correlations. For example, the skewness of the u -velocity distribution, $\overline{u^3} / (\overline{u^2})^{3/2}$, or the third central moment, is zero for a normal distribution. Also the corresponding fourth central moment, or the flatness factor $\overline{u^4} / (\overline{u^2})^2$ has a 'normal' value of three. A joint-normal distribution implies that the flow is homogeneous.

2.1.3 Homogeneity and Isotropy

A transport equation for the covariance $\overline{u_i(x) u_j(x + \underline{s})}$ can be written by adding u_i times the transport equation for u_j to u_j times that for u_i and then averaging. It is given by Bradshaw (1976a p 16) as:-

$$\begin{aligned} \frac{\partial \overline{u_i u_j^*}}{\partial t} + \overline{u_j^* u_{\ell} \frac{\partial u_i}{\partial x_{\ell}}} + \overline{u_i u_{\ell}^* \frac{\partial u_j^*}{\partial x_{\ell}^*}} = \\ - \frac{1}{\rho} \left(\overline{u_j^* \frac{\partial p}{\partial x_i}} + \overline{u_i \frac{\partial p^*}{\partial x_j^*}} \right) + \nu \left(\overline{u_j^* \frac{\partial^2 u_i}{\partial x_{\ell}^2}} + \overline{u_i \frac{\partial^2 u_j^*}{\partial x_{\ell}^{*2}}} \right) \end{aligned} \quad \dots (2.14)$$

where u_j^* is written for $u_j(x + \underline{s})$. Substitution of U_i as the sum of mean and fluctuating components yields a very complicated expression.

However, it can be simplified by assuming that statistical quantities are independent of position (Batchelor 1953, p. 34) i.e.:-

$$\overline{u_i(\underline{x})} = 0$$

$$\overline{u_i(\underline{x}) \frac{\partial u_i(\underline{x})}{\partial x_j}} = \frac{1}{2} \overline{\frac{\partial u_i^2(\underline{x})}{\partial x_j}} = 0$$

... (2.15)

which are the necessary conditions for homogeneous turbulence. In this case then, there is no mean flow and the spatial transport of $\overline{u_i^2}$ is zero. Most turbulent flows are inhomogeneous but the energy transfer processes are essentially the same whether the flow is homogeneous or not.

Equation (2.14) together with the averaged Navier-stokes and continuity equations do not provide a closed set of equations for a complete solution to the spectrum tensor $\overline{u_i u_j}$. If the equations were not averaged, then solution would be possible; but averaging introduces higher order correlations, for which it is possible to write transport equations also. However, higher order transport equations only introduce correlations of even higher order. Therefore it is necessary at some stage to introduce approximations to the higher order correlations. This is known as the problem of "closure". Approximations introduced into equation (2.14) imply a "spectral closure" of inhomogeneous turbulence which is very complicated. Therefore spectral closures are usually limited to homogeneous turbulence. However most closure work or 'modelling' refers to approximations made in the transport equation for $\overline{u_i u_j}$, the single-point second-order correlation. This procedure gives a realistically soluble set of equations and is discussed in Chapter 7.

Substitution of the mean and fluctuating components of velocity into Equation (2.4) gives after averaging:

$$\bar{E} + \epsilon = \frac{1}{2} \nu \left(\overline{\left(\frac{\partial \bar{u}_i}{\partial x_j} + \frac{\partial \bar{u}_j}{\partial x_i} \right)^2} + \overline{\left(\frac{\partial u_i}{\partial x_j} + \frac{\partial u_j}{\partial x_i} \right)^2} \right) \quad \dots (2.16)$$

where $E = \bar{E} + \epsilon$. \bar{E} is the dissipation of kinetic energy by mean velocity gradients and ϵ is the turbulent energy dissipation rate:

$$\epsilon = \frac{1}{2} \nu \overline{\left(\frac{\partial u_i}{\partial x_j} + \frac{\partial u_j}{\partial x_i} \right)^2} \quad \dots (2.17)$$

The energy cascade is an essentially random process and therefore does not have any directional preferences. As a result, the small-scale dissipating motions are statistically isotropic ($\overline{u^2} = \overline{v^2} = \overline{w^2}$). This is in fact not quite true as the small-scale motions fluctuate in space and time according to the large-scale fluctuations. However, with the simplifications of locally (small-scale) isotropic turbulence which is generally valid for high-Reynolds number flows, equation (2.17) reduces to:

$$\epsilon = \nu \overline{\left(\frac{\partial u_i}{\partial x_j} \right)^2} \quad \dots (2.18)$$

It is important to note that ϵ is set by the rate of energy transfer in the energy cascade and therefore by the larger energy-containing eddies. The viscosity determines the minimum size of eddy that can exist. Townsend (1961) showed, by dimensional arguments that:

$$\epsilon = \frac{k^{3/2}}{L_\epsilon} = C_{k,2} \frac{k^{3/2}}{\ell} \quad \dots (2.19)$$

and the turbulent kinetic energy is proportional to the turbulent shear stress. Then E is represented by a single length and velocity

scale, viz: L_ϵ , the eddy dissipation length scale and k the turbulent kinetic energy.

With the assumption of local isotropy, and that the statistics of the small-scale motions are determined uniquely by ϵ , ν and the wave number magnitude $n = |\underline{n}|$, Kolmogorov's universal equilibrium assumption uses velocity and length scales defined by:

$$\eta = (\nu/\epsilon)^{1/4} \quad \text{and} \quad \nu_\epsilon = (\nu\epsilon)^{1/4} \quad \dots (2.20)$$

If the wave-number spectrum ϕ_{ij} is used, then it is spherically symmetric in the region of local isotropy and

$$\phi_{ii}(\underline{n}) = \nu_\epsilon^2 \eta^3 f(n\eta) \quad \dots (2.21)$$

There may also exist a region at lower wave numbers in which the assumption of universal equilibrium is valid but in which the eddy structure is independent of viscosity. In this inertial subrange, ϕ_{ii} becomes:

$$\begin{aligned} \phi_{ii}(\underline{n}) &= C \epsilon^{2/3} n^{-11/3} \\ \text{and } \phi'_{ii}(n_1) &= C' \epsilon^{2/3} n^{-5/3} \end{aligned} \quad \dots (2.22)$$

where C and C' are constants.

Even though the concepts of local isotropy and universal equilibrium strictly refer to homogeneous turbulence, they are useful definitions for inhomogeneous flows also.

2.2 SHEAR LAYERS

Practically important flows such as shear layers are strongly inhomogeneous. In free turbulent shear flows, e.g. a free jet, inhomogeneity is caused by the spreading of the flow into the ambient irrotational fluid (entrainment). In wall shear flows it arises due

to the effect of the wall. With the consideration of only single-point correlations, a solution of the equations of motion is realistic. In this case the double velocity correlations are called Reynolds stresses.

2.2.1 Reynolds Stresses

The Reynolds stress tensor is $-\overline{\rho u_i u_j}$ and is a second order correlation. It therefore represents a set of nine stresses acting in the x_i -direction on a plane normal to the x_j -direction. Alternatively, the stress tensor represents the transfer of u_i -component momentum in the u_j -direction by the turbulence. Hence the stress components are apparent stresses. In Newtonian fluids the shear stresses ($i \neq j$) are diagonally symmetric. Then the effective number of component stresses is only six. In many shear flows, at least one of the shear stresses is zero by flow symmetry. One half of the sum of the normal stresses ($i = j$) is the turbulent kinetic energy, viz:

$$k = \frac{1}{2} \overline{q^2} = \frac{1}{2} \overline{u_i^2} \quad \dots (2.23)$$

2.2.2 Transport Equations

Following the procedure outlined in §2.1.3, the transport equation for $\overline{u_i u_j}$, the single-point correlation, can be written as follows:

$$\begin{aligned} \frac{D(\overline{u_i u_j})}{Dt} = & - \left(\overline{u_j u_\ell} \frac{\partial \overline{u_i}}{\partial x_\ell} + \overline{u_i u_\ell} \frac{\partial \overline{u_j}}{\partial x_\ell} \right) & (a) \text{ production} \\ & + \frac{p'}{\rho} \left(\frac{\partial \overline{u_i}}{\partial x_j} + \frac{\partial \overline{u_j}}{\partial x_i} \right) & (b) \text{ redistribution} \end{aligned}$$

$$\begin{aligned}
 & - \frac{\partial}{\partial x_\ell} \left(\overline{u_i u_j u_\ell} - \nu \frac{\partial \overline{u_i u_j}}{\partial x_\ell} + \frac{p'}{\rho} (\delta_{j\ell} u_i + \delta_{i\ell} u_j) \right) \\
 & \hspace{15em} \text{(c) transport} \\
 & - 2 \nu \frac{\partial \overline{u_i}}{\partial x_\ell} \frac{\partial \overline{u_j}}{\partial x_\ell} \hspace{15em} \text{(d) destruction} \\
 & \hspace{20em} \dots (2.24)
 \end{aligned}$$

where in the usual form (summed over repeated indices):

$$\frac{D(\overline{u_i u_j})}{Dt} = \overline{U_\ell} \frac{\partial \overline{u_i u_j}}{\partial x_\ell}$$

represents the rate of transport of $\overline{u_i u_j}$ through a unit control volume by the mean flow. It is assumed that the flow is steady and body forces are neglected. The kronecker delta operates so that $\delta_{ij} = 1$ for $i = j$ and $= 0$ for $i \neq j$. Equation (2.24) is the transport equation for Reynolds stress which with appropriate approximations, forms a closed set of equations with the mean momentum and continuity equations. Its component terms can be related to the physical process involved.

(a) Production

The generation term is a consequence of the interaction between the turbulent motion and the mean velocity gradient.

(b) Redistribution

This is called the pressure-strain term; it is the product of pressure fluctuations and the fluctuating rate of strain. It represents the effects of pressure fluctuations in acting to equalise the normal stresses and to reduce the shear stresses i.e. the tendency toward isotropy found in homogeneous turbulence, (Townsend (1976)).

(c) Transport

The three component terms are transport of $\overline{u_i u_j}$ by velocity fluctuations, viscous stress fluctuations and pressure fluctuations respectively. Viscous transport is negligible at high Reynolds

numbers (or away from the viscous sublayer - §2.2.4), as then it will only be significant in the small-scale motions which are isotropic, i.e. with no preferred direction. Transport by pressure fluctuations are thought to be smaller than term (b).

(d) Destruction

The destruction term provides the dissipation of turbulent kinetic energy by viscous stress fluctuations. Again for high Reynolds numbers the small-scale motions are isotropic and therefore this term will be negligibly small in the shear stress equation ($i \neq j$).

The physical processes outlined above are better described by the transport equation for turbulent kinetic energy, formed by addition of the transport equations for each of the three normal stresses:

$$\frac{Dk}{Dt} = \overline{u_i u_\ell} \frac{\partial \bar{u}_i}{\partial x_\ell} \quad \text{(a) production}$$

$$- \frac{\partial}{\partial x_\ell} \left(\overline{\frac{p' u_\ell}{\rho}} + \overline{\frac{q^2 u_\ell}{2}} \right) - \nu \frac{\partial^2 k}{\partial x_\ell^2} \quad \text{(c) transport}$$

$$- \nu \frac{\partial^2}{\partial x_\ell^2} \left(\overline{\frac{\partial u_i}{\partial x_\ell}} \right) \quad \text{(d) destruction}$$

. . . (2.25)

where $k = \overline{q^2}/2$. The terms in this equation are classified in the same way as for $\frac{D}{Dt} (\overline{u_i u_j})$. The production term is the rate at which mean velocity gradients do work against the Reynolds stresses, thereby transferring energy of the mean flow to the turbulent kinetic energy. The redistribution term of equation (2.24) vanishes by continuity when the three equations for $\frac{1}{2} \overline{u_i^2}$ are summed. This is to be expected as they represent exchange between the three normal stresses. The destruction term now becomes the dissipation of turbulent kinetic energy (equation

(2.18)) by the viscous stress fluctuations and its conversion to heat. This equation therefore describes the energy cascade. The transport equations for the Reynolds stresses and turbulent kinetic energy are shown in Appendix F.

Another practically important transport equation is that for ϵ itself. It is important as it is often used as the length scale transport equation in turbulence modelling (§ 7.1.3). Its development is complicated and is given by Hanjalic and Launder (1972) as:

$$\begin{aligned} \frac{D\epsilon}{Dt} = & -2 \nu \frac{\partial \bar{u}_i}{\partial x_k} \left(\frac{\partial u_i}{\partial x_\ell} \frac{\partial u_k}{\partial x_\ell} + \frac{\partial u_\ell}{\partial x_i} \frac{\partial u_\ell}{\partial x_k} \right) - 2 \nu \frac{\partial u_i}{\partial u_k} \frac{\partial u_i}{\partial u_\ell} \frac{\partial u_k}{\partial u_\ell} \\ & - 2 \left(\nu \frac{\partial^2 u_i}{\partial x_k \partial x_\ell} \right)^2 - \frac{\partial}{\partial x_k} \overline{u_k \epsilon'} - \nu \frac{\partial}{\partial x_i} \left(\frac{\partial p'}{\partial x_\ell} \frac{\partial u_i}{\partial x_\ell} \right) \end{aligned}$$

. . . (2.26)

where ϵ' is the fluctuating rate of dissipation. The equation is exact for high Reynolds numbers.

2.2.3 Local Equilibrium and Self-Preservation

Townsend (1961) distinguished areas in the inner layer of a turbulent wall flow (but outside the viscous sublayer) in which local rates of energy production and dissipation are much larger than the transport terms. These areas are therefore described as being in local equilibrium because transport terms are negligible. In slowly-changing boundary layers, where the length and velocity scales of the turbulence are proportional to those of the mean flow, local equilibrium is a good approximation for the outer part of the boundary layer as well. In this region the mean and turbulent transport terms tend to be equal and opposite.

Self-preservation is an extension of the assumption of local equilibrium. For a shear layer to be self-preserving, restrictive boundary conditions are required and the transport terms in the Reynolds stress transport equations are not negligible. The ratio of generation to the destruction terms is a simple function of y/δ ; it is only unity in the inner layer. Self-preserving shear layers must have dynamically similar profiles; that is not only the mean velocity profiles, but also profiles of Reynolds stress and other turbulence quantities must be representable by a single velocity and length scale. It is not surprising therefore that truly self-preserving flows are rare. However, certain shear layers, with unrestrictive boundary conditions, in which the Reynolds number is high enough and y/δ is outside the viscous sub-layer, can attain near-similar profiles of mean velocity when fully developed.

When a flow is considered to be in local equilibrium or self-preserving, simple empirical relations between Reynolds stress components and the mean rate of strain can be found.

2.2.4 Turbulent Flow Near a Wall

For regions of turbulent flow sufficiently close to a wall, velocity fluctuations are damped and the fraction of shear stress that is a direct result of viscosity increases. For this region, distances perpendicular to the wall are considerably smaller than the flow dimensions and in particular, derivatives of mean values in the x-direction are negligible compared with those in the y-direction. Hence the equations of motion can be simplified and the shear stress can be considered constant, equal to the value at the wall, τ_w . By dimensional analysis:

$$\bar{U} = u_\tau f\left(\frac{u_\tau y}{\nu}\right) \quad \dots (2.27)$$

where $u_\tau = \sqrt{\tau_w/\rho}$. The universal 'law of the wall' is typically valid for $y < 0.1 \sim 0.2 \delta$. In the viscous sub-layer (approximately $0 < y < 40 \nu / u_\tau$) viscous effects dominate. However, outside this region, but still inside the constant stress layer, the turbulent contribution to the shear stress is sufficient for viscosity to be neglected. Equation (2.27) then has the special semi-logarithmic form:

$$\frac{\partial \bar{U}}{\partial y} = \frac{u_\tau}{K y}$$

$$\frac{\bar{U}}{u_\tau} = \frac{1}{K} \ln \frac{u_\tau y}{\nu} + C \quad \dots (2.28)$$

where K is supposedly a universal constant, experimentally determined to be approximately 0.41, and $C \approx 5.2$ for a smooth wall. This region of flow, the inner layer, is the local equilibrium region in which turbulent transport terms are negligible. The outer layer is dominated by the larger eddies and is intermittent for $y > 0.4 \delta$. Vorticity is transmitted to the irrotational ambient fluid by viscous stresses; hence the term "viscous superlayer", the thickness of which is governed by the wavelength of the smallest eddies.

2.3 CLASSIFICATION OF SHEAR LAYERS

Equation (2.1) is the instantaneous momentum equation. The equation for mean momentum can be obtained by substituting $U_i = \bar{U}_i + u_i$ and averaging:

$$\bar{U}_\ell \frac{\partial \bar{U}_i}{\partial x_\ell} = - \frac{\partial \bar{p}}{\partial x_i} - \frac{\partial \overline{u_i u_\ell}}{\partial x_\ell} + \nu \frac{\partial^2 \bar{U}_i}{\partial x_\ell^2} \quad \dots (2.29)$$

Body forces are neglected and the flow is considered to be steady. Only two-dimensional shear layers are considered, hence the dummy index ℓ .

is repeated only twice. Shear layer axes are used for the equations of motion. The x-direction coincides approximately with the mean flow streamlines and is parallel to a wall or axis of symmetry. The y-direction is everywhere perpendicular to it.

Undistorted shear layers are simply classified because streamwise Reynolds stress gradients are often insignificant. However, for perturbed shear layers this is no longer the case and a more rigorous classification is necessary. Following Bradshaw (1973, 1975, 1976 b and 1978) a "complex shear layer" is defined as one in which extra rates of strain have a significant effect on the turbulence structure on top of that of the simple shear (usually $\frac{\partial \bar{U}}{\partial y}$). An "extra rate of strain" is an additional term appearing in the production term of the Reynolds stress transport equations whose size is explicitly changed by the flow conditions. Bradshaw (1975) considers the extra strain rate effects caused by streamline curvature, divergence and rotation amongst others. Inspection of equation (F.7) for example, reveals that the production term is explicitly changed by the curvature term U/rh . A general extra rate of strain e can be used for order of magnitude comparisons.

2.3.1 Boundary Layer/Thin Shear Layer

The turbulence structure of a simple shear layer is unaffected by the magnitude of the extra strain rate, e . In a thin shear layer ($\partial \bar{U} / \partial y \gg e$), e does affect the turbulence, but not the mean flow. Therefore, $\delta \ll x$, and the static pressure difference across the layer and the normal-stress gradients are negligible. Equation (2.29) therefore reduces to:-

$$\bar{U} \frac{\partial \bar{U}}{\partial x} + \bar{V} \frac{\partial \bar{U}}{\partial y} = - \frac{1}{\rho} \frac{d\bar{p}}{dx} + \frac{\partial}{\partial y} \left(-\bar{uv} + \nu \frac{\partial \bar{U}}{\partial y} \right)$$

where

$$- \frac{1}{\rho} \frac{d\bar{p}}{dx} = \bar{U}_{\infty} \frac{d\bar{U}_{\infty}}{dx} \quad \dots (2.30)$$

The assumptions above are the same as Prandtl's boundary layer assumptions and equations (2.30) are the boundary layer form of the momentum equation.

The transport equation for turbulent kinetic energy becomes:-

$$\begin{aligned} \frac{Dk}{Dt} = & - \bar{uv} \frac{\partial \bar{U}}{\partial y} - (\bar{u}^2 - \bar{v}^2) \frac{\partial \bar{U}}{\partial x} \\ & - \frac{\partial}{\partial y} \left(\bar{v} \frac{\bar{q}^2}{2} + \frac{\bar{p}'v}{\rho} \right) - \nu \frac{\partial^2 k}{\partial y^2} \end{aligned} \quad \dots (2.31)$$

An important simplification exists for the case of a local equilibrium flow where the transport terms in equation (2.3.1) are negligible.

Then retaining only the major production term;

$$- \bar{uv} \frac{\partial \bar{U}}{\partial y} = - \epsilon \quad \dots (2.32)$$

which, with use of equation (2.19) becomes:

$$\ell_o (\partial \bar{U} / \partial y)^2 = - \bar{uv} \quad \dots (2.33)$$

This is Prandtl's mixing length hypothesis which is strictly only valid for the equilibrium region of a simple shear layer because extra strain rates are ignored in the approximation of equation (2.31).

For the reasons stated in § 2.2.3, however, ℓ_o is a useful length scale for the calculation of a simple shear layer. See § 7.1.1.

A consequence of equation (2.33) in the log-law region of a wall shear layer is given by:-

$$\frac{\partial \bar{U}}{\partial y} = \frac{u_\tau}{K_y} = \left(\frac{-\overline{uv}}{\ell_o} \right)^{\frac{1}{2}}$$

where $u_\tau = -\overline{uv}$

$$\therefore \ell_o = K_y \quad \dots (2.34)$$

The last equation describes the variation of the mixing length in the log-law region.

2.3.2 Fairly Thin Shear Layer

For cases where $\frac{\partial \bar{U}}{\partial y} > 10 \epsilon$, the turbulence structure of the shear layer is greatly affected by the extra rate of strain, ϵ . Therefore the Reynolds stress gradients are significant in spite of the presence of possibly large pressure gradients. δ is considered as only one order of magnitude less than x . The flow studied in this project falls into this category and the approximations to the equations of motion are set out in Chapter 6. Previous work concerning the changes in turbulence structure is reviewed in § 2.5 and 2.6.

2.4 PREVIOUS WORK ON WALL JETS

This section reviews previous studies of wall jets on flat surfaces which are quite well documented. Earlier, less detailed work concerning wall jets on curved surfaces and cones is also reviewed. All the work reported below refers to two-dimensional cases although there is some detailed published work on three-dimensional wall-jets on both flat and curved surfaces by Catalano et al (1977). Three-dimensional wall jets are not strictly relevant to this investigation and are not considered further. There are also several review articles on turbulent jets in general by Newman (1961, and 1969) which serve as useful introductions to wall jets.

2.4.1 Turbulent Wall Jets On Flat Surfaces

Early theories concerned with wall jets were based on the near-similar solution obtained by Glauert (1956) for the turbulent case. For the purpose of analysis, the mean velocity profile can be considered as a typical half-jet up to the velocity maximum (the "outer layer"), inside which is a typical wall layer, (the "inner layer" - not directly associated with the law of the wall, § 2.2.4). Glauert assumed that the shear stress in the inner layer varied as \bar{U}^6 (Blasius's pipe-flow formula) and that therefore the velocity varies as $y^{1/7}$. The outer layer was assumed to have a constant eddy viscosity. A solution was sought in which the mean velocity profile varied according to:

$$U_m \propto x^a, \quad y_{m/2} \propto x^b \quad \dots (2.35)$$

although such a similarity solution can only be approximate because of viscous effects in the inner layer. A corollary of the above assumptions is that the shear stress is zero at the velocity maximum.

The values of a and b were found by Glauert to be dependent on the matching procedure used for the inner and outer layer solutions, but are approximately - 0.5 and 1.0 respectively. Schwarz and Cosart (1960) experimentally determined $a = -0.555$ and showed that the assumption of self-preservation implies $b = 1.0$. Myers et al (1963) reported a value of $a = -0.490$. Bradshaw and Gee (1962), however, noted two discrepancies in Glauert's theory. Firstly, the Blasius pipe-flow surface friction formula underestimated the surface friction by 25% and the experimental inner law was found not to be semi-logarithmic in form for the wall jet in still air. For the corresponding jet under a free stream, the inner law was found to be accurately semi-logarithmic. This therefore casts some doubt over the defect law overlap assumption in which it is expected that the law of the wall and the defect law

overlap in the log-law region. The second discrepancy was that the shear stress was not zero at the velocity maximum, therefore invalidating the separation of the mean velocity profile into an inner and outer layer. In spite of these two discrepancies, the similarity solution gives accurate prediction for the mean velocity of a turbulent wall jet. Bradshaw and Gee (1962) also found that the wall shear stress is well represented by:-

$$\frac{\tau_w}{\frac{1}{2} \rho \bar{U}_m^2} = 0.0315 \left(\frac{\bar{U}_m y_m}{\nu} \right)^{-0.182} \quad \dots (2.36)$$

in the range $3 \times 10^4 < \frac{\bar{U}_m y_m}{\nu} < 15 \times 10^4$ for a wall jet in still air.

Kacker and Whitelaw (1968, 1971) present a comprehensive set of experimental data for wall jets in a moving stream. Provided the ratio of maximum jet velocity to free stream velocity (\bar{U}_m/\bar{U}_e) exceeds unity, then the essential characteristics of a jet are maintained, although Irwin (1973) showed that the necessary condition for a jet to be self-preserving in a moving stream is:-

$$\bar{U}_e \propto (x_0 + x)^m \quad \dots (2.37)$$

where x_0 is the distance between the hypothetical origin of the jet and the slot. m is a function of \bar{U}_m/\bar{U}_e that equals -0.5 for $\bar{U}_e = 0$ and $\tau_w = 0$. Kacker and Whitelaw (1968) found that, in the region of twenty slot widths downstream, the law of the wall was in fairly good agreement with the experimental data for $K = 0.42$ and $C = 5.45$.

Also the point of zero shear stress was again found to be closer to the wall than the velocity maximum, an observation corroborated by Wilson and Goldstein (1976) and Irwin (1973). This was explained by the latter author to be the result of the difference between the diffusion rates of $\bar{u}v$ towards the velocity maximum, where local

production of \overline{uv} is at a minimum. The diffusion of positive \overline{uv} from the outer layer exceeds that of negative \overline{uv} from the wall region, thereby increasing the shear stress at the velocity maximum.

In the case of Irwin (1973), a wall jet in a free stream was studied, but with the additional constraint that the ratio of $\overline{U_m}/\overline{U_e}$ was constant thereby inducing a fairly severe positive pressure gradient. The law of the wall was again found to be a good fit to data in the region of $y < 1000 \sqrt{\nu/u_\tau}$ when the same values of K and C were used as those used by Kacker and Whitelaw (1968). Both the mean velocity, shear stress and turbulence intensity profiles were found to be closely self-preserving for distances sufficiently downstream, except where the position of zero shear stress became closer to the wall as x increased. $\overline{u^2}$ showed a minimum at the point of zero shear stress, and was also the largest of the three turbulence intensities. An energy balance was also carried out. It revealed that the rates of production and dissipation of turbulent kinetic energy were nearly equal for the whole jet width except near the velocity maximum ($0.05 < y/y_m/2 < 0.6$). This was attributable to the mean-flow transport and diffusion terms cancelling each other in the outer regions of the jet and their smallness near the wall. Also the production term did not become negative, not even when $\partial\overline{U}/\partial y \rightarrow 0$.

2.4.2 Turbulent Wall Jets With Streamline Curvature

Newman (1961) and Bradshaw and Gee (1962) first noted the increased growth rate of specifically a jet on a curved surface and the qualitative explanation of centrifugal instability described in Chapter 1 was used to explain it. Since then most work has been concentrated on the study of mean-velocity profiles of jets on circular cylinders.

Guittou (1967) showed that for a curved turbulent wall jet to be self-preserving, the ratio of jet thickness to wall radius of curvature should be constant. For this to be so, the wall radius is directly proportional to the distance x along the wall, and forms a logarithmic spiral surface. Giles et al (1966) measured mean-velocity and turbulence intensity profiles on such a surface and they were found to be similar. Owing to a lack of self-preservation of curved wall jets in general, where a log-spiral surface curvature is a too restrictive requirement, early curved wall jet predictions relied on empirical growth rates. Newman (1961) used:

$$\frac{y_{m/2}}{x} = 0.11 \left(1 + 1.5 \frac{y_{m/2}}{r} \right) \quad \dots (2.38)$$

whilst Guittou (1964), correlating the data of Fekete (1963) obtained:

$$\frac{y_{m/2}}{x + x_0} = 0.067 \left(1 + 4.48 \left(\frac{y_{m/2}}{r} \right) - 1.34 \left(\frac{y_{m/2}}{r} \right)^2 \right) \quad \dots (2.39)$$

Wilson and Goldstein (1976) used:

$$\frac{y_{m/2}}{t} = 0.0787 \left(\frac{x}{t} + 6.0 \right) \left(1 + 2.956 \left(\frac{y_{m/2}}{r} \right) - 0.1599 \left(\frac{y_{m/2}}{r} \right)^2 \right)$$

$$\left(\frac{\bar{U}_s}{\bar{U}_m} \right)^2 = 0.0359 \left(\frac{x}{t} + 6.0 \right)^{1.05} \left(1 + 3.354 \frac{y_{m/2}}{r} \right) \quad \dots (2.40)$$

and also demonstrated the non-selfpreserving nature of the flow by reference to profiles of \bar{V}/\bar{U}_m which were not similar for the curved case, but were for a wall jet on a flat plate. Profiles of \bar{U}/\bar{U}_m were too insensitive to show the degree of similarity.

A review of work on the turbulence structure of wall jets with streamline curvature is deferred until § 2.6.

2.4.3 Axisymmetric Turbulent Wall Jets

Radial, conical and cylindrical wall jets are treated collectively here as they all have basically the same axisymmetric geometry. The radial and cylindrical cases can be considered as limits to a general conical wall jet where $0 < \alpha < 90^\circ$.

Bakke (1957) made pitot-tube measurements in a radial wall jet, the results of which were used to obtain best agreement with Glauert's theory by adjustment of a single constant. The similarity constants a and b were found to be -1.12 and 0.94 respectively, i.e. the jet growth rate is approximately the same and the velocity decay rate is about ^{twice} ~~half~~ that of a corresponding plane wall jet. Poreh et al (1967), using hot wire probes, also found the mean velocities to be similar and in good agreement with Glauert's theory at sufficiently large distances downstream. The turbulence intensity profiles showed a limited degree of similarity. The data showed a slightly smaller jet growth rate than that of Bakke and using $K = 0.4$ and $C = 5.5$ in the law of the wall, a shift in the inner layer velocity profile was noted. Starr and Sparrow (1967) also noted, for a cylindrical wall jet, the same shift from the law of the wall line calculated using $K = 0.4$ and $C = 5.1$. The values used by Irwin (1973) and Kacker and Whitelaw (1968) for the flat-plate wall jet are not significantly different from those stated above, therefore the shift may be attributed to the axisymmetry and consequently the modified turbulence structure of the radial and cylindrical wall jets. Starr and Sparrow (1967) also developed empirical Coles-type wake functions in order to correct the wall jet inner layer velocity profiles for transverse curvature effects. Both they and Poreh et al (1967) noted that the position of zero shear stress did not consistently coincide with the velocity maximum. Not surprisingly therefore, neither authors found the shear stress to be proportional to the mean velocity gradient in the

region outside the velocity maximum. Sharma (1981) used pitot tube measurements for a comparison of the law of the wall constants for radial, conical and cylindrical wall jets. All the inner layers of the velocity profiles were sufficiently well correlated by the law of the wall when $K = 0.55$ and $C = 7.6$ for $y U_T/\nu < 200$. However the accuracy of the data appears to be rather uncertain, as there is no record of corrections for turbulence to the pitot readings and the ratio of pitot outside diameter to jet width was large.

2.5 THE EFFECTS OF EXTRA RATES OF STRAIN ON TURBULENT FLOW

Bradshaw (1973) provides a very thorough discussion of how extra strain rates affect turbulence. The discussion is primarily concerned with streamline curvature, being the single most important extra rate of strain, but also includes a study of the effects of divergence, dilatation and longitudinal acceleration. The most important fact, pertinent to all turbulent flows subjected to an extra rate of strain, is that the effect on the turbulence structure is an order of magnitude greater than that predicted by the extra terms in the Reynolds stress transport equations. The reason is that on top of these explicit changes to the production and transport terms (see Appendix F), higher order correlations are also changed, thereby implicitly changing the sizes of all the terms. This has important implications for calculation methods (see § 7.4) and these implicit changes are generally more important than the explicit changes. Bradshaw (1973) uses the local equilibrium approximation to develop a first order correction for the effects of small extra strain rates on thin shear layers. Defining

$$f = 1 + a \frac{e}{\partial \bar{U} / \partial y} \quad \dots (2.41)$$

to account for the explicit changes in the production terms, where a is $O(1)$, then:-

$$-\overline{uv} \frac{\partial \overline{U}}{\partial y} \cdot f = \frac{(-\overline{uv})^{3/2}}{L_{\epsilon,0}} \quad \dots (2.42)$$

where $L_{\epsilon,0}$ is the dissipation length scale for a simple shear layer. However, the observed changes are of order F where F is $O(10f)$. Therefore adjustment of the length scale is required by use of:

$$L_{\epsilon} = \frac{F}{f} \cdot L_{\epsilon,0}$$

implying

$$F = 1 + \alpha \frac{e}{\partial \overline{U} / \partial y} \quad \dots (2.43)$$

where α is $O(10)$. This approach is expected to be valid only for small e , and does not take into account 'history' effects, i.e. modification of the larger, and therefore non-local, eddy structure. The value of α is not expected to be universal either, and equation (2.43), although derived by use of the local equilibrium assumption, could be used in flows not far from local equilibrium. α would then inevitably contain a factor to account for the inaccuracy of the local equilibrium assumption.

2.6 THE EFFECTS OF STREAMLINE CURVATURE ON TURBULENT FLOWS

The qualitative concepts of stabilising and destabilising curvature were introduced in Chapter 1. The differentiation between stably and unstably curved flows provides a useful sub-class of curved flow. Therefore boundary layers with concave curvature and wall jets with convex curvature are discussed together, although the implied connection between the two is tenuous due to the lack of detailed experimental data for the latter. However some thorough measurements have been made in

stably and unstably curved boundary layers notably by Smits et al (1979a) and So and Mellor (1972), and these studies provide a useful comparison between the effects of the two types of curvature.

According to the F-factor analysis of Bradshaw (1973), a linear correction formula for streamline curvature is:

$$F = 1 - \alpha \frac{\bar{U}/rh}{\partial \bar{U}/\partial y} \quad . . . (2.44)$$

where the extra rate of strain is $-\bar{U}/rh$ in shear layer coordinates appropriate to Figure 1.2. Bradshaw also gives a thorough review of previous research on turbulent flows with streamline curvature, starting with Prandtl's buoyancy-curvature analogy and including curved duct and rotating cylinder flows. These flows exhibit curvature effects of order F. The more pertinent studies relate to mixing layers and boundary layers on curved surfaces.

2.6.1 Longitudinal Vortices

One of the most striking features of an unstably curved flow is the appearance of longitudinal vortices, a basically inviscid phenomenon. The displaced-element arguments used in Chapter 1 to explain the increased growth rate of a mixing layer with a negative gradient of angular momentum can be extended to predict the occurrence of streamwise vortices. (Bradshaw and Cebeci (1977 p. 304)). Their diameter (half a spanwise wavelength) is roughly the same as the shear layer thickness and the streamwise wavelength is effectively infinite (a typical streamwise wavelength of longitudinal vorticity of a large eddy would be only of the order of a few boundary layer thicknesses). The strength of the vortex increases with distance downstream assuming the curvature continues. The occurrence of these vortices was first noticed by Tani (1962)

in a boundary layer although Taylor and Görtler had previously predicted their appearance in laminar flows. They are therefore called Taylor-Görtler vortices also.

Tani (1962) found spanwise variations in mean velocity of a boundary layer on a concave surface. The variations were of a definite wavenumber for both laminar and turbulent cases. Accordingly he adapted the Görtler stability parameter, used for laminar flows,

$$G = \frac{\bar{U}_e \theta}{\nu} \left(\frac{\theta}{r} \right)^{\frac{1}{2}} \quad \dots (2.45)$$

by replacing ν with the effective viscosity ν_{eff} in order to predict the appearance of vortices in a turbulent flow. However, as Bradshaw (1973) suggests, a critical Görtler number at which the turbulence becomes dominated by longitudinal vortices is somewhat arbitrary although it provides a quantitative comparison of the likelihood of their occurrence. Patel (1969b) also found spanwise variations in mean velocity and skin friction coefficient, where the surface shear stress is low beneath vortex motion away from the wall (trough) and high beneath vortex motion towards the wall (crest). Hence a pair of quasi-steady or steady contra-rotating vortices would give rise to the observed spanwise variations.

Bradshaw (1973) draws attention to the need for distinguishing between steady and "steady" vortices (using his quotation marks). Steady vortices are referred to as such because they contribute to the mean flow spanwise variations. "Steady" vortices refer to those which, although they have a time scale much larger than the rest of the turbulent motion, are not constrained well enough to contribute to any mean spanwise periodicity. Thus steady vortices can produce three-dimensionality in a nominally two-dimensional flow, whilst "steady"

vortices, sufficiently unsteady not to contribute to the mean periodicity, contribute to the Reynolds stresses only and the mean flow is legitimately two-dimensional but with the shear stresses \overline{uw} and \overline{vw} non-zero. Bradshaw also discusses two means of constraint on longitudinal vortices. One is the influence of wall boundaries where the distance between them must be an integer number of vortex diameters. The other is the influence of upstream disturbances (e.g. vorticity induced by wind tunnel damping screens) which could have some effect on the mean spanwise positions of vortices which can be locked to the initial disturbances when the flow is unstably curved.

The practical necessity of an integral number of vortices makes calculation of wavelengths difficult. Also for a rapidly growing shear layer, the number of vortices must increase if their wavelength is not to become an over-small fraction of the shear layer width. Bradshaw (1973) suggests that the appearance of "steady" vortices in an unstable jet flow is unlikely, simply because of the large-growth rate which would require the frequent re-adjustment of the spanwise wavelength in order to maintain the preferred ratio of wavelength to shear layer thickness.

2.6.2 Unstably-Curved Wall Shear Layers

The earliest authoritative study of the turbulence structure of a wall jet with destabilising curvature is that of Guitton (1970) and subsequently Guitton and Newman (1977). Their work can be regarded as a sequel to that of Giles et al (1966) who made Reynolds stress measurements in a wall jet on both concave and convex log-spirals. Guitton used corrections of up to fourth-order correlations for the second order correlations and linearized the hot-wire signal. He measured the Reynolds stress components, the third order correlations $\overline{uv^2}$ and $\overline{uw^2}$ and the intermittency and flatness factors for spirals with $x/r = 0, 2/3$ and 1.

He also compares his results to those of Giles et al (1966) for the case $x/r = 1$. One of the major problems was the establishment of two-dimensional flow. Two methods were used to check for two-dimensionality: firstly, the comparison of the measured shear stress distribution with that calculated from the two-dimensional integral momentum equation using the mean velocity data, and secondly, the spanwise measurements of total pressure. The non-two-dimensionality of the flow can be attributed to two effects. The secondary flows (i.e. "skew-induced" after the definition of Bradshaw and Cebeci (1977 p. 320)), occurring in the corners with the end walls could have significant effect on the displacement thickness of the end wall boundary layers thereby causing some divergence or convergence of the flow at centre-span. Also, it has been found by Guitton and Newman (1977) and Fekete (1963) that the flow is extremely sensitive to initial disturbances, i.e. non-uniformity in the initial flow or slot geometry. These two effects were corrected for as far as possible and then the flow showed no signs of any spanwise periodicity.

After attention to the initial conditions, the flow was found to be self-preserving in most cases, although some of the $\overline{u^2}/\overline{u_m} \sim y/y_m/2$ profiles were not similar near the wall. It appeared that the outer layer exerted a higher influence on the near-wall regions as the curvature increased. For the $x/r = 2/3$ case, the position of zero shear stress was at $y/y_m = 0.3$ whilst for the $x/r = 1$ case, it was at $y/y_m = 0.1$. Also the law of the wall with $K = 0.42$ and $C = 5.45$ applied for $yu_T/\nu < 150$ but only in the $x/r = 2/3$ case, the implication being that the curvature effected the near-wall region in the $x/r = 1$ case. However, Bradshaw (1973 p 56) argues that curvature effects on the law of the wall are negligible.

Apart from the increase in turbulence energy over the flat-plate geometry, the most interesting results were those relating to the non-dimensional turbulence parameters $\overline{v^2}/\overline{u^2}$, \overline{uv}/q^2 (a measure of the efficiency of the turbulence in producing shear stress) and the profiles of $\overline{uv^2}$. The ratio $\overline{v^2}/\overline{u^2}$ was found to increase with increasing curvature, i.e. the radial motion is increased with increasing instability. However, profiles of \overline{uv}/q^2 appeared to be insensitive to curvature maintaining their flat-plate wall jet values. Therefore the turbulence shows a much higher degree of self-preservation when the turbulence parameters are scaled relative to one another as suggested by Bradshaw et al (1967). The third order product $\overline{uv^2}$, and to a lesser extent $\overline{uw^2}$, were both significantly affected by the curvature. In the $x/r = 0$ case, $\overline{uv^2}$ has a negative value near to the wall, which almost disappears when $x/r = 1$. Thus turbulent transport of negative \overline{uv} away from the wall is much reduced, implying a smaller effect of the wall on the outer jet. This reduction therefore agrees with the observation that the position of zero shear stress moves towards the wall as the curvature increases.

The intermittency measurements showed that the value of $y/y_{m/2}$ at which the intermittency was constant moved towards the wall for increasing curvature. Bradshaw (1973) offers an explanation by way of the existence of unsteady large-eddy vortices. Bradshaw and Gee (1962) used the $R_{22}(0,0,s)$ correlation to trace the existence of unsteady longitudinal vortices which would show up as a larger negative region in the correlation at say $y = y_{m/2}$. However, no such effect was observed in the data when compared with the same correlation in a flat-plate wall jet. Therefore either these vortices do not exist at $y = y_{m/2}$ or are of quite a different length scale to the large eddies, i.e. s.

Wilson and Goldstein (1976), make no mention of either the problems concerning the two-dimensionality of the flow, nor the possible existence of longitudinal vortices. The ratio of jet width to slot height was about 85 whereas in Guitton's case it was about 200. Therefore some end-wall effects are to be expected. The hot-wire signal was effectively linearized during the analysis. The effect of curvature on self-preservation was discussed in § 2.4.2 and apart from this, the turbulence data showed similar curvature effects to those of Guitton (1970). The ratio of $\overline{v^2}/\overline{u^2}$ was increased, whilst \overline{uv}/q^2 was unaffected by the curvature.

Experimental studies of boundary layers on concave walls offer a further source of information on unstably curved shear layers. Meroney and Bradshaw (1975), So and Mellor (1972, 1975) and Smits et al (1979a) are among these and they all did parallel studies of stabilising curvature. For a curvature of only $\delta/r = 1/100$, Meroney and Bradshaw observed steady longitudinal vortices that could be consistently reproduced and showed a wavelength of about one half the boundary layer height. The surface pressure exhibited a spanwise periodicity and the non-dimensional plots of $\overline{u^2}$ showed a significant variation across the width of a longitudinal vortex. However, it was assumed that the lateral velocities associated with the vortex system did not affect the hot-wire analysis. The remaining Reynolds stress profiles showed the expected increase in turbulent kinetic energy and a larger region of higher shear stress near the maximum of the profile.

So and Mellor (1972, 1975) also established the presence of longitudinal vortices for $\delta/r \simeq 1/12$. The curvature of the convex wall was adjusted so that the pressure distribution along the concave test wall remained constant. Air jets were used to accelerate the end-wall

boundary layers in order to reduce the effects of secondary flows. The spanwise variations in mean velocity were smaller than those found by Patel (1969b) who used approximately the same value of δ/r , although, oddly enough, the variations in wall shear stress were negligible. The turbulence intensities changed in the expected sense and in particular the components \overline{uw} and \overline{vw} were found to be non-zero; \overline{uw} was positive at a trough and negative at a crest of the mean spanwise variations whilst \overline{vw} changed in the opposite sense. The ratio \overline{uv}/q^2 had a value in the region of 0.15, its flat-plate value, whilst $\overline{v^2}/q^2$ showed the expected increase in the radial component of turbulence intensity. The turbulence data are presented without distinguishing between crest and trough spanwise locations which makes interpretation difficult. However most of the data seem to fall broadly into two groups on most of the plots.

Smits et al (1979a) examined the boundary layers downstream of a 20° and 30° arc of 'impulse' curvature ($\delta/r = 1/12$, concave; $\delta/r = 1/16$, convex). A true curvature impulse would require an infinite extra strain rate so that the turbulence structure changed instantaneously. In practice one cannot be applied. Steady longitudinal vortices were found on the concave wall which persisted indefinitely downstream. Thus measurements were made at the crest and trough spanwise positions in the flat section downstream and all the data in these two cases were treated separately. The pressure gradient downstream of the bend was small, therefore allowing a quantitative assessment of 3-D effects using the momentum integral equation. A hypothetical origin of the divergence could be calculated using values of C_f and θ . The data showed lateral divergence at crests and convergence at the troughs, which indicates a pair of contra-rotating vortices by reference to the continuity equation. The spanwise variations in C_f , \overline{V} and \overline{U} varied in phase with one another with a wavelength approximately one half of the boundary layer thickness at entry to the curved section. The bulk of the data

concerns the Reynolds stresses, third order correlations and the applicability of the law of the wall. These are discussed in great detail and only the more important items are noted here.

The turbulence structure recovers from the curvature only very slowly. At exit from the curved region, there are large values of $\partial(-\overline{uv})/\partial y$ which reduces $\partial U/\partial y$ in the outer edges of the boundary layer. Thus production of shear stress and turbulent kinetic energy falls below those values at entry to the curved section. Therefore the return of the turbulence to its pre-curvature self-preserving values is not monotonic. Bradshaw (1973) and Smits et al discuss the use of ordinary differential equations to account for 'history' effects (i.e. the effect of mean transport on Reynolds stress) in perturbed shear layers. These equations could be used in calculation methods to allow for a finite response time of a shear layer to an extra rate of strain and also for recovery after one is removed.

Both trough and crest data show non-monotonic reduction to self-preserving values. The ratio

$$a' = \frac{\overline{uv}}{3/2(\overline{u^2} + \overline{v^2})} \sim \frac{\overline{uv}}{\overline{u^2} + \overline{v^2} + \overline{w^2}}$$

was used as a dimensionless parameter for the data as $\overline{w^2}$ was not measured. For the crest position, a uniform value of 0.13 over most of the boundary layer width before the curved section rose to about 0.20 afterwards. Thereafter a' showed the same non-monotonic decrease, falling below 0.13 before increasing. This shows that the efficiency of maintaining the shear stress falls during the recovery section. $\overline{v^2}/\overline{u^2}$ rises at the end of the curved section, high values persisting at crests

and low values at troughs. It is little affected by curvature near the wall. The triple products $\overline{uv^2}$ and $\overline{q^2v}$, the turbulent transport velocities of \overline{uv} and $\overline{q^2}$ respectively are significantly affected. They increase by factors of between two and three for the 30° case.

2.6.3 Stably-Curved Wall Shear Layers

These are less relevant to the present investigation and are mentioned very briefly. Wyngaard et al (1968), a sequel to Rapp and Margolis (1967) and Margolis and Lumley (1965), studied both stable and unstable mixing layers in a curved duct. After correction to the dissipation measurements, an energy balance showed that the production and transport of kinetic energy was inhibited in the stable case and augmented in the unstable case. Castro and Bradshaw (1975) also studied the effects of stabilising curvature on a mixing layer. They found the same non-monotonic return of the turbulence to its uncurved self-preserving values as reported by Smits et al (1979a). The Reynolds stresses were found to decrease in the region of maximum curvature although suppression of the triple products associated with turbulent transport allowed an increase in turbulence intensity above the self-preserving values in the middle of the layer where production is at its highest. Smits et al (1979a) found that in the convex case, recovery to self-preservation was very much quicker than in the concave case. The stabilising effects were so large that the turbulence collapsed so that newly created turbulence experienced hardly any curvature effects. So and Mellor (1973) noted that $\overline{v^2}/\overline{u^2}$ was reduced by stabilising curvature.

2.7 THE EFFECTS OF STREAMLINE DIVERGENCE ON TURBULENT FLOWS

2.7.1 Relevance to the Present Work

The extra rate of strain associated with streamline divergence is, for a cartesian coordinate system, $\partial \overline{W}/\partial z$ (Bradshaw (1973)). For the

present flow where shear layer axes are used and where the circumferential direction is designated by z , it is:

$$e = \frac{\bar{U} \sin \alpha + \bar{V} \cos \alpha}{R} \quad \dots (2.46)$$

For a diverging flow (α positive), $\partial W / \partial z$ is positive as shown by equation (2.46); it is negative for a converging flow (α negative).

The F-factor correction equation of Bradshaw (1973) then becomes:

$$F = 1 + \alpha \frac{(\bar{U} \sin \alpha + \bar{V} \cos \alpha)}{R \partial \bar{U} / \partial y} \quad \dots (2.47)$$

It is worth noting that this extra rate of strain only appears in the production term of the transport equation for $-\overline{uv}$, equation (F.7).

(With reference to the continuity equation, for a positive value of $\partial \bar{W} / \partial z$, $\partial \bar{U} / \partial x$ becomes more negative implying an increased velocity decay rate). But the additional production terms act in the opposite sense to the main term $\partial \bar{U} / \partial y$, thereby reducing the production of $-\overline{uv}$. The observed increase in turbulence intensity is therefore attributable to the implicit changes in the other terms of equation (F.7) for positive $\partial \bar{U} / \partial y$ and \overline{uv} .

2.7.2 Previous Work

The literature concerning the effect of this extra strain rate on turbulent flows is much less complete than that for streamline curvature; more correctly, studies involving divergence have, by nature of the experiments, often included the effects of other extra rates of strain. For example, Patel et al (1974) studied a boundary layer near the tail of a body of revolution. This converging flow therefore showed the effects of convex streamline curvature and also transverse curvature where δ/R was large. The only work to date which has studied pure divergence effects is that of Smits et al (1979b). A detailed study

was made of a boundary layer on a cylinder-flare body where a fully developed boundary layer was subjected to lateral divergence on a cone. Transverse curvature effects were not apparent; $\delta/R = 1/4$ at the beginning of the flared section and decreased further downstream. In order to avoid three-dimensional effects at the cylinder-flare junction, a 20° curved section was used for smooth transition and the effects of the concave curvature appeared to die out fairly rapidly. A comparison with the data of the comparison work, Smits et al (1979a), allowed a qualitative assessment of the effect of only divergence on the flow structure.

The same measurements were made in this study as by Smits et al (1979a). The first traverse position was upstream of the transition section, the next immediately downstream of it and the remainder were on the flare. After attention to the effects of pressure gradient in the transition section, circumferential measurements were made with a Preston tube. These showed small variations which decreased downstream. No periodicity of wavelength 2δ was found and therefore it was concluded that no steady longitudinal vortices existed. None of the Reynolds stress profiles showed the collapse of turbulence after the removal of curvature exhibited in the case of destabilising curvature as found by Smits et al (1979a). Measurements far downstream of the curved transition section show that divergence effects are highly significant - of the same order as those of streamline curvature. For instance the shear stress data show the expected increase over the transition section, but they maintain their above-self-preserving values for the whole of the test region, falling gradually as the extra rate of strain $\partial \bar{W}/\partial z$ does. The position of the peak in these profiles moves steadily outwards as the downstream distance increases. Consequently $\partial \bar{U}/\partial y$ does not fall

and shear stress generation remains high. Hence the turbulence does not collapse downstream of the curved section.

The dimensionless structural parameter $a = -\overline{uv}/q^2$ is close to 0.15 at the first traverse station. It increases through the curved section and thereafter maintains a value above 0.15 except near the wall. This is ascribed to 'inactive' motion (Townsend (1976 p 123)) near the wall where $\overline{u^2}$ and $\overline{w^2}$ are preferentially increased over $\overline{v^2}$ and \overline{uv} . Plots of $-\overline{uv}/\overline{v^2}$ and $\overline{v^2}/\overline{u^2}$ support this conclusion and show an increase in $\overline{v^2}$ in the outer regions of the boundary layer. Non-dimensional plots of mixing length show little relation, if any, between mixing length and boundary layer width and suggest α , in equation (2.47) to be about ten. The triple products are magnified by a factor of five or more. The large but slow increase in these turbulent transport terms indicates modification of the large eddies in the outer part of the boundary layer and illustrates their long response time. An energy balance reveals very large increases in turbulent diffusion as expected from the above statements concerning the triple products. Plots of the dissipation length scale shows a general trend of an outward going maximum similar to that of the shear stress profiles.

2.8 SUMMARY

All measurements made in boundary layers on convex surfaces show the same increase in turbulence activity, specifically large increases in second and third order correlations, resulting in an increased shear layer growth rate. Experimental evidence also suggests the presence of steady or quasi-steady longitudinal vortices giving rise to crest and trough spanwise locations of wall shear stress. Values of second and third order correlations appear to be higher at the trough locations.

In the case of an impulse of curvature, the effects appear to be dependent on the total turning angle rather than δ/r , and the return to self-preserving values of turbulence quantities is not monotonic, indicating modification of the large eddy structure.

In the case of wall jets on convex surfaces, a similar increase in turbulence activity is found, although there is no evidence to prove the existence of longitudinal vortices. For all cases of unstably curved wall shear layers, the establishment of as near two-dimensional conditions as possible in the initial flow is of prime importance, and is made difficult by the three-dimensional effects of wind tunnel screens and secondary flows in duct corners. Stably curved wall shear layers show an opposite trend of turbulence suppression.

The less documented effects of streamline divergence on turbulent shear layers are of the same order as those of streamline curvature. A diverging shear layer appears to be destabilised leading to an increase in turbulence activity.

CHAPTER 3

APPARATUS AND EXPERIMENTAL PROCEDURE

The major part of the experimental work was carried out at Durham. This involved the design, construction and use of a model flare. Detailed flow measurements were taken using both hot-wire anemometers and a specially designed three-hole probe. Experimental work was also undertaken at B.P. Sunbury during the period of October to December 1979 on a full scale Indair flare. This work is described later on in this chapter and is referred to as 'large scale' tests.

3.1 MODEL FLARE TESTS

3.1.1 Flare and Plenum Chamber

The model flare was an exact 3/5 model of the flare used at Sunbury in the large scale tests - an eight inch Indair flare (I8-H-VS). In order to maximise use of the available air supply and also to facilitate probe mounting, a half-axisymmetric model was used, the flare and plenum chamber being mounted on a horizontal base-plate as shown in Figure 3.1. It was assumed that the presence of the base-plate would not have any effect on the flow (e.g. secondary flows) along the centre-line which was used for all the principal traverses. The surface pressure tappings detailed in Figure 3.2 were staggered either side of the centre-line to avoid possible interference with the flow.

In spite of the manufacturing difficulties, the flare was machined out of a solid block of mild steel. Machining was not only necessary on the outside to produce the flare contour, but also on the inside to allow mounting of a screw-thread assembly and an exit for the surface pressure tappings. The screw-thread assembly was fixed to the base-plate and therefore allowed a fine degree of adjustment to the slot

width measured by a micrometer screw-gauge. The motion of the flare was controlled by four feet which could slide in grooves milled into the base-plate. After adjustment the flare was clamped in position.

The plenum chamber was also cut from mild steel, in two pieces to allow a contraction of 4.84:1 so that the radius of the chamber at the throat was of the correct dimensions. The lip of the slot was machined to a radius (see Figure 3.1) and then given a flat so that the slot was plane. As the rig was being assembled, the accuracy of the slot was assessed. Slip gauges were used to check the uniformity of the slot both at nominally zero and nominally 5.0 mm slot widths. The variation was no more than 0.07 mm which for a nominal slot width of 5 mm represents 1.4% accuracy. The accuracy of the flare centre-line position relative to that of the base-plate centre-line was the best that could be achieved by use of the vertical milling machine to cut the feet on the flare and their grooves in the base-plate.

3.1.2 Air Supply

A 60 x 30 inch diameter welded air receiver was maintained at a pressure between 50 and 90 p.s.i.g. by two Broom and Wade BW11 compressors, each capable of producing 65 c.f.m. after cooling. The upper limit to the flow could be extended by using the air receiver as a blow-down facility. The maximum throughput recorded could be maintained at 180 s.c.f.m. (0.1 Kg/sec) for an interval of two to three minutes.

The pipe work connecting the air receiver to the rig was of $1\frac{1}{4}$ " diameter B.S.P. (see Figure 3.3). The air was filtered and regulated by a Norgren filter (30 CG 10, 25 micron element) and regulator

(11-908-910). In order to improve the regulation characteristics, a feedback pilot regulator (11-204-004) was also used. This was supposed to give a constant downstream pressure irrespective of any changes in upstream pressure. However, in spite of the pilot regulator, the downstream pressure did fluctuate according to the supply pressure of the air receiver. Consequently the flowrate did tend to drift. This could be compensated for by using a bleed control valve to maintain a constant pressure in the plenum chamber during the course of a traverse. The pressure in the plenum chamber was measured by either a mercury or water manometer. In cases where the supply pressure of the plenum chamber was high, a pressure gauge was used which had been previously calibrated against a Budenburg gauge tester.

The air mass flowrate was measured by an orifice plate with D and D/2 tappings, designed according to B.S. 1042. The size of the orifice plate could be changed to suit the operating conditions and therefore minimise any errors in flowrate measurement. Downstream of the orifice plate a T junction controlled by globe valves directed the air flow to the flare or to the calibration nozzle. Before any measurements were made, the supply pipe-work downstream of the regulator and the rig itself were tested for any leaks. During the course of a traverse, the temperature of the supply air increased due to the heating effect of the compressors. This was always monitored and was never more than 20° C above ambient at the rig. Therefore temperature changes during the course of any one traverse were ignored.

The carry-over of oil from the compressors was always a problem and had to be constantly monitored. Even a fine oil mist in the supply tended to break the delicate hot-wire probes or cause some inaccuracy in their calibration.

3.1.3 Traverse Gear

A dove-tail slide was mounted parallel with the base-plate centre-line. On it was mounted a rack and pinion, the axis of which was perpendicular to the axis of the dove-tail slide. Together they formed a compound slide for positioning of probes in the horizontal plane. See Figure 3.4. On this was mounted a vertical pillar with a guide rail on which travelled a vertical slide. The slide served as a mounting for a rotary head calibrated in degrees and accurate to five minutes of arc. A DISA 55H01 traversing mechanism was mounted on the rotary head and by use of a gear, permitted either a 10 mm or 10 cm maximum traverse length. The traversing mechanism housed a ten-turn potentiometer allowing electrical measurement of the probe position once a traverse was set up. The combined motion of the two horizontal slides, the vertical slide and the rotary head gave the required three degrees of translation and one of rotation.

3.1.4 Probes

(a) Three-Hole Probes

These probes were especially made in the Engineering Department at Durham as none are commercially available. Two were made of different sizes, each consisting of three total pressure tubes soldered together (see Figure 3.4a). The two outer tubes were bevelled at angles between 40° and 45° for maximum sensitivity to the inclination of the mean flow direction relative to the flare surface. Thus it is assumed that the centre tube measures the full dynamic head and the outer two measure proportions of it, depending on the mean flow angle. The size of the tubing was selected to give a compromise between the response time for the probe and the size of the probe. The response time is inversely proportional to the fourth power of the tube diameter. Therefore a larger tube size substantially reduces the response time

whilst increasing the size of the probe and interference of the flow. The smaller probe was used in the model flare traverses and required about 30 secs for a steady state reading.

The full calibration of these probes is given in Appendix A together with the corrections used for the effects of turbulence, transverse velocity gradients and Mach number. From the three items of data available at each traverse point, the two mean velocities \bar{U} and \bar{V} are calculated as well as the inclination of the total velocity vector relative to the local flare surface, θ . This data was used to verify and supplement the hot-wire data.

(b) Hot-Wire Probes

These probes were used to obtain turbulence data and more accurate data of the mean flow. A full description of their use and the necessary data analysis is given in chapter four. A brief description of the probe design and geometries is given here.

Four wire orientations were required to provide enough information from which the flow variables wanted could be obtained. Therefore, from the currently available configurations of hot-wire probes from DISA, the types 55P14, 55P53 and 55P54 were selected. These are shown in Figure 3.4b. All the probes consist of two or four prongs moulded into a ceramic body. The wires are all of 5 μm diameter and made of platinum-coated tungsten. Both metals have similar temperature coefficients of resistivity ($\alpha_{20} \approx .36\% / ^\circ\text{C}$); the platinum coating makes welding to the prongs easier whilst the tungsten provides strength. The single wire probe (55P14) has an active length of 1.25 mm. The cross wire probes have prongs placed 3 mm apart. The wires between them are

gold-plated at the ends, reducing the active length of the wire to 1.25 mm. This is done to minimise prong interference of the flow around the active portion of the wire, and also reduces cooling of the wire by the prongs. These probes are fragile and easily broken by mis-handling or by dirt particles. Broken probes were sent to DISA for repair. The consistency of the probe geometry for probes of the same type was not always what might have been desired, particularly after repair.

All the wires were operated with an overheat ratio of 0.8, i.e. $T_w - T_{amb} = 222.2\text{ }^{\circ}\text{C}$, and the upper limit to their frequency response was about 400 kHz, for use in air.

3.1.5 Calibration Nozzle

As shown in Figure 3.3, a calibration nozzle was mounted adjacent to the flare. The nozzle was 16 mm in diameter and was machined so as to give a smooth contraction from the $1\frac{1}{4}$ inch diameter pipe down to the nozzle exit. There was a 0.6 m upstream length of pipe free of any bend or obstruction. Consequently, within the potential core of the emerging jet, the turbulence intensity was measured as no more than 0.64%, and any probe to be calibrated was placed in the potential core with a small pitot-static tube to measure the dynamic head. Both the three-hole and hot-wire probes were calibrated in this fashion.

3.1.6 Instrumentation

(a) Calibration Manometer

All probes were calibrated against a reference dynamic head measured by an electromanometer (type M8, Mercury electronics). This provides a one volt d.c. output for a maximum input of either 1000 or 3000 mm water, depending on the pressure cell used.

(b) Three-Hole Probe Pressure Transducers

In order to reduce the time required for a three-hole probe traverse, three separate pressure transducers were used, therefore reducing the time spent waiting for the probe response time approximately by two-thirds. The transducers were of the strain gauge type (Schaevitz EM type P722, vented gauge) with a full scale output of 25 mV for 1.5 bar maximum input. They were required to be robust as these transducers were also used for the full scale outdoor tests. A high gain stable d.c. amplifier was also required for amplification of the transducer outputs as their wide range was only used in the full scale tests. The amplifier had a gain of 1000 and was constantly checked for drift by having a reference input voltage built into the circuitry.

(c) Hot-Wire Equipment

The choice of hot-wire analysis dictates what equipment is necessary. A maximum of two anemometer channels was required. Therefore, two DISA anemometers (55M10, 55D01) and two linearizers (55D15) were required. Where possible, the newer 55M10 anemometer with the standard bridge was used in preference to the 55D01 unit. With use of the standard bridge, the 55M10 unit has an upper limit to its frequency response of 200 kHz, whilst for the 55D01 unit it is about 150 kHz for the same flow conditions. However, the upper limit to the frequency response is set usually by the linearizer and is 70 - 100 kHz for a typical voltage output of 3 - 2 volts. The linearized signals were passed to a DISA turbulence processor (55B25) which is able to produce various functions of up to two input signals and integrate the combined signal, using a preselected time constant. The time constant used was one second requiring an integration time of about ten seconds, and its use gave a steady state value of the integrated signal. The two input channels

of the turbulence processor have separate variable gains and can be either a.c. or d.c. coupled to the input signals. A R.M.S. voltmeter (55D35) was also required for estimation of turbulence intensities in the calibration nozzle. A schematic diagram of the instrumentation is given in Figure 3.3.

(d) Data Acquisition

All data recorded was either initially a d.c. value or the integrated value of an a.c. signal. Therefore the rate at which data was to be sampled was not a problem. A data transfer unit (Solartron 3230) provided up to twenty channels that could be sampled either automatically over a preset range or individually. The channel sample data rate was determined by digital instrument setting, the word length and recording rate of the output recorder. Two output driver units were linked to an Addmaster serial entry printer and to a Facit high speed paper tape punch which provided data coded in ASCII/ISO 8 level code. The tape provided an easy means of data transfer to a Varian '73 computer or later to an IBM 370/168 for analysis and plotting.

A box of preset potentiometers with matched resistances provided a means of entering data for which there was no analogue signal (e.g. ambient temperature) and also for entering integer data which, for example, could be the number of traverse or calibration points.

3.1.7 Plotting Routines

By use of standard 'GHOST' plotting routines available on the IBM 370/168 computer, a series of seven plots could be generated for each hot-wire probe traverse and three plots for each three-hole probe traverse. The plotting routines used provided drawing and annotation of axes, suitable for A4 size paper, point plotting and the drawing of

a least-squares best fit line through the data points. The curve fitting was done interactively so that a best fit could be chosen before obtaining a hard copy.

3.1.8 Traverses

A traverse was set up by measuring the height of the axis of the rotary head above the base-plate and using simple trigonometry to find the required position of the dove-tail slide for a selected traverse angle. The slides all had verniers and therefore positional accuracy could be read to 0.1 mm. The probe could be lined up with the centre-line scribed on the plenum chamber near the throat to ensure that it was on the centre-line of the flare. All traverses were done along a normal to the surface for a specified angle of inclination to the horizontal. In the plane perpendicular to the traverse direction, the positional accuracy was probably no better than 0.5 mm. However, the accuracy in the direction of the traverse was much better because the traverse potentiometer could read to an accuracy of 0.01 mm. Before every traverse, the probe had to be zeroed at the flare surface. In the case of the three-hole probe, an addition to the traverse distance was required to allow for the diameter of the tubing. If carefully manipulated, the hot-wire probes could be placed very accurately close to the surface without actually touching it, by noting any increase in bridge voltage of the anemometer caused by cooling of the probe.

For the hot-wire traverses, it was necessary to adopt a multi-probe technique rather than a multi-position technique in order to obtain the required number of wire positions. The mean flow velocities and Reynolds shear stresses, that were wanted from the analysis, required inclination of the wires in both the XZ and XY planes. Together with the

geometry of the flare, this dictates that at least two different probe geometries are required where further wire orientations can be obtained by rotation of the probe. The probes used gave four wire positions from three different probe types. Therefore for each traverse position three traverses were done. This not only placed a lot of trust in the positional accuracy of the probe, but also assumed stationary turbulence. In order to minimise positional errors, all the traverses were completed at one position before moving onto the next traverse. This meant that the anemometers and linearizers had to be reset for every traverse.

In all but one of the sets of traverses, the maximum flow was limited to below $M = 0.3$ to avoid compressibility effects and temperature fluctuations. Other limits were also set by some of the instrumentation. A large slot width was used for the detailed hot-wire traverses as the 55P53 probe could not go closer to the wall than 1.06 mm. With a large slot width a larger proportion of the jet was available. Most of the traverses were done at 20° , 30° , 45° , 60° , 75° , 90° , 100° and thereafter at 10 mm intervals on the flat portion of the flare surface. The detailed hot-wire work was done at

$$P_o/P_{atm} = 1.020, \quad t = 5 \text{ mm} \quad Re_s = 2.17 \cdot 10^4$$

Further three-hole traverses were done at

$$P_o/P_{atm} = 1.0602, \quad t = 2 \text{ mm} \quad Re_s = 1.37 \cdot 10^4$$

and at $P_o/P_{atm} = 1.974, \quad t = 0.7 \text{ mm}, \quad Re_s \approx 1.95 \cdot 10^4$

3.2 LARGE SCALE TESTS

3.2.1 Flare and Air Supply

The eight inch Indair flare (dimensions are available in Figure 3.1 by multiplying those shown by 5/3) was mounted vertically and connected

by four inch diameter hose to an Artowest²Rolls-Royce gas turbine with a modified compressor for use as an air supply. The maximum flowrate was about 1500 s.c.f.m. and the maximum supply pressure 30 p.s.i.g. The air temperature in the plenum chamber varied between 120° and 180° C. No facility was available either for surface pressure tappings on the flare, or for flowrate measurements.

3.2.2 Traverses

Using the same equipment as that for the three-hole probe traverses on the model flare, traverses were carried out to provide extra data from a larger flare. The larger of the two three-hole probes was used. The traversing mechanism described in § 3.1.3 was mounted on a vertical gantry with fixed locations which corresponded to a particular angle of traverse on the flare. Traverses were done at $t = 2.51$ mm, $P_o/P_{atm} = 1.34$ and $P_o/P_{atm} = 2.43$ ($Re_s \approx 2.34 \cdot 10^4$ and $4.59 \cdot 10^4$ respectively) and $t = 3.99$ mm, $P_o/P_{atm} = 1.34$ and $P_o/P_{atm} = 2.44$ ($Re_s \approx 3.72 \cdot 10^4$ and $6.67 \cdot 10^4$ respectively.)

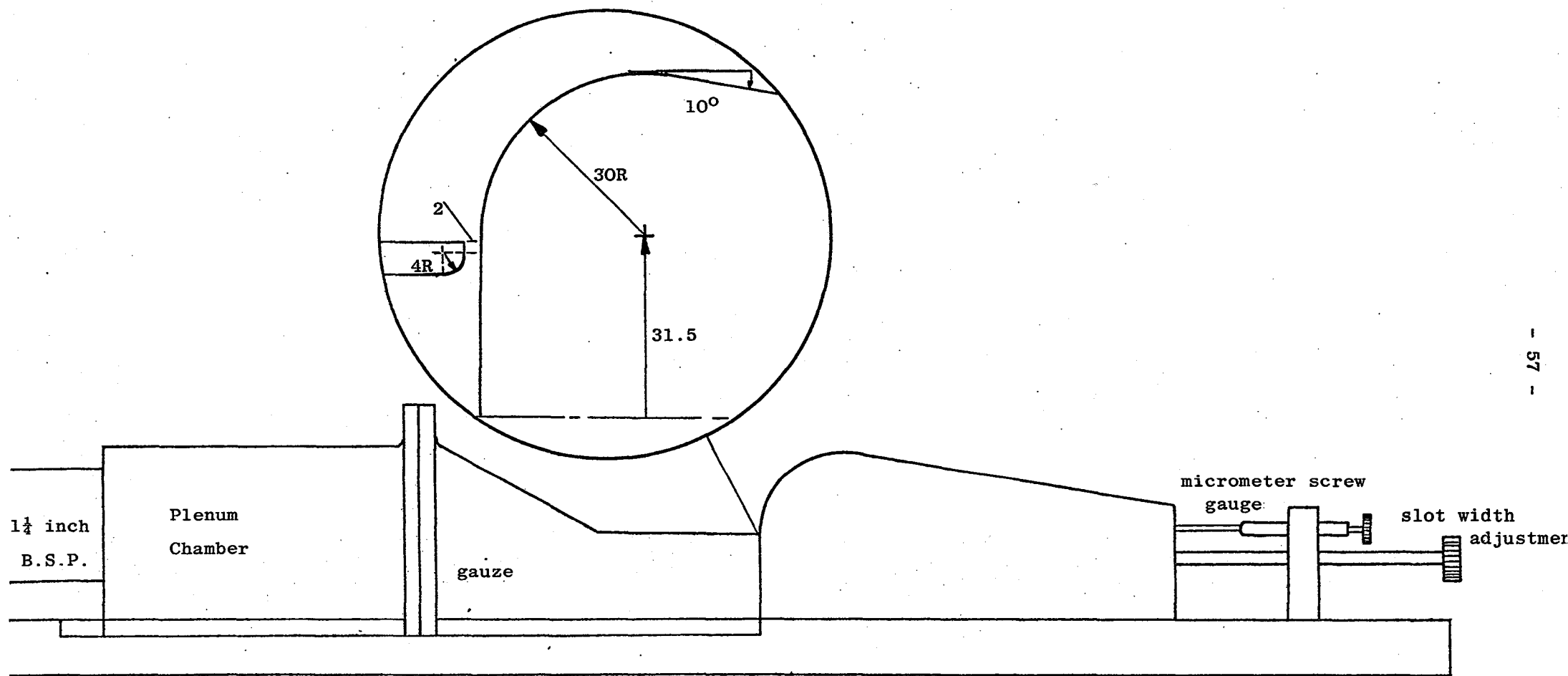
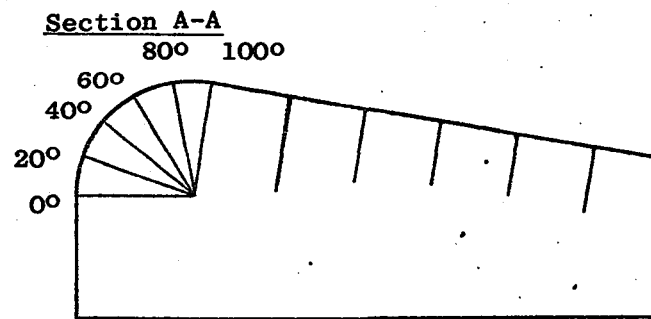
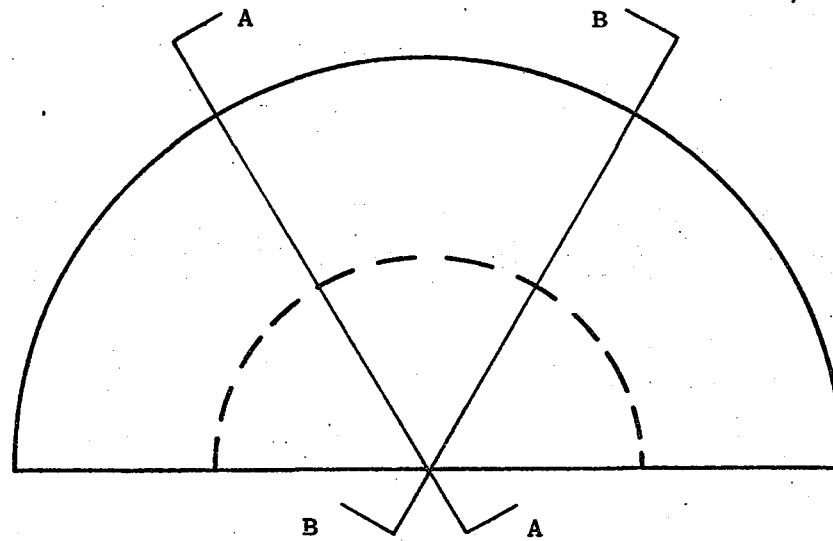


FIG. 3.1 Basic Elements of Flare Model (Dimensions in mm - not to scale)



tappings at 10 mm
intervals on flat
section

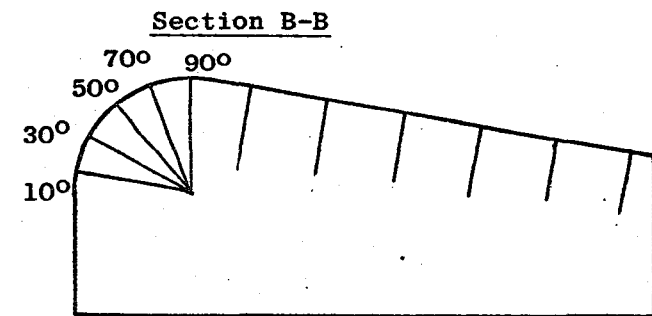


FIG. 3.2 Distribution of Surface Pressure Tappings

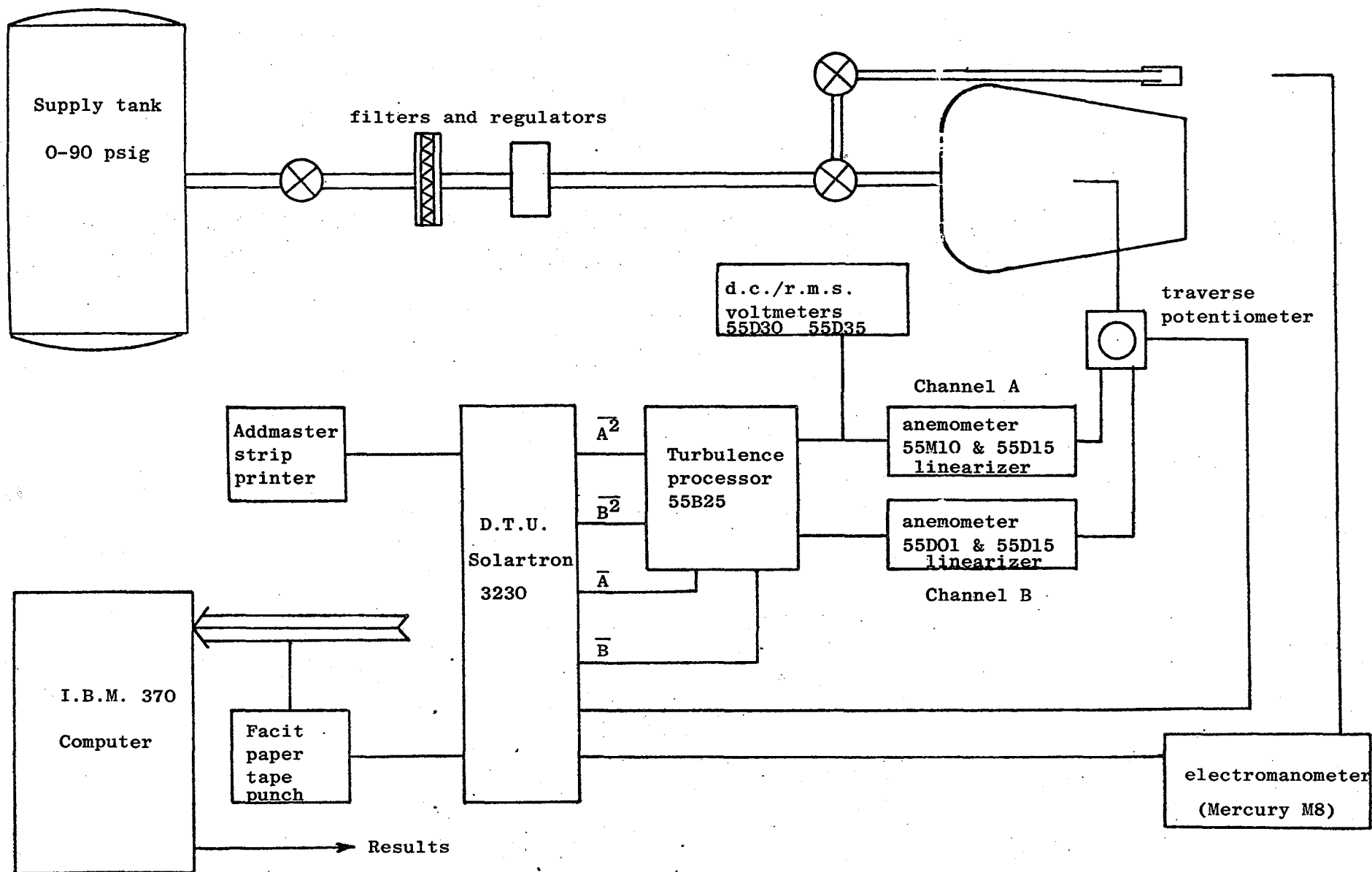


FIG. 3.3 Schematic Diagram of Rig

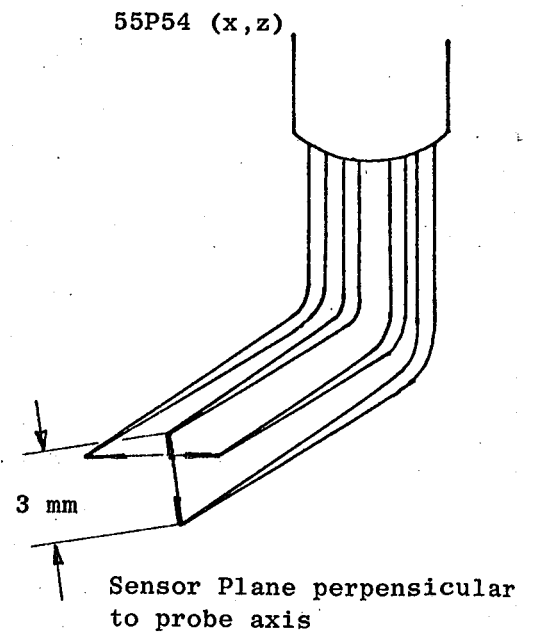
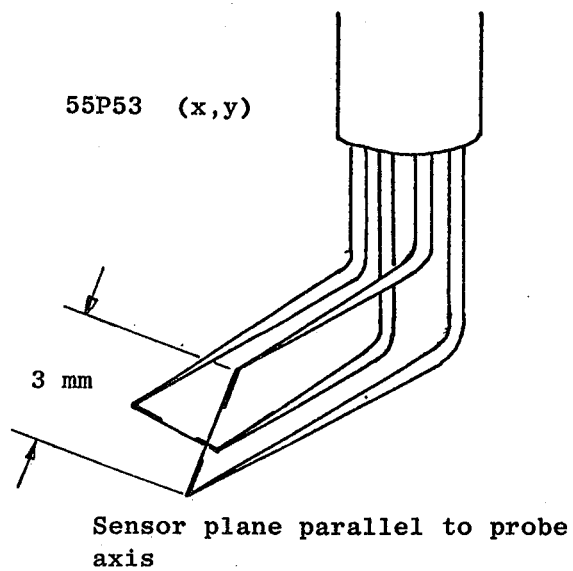
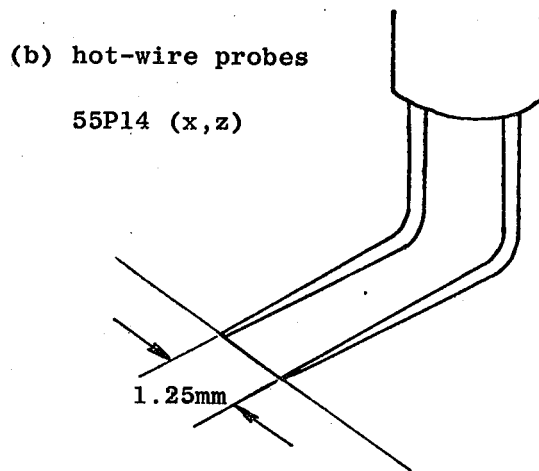
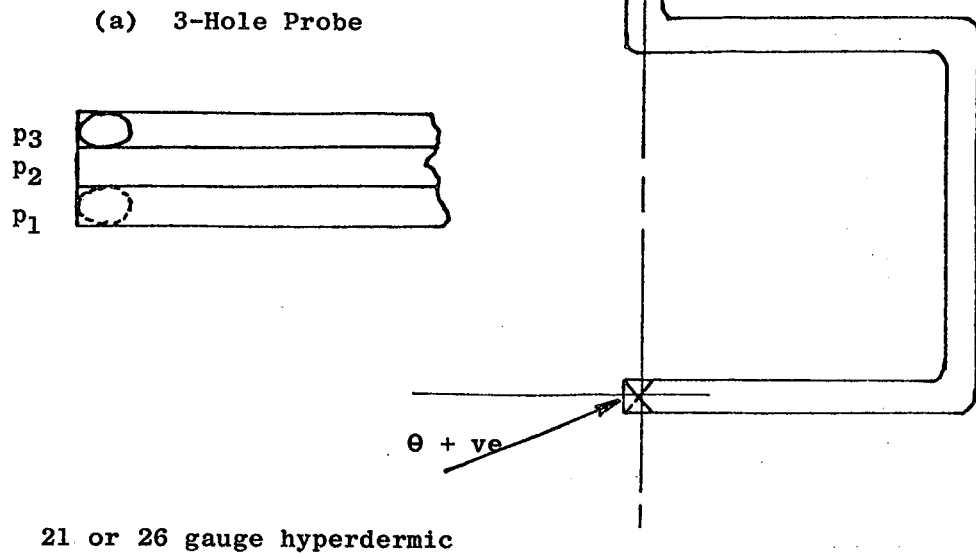
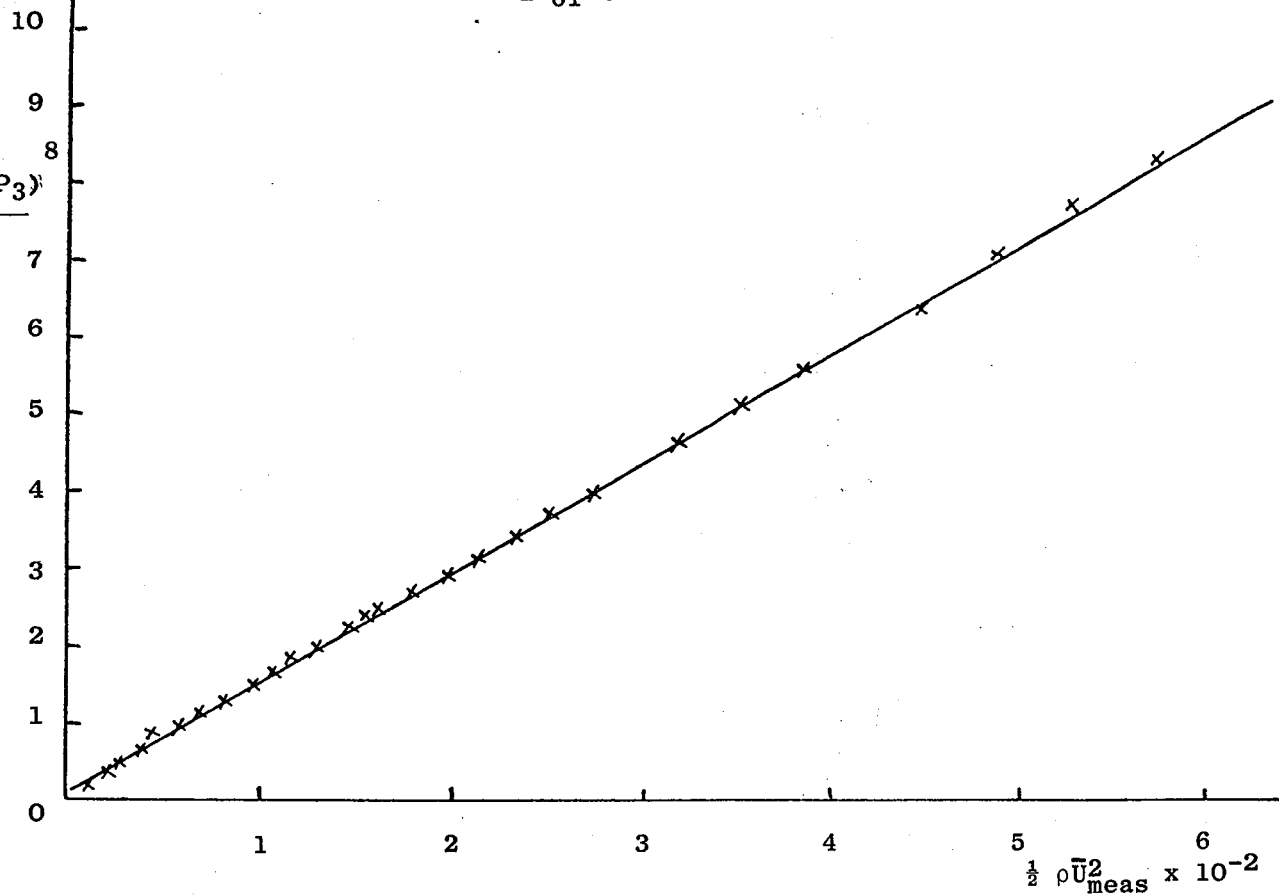


FIG. 3.4: Probe Geometries

$$\frac{P_2 - (P_1 + P_3)}{2} \times 10^{-2}$$



$$\frac{P_1 - P_3}{P_2 - (P_1 + P_3)} \times 2$$

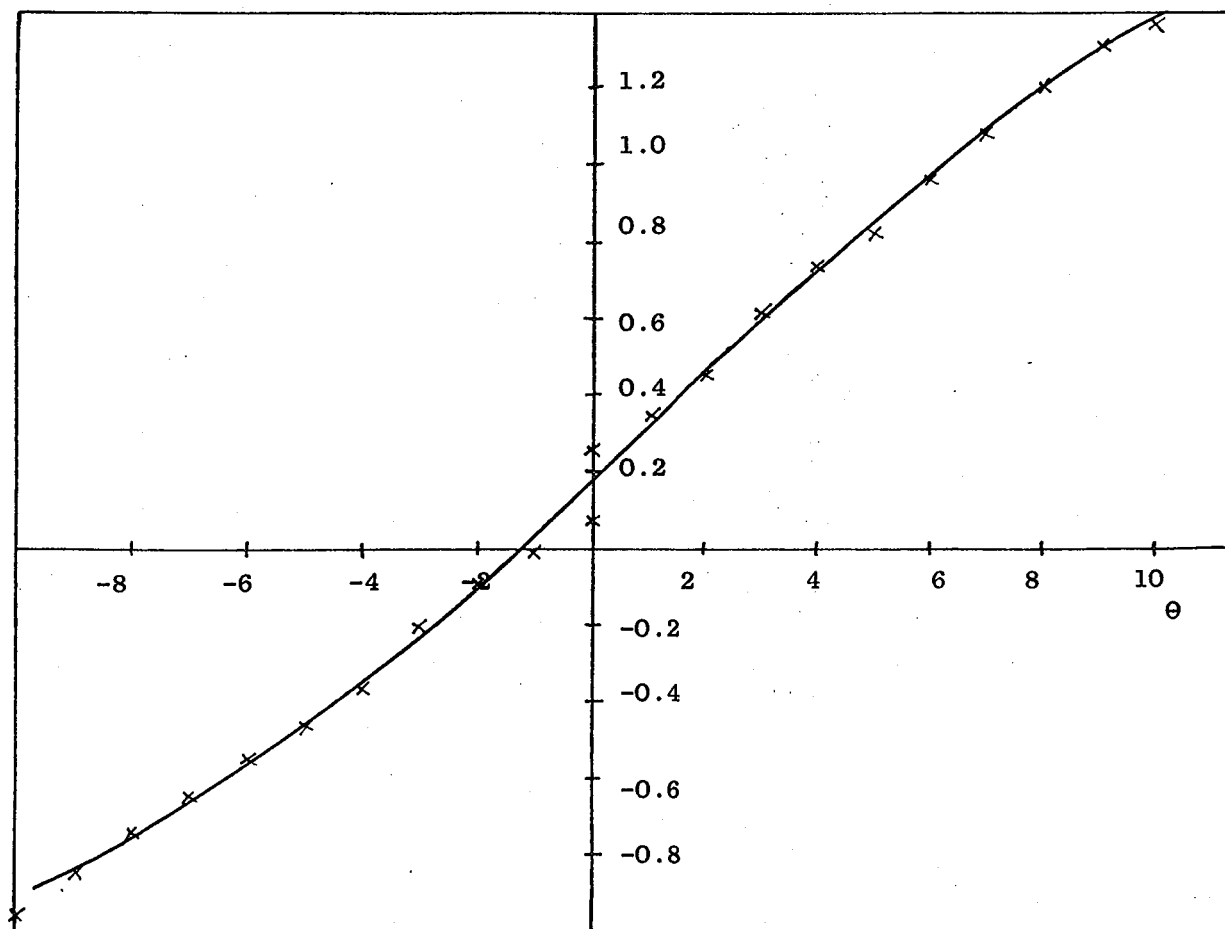


FIG. 3.5: Velocity and Pitch Calibrations for 3-hole Probe

CHAPTER 4

HOT-WIRE ANALYSIS

4.1 INTRODUCTION

The factors which determine the heat loss from a hot-wire are complex. Thus the first requirement for any analysis is to be able to propose a sufficiently accurate relationship between the voltage across the wire and the effective cooling velocity incident on the wire. A full treatment is given in the standard texts of Hinze (1975) and Bradshaw (1971).

In the majority of cases, the heat lost from the wire to the surrounding fluid depends on:-

- (a) the effective cooling velocity
- (b) the temperature difference between the wire and the fluid
- (c) the physical properties of the fluid
- (d) the geometry and physical properties of the wire.

Radiative heat loss can be ignored except very close to other heat conducting solids and buoyant convection caused by local heating of the fluid is negligible except at very low wire Reynolds numbers, Re_w , (typically 1 - 5 m/s in air for a wire with $l/d = 250$). If the hot-wire probe forms one arm of a wheatstone bridge circuit, it can be operated so that either the current through it is kept constant (C.C.A.) or so that its temperature remains constant (C.T.A.), see Figure 4.1. For constant current operation, the resistance of the wire fluctuates. At high frequencies, the thermal inertia of the wire attenuates its amplitude response and therefore an amplifier is necessary to compensate the frequency response. The C.C.A. is now rarely used except for very low currents when the probe is used to measure temperature. With

the aid of fast developing electronics the C.T.A. has now become more or less universal. For constant temperature operation, the current in the wire fluctuates and heat loss is compensated for by additional current. (Figure 4.1). A higher gain on the servo-amplifier gives a quicker response for compensating the cooled wire and the error voltage is reduced more quickly. But with a high loop gain, the anemometer system can become unstable. Thus the bridge must be balanced before operation. The setting up procedures for the anemometers are given in detail in the relevant DISA manuals.

If the overheat ratio of a hot-wire used in one arm of a C.T.A. is kept constant for both calibration and use, then item (b) above is accounted for by calibration, assuming the temperature of the fluid is constant. The remaining items are accounted for in a series of semi-empirical calibration laws that have been proposed, the first of which was by King (1914):-

$$Nu_w = A + B Re_w^{0.5} \quad \dots (4.1)$$

Later workers produced equations similar to King's law but incorporating the Prandtl Number. Collis and Williams (1959) produced a modified form of King's law for the range $0.01 < Re_w < 140$:

$$Nu_w \left(\frac{T_m}{T_f} \right)^{-0.17} = A + B Re_w^n \quad \dots (4.2)$$

The exponent n was found to vary between 0.45 and 0.51. These workers were the first to identify a marked dependence of the constants A , B and n on Re_w . For a constant property fluid (item C) King's law reduces to

$$E_B^2 = A + B U_{eff}^{0.5} \quad \dots (4.3)$$

with modified constants. Siddall and Davies (1972) modified this version to:-

$$E_B^2 = A + B U_{eff}^{0.5} + C U_{eff} \quad . . . (4.4)$$

in order to account for any dependence that the constants in equation (4.3) may have on Re_w , and a significantly better representation of calibration data was obtained.

The remaining question is whether a universal calibration of the form of equations (4.3) or (4.4) can be trusted or whether a significant variation in the constants can be expected from probe to probe. It was mentioned in § 3.1.4(b) that there was often a noticeable difference in the geometry of probes of the same type, particularly after repair. Thus a universal calibration would fail to take account of item (d) in the list of factors governing the wire heat loss. Therefore, it was necessary to calibrate probes individually using the semi-empirical calibrations above as no more than a guideline to the form of calibration required. In this case then, equation (4.3) is written more generally as:

$$E_B^2 = A + B U_{eff}^n \quad . . . (4.5)$$

4.2 LINEARIZATION

All of the accepted hot-wire calibrations are significantly non-linear. This presents a major difficulty when turbulent quantities are to be measured, as these are related to the fluctuating voltage by the gradient of the calibration dE_B/dU_{eff} which changes according to \bar{U}_{eff} . If the turbulent fluctuation is small then acceptable results can be obtained by using the gradient at \bar{U}_{eff} . But for larger intensities, the calibration has to be linearized, or a better approximation found to the gradient at U_{eff} .

4.2.1 Analogue Linearization

An analogue linearizer can be used to compensate the curvature of the wires response. The DISA 55D15 linearizer has a transfer function:-

$$E_L = K(E_{IN} - E_{IN0})^{1/n} \quad \dots (4.6)$$

Assuming the wire calibration of equation (4.5) where:

$$E_{IN0} = A \quad \text{and} \quad E_{IN} = E_B^2$$

then

$$E_L \propto U_{eff}$$

Because buoyant convection is prominent at $U_{eff} = 0$, the equation is more usually written:

$$E_L = E_0 + C U_{eff} \quad \dots (4.7)$$

4.2.2 Effective Linearization - Taylor Expansion Method

With equation (4.5) rewritten as:-

$$U_{eff} = \left(\frac{E_B^2 - A}{B} \right)^{1/n} \quad \dots (4.8)$$

U_{eff} is a continuous function of E_B only, with finite derivatives for positive U_{eff} . Therefore $U_{eff} = \bar{U}_{eff} + u_{eff}$ can be rewritten as a Taylor expansion of E_B about the point \bar{E}_B ($E_B = \bar{E}_B + e_B$), giving an estimate for U_{eff} .

4.2.3 Comparison of Linearization Techniques

The type of flow studied in this investigation is characterised by large mean velocity gradients and high turbulence intensities (>30%). Therefore large variations in \bar{U}_{eff} and U_{eff} are to be expected. Brunn (1971) assesses the effects of turbulent velocities on the accuracy of the use of linearized and unlinearized calibrations. Calibrations of

the form of equations (4.5) and (4.7) were compared and significantly better accuracy was obtained with a linearized calibration. For example, at a velocity of 30 m/s, the turbulence intensity had to be $< 18\%$ for no more than a 1% uncertainty in the velocity estimate when a linearizer was not used. Several linearization transfer functions of the form of equation (4.6) were compared and the inversion (i.e. $U_{\text{eff}} = f(E_B)$) of the calibration of Siddall and Davies (1972) was found to give the best agreement with data for the whole range 0 - 150 m/s. Other literature of the subject of linearization, Klatt (1973) and Parthasarathy and Tritton (1963) is less helpful as the non-linear relationship (4.5) is confused with the non-linear form of U_{eff} when composed of three mutually perpendicular velocity components. See § 4.3.

However, the DISA 55D15 linearizer assumes that the constants in equation (4.5) are non-variant with velocity. Therefore errors could be expected for large ranges of U_{eff} . In this study, the velocity range of interest is approximately $15 \text{ m/s} < U_{\text{eff}} < 70 \text{ m/s}$. For this range, the linearity of the linearized anemometer output was checked. With $n = 0.33$, equation (4.7) fitted the calibration data well for both the miniature and gold-plated wire probes, in spite of the slight variation of calibration constants with U_{eff} . See Figures 4.2. Newer versions of DISA linearizer allow for variation of the exponent n in the calibration (4.5) (55D10 and 55M25) and therefore use of these linearizers would allow a greater velocity range to be studied.

However, against the use of an analogue linearizer it may be said that it provides an extra source of error to the hot-wire signal. Drift, to which the linearizer is especially prone, noise and limitations to

frequency response all effect the signal. The way in which the hot-wire signal is linearized also influences the choice of analysis of U_{eff} . An analogue linearizer with $E_L \propto U_{eff}$ greatly simplifies the analysis whereas approximation of the calibration by using a Taylor series complicates the analysis. In both cases the number of wire positions required equals the number of mean velocities and velocity correlations available from the analysis. With the confirmation that a linearized anemometer output of the form of equation (4.7) agreed well with calibration over the required velocity range, the 55D15 analogue linearizer was used.

4.3 RESOLUTION OF EFFECTIVE COOLING VELOCITY

The preceeding sections show how a satisfactory relationship can be proposed between the instantaneous effective cooling velocity and the instantaneous output voltage from a linearized or unlinearized C.T.A. With certain restrictions, a linear relationship between E_L and U_{eff} can be used. The remaining task involves the resolution of U_{eff} into velocity components relative to the hot-wire, and how these can be manipulated to give velocities relative to the co-ordinate system defined for the flow field.

Defining U_N , U_B and U_T as instantaneous velocity components relative to the wire, (Figure 4.3) U_{eff} can be written as:

$$U_{eff}^2 = U_N^2 + k_2^2 U_B^2 + k_1^2 U_T^2 \quad \dots (4.9)$$

c.f. Jørgensen (1971) and Rodi (1975a) amongst others. k_1 and k_2 are sensitivity coefficients; k_1 is a yaw factor and k_2 a pitch factor. Both are dependent on l/d and prong spacing. k_2 is dependent on the prong length. For an infinitely long wire, $k_1 = 0$ and $k_2 = 1.0$; their actual

values are slightly larger so that k_1 accounts for heat conduction to the prongs and k_2 for cooling effects on the prongs. Using both miniature and gold-plated wire probes, Jørgensen (1971) calibrated for both k_1 and k_2 , using a constant reference velocity U whilst varying the yaw (α) and pitch (θ) angles separately. Both coefficients were found to be not only angle dependent but also velocity dependent. Because of the trigonometric relationships between U_N , U_T and α , and U_N , U_B and θ , it is inherently impossible to calculate values of k_1 and k_2 that are independent of U_N , U_B , U_T and therefore U_{eff} . Even if it were possible, use of k_1 and k_2 as functions of angle and velocity would require prior knowledge of the flow field. Therefore average values have to be used.

TABLE I : SENSITIVITY COEFFICIENTS

PROBE	k_1	k_2
55P14	0.4	1.1
55P53	0.23	1.03
55P54	0.23	1.03

The values of k_1 and k_2 in Table I were selected for the analysis from Jørgensen's data with regard to the likely values of U , θ and α to be encountered in the flare flow, and assumed to be constant for all probes of the same type. Individual calibration of the wires for k_1 and k_2 was not done as it requires very accurate measurements and is therefore a considerable amount of work for a small improvement in accuracy of k_1 and k_2 . In any case, their use in the analysis is approximate. The values were compared with values used by other workers

viz: Champagne et al (1967), Durão and Whitelaw (1974) and Brunn (1969). See Table II .

TABLE II: PUBLISHED VALUES FOR SENSITIVITY COEFFICIENTS

Author	k_1	k_2	Comments
Durão and Whitelaw (1974)	0.13	1.05	DISA gold-plated sensor probe
Rodi (1975a)	0.0	0.96	DISA 55F13 probe k_1 velocity dependent $U \leq 7.5$ m/s
Champagne et al (1967)	0.2	-	$l/d = 200$

4.4 REMAINING SOURCES OF ERROR

4.4.1 Shear Effect on Wires

The wires of the 55P53 probe have a large mean velocity gradient along their length causing a skew temperature distribution along the wire. Gessner and Moller (1971) measured temperature distributions of wires for various l/d in flows with a defined mean velocity gradient, and used the data to develop correction curves from which the averaged anemometer output voltage could be corrected. But this involves prior knowledge of the mean velocity gradient, therefore requiring an iterative correction sequence. The presence of a mean velocity gradient causes an underestimation in both the mean and R.M.S. anemometer voltage output. The effect is reduced for wires at low l/d .

No correction was applied to the voltage output of wires exposed to a large mean velocity gradient, not only because of the difficulties

stated above, but also because the wires were all of dimensions where $l/d = 250$. Therefore, the error in voltage output was estimated at no more than 7% for the values of mean velocity gradient expected.

4.4.2 Wall Proximity

Oka and Kostić (1972) measured the effect of a cold wall near a hot-wire with $l/d = 200$. No effect was observable for $yU_T/\nu > 4$ which is equivalent to $y = .13$ mm for $U_T = 0.5$, a minimum value expected for U_T . Accurate traverse data was not available for $y > 1.06$ mm as this was the minimum distance between the wall and the centre of the 55P53 probes which were inclined in the plane perpendicular to the wall. Therefore the effect of wall cooling was never apparent in the data.

Bradshaw (1971) lists several other causes of error associated with hot-wires and their instrumentation.

4.5 ANALOGUE/DIGITAL DATA ANALYSIS

With the advent of small and fast electronic instrumentation, the digital acquisition of hot-wire data is now established. The hot-wire signal can be recorded on magnetic tape prior to being digitised for storage or data can be transferred direct to an on-line computer for analysis. A digital analysis obviously requires more work to set up, but once done gives versatility to the analysis, changeable by software rather than by instrumentation. It does have the disadvantage that no immediate visual display of the analysed data is possible but does remove inaccuracies associated with the analogue instrumentation. Analogue analysis was used in this study, thus only averaged data was recorded.

4.6 REVIEW OF SIGNAL ANALYSES

Three methods of analysing hot-wire data were investigated before the method used was selected. These are described below together with reasons why they were not used.

4.6.1 Conventional Method

Appendix B contains four equations ((B.2), (B.4) and (B.6)), for the effective cooling velocity for a hot-wire with the four orientations shown in Figure 4.4. In this method the signals \bar{E} and $\bar{e}^2 = (\bar{E} - \bar{E})^2 = \bar{E}^2 - \bar{E}^2$ are measured. A solution becomes available by taking the square root of both sides and expanding the right-hand side of the equation under the square root. Thus equation (B.2) becomes, after averaging:-

$$\bar{U}_{\text{eff}} (0)_{xz} = \bar{U} \left[1 + \frac{k_2^2}{2} \left(\frac{\bar{v}^2}{\bar{U}^2} + \frac{\bar{v}^2}{\bar{U}^2} - \frac{2 \bar{v} \bar{uv}}{\bar{U} \bar{U}^2} + \frac{\bar{v}^2 \bar{u}^2}{\bar{U}^2 \bar{U}^2} \right) + \frac{k_1^2 \bar{w}^2}{2 \bar{U}^2} \right] \quad \dots (4.10)$$

where third order terms and higher are neglected ($\bar{v} \simeq \bar{U}$). $\bar{u}_{\text{eff}}^2 = (\bar{u}_{\text{eff}}^2 - \bar{U}_{\text{eff}}^2)$ can be obtained from \bar{e}^2 directly, assuming a linearizer is used, so that $\bar{u}_{\text{eff}}^2 \propto \bar{e}^2$.

$$\text{Then:- } \bar{u}_{\text{eff}}^2 = \bar{u}^2 \left(1 - \frac{\bar{v}^2}{\bar{U}^2} \right) + \frac{2 \bar{v} \bar{uv}}{\bar{U}} k_2^2 \quad \dots (4.11)$$

where third order terms and higher are neglected also. With the same approximations \bar{uv} is available from the $\bar{U}_{\text{eff}} (45)_{xy}$ and $\bar{U}_{\text{eff}} (-45)_{xy}$ response equations:

$$\bar{uv} = \frac{\bar{u}_{\text{eff}}^2 (45)_{xy} - \bar{u}_{\text{eff}}^2 (-45)_{xy}}{2(1 - k_1^2)} \quad \dots (4.12)$$

With further simplifying assumptions ($\bar{V} = 0$, $\bar{v}^2 = 0$) \bar{U} and \bar{u}^2 are available from equations (4.10) and (4.11) respectively. Alternatively with more wire orientations, more response equations are available to give a fuller solution.

It is important to note the approximations made. \bar{U} is obtained from equation (4.10) by assuming second order terms and higher are negligible with respect to \bar{U} . \bar{u}^2 is obtained from equation (4.11) by neglecting terms of third order and above. In the highly turbulent flow of a jet this assumption is too restrictive. Guitton and Newman (1977) found it necessary to use terms up to fourth order. This increases the number of unknowns as approximations to higher order correlations are required. There is thus an equivalent increase in the number of wire orientations required for solution and the procedure is likely to have significant cumulative measurement errors.

4.6.2 Statistical Methods

A method was proposed by Zarić (1969) and evaluated by Durst and Whitelaw (1970) for application to highly turbulent flows. It relies on the assumption that the probability density distributions of the velocity components are normal (Gaussian), i.e. that they have zero skewness and the flatness factor equals three. These functions are likely to be far from normal in the outer regions of a turbulent jet. Also, skewness of the distributions is connected with the convection of turbulent energy by the turbulence itself. In a strongly curved flow with destabilising curvature, turbulent transport terms are significantly increased. Therefore in a strongly perturbed jet, a Gaussian probability density distribution is a restrictive assumption.

A similar method was proposed by Dworak and Syred (1972) in which second order correlations are expressed as variances and covariances of the anemometer output signals. The resulting functions required a Taylor series expansion of the calibration to remove the square root and only terms up to second order were retained. Therefore third order terms and higher are neglected implying normal skewness and flatness. Fair agreement was found with experimental data from an axisymmetric free jet.

To conclude, Durst and Whitelaw (1970) found that the method could be used in limited flow regions where Gaussian assumptions were valid, but that the analysis was not a very practical approach.

4.6.3 Method of Acrivlellis (1977a, b and 1978 a, b)

The conventional method described above is approximate because in order to obtain a solution, the square root of a function has to be expanded binomially. Therefore Acrivlellis suggested analysis of the squared signal with the use of a linearizer. Unfortunately, he made a fundamentally false assumption (Bartenwerfer (1979)). He assumed that, for example, the equation

$$\overline{u_{eff}^2} = \overline{u^2} + k_2^2 (\overline{v^2} + \overline{w^2}) + k_1^2 \overline{w^2} \quad \dots (4.13)$$

could be written as an a.c. signal equivalent to the equation (B.3) where $\overline{u_{eff}^2} \propto \overline{e^2}$ was obtained by a.c. coupling to a R.M.S. meter. By a.c. coupling, the a.c. signal is separated from the d.c. signal before squaring and averaging, whilst $\overline{u_{eff}^2}$ is obtained in the analysis after squaring and averaging. Thus the method is only mathematically correct for $\overline{u^2} = \overline{v^2} = \overline{w^2} = 0$ and leads to large inaccuracies for a turbulence intensity > 10%.

4.7 SELECTED ANALYSIS

The methods described above are unsuited to a jet flow because of restrictive assumptions concerning the turbulence intensity and the shapes of the probability density distributions of the velocity fluctuations. This method uses the squared signal from a linearized anemometer and up to a point makes no assumptions concerning the nature of the flow. Some approximations are however necessary. These are discussed in

§ 4.8. The method was suggested by Durst (1971) and Durst and Rodi (1972); it was later used for analysis of data from measurements made in a round jet by Rodi (1975) and Durão and Whitelaw (1973 and 1974).

4.7.1 Recorded Data

For each of the four wire positions shown in Figure 4.4, the signals \overline{E}^2 and \overline{E} were recorded. Therefore a maximum of eight variables are available from eight response equations.

4.7.2 Reduction of Effective Cooling Velocities to Total Velocity Components

The four equations for \overline{U}_{eff}^2 are first used to obtain the total velocity components $\overline{U}^2 + \overline{u}^2$, $\overline{V}^2 + \overline{v}^2$, \overline{w}^2 and $\overline{U}\overline{V} + \overline{u}\overline{v}$ by matrix inversion. This is done in appendix C. No assumptions about the flow structure have been made up to this point except two-dimensionality.

4.7.3 Separation of Mean and R.M.S. Components

Equation (C.2) is obtained by binomial expansion for $\overline{U}_{eff}(\alpha)_{xy}$ retaining terms up to second order only, but assuming $\overline{V} \gg \overline{U}$. Regrouping terms so that values of total velocity components can be substituted, provides two non-linear fourth order polynomials in \overline{U} and \overline{V} for $\alpha = \pm 45^\circ$ (Equation (C.3)). The coefficients are functions of the total velocity components and the wire constants. These two equations were solved by

a Newton-Raphson technique for solutions to \bar{U} and \bar{V} . Therefore, the individual components \bar{u}^2 , \bar{v}^2 , \bar{w}^2 and \bar{uv} are also obtainable.

4.7.4 Solution for $y < 1.06$ mm

In this case the 55P53 probe was unable to give data sufficiently close to the wall. Therefore only four sets of data were available viz: $\bar{U}_{\text{eff}}^2(0)_{xz}$, $\bar{U}_{\text{eff}}(0)_{xz}$, $\bar{U}_{\text{eff}}^2(45)_{xz}$ and $\bar{U}_{\text{eff}}(45)_{xz}$. For regions close to the wall, the assumption $\bar{V} = 0$ is not unjustified. With this simplification, a solution for U , \bar{u}^2 , \bar{v}^2 and \bar{w}^2 is obtainable. This is done in appendix D.

4.8 ASSESSMENT OF THE ANALYSIS

The total velocity components are derived without any assumptions and the accuracy of the analysis relies solely on the constants of each wire. However, in order to separate the mean and R.M.S. components, some simplifying assumptions have to be made. These are that the correlations of third order and above are negligible with respect to the mean where as the conventional method assumes second order correlations are negligible also. The neglect of third order terms and above implies the same approximation as for a statistical method in which a normal probability distribution of the velocity fluctuations was assumed. However in the method of Dvorak and Syred (1972), this approximation was made for all wire response equations (i.e. in the calibration) rather than just for two of them as in this case. In this analysis it was assumed $\bar{V} \approx \bar{U}$ rather than $\bar{V} \ll \bar{U}$. Therefore terms such as $\frac{\bar{V}}{\bar{U}} \frac{\bar{u}^2}{\bar{u}^2}$ were taken as second rather than third order.

There is some redundancy of data for traverse points where use of all four wire positions is possible. This is because only six flow

variables were obtained from eight items of data. However, the values of $\bar{U}_{\text{eff}}(45)_{xz}$ and $\bar{U}_{\text{eff}}(0)_{xz}$ were not used for the full analysis because the use of the corresponding binomial expansions to separate the mean and R.M.S. components of velocity often failed to give converged solutions.

The reasons for this are discussed in Chapter 9. It would be possible to extend the present analysis to include two extra flow variables by their inclusion in the expansion equation (C.2). This was not done, however. It should be noted, also, that without the use of a linearizer, this analysis would be too cumbersome to use.

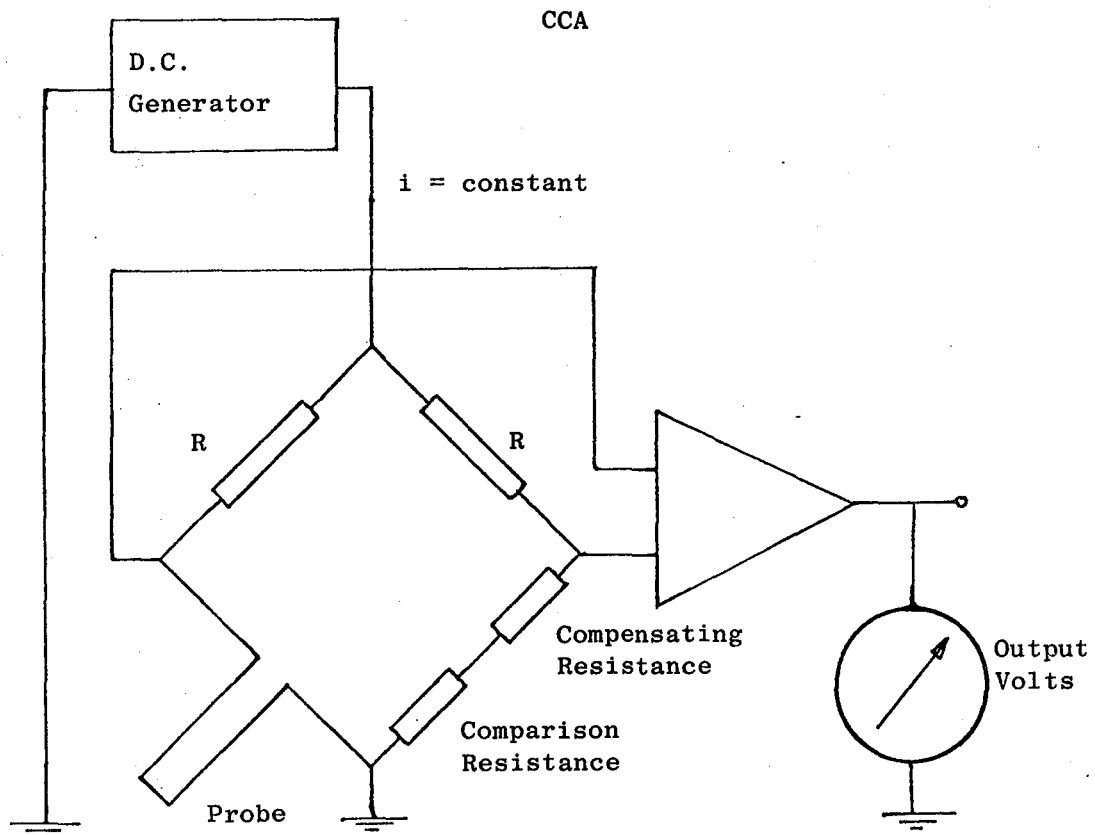
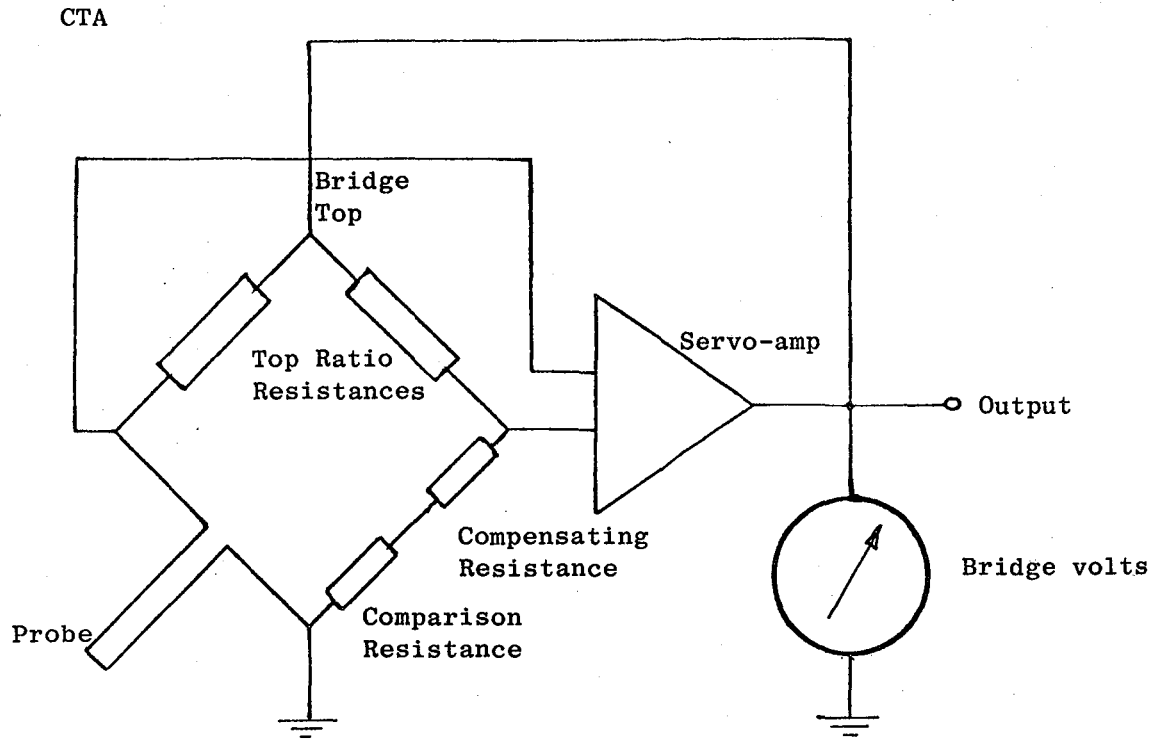
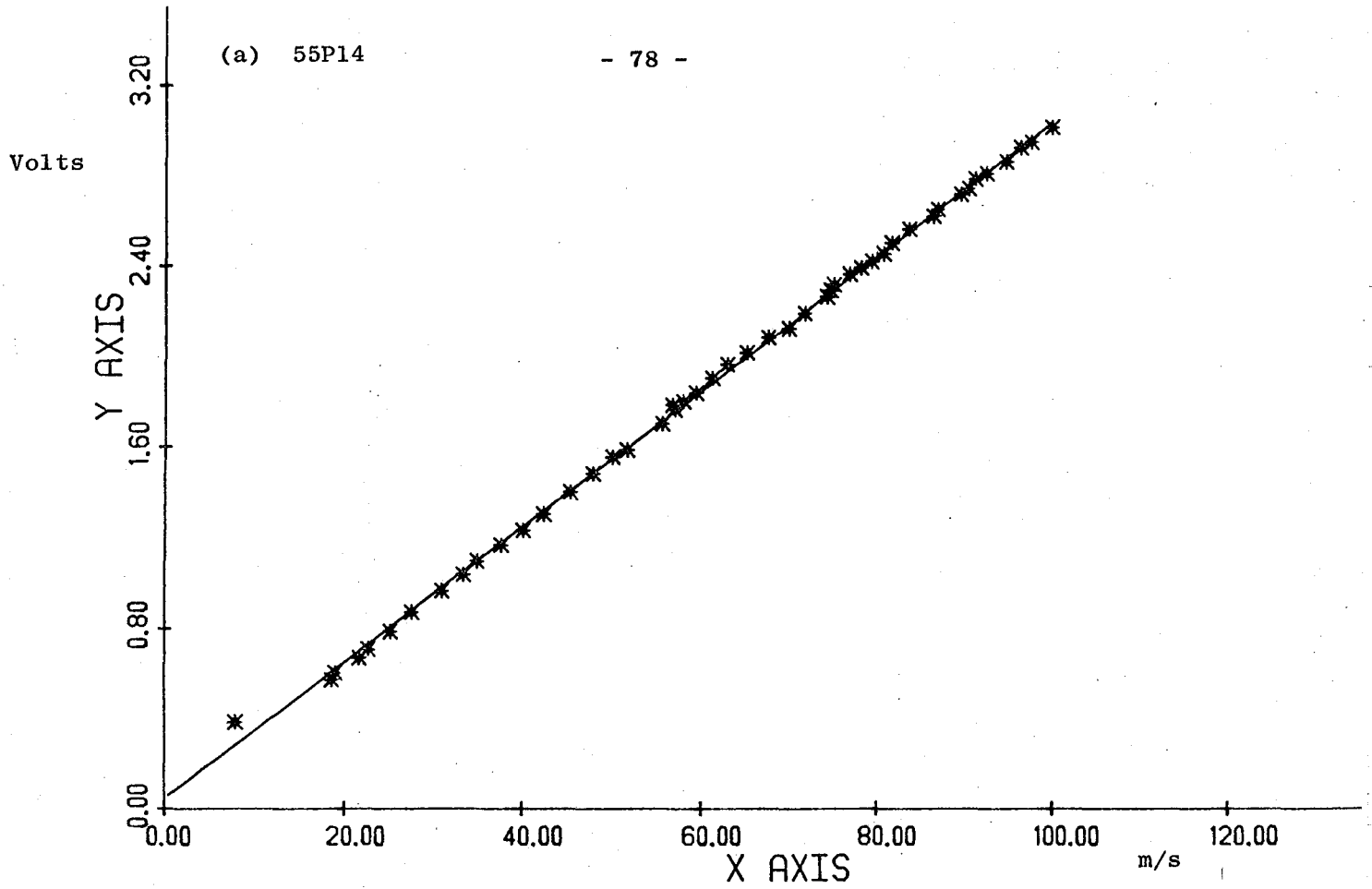


FIG. 4.1: CTA and CCA Configurations

(a) 55P14

- 78 -



(b) 55P54

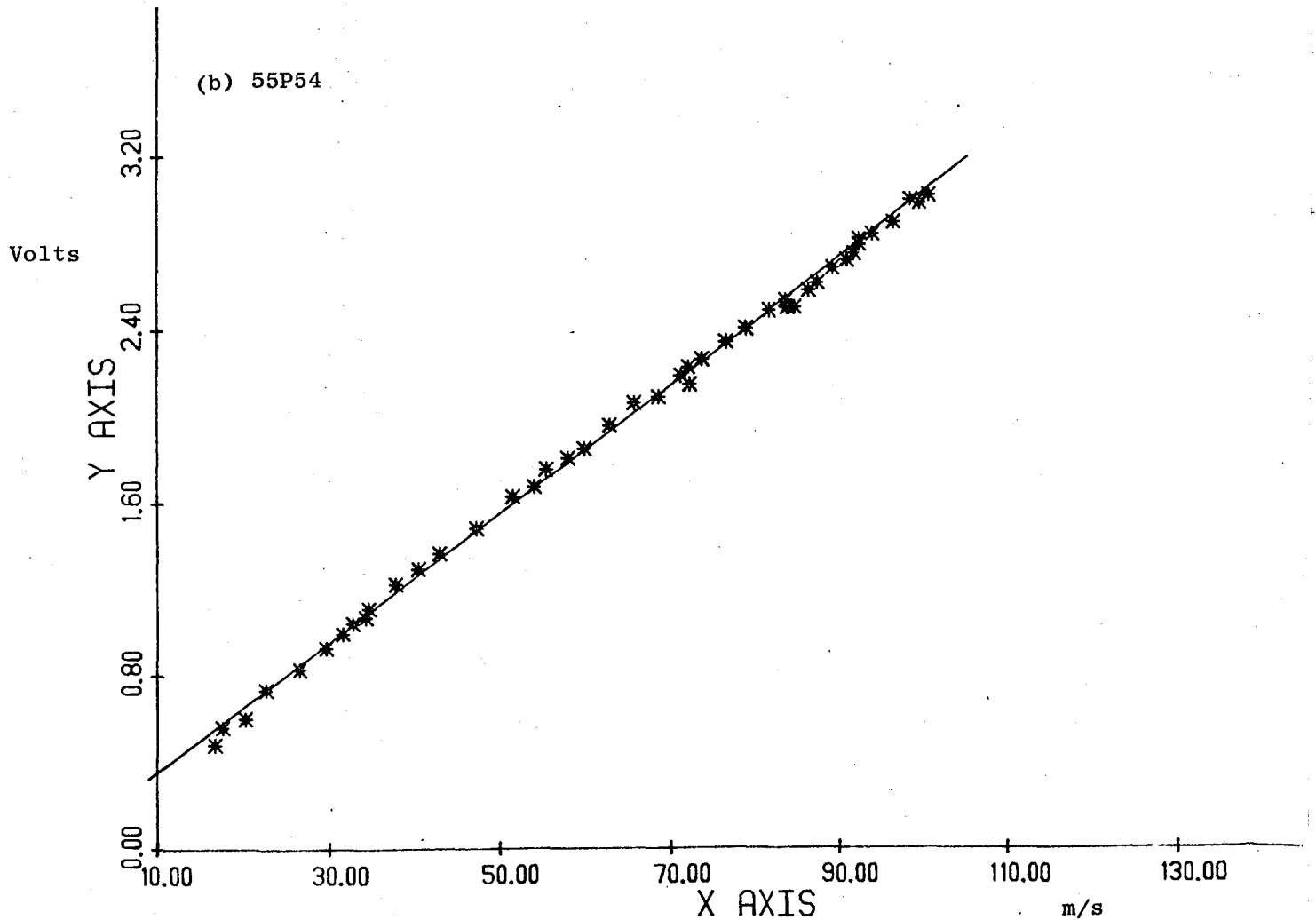


FIG. 4.2: Linearization checks for $n = 0.33$

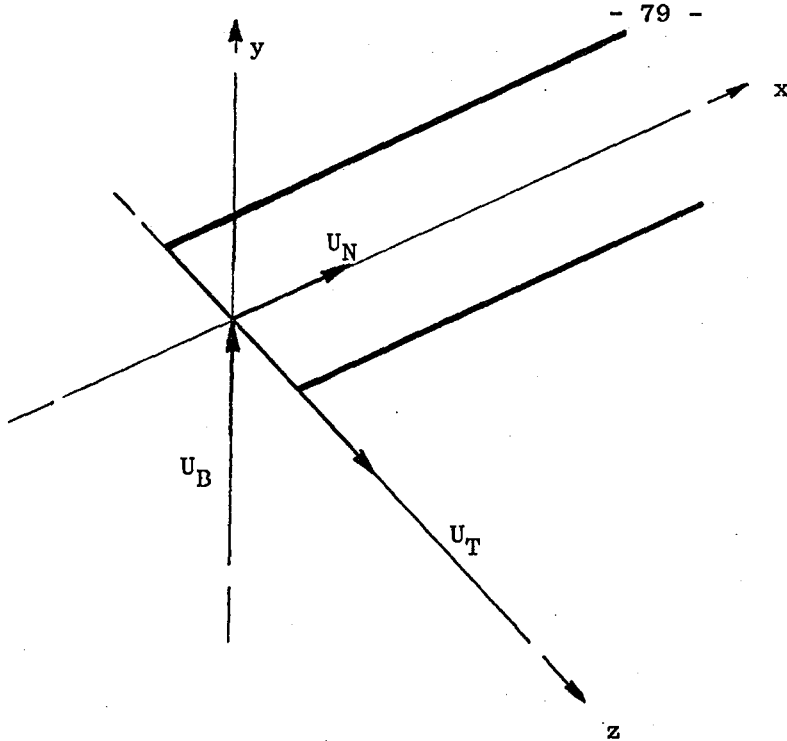


FIG. 4.3 Definition of U_N , U_B and U_T

U_N , U_B and U_T defined relative to the wire

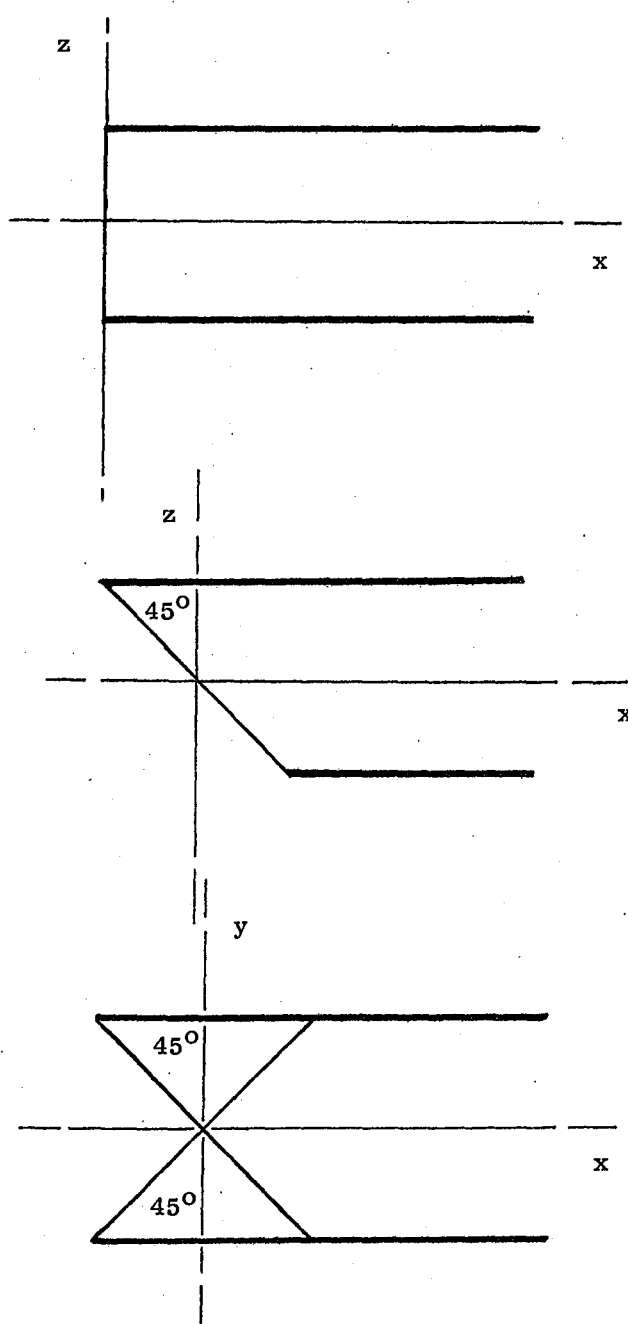


FIG. 4.4 Hot-wire orientations

$\bar{U} + u$, $\bar{V} + v$ and w defined relative to the coordinate system

CHAPTER 5

EXPERIMENTAL RESULTS

5.1 ESTABLISHMENT OF QUASI-TWO-DIMENSIONAL CONDITIONS

Preliminary radial traverses using a three-hole probe showed significant three-dimensionality of the mean flow. As mentioned in Chapter 3, the slot lip was honed to attain a slot width accuracy of 0.07 mm and the position of the flare relative to the slot lip was carefully checked in order to reduce these effects. A gauze was also inserted into the plenum chamber (figure 3.1) to minimise any jet effect caused by the supply pipe. Thus upstream non-uniformities likely to cause three-dimensional effects in the jet were minimised. Another cause of three-dimensionality, jet divergence or convergence caused by the skew-induced secondary flows at the base-plate was also considered. The jet thickness was noted to be much larger adjacent to the base-plate because of secondary flows, a phenomenon also noted by Guitton (1970). Usual checks for two-dimensional flow include investigation of the upstream flow before the beginning of curvature in order to compare with established experimental data. However, this was not practically feasible in this case, nor would it give any indication of the degree of three-dimensionality caused by secondary flows. Approximate measurements of $\overline{U}_{\text{eff}}^2(+45)_{xz}$ and $\overline{U}_{\text{eff}}(+45)_{xz}$ however, showed some discrepancy between $\overline{U}_{\text{eff}}(+45)_{xz}$ and $\overline{U}_{\text{eff}}(-45)_{xz}$ and between $\overline{U}_{\text{eff}}^2(+45)_{xz}$ and $\overline{U}_{\text{eff}}^2(-45)_{xz}$. This indicates that the assumptions of $\overline{W} = 0$ and $\overline{uw} = 0$, used in the hot-wire analysis were not valid and that three-dimensional effects in the flow were not completely eradicated.

5.2 DISCHARGE COEFFICIENT DATA

Mass flowrates were measured by an orifice plate and readings corrected according to B.S. 1042 for the effects of Reynolds number

and Mach number. They were also corrected for a 'zero flow' reading by extrapolation of a mass flowrate versus slot area plot to zero flow-rate. Thus a nominally zero^{area} was in fact equal to 9.67 mm^2 . Theoretical values of mass flowrate were corrected iteratively for any total head loss in the plenum chamber caused by a finite velocity at the pressure tapping. In practice the losses were never greater than 0.01%. Plots of discharge coefficient versus pressure ratio are shown in figures 5.1. The values of C_D at the critical pressure ratio are all $1.0 \pm .045$. In order to remove any errors due to slot width measurement or leaks in the air supply, the data are also presented normalised with respect to the value of C_D at the critical pressure ratio for each slot width. The plots show a clear trend, at below choking pressures, of an increase in the value of normalised C_D (C_{DN}) as the slot width increases. This is because of the assumptions of uniform flow across the slot which become more inaccurate at smaller slot widths. This trend is expected. However, the increase in normalised C_D above unity for small slot widths and above choking pressures is less readily explained. The effect of distortion of the rig whilst under pressure, although not likely, would explain an increase in values of discharge coefficient and would be more prevalent at smaller slot widths. Another possible reason is that at small slot widths, values of normalised C_D are more sensitive to leaks in the air supply downstream of the orifice plate. However, all the values of C_D are significantly higher than the corresponding case of a flat wall downstream of a plane slot because the sub-ambient pressure distribution induced by the convex curvature. Gregory-Smith and Robinson (1982) investigate the effect of convex curvature on discharge coefficient using different slot geometries.

5.3 STATIC PRESSURE MEASUREMENTS

Surface pressure measurements are shown in figure 5.3. The dotted line shows the data of Newman (1961) who uses the definition of Re_p for a circular cylinder, and it maintains a roughly constant value of $P_{stand} = 1.4$. The plots are as expected except for the 30% increase in pressure between the 60° and 70° positions. This jump appeared consistently in all surface pressure plots, even when the slot was choked. At their face value, these plots appear to indicate a region of separation, reverse flow and subsequent reattachment. This was checked by smoke tests which showed no such region. The fact that the noted rise in pressure was independent of supply pressure corroborates this. This rise is due to a slight surface imperfection and also errors in position and angle of the pressure tapings. The positioning and drilling of these was in fact an awkward process and difficult to do accurately because of the geometry of the flare.

For the case of $P_o/P_{atm} = 1.02$ (hereafter referred to as 'Case A'; the $P_o/P_{atm} = 1.0602$ data is referred to as 'Case B'.), there is a region of positive pressure immediately downstream of the slot. In this case, however, the region of negative pressure gradient disappears with higher slot exit velocities. This phenomenon could therefore be attributable to a small region of separation caused by attachment of the flow to the slot lip. It was also noted by Newman (1961) who attributed the cause to curvature of the rapidly entrained flow near the slot. In the former case, it is an effect induced by the geometry of the slot lip whilst in the latter case it is caused by the geometry of the flare itself. But the presence of a negative wall pressure gradient here does cast doubt on the validity of profiles immediately downstream of the slot.

Complete static pressure profiles for case A are shown in figure 5.4. These data are unremarkable and merely demonstrate the change in static pressure. They also show how the effect of the transition from the curved to flat section is passed upstream by the pressure which starts increasing (P_{stand} decreasing) at $\theta = 10 - 20^\circ$. Extrapolation to $\xi = 0$ gives values of P_{stand} in reasonable agreement with the values measured by the surface pressure tapings. The data of figure 5.4 were calculated by subtraction of the hot-wire data from the corresponding values of total pressure, rather than from the three-hole probe calibration for static pressure.

The agreement between these profiles and the wall static pressure measurements ought to be better, particularly for the 20° and 30° profiles. However, as stated above, the profile data for these two profiles is likely to be unsatisfactory, and therefore the calculation of static pressure also. Another likely source of error concerns the resolution of the turbulence intensities by the total-pressure probe itself. It was assumed that the probe is equally sensitive to all three components.

5.4 MEAN VELOCITY PROFILE DATA

Figure 5.5 shows the \bar{U} profiles from the hot-wire data for case A. The next two sets of plots are from three-hole probe data and show $\sqrt{\bar{U}^2 + \bar{V}^2}$, although the difference between this total velocity and \bar{U} is negligible. Figures 5.5 and 5.6 are therefore a direct comparison, although the hot-wire profiles contain extra points near the wall, ($y < 1.06 \text{ min}$) produced from the approximate analysis (Appendix D). The agreement is satisfactory except in the case of $\theta = 40^\circ$ and 90° where the discrepancy is caused by drifting of the supply despite being monitored during a traverse. The hot-wire probe is obviously more

sensitive in the outer regions of the jet as indicated by the fuller profiles obtained. The data of figure 5.7 were not corrected for the averaging of turbulence by the three-hole probe.

All these profiles were fitted with least square curve fits which were interpolated for values of y_m , $y_{m/2}$ and \bar{U}_m . Growth and velocity decay rates for the two cases are shown in figures 5.8 and 5.9. The growth rate data are compared with an experimental best fit line for a wall jet on a circular cylinder. A flat plate wall jet and a radial wall jet grow at approximately the same rate, therefore with the addition of streamline curvature to both flows, the growth rates can be expected to be still approximately the same. The lack of agreement for case A illustrates the effect of a larger slot width increasing the size of the potential core of the jet and therefore also its development length to a fully developed jet to which the growth law applies. Also, the effect of axisymmetry on the mean flow is apparent where $y_{m/2}/t$ actually decreases in the early stages of the jet development. This is shown by both hot-wire and three-hole probe data which generally show good agreement, except for case A where $\theta > 75^\circ$. For then, percentage errors in mean velocities are large enough to make accurate determination of $y_{m/2}$ difficult.

Figures 5.10 - 5.13 show the non-dimensional mean velocity data for the two cases compared with Glauert's profile for a self-preserving flat plate wall jet. Figure 5.10 shows the \bar{U}/\bar{U}_m profiles for $\theta < 75^\circ$ only, for which the data collapse fairly well to a single line giving a mistaken impression of similar mean velocity profiles. Figure 5.14 however, shows this not to be the case, where profiles of \bar{V}/\bar{U}_m are distinctly non-similar. Profiles of \bar{U}/\bar{U}_m must therefore be non-similar

also for satisfaction of the continuity equation. The centrifugal body forces are therefore strong enough to affect the mean flow as well as the turbulence structure - a 'fairly thin' shear layer. Figure 5.11 shows the same data as that of the previous figure with the additional data from the remaining traverses i.e. $\theta > 90^\circ$. This additional data shows a marked deviation from Glauert's profile in the region $0.3 < \xi < 1.0$. This is shown also in figures 5.12 and 5.13 although profiles on the curved part of the flare are not distinguished from those in the transition and recovery regions. These non-dimensional profiles are thicker resulting in larger values of $\partial \bar{U} / \partial y$ on both sides of the velocity maximum. The mean flow is therefore strongly perturbed in this region, as also shown by the profiles of \bar{V} / \bar{U}_m .

5.5 CONVENTIONAL SECOND ORDER CORRELATIONS

Profiles of the turbulent intensities and shear stress are presented in figures 5.15 - 5.18. The intensities are all very high, as expected, in the region of 25 - 55%. None of the data show any degree of similarity. The \bar{u}^2 intensity profiles show the most amount of scatter since the ratio $\bar{u}^2 / (\bar{U}^2 + \bar{u}^2)$ is the smallest of all the ratios of Reynold's stress to total squared velocity. The \bar{w}^2 intensities are the least scattered data, a consequence of the solution method for the hot-wire response equations where \bar{W} is nominally zero. \bar{w}^2 is directly obtainable therefore, without recourse to expansions for \bar{U}_{eff} which use the approximation of negligible third order correlations. The \bar{v}^2 and \bar{w}^2 intensity profiles at the 20° and 30° positions show negative values nearer the wall (plotted as zeroes). This is a consequence of the slot lip effects mentioned in § 5.3 and the inapplicability of the hot-wire technique used here in regions of recirculating flow. Inevitably, the data is somewhat incomplete for $\xi > 1.4$ due to errors associated with the intermittency of the flow.

These results are first discussed for $0^\circ < \theta < 90^\circ$ without reference to the data in the transition and recovery regions, i.e. where $dr/dx = \infty$ at $\theta = 100^\circ$ and the subsequent response to a sudden change in surface curvature. At $\theta = 90^\circ$, the geometry changes from diverging to converging, but this is not a sudden change as in the case of streamwise curvature; dR/dx merely changes sign, after passing through zero and maintains a constant value. The results are interpreted in terms of the effect of streamwise curvature and divergence on the turbulence structure despite the presence of large cross-stream and streamwise mean pressure gradients. These do not appear explicitly in the Reynolds stress transport equations (equations (F.4) - (F.7)) and only affect the turbulence structure via the mean momentum equations. These gradients therefore do not affect the turbulence structure directly.

The $\overline{u^2}$ intensity profiles show pronounced peaks at $\xi \approx 0.6$, coinciding with the position of large negative values of $\partial \bar{U}/\partial y$. The main production term of $\overline{u^2}$ is therefore at a maximum. Subsequently this peak diminishes as both \bar{U} and $\partial \bar{U}/\partial y$ decrease in magnitude. Also triple products are likely to increase with distance downstream and therefore turbulent transport increases $\overline{u^2}$ in the outer edges of the jet. At $\theta = 75^\circ$ and 90° , the values of $\overline{u^2}$ reach a maximum for the flow and are more or less constant across the jet width. At $\theta = 75^\circ$ the jet has become wide enough for the data to show a peak on the wall side of the \bar{U} -profile maximum. The minimum in $\overline{u^2}$ coincides with the position of zero $\partial \bar{U}/\partial y$. Also since the shear stress is still positive in this region, production of $\overline{u^2}$ is actually suppressed. However, further in towards the wall, production increases owing to negative values of shear stress and large values of positive $\partial \bar{U}/\partial y$.

The $\overline{v^2}$ intensity profiles do not show the peakiness of their $\overline{u^2}$ counterparts. For large curvature, the dominant production term is $2 \overline{uv} \overline{U}/r$ - a curvature rather than a shear term. Hence production is not likely to be locally large in any region of the profile, although at $\theta = 90^\circ$, the profile is wide enough for the data to show a decrease near the wall where \overline{U} is small and \overline{uv} has become negative, thereby suppressing production.

The transport equation for $\overline{w^2}$ intensity contains no major production terms and exists primarily by redistribution of energy from the other two intensities. Characteristically, the $\overline{w^2}$ profiles are all rather flat and show a consistent increase downstream up to 90° . The stream-wise variation is quite large compared with the $\overline{u^2}$ and $\overline{v^2}$ components, and bearing in mind that the advection term of the transport equation (equal to the sum of the remaining component terms) is small, the small cross-stream variation in $\overline{w^2}$ is explained. Of the three intensities, $\overline{v^2}$ increases initially most rapidly, being the largest at $\theta = 45^\circ$. But at $\theta = 60^\circ$, $\overline{w^2}$ is more or less equal to the corresponding profile of $\overline{v^2}$, and at 90° $\overline{w^2}$ is the largest intensity.

The shear stress profiles all lie very close together and are rather hard to distinguish for $\theta > 45^\circ$. It should be noted here that the production term for \overline{uv} is the only one of the Reynolds stresses to contain a divergence term, viz: $h\overline{uv} (\overline{U} \sin \alpha + \overline{V} \cos \alpha)/R$. This helps to explain why the fully developed profiles up to $\theta = 90^\circ$ are much the same; the additional divergence term is most 'productive' for small θ , decreasing as \overline{U} decreases and R increases. Thus this term contributes to the production of \overline{uv} (the major terms in the transport equation) only in the early stages of the jet development. The curvature production term depends on the anisotropy of $\overline{v^2}$ and $\overline{u^2}$ which is greatest for

small θ , and acts to reduce production since $\overline{v^2} > \overline{u^2}$. Thus the major shear production term $-h \overline{v^2} \partial \overline{U} / \partial y$ is not significantly increased by the combined effects of curvature and divergence.

The profiles of \overline{uv} at stations sufficiently far downstream to permit complete data to be recorded on the wall side of the velocity maximum, show negative values of \overline{uv} , a consequence of the production of positive \overline{uv} very near the wall being negative. The position of zero shear stress is consistently closer to the wall than the corresponding velocity maxima and gets closer to the wall as x/t increases.

The remaining profiles for $\theta = 90^\circ$ and beyond show some very interesting effects. Both the $\overline{u^2}$ and $\overline{w^2}$ intensity profiles show a marked decrease at $\theta = 100^\circ$ and thereafter reach minima at $\theta = 100^\circ + 10$ mm. In the case of the $\overline{u^2}$ intensity, this minimum at $\xi = 0.5$ is less than the corresponding value on the 20° and 30° profiles. Thereafter it recovers to reach values at $\theta = 100^\circ + 20$ mm not far below those of the 90° profile. Thus the response to the removal of curvature is not monotonic. With the continued application of the extra rate of strain induced by a constant rate of convergence, it is expected that the value of $\overline{u^2}$ will not be maintained and will decrease once again although gradually. The behaviour of the $\overline{w^2}$ profiles is the same, although the values of $\overline{w^2}$ at $\theta = 100^\circ + 20$ mm are significantly less than those at $\theta = 90^\circ$.

The $\overline{v^2}$ intensity profiles appear to be more sensitive to the sudden change in curvature. The removal of curvature is first apparent at $\theta = 90^\circ$ where $\overline{v^2}$ decreases sharply for $\xi < 0.7$. It continues to decrease at the next station, but increases slightly in the region of $\xi = 0.7$ at

$\theta = 100^\circ + 10 \text{ mm}$. At the next station the values of $\overline{v^2}$ decrease once again due to the effect of convergence. All three intensities therefore show the same non-monotonic response to the removal of curvature, although the $\overline{v^2}$ component appears to react sooner. The recovery is slow in comparison with the jet growth rate, although the subsequent effects of convergence are apparent at the last traverse position, rather than those of the non-monotonic response to the removal of curvature.

5.6 STRUCTURAL PARAMETERS

In order to characterise structural changes indicated by the plots of shear stress and turbulence intensities, dimensionless ratios are required. These correspond to the empirical input to calculation methods as they reflect the larger implicit changes in the Reynolds stress transport equations as opposed to the explicit extra terms. Accordingly, the dimensionless quantities $a_1 = \overline{uv}/q^2$, $R_{uv} = \overline{uv}/(\overline{u^2} \cdot \overline{v^2})$ and $\overline{v^2}/\overline{u^2}$ are now considered.

The ratios a_1 and R_{uv} are little affected by the streamline curvature itself. Both maintain fairly constant values of 0.12 and 0.4 respectively up to $\theta < 90^\circ$. Then both parameters show a marked non-monotonic response to the removal of curvature. They decrease at $\theta = 90^\circ$ and subsequently increase, a_1 rising to 0.2 and R_{uv} to 0.55 at $\theta = 100^\circ + 10 \text{ mm}$. At the next station however, they have begun to decrease once again. Both parameters show a marked decrease at the last two stations for $\xi < 0.5$.

The ratio of $\overline{v^2}/\overline{u^2}$ illustrates the preferential increase of the $\overline{v^2}$ intensity by the effect of streamline curvature. Over nearly all the

jet width, except close to the wall where the $\overline{v^2}$ intensity is suppressed, $\overline{v^2}/\overline{u^2}$ increases dramatically above values for a corresponding flat-plate wall jet. The data at $\theta = 30^\circ$ (not shown in figure 5.21) correspond to those of a wall jet with streamline curvature only, typically $\overline{v^2}/\overline{u^2} = 1.0$, but at $\theta = 45^\circ$ a maximum of 4.5 exists at $\xi = 0.45$. Thereafter, the ratio decreases and at $\theta = 90^\circ$, falling below 1.0. It subsequently increases to 2.0 in the outer part of the jet, but at $\theta = 100^\circ + 20$ mm decreases once again to values close to 0.5 over nearly the whole jet width. Very large values of $\overline{v^2}/\overline{u^2}$ at $\theta = 45^\circ$ and 60° are caused by small values of $\overline{u^2}$ in the region of $\xi = 0.5$ rather than large values of $\overline{v^2}$.

5.7 RESULTS FROM LARGE SCALE TESTS

The remaining three figures are the results of three-hole probe measurements made on a large flare at a higher supply pressure. Figures 5.22 - 5.24 are supplementary data principally of use for studying the effects of scaling on the model data. This data is therefore of use as test data for the calculation method. The data of figures 5.23 and 5.24 show the same effects of curvature on the mean flow as described above. The non-dimensional mean velocity profiles are distorted, and the jet growth/velocity decay rate show the same trend as those of figures 5.8 and 5.9.

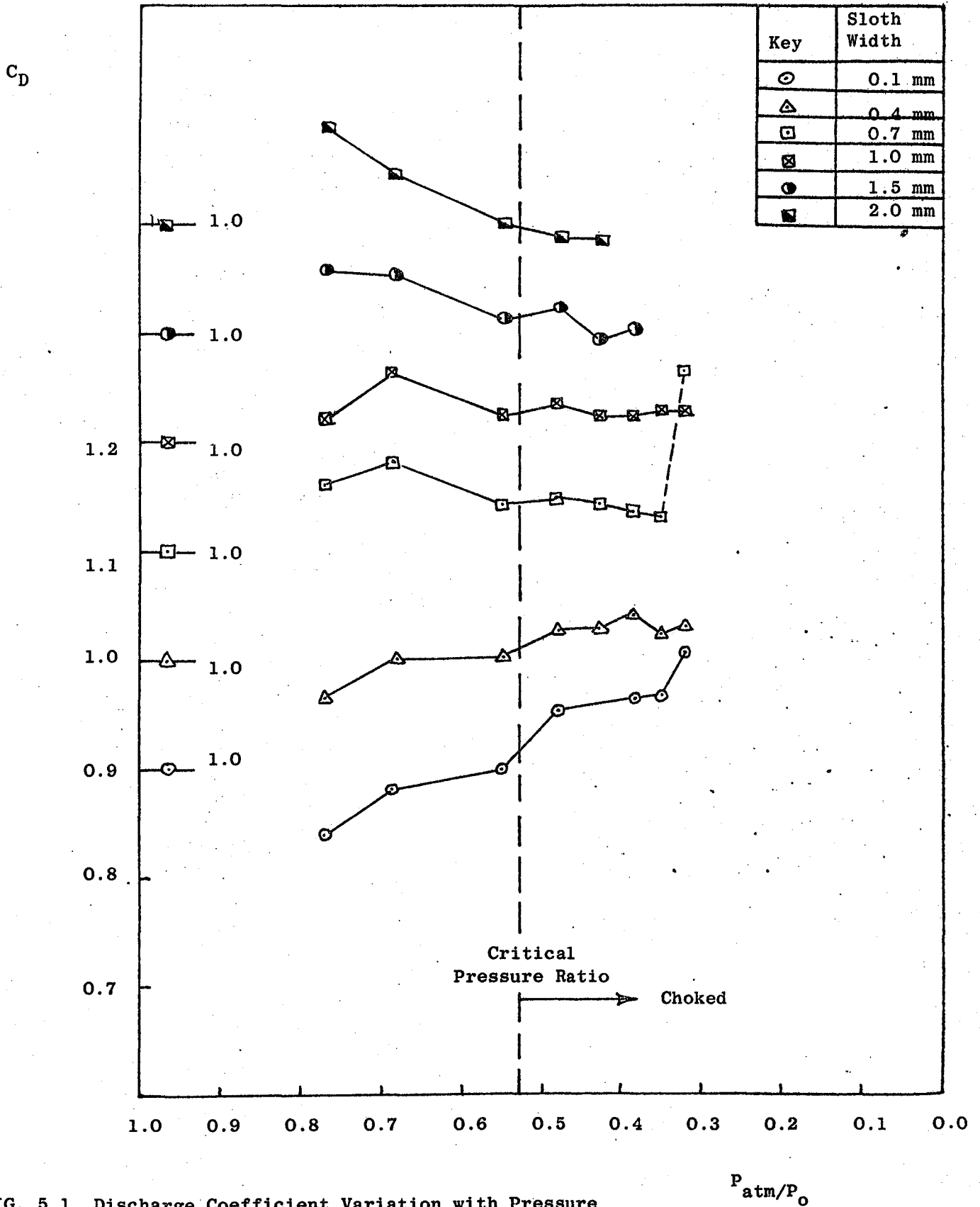


FIG. 5.1 Discharge Coefficient Variation with Pressure Ratio and Slot Width

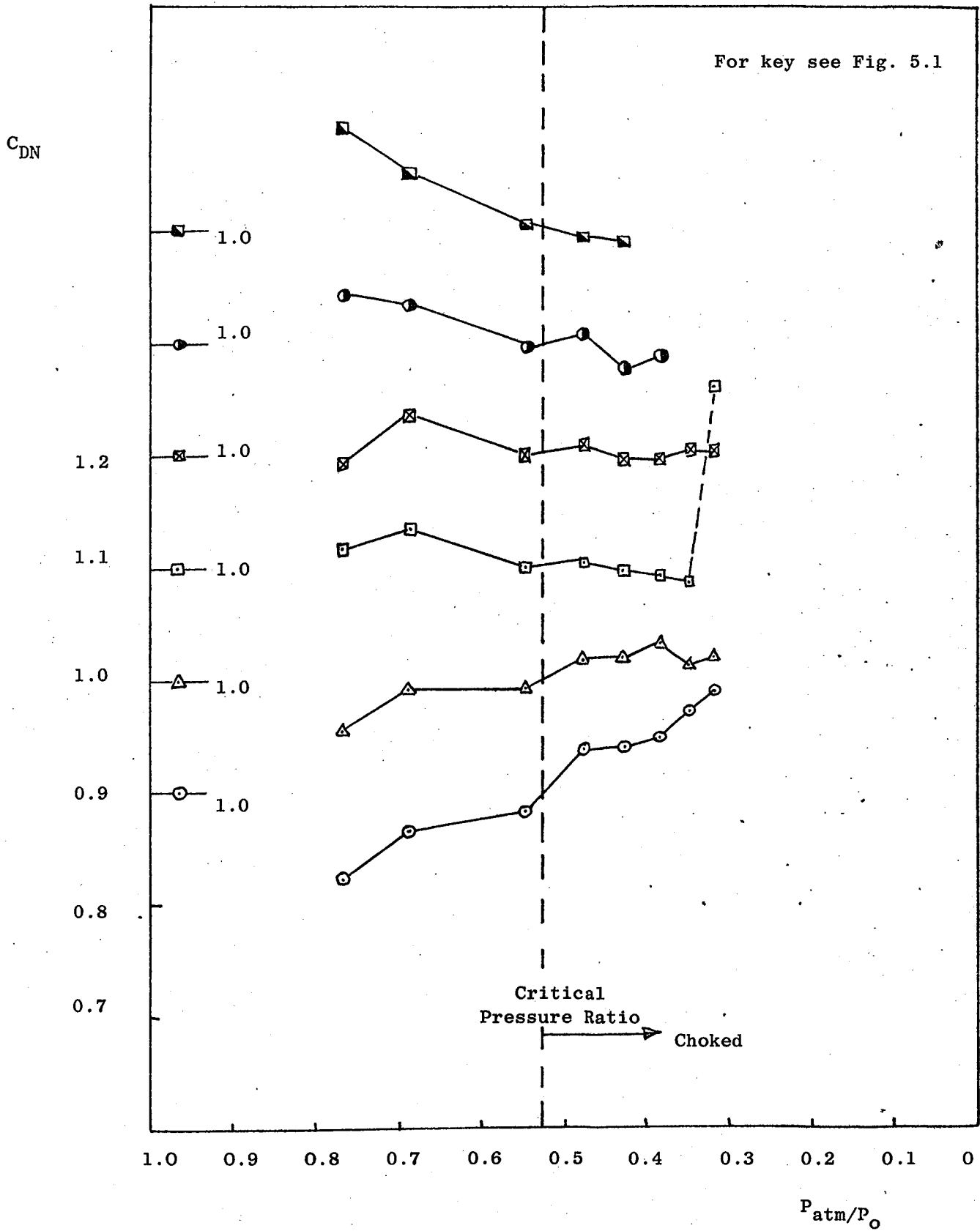
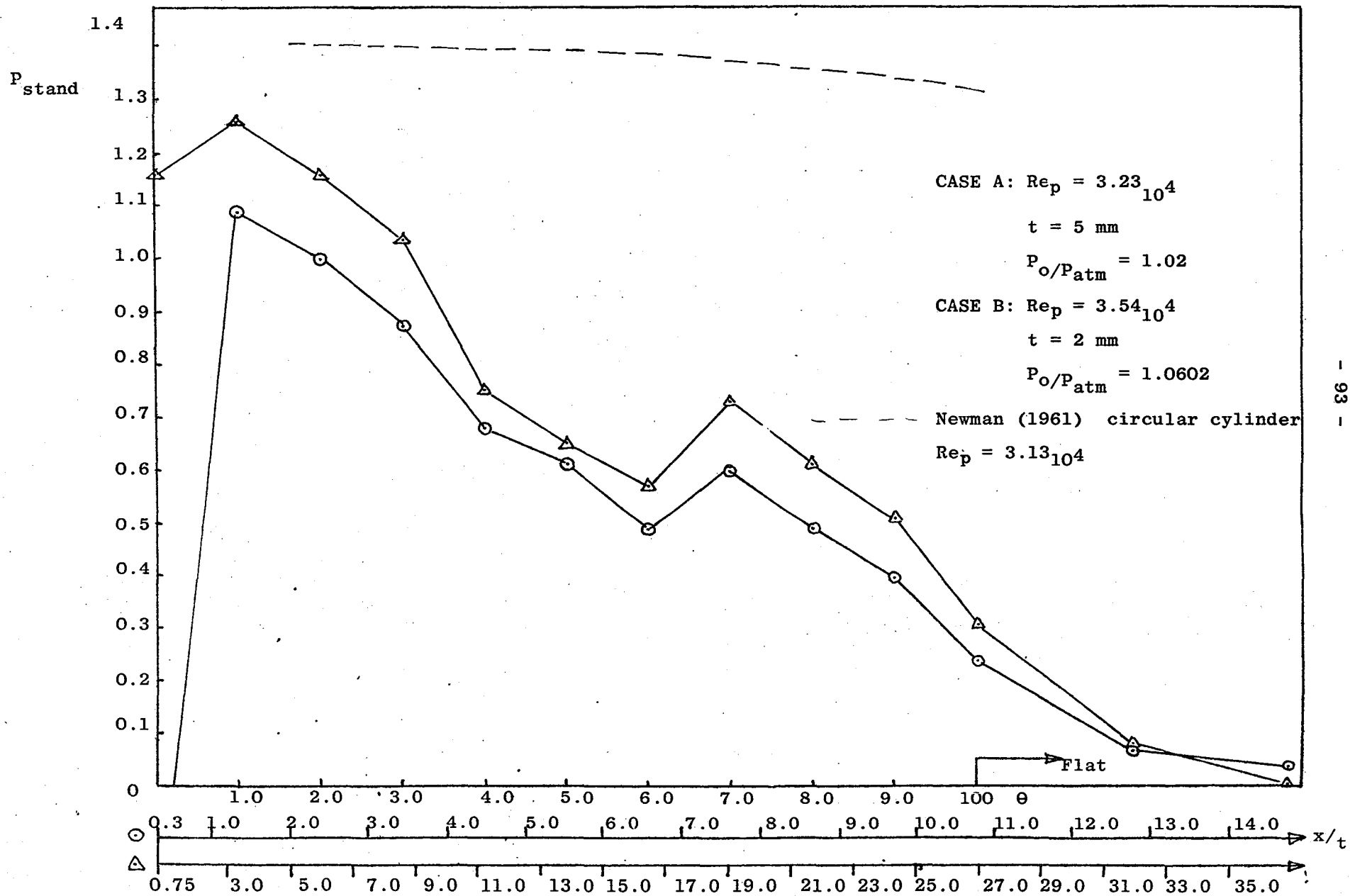


FIG. 5.2 Reduced Values of C_D

FIG. 5.3 Wall Pressure Variation in Streamwise Direction



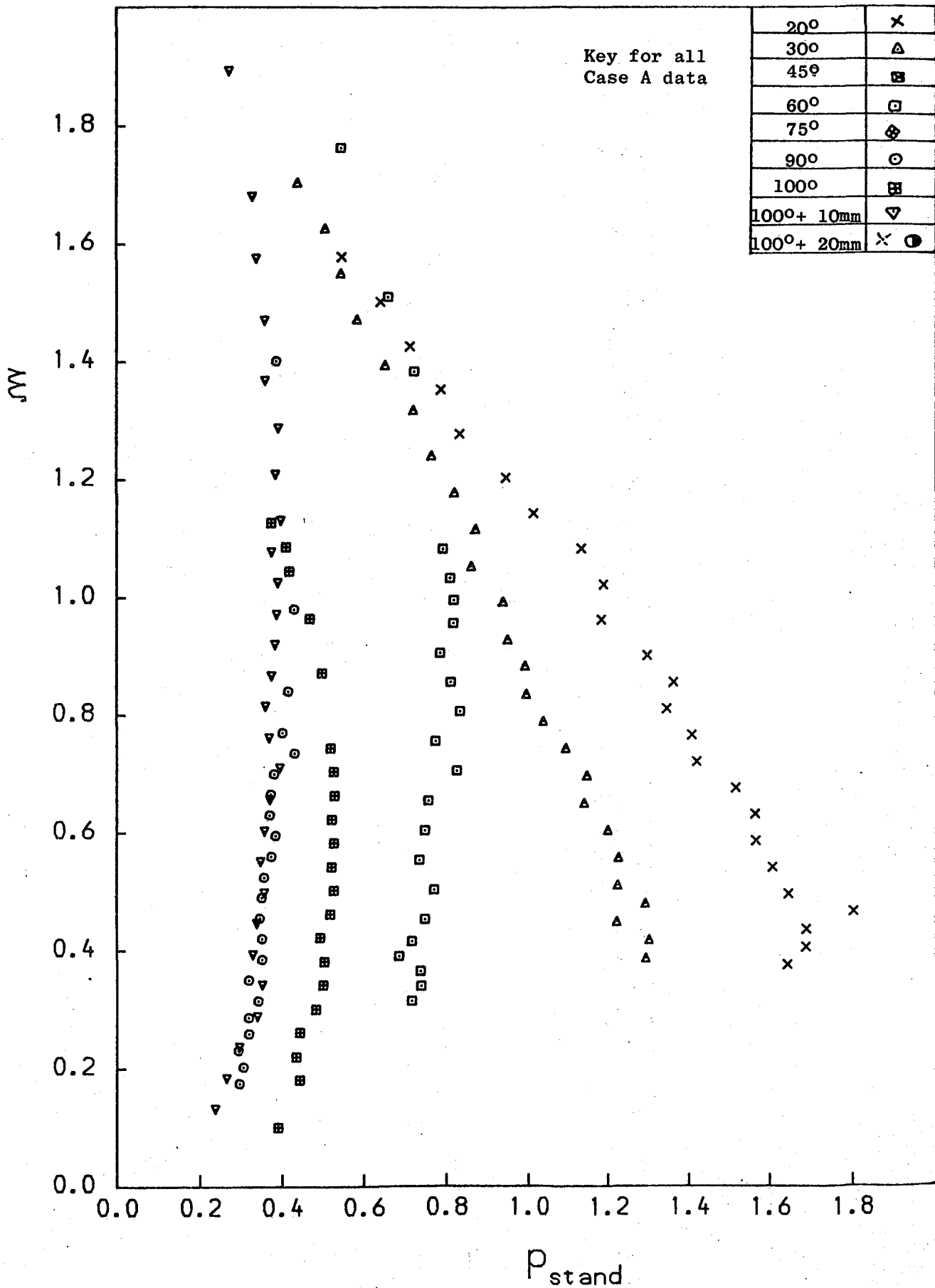


Fig. 5.4: Case A: Static Pressure Profiles

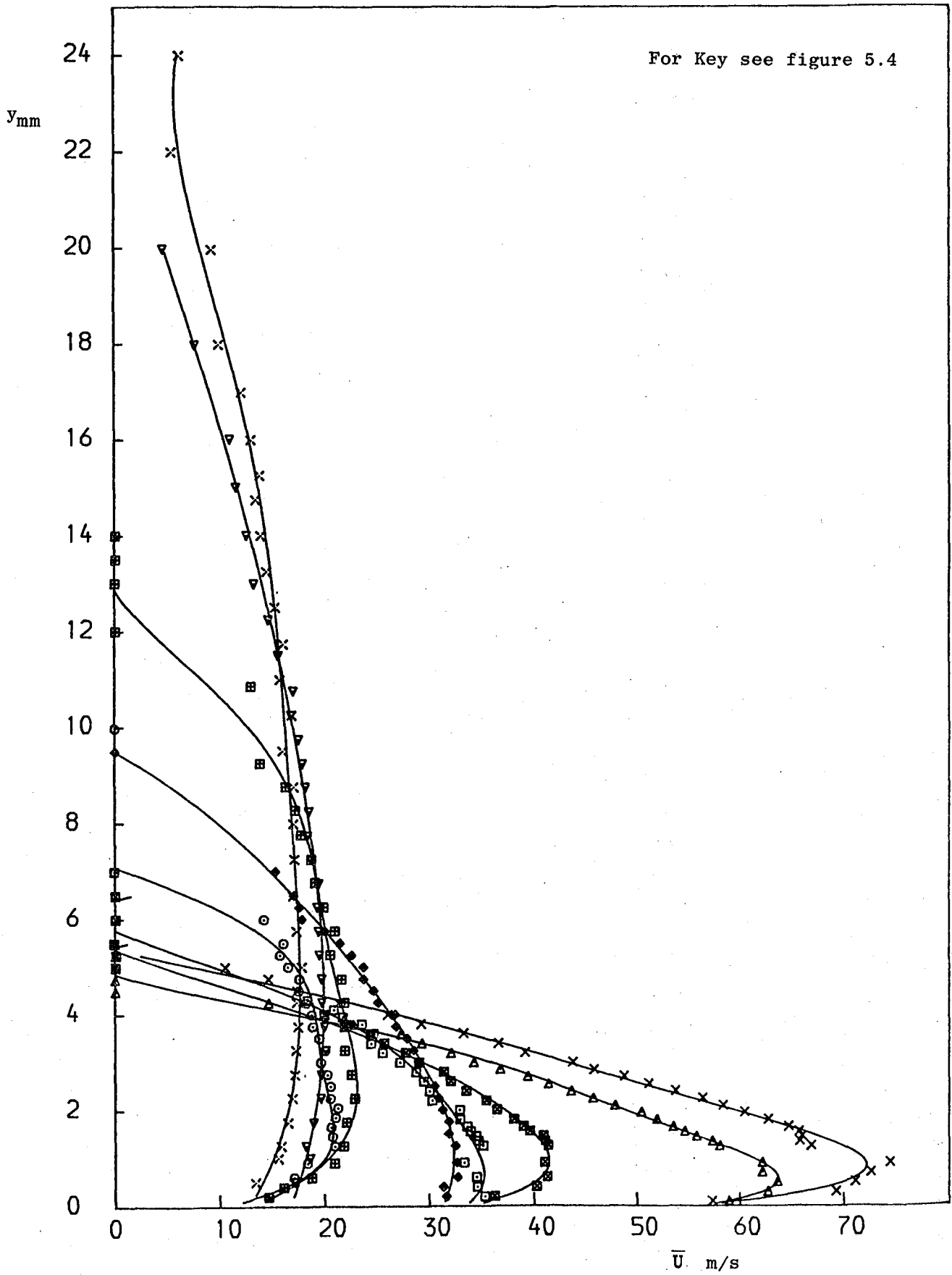


Fig. 5.5: Case A: \bar{U} v y (hot-wire probe)

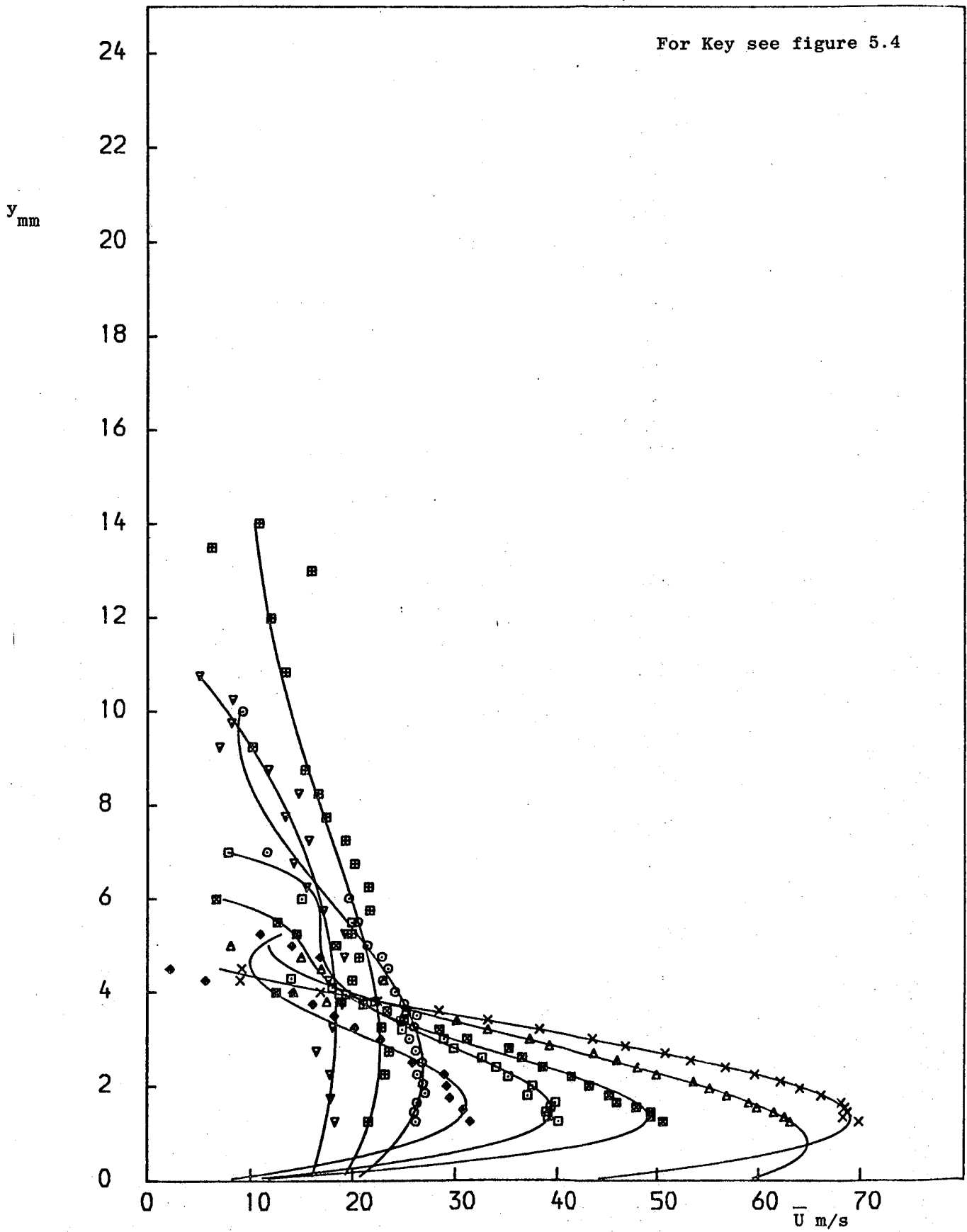


FIG. 5.6: Case A: \bar{U} v y (3-hole probe)

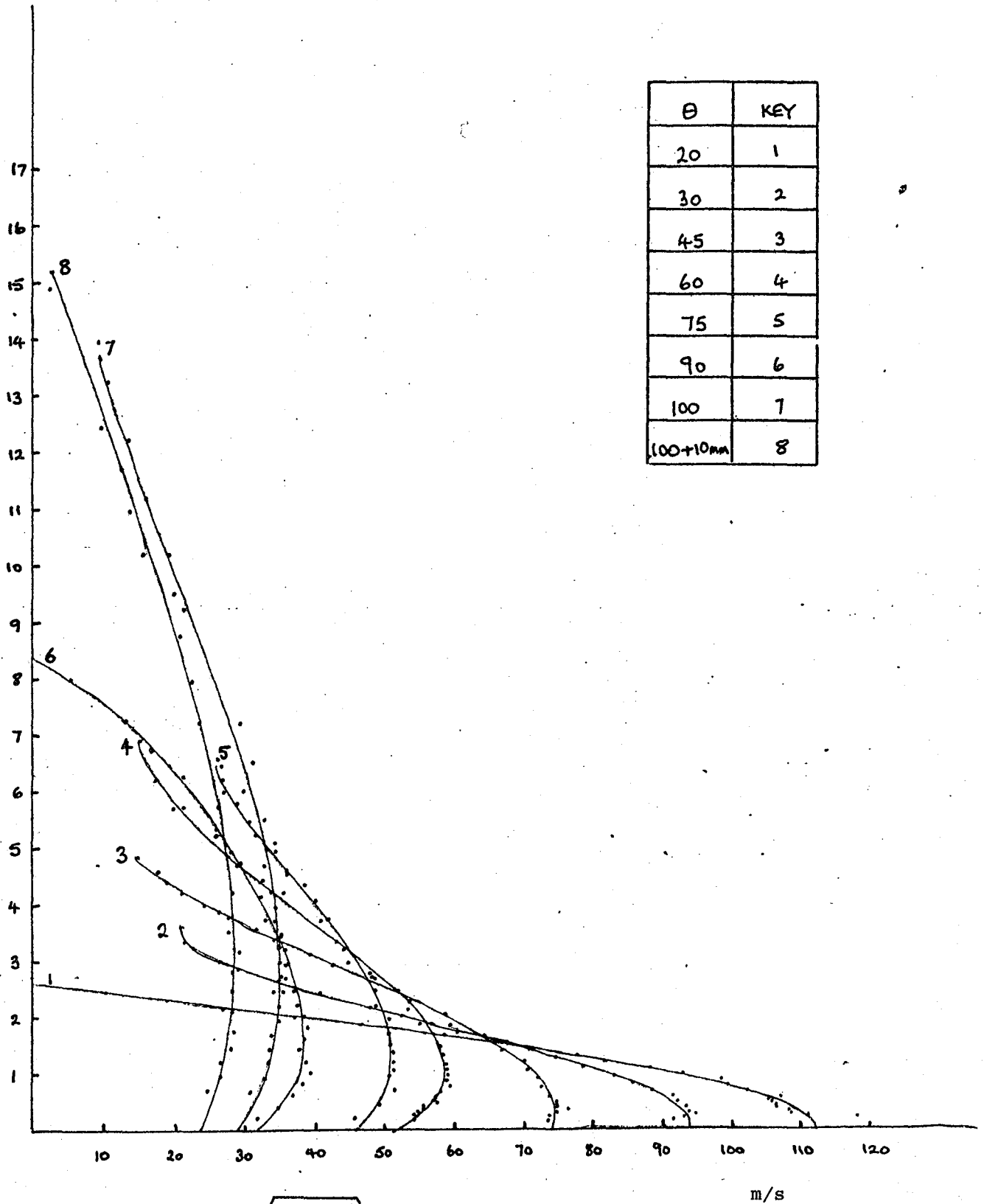


FIG. 5.7 Case B: $\sqrt{U^2 + V^2}$ v. y (3-hole probe)

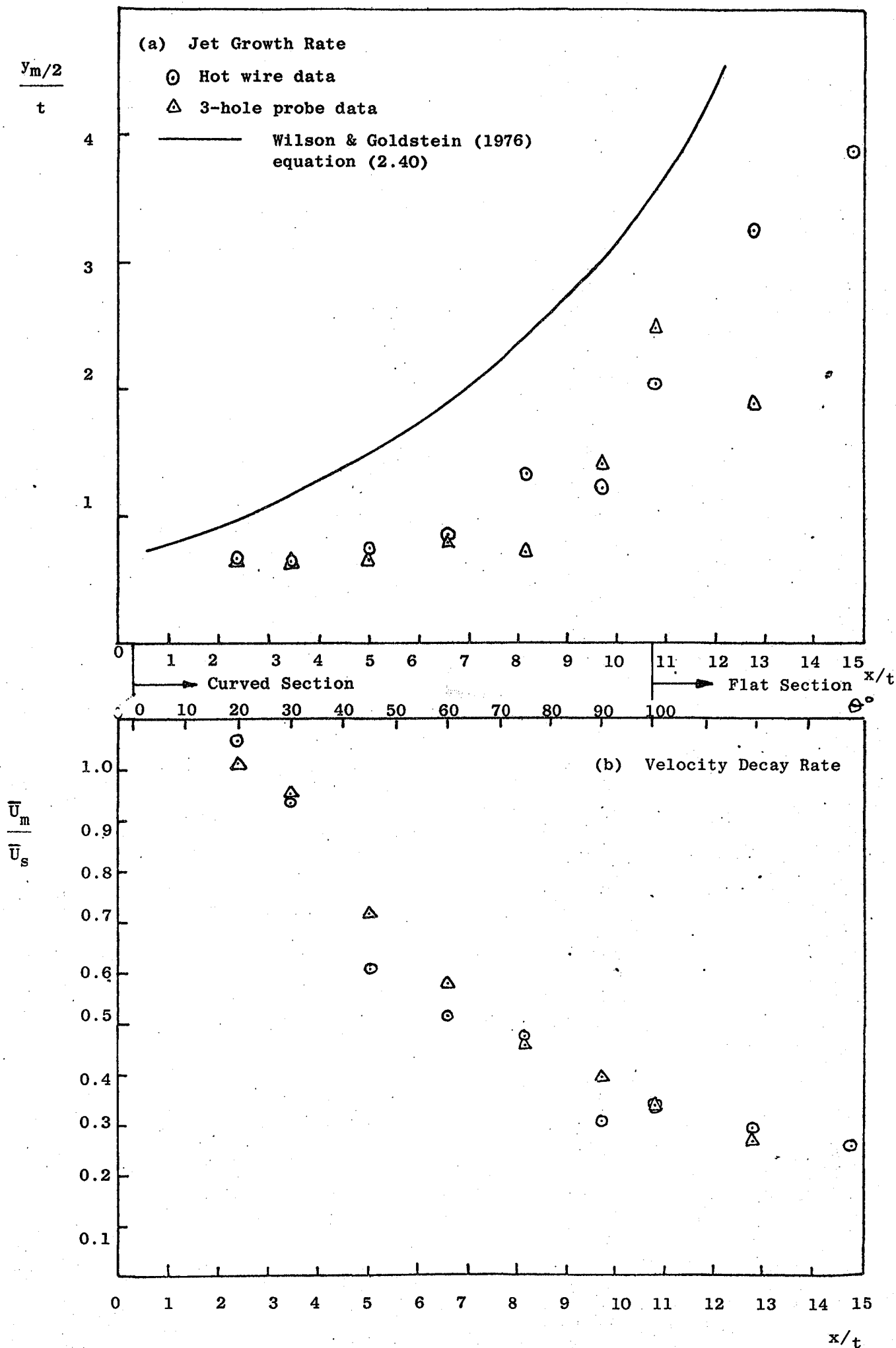


FIG. 5.8 Case A: Growth/Velocity Decay Rate

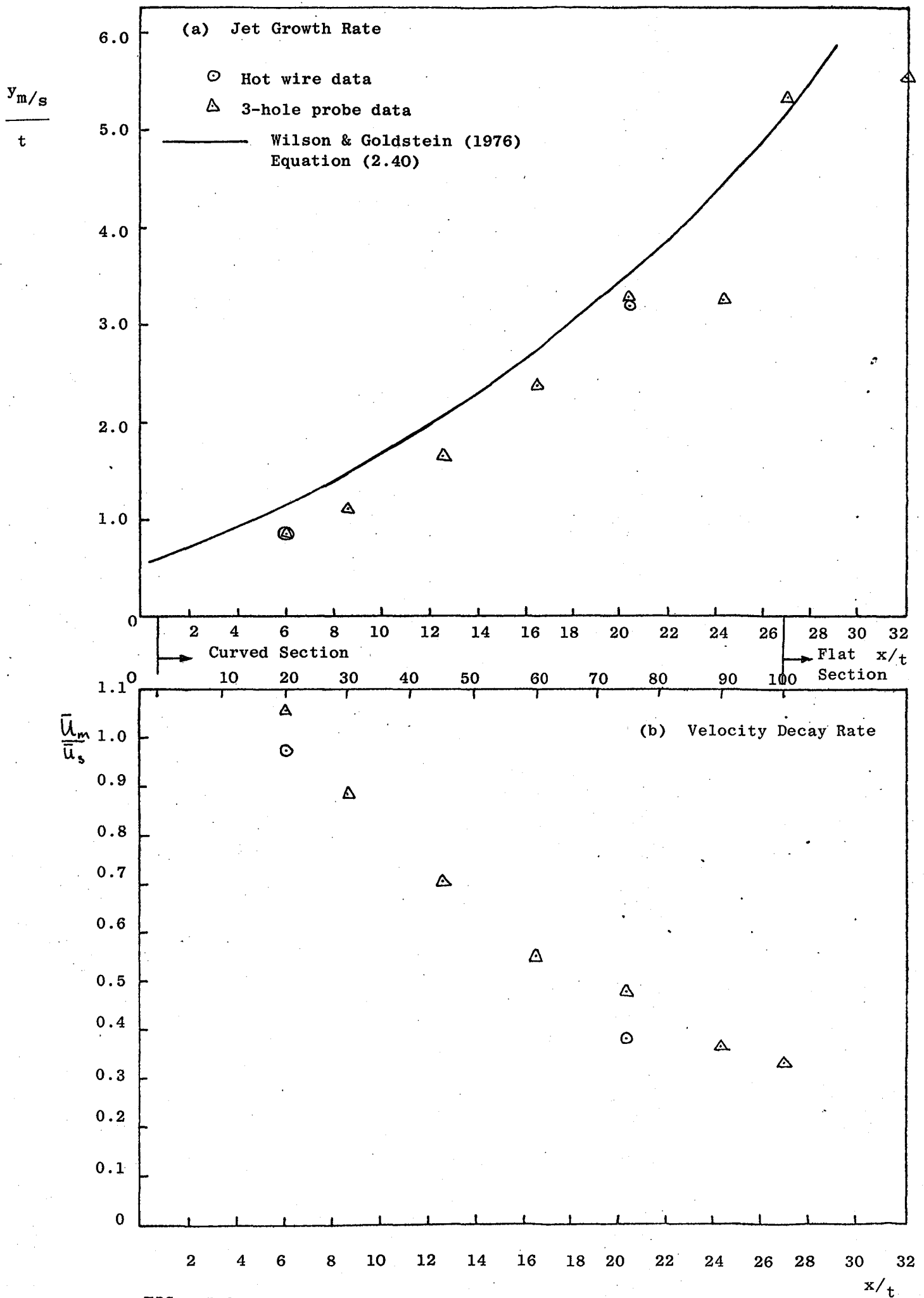


FIG. 5.9 Case B: Growth/Velocity Decay Rate

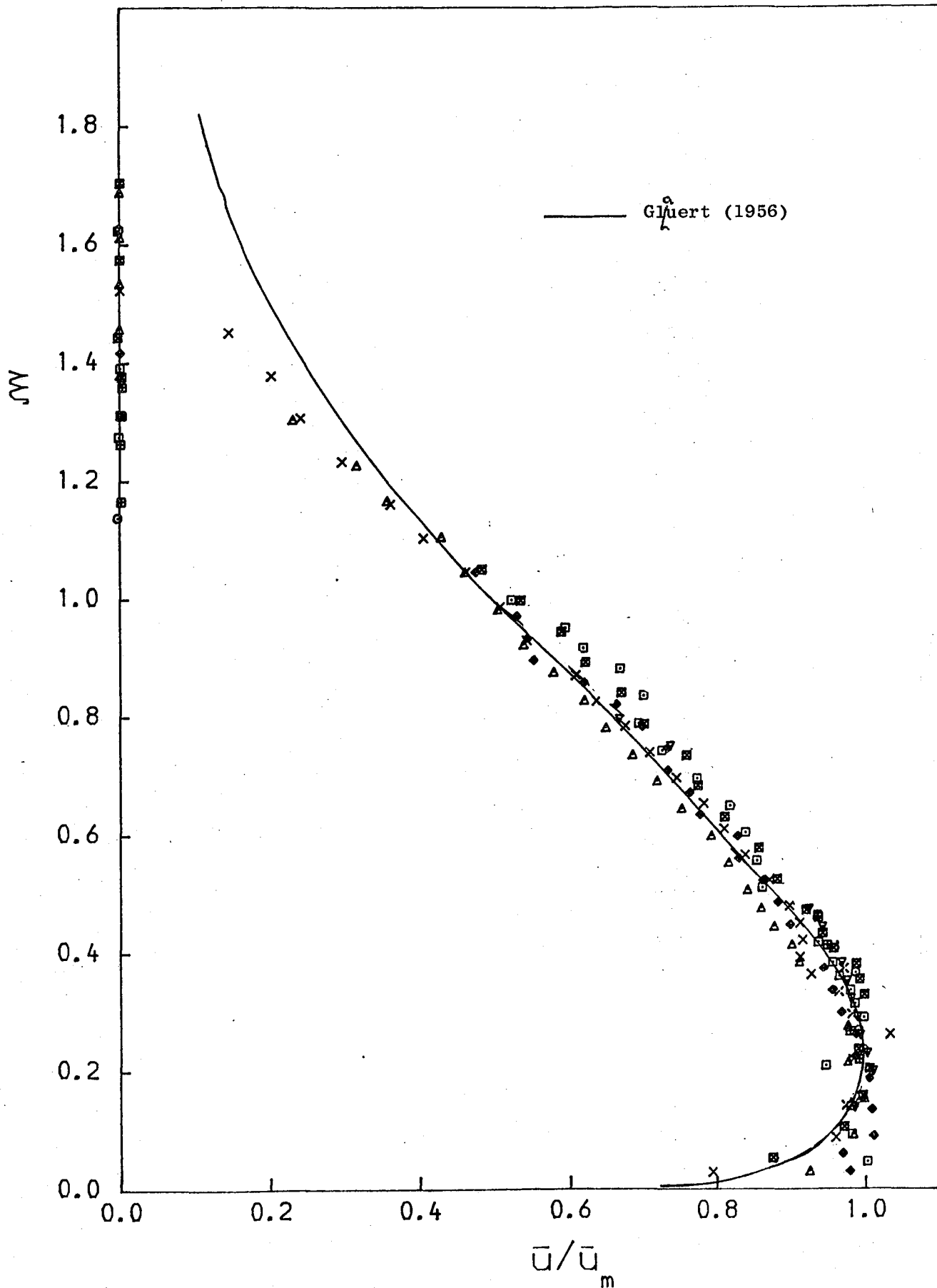


FIG. 5.10: Case A: \bar{U}/\bar{U}_m v ξ (hot-wire probe)- $\theta = 20^\circ$ - 75° only

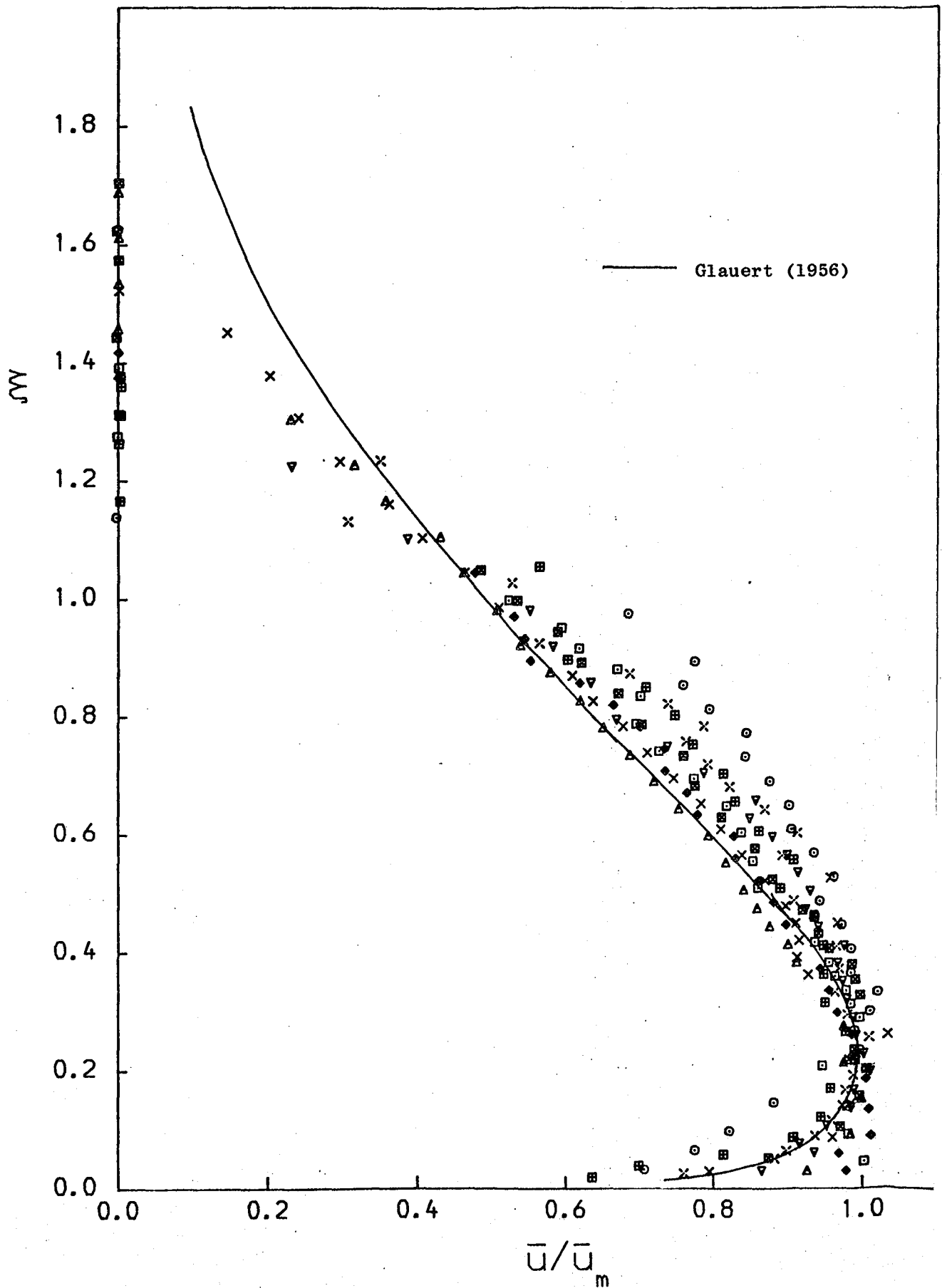


FIG. 5.11: Case A: \bar{u}/\bar{u}_m v ξ (hot -wire probe)

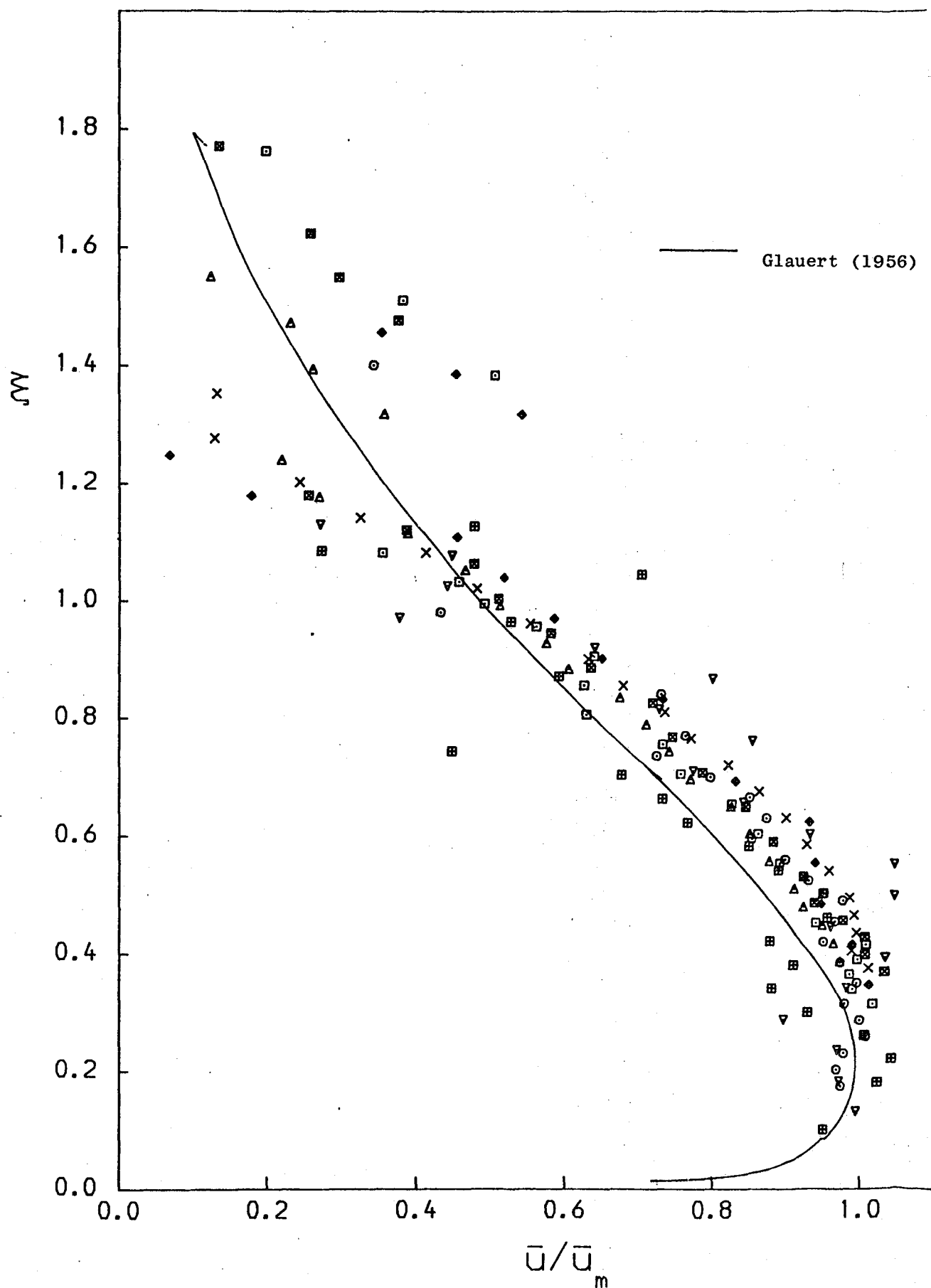


FIG. 5.12: Case A: \bar{u}/\bar{u}_m v ξ (3-hole probe)

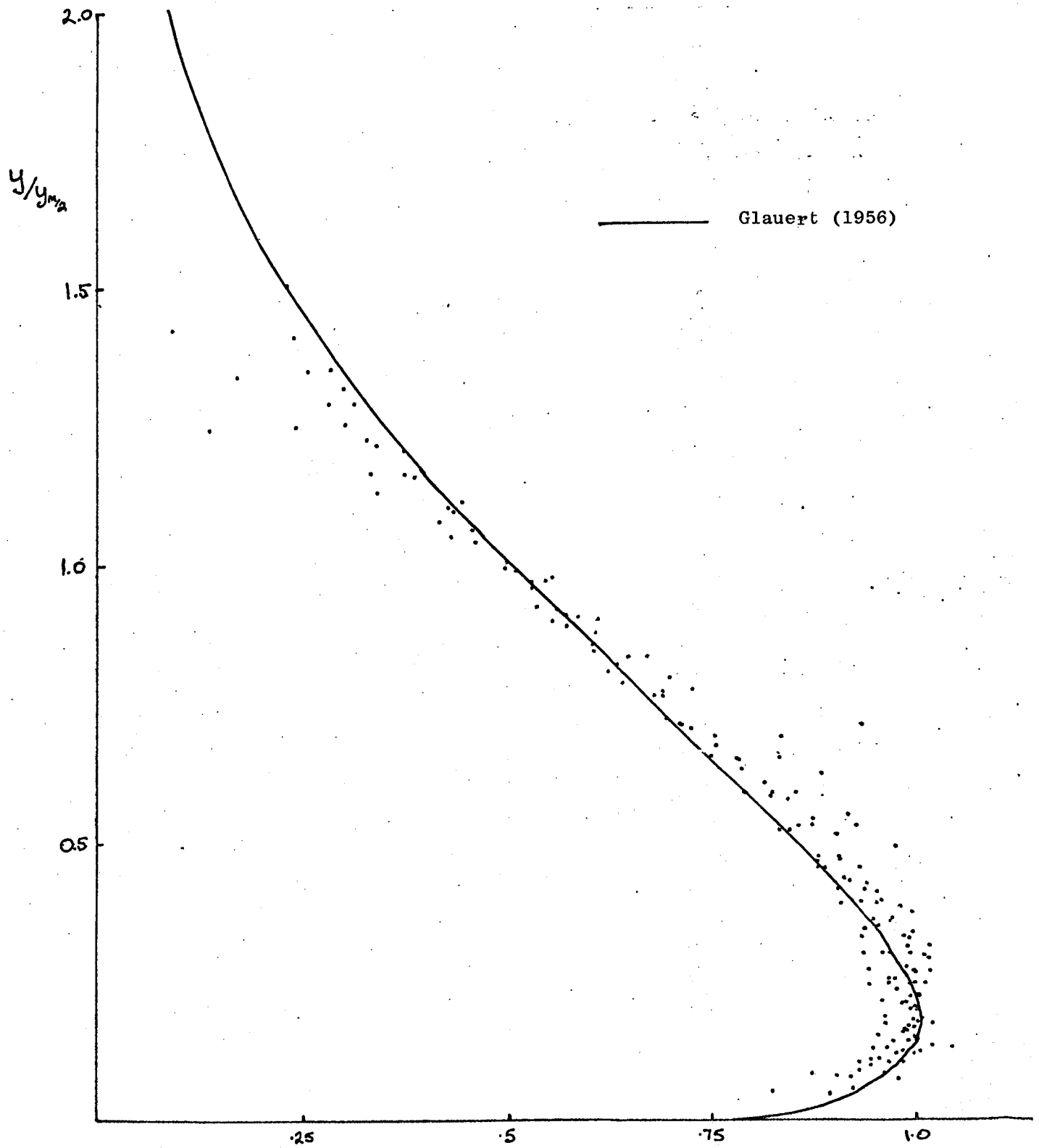


FIG. 5.13 Case B: Non-Dimensional $\sqrt{\bar{U}^2 + \bar{V}^2}$ v. ξ (3-hole probe)

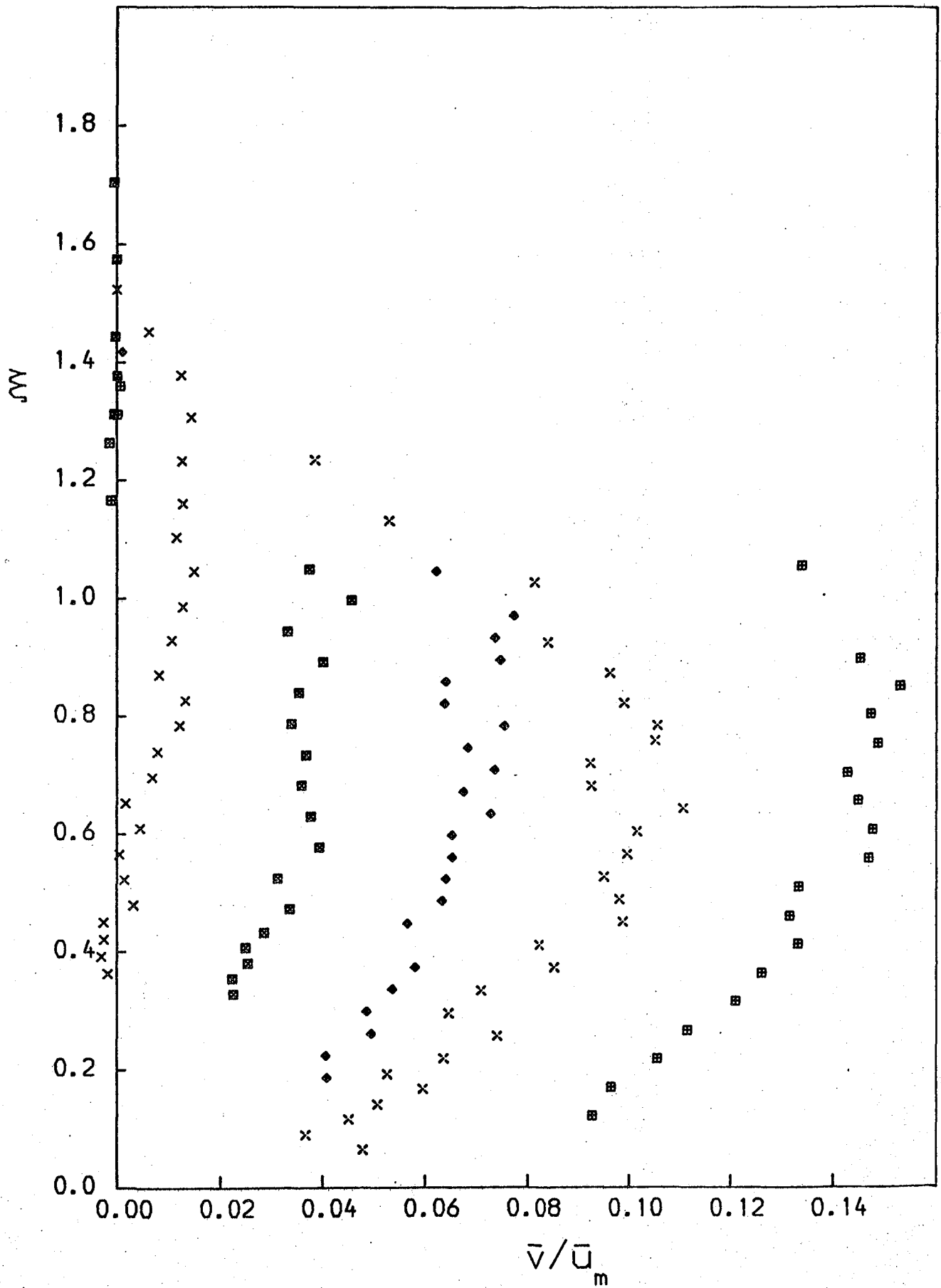


FIG. 5.14: Case A: \bar{v}/\bar{u}_m v ξ (hot-wire probe)

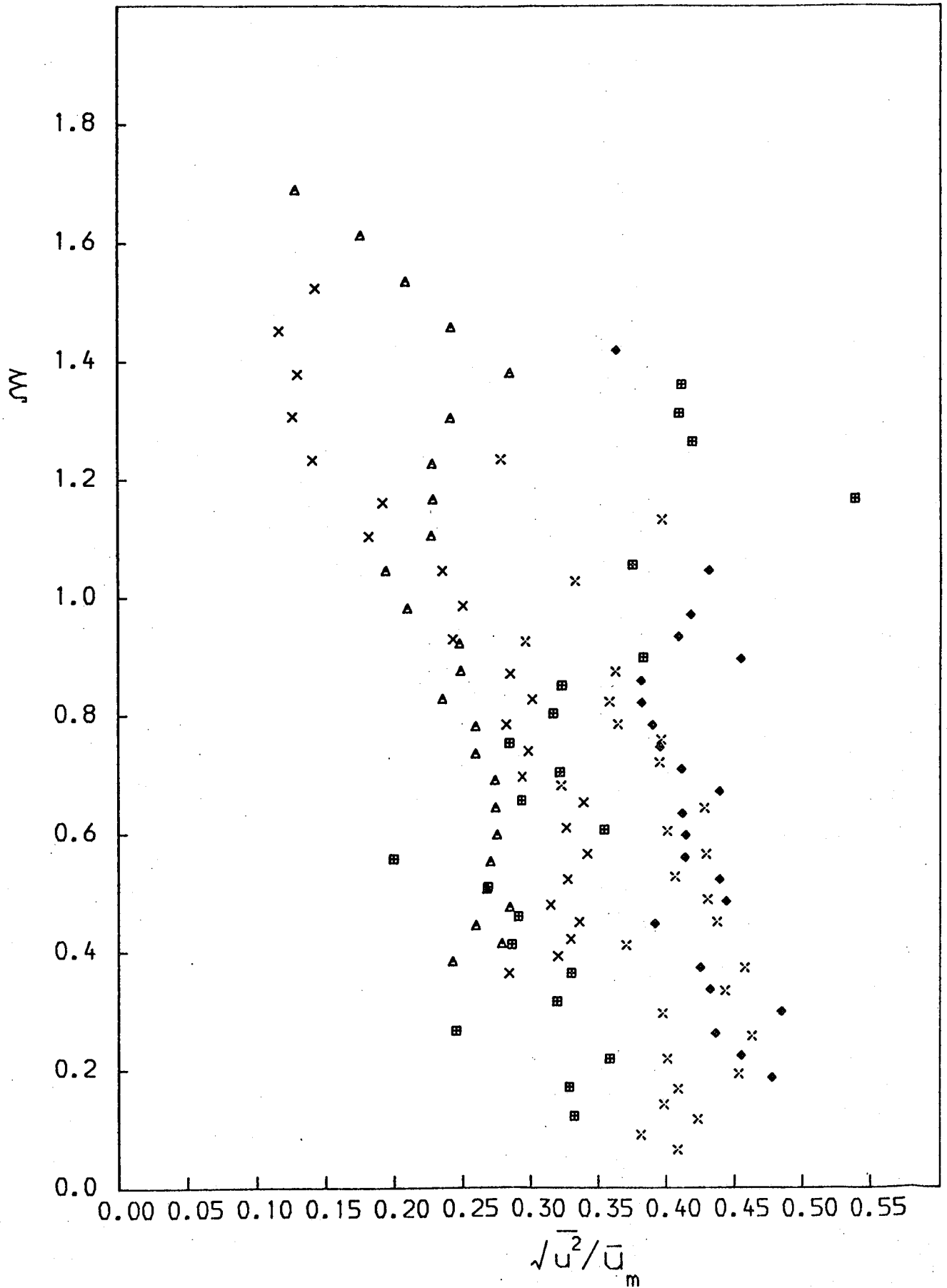


FIG. 5.15: x-Component Normal Stress Profiles

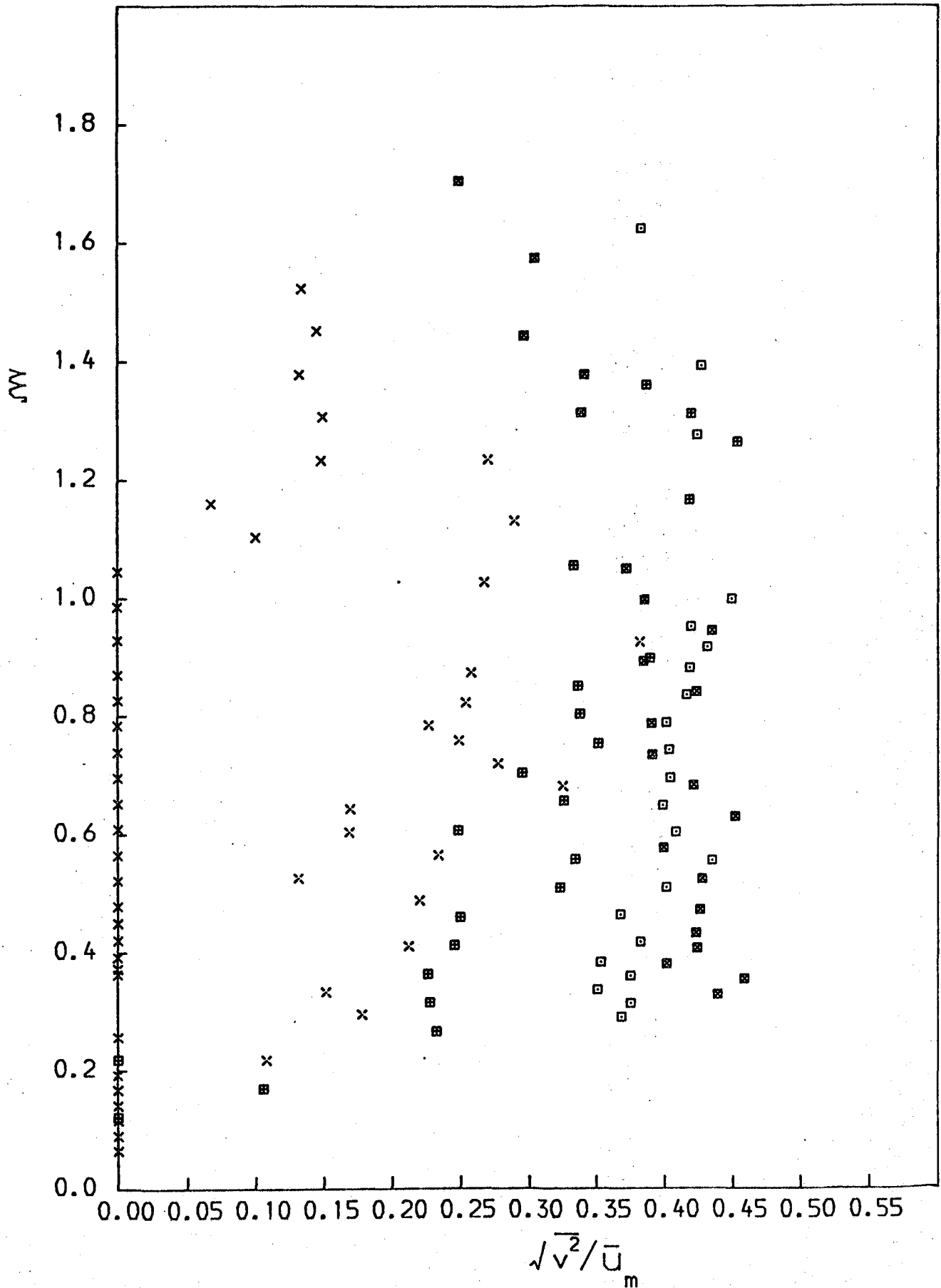


FIG. 5.16: y-Component Normal Stress Profiles

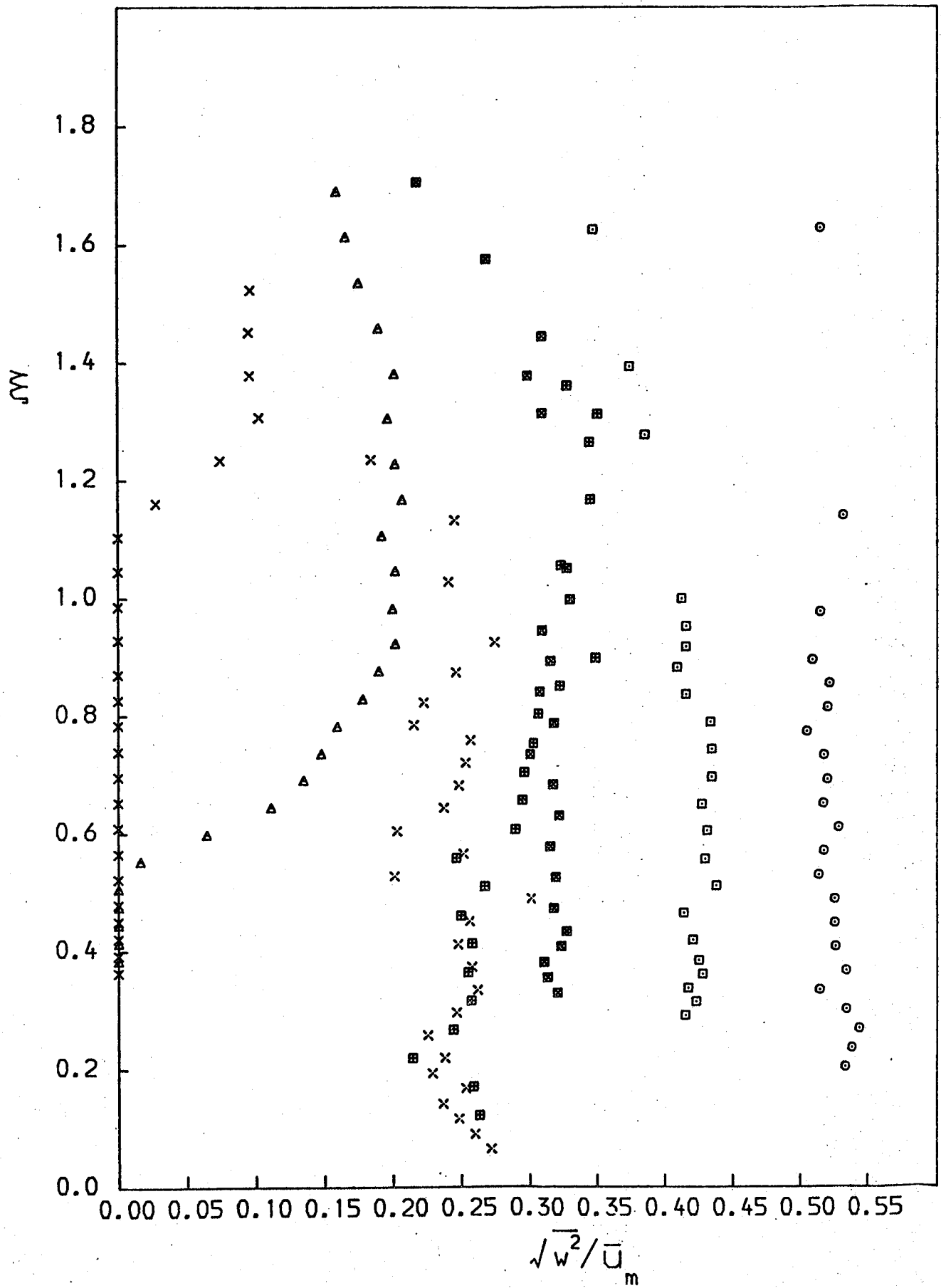


FIG. 5.17: z.Component Normal Stress Profiles

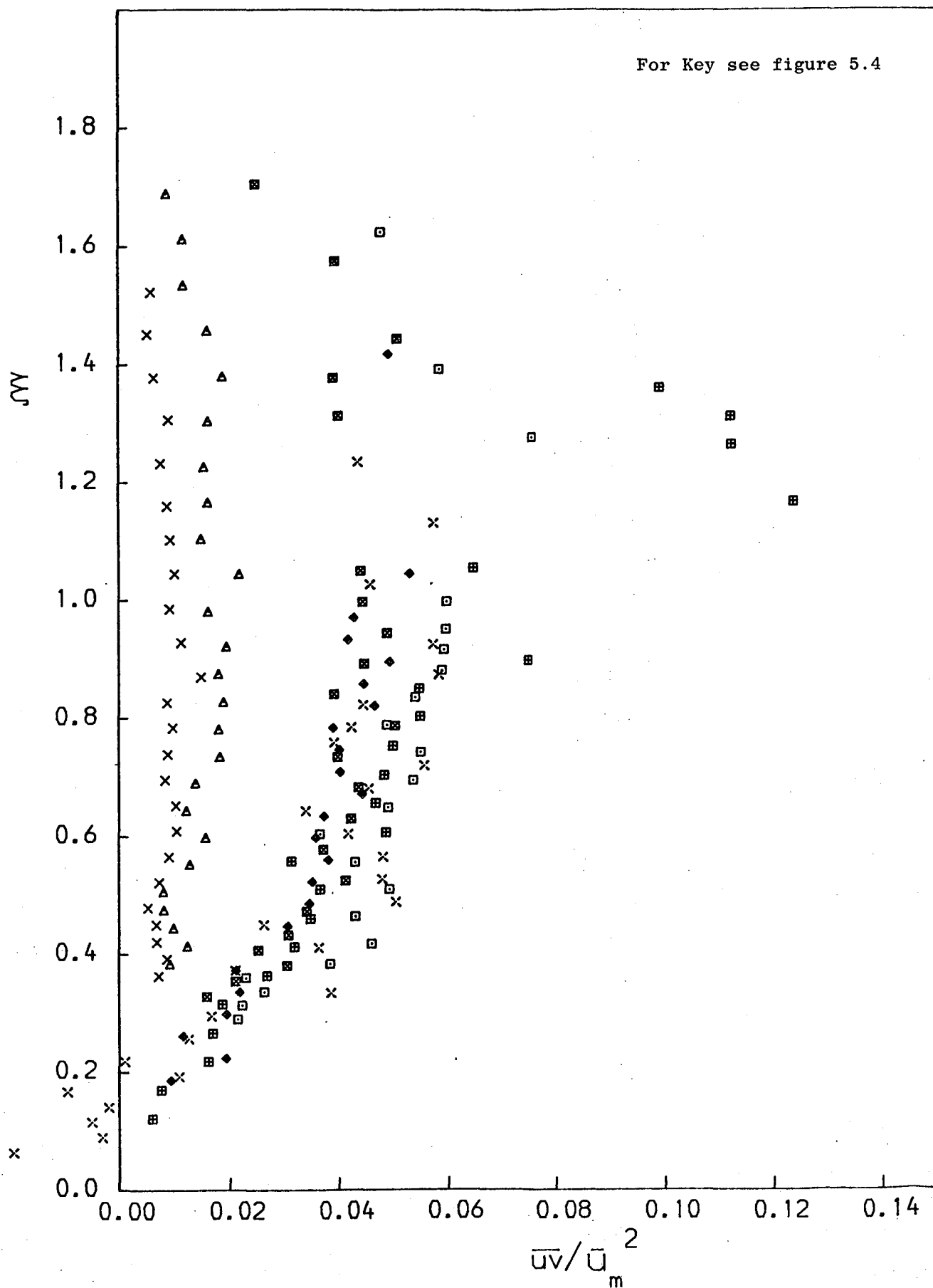


FIG. 5.18: Shear Stress Profiles

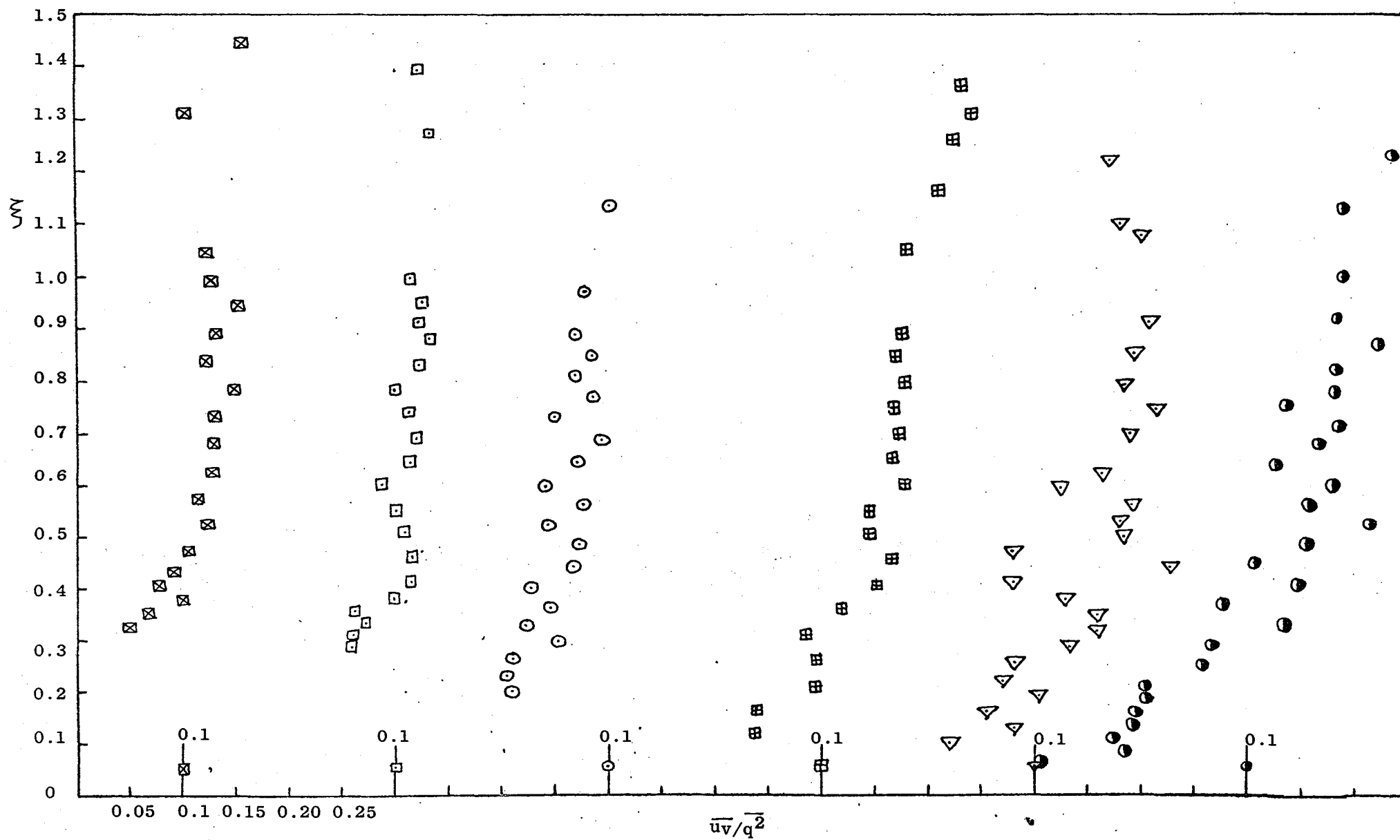


FIG. 5.19 Structural Parameter \overline{uv}/q^2

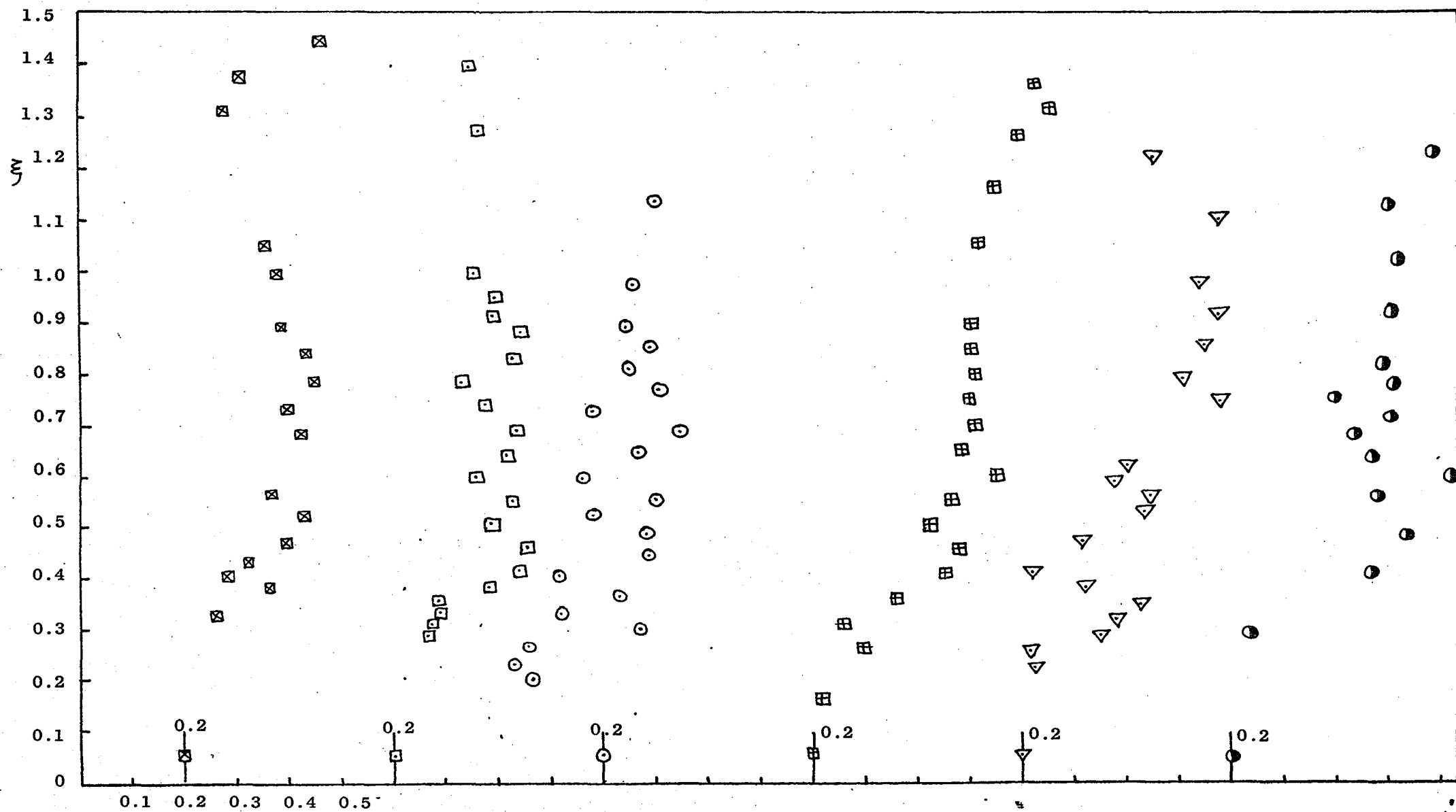


FIG. 5.20 Structural Parameter $R_{uv} = \overline{uv} / \sqrt{u^2 \cdot v^2}$

R_{uv}

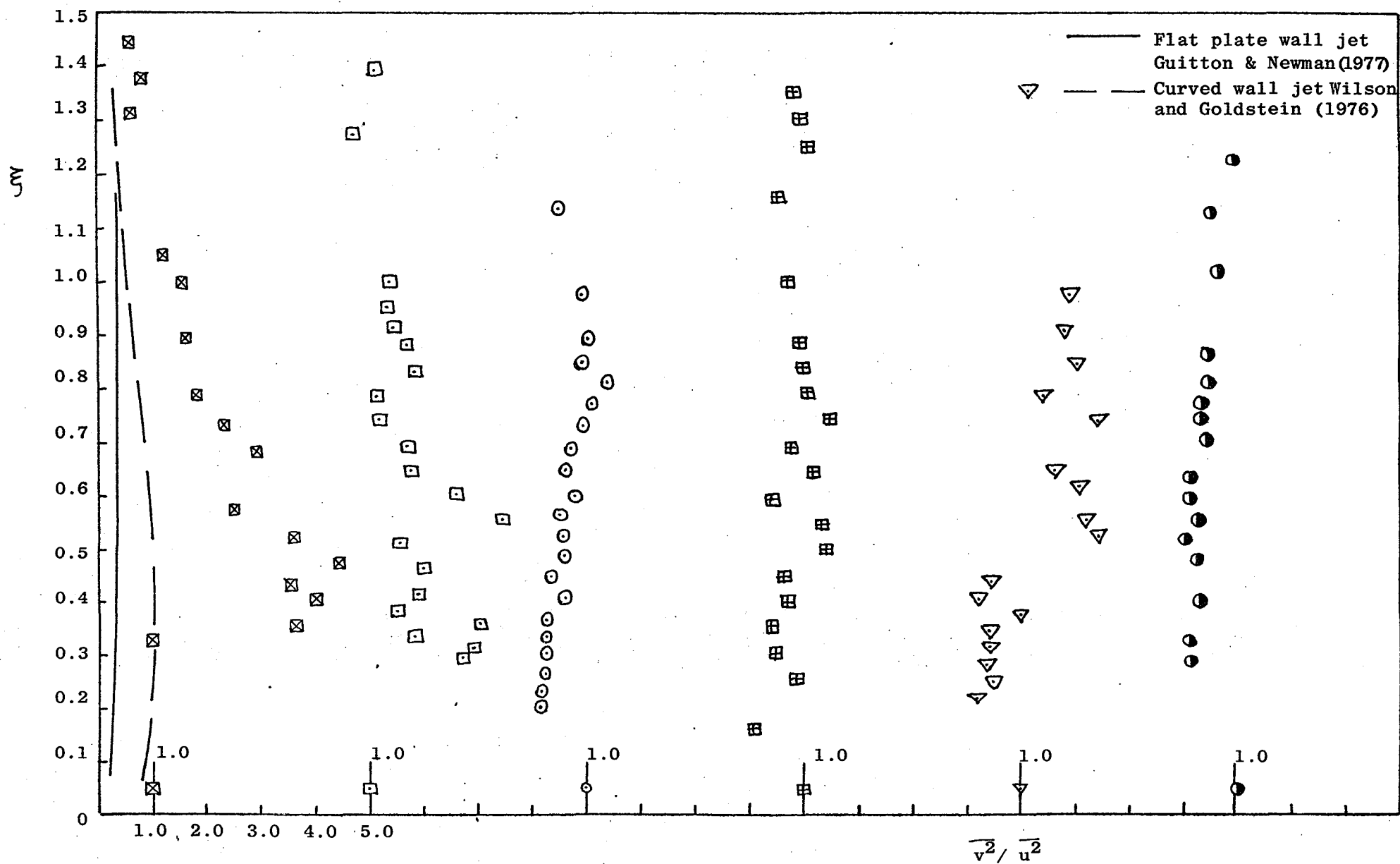


FIG. 5.21 Structural Parameter $\overline{v^2}/\overline{u^2}$

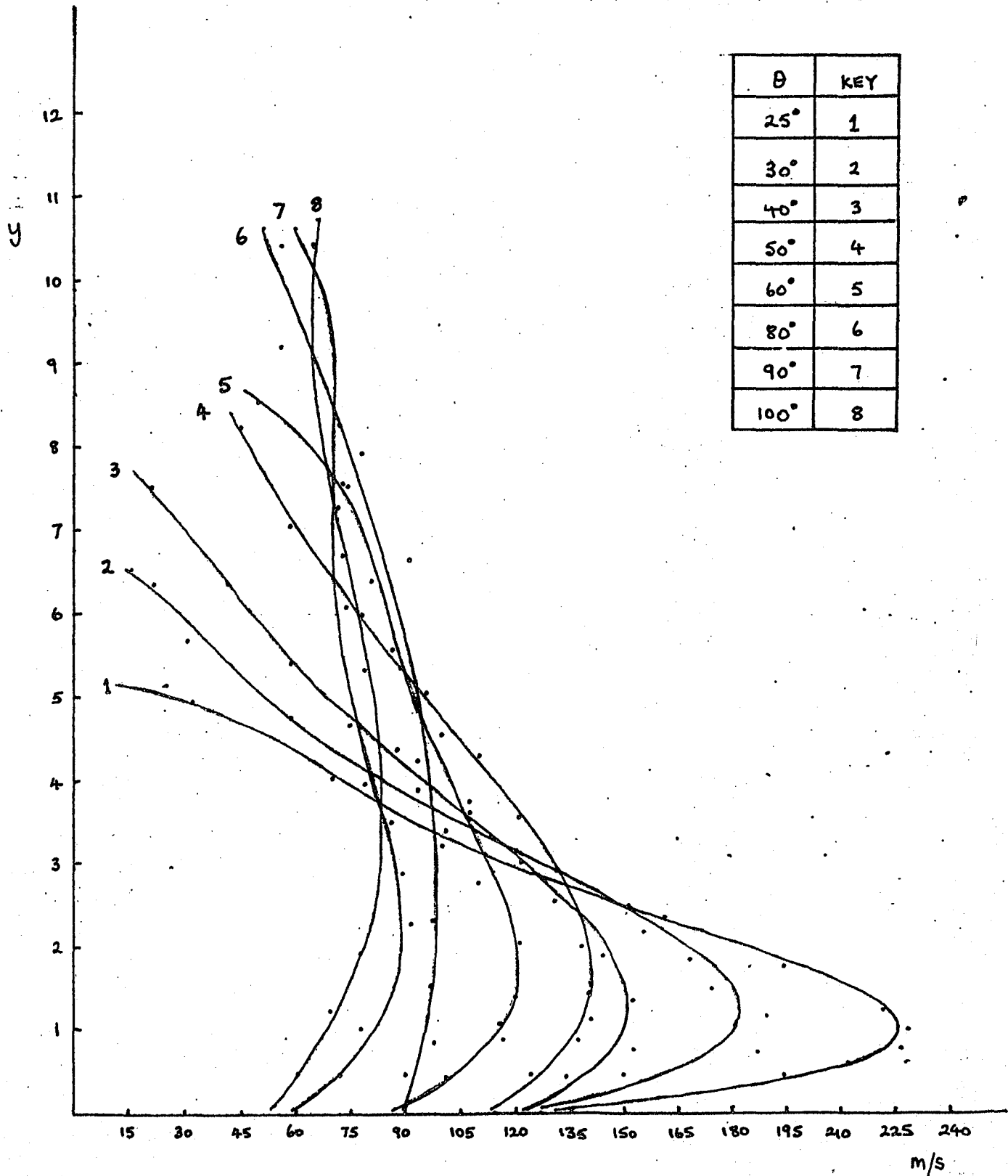


FIG. 5.22 Full Scale Tests: $\sqrt{U^2 + V^2}$ v. y

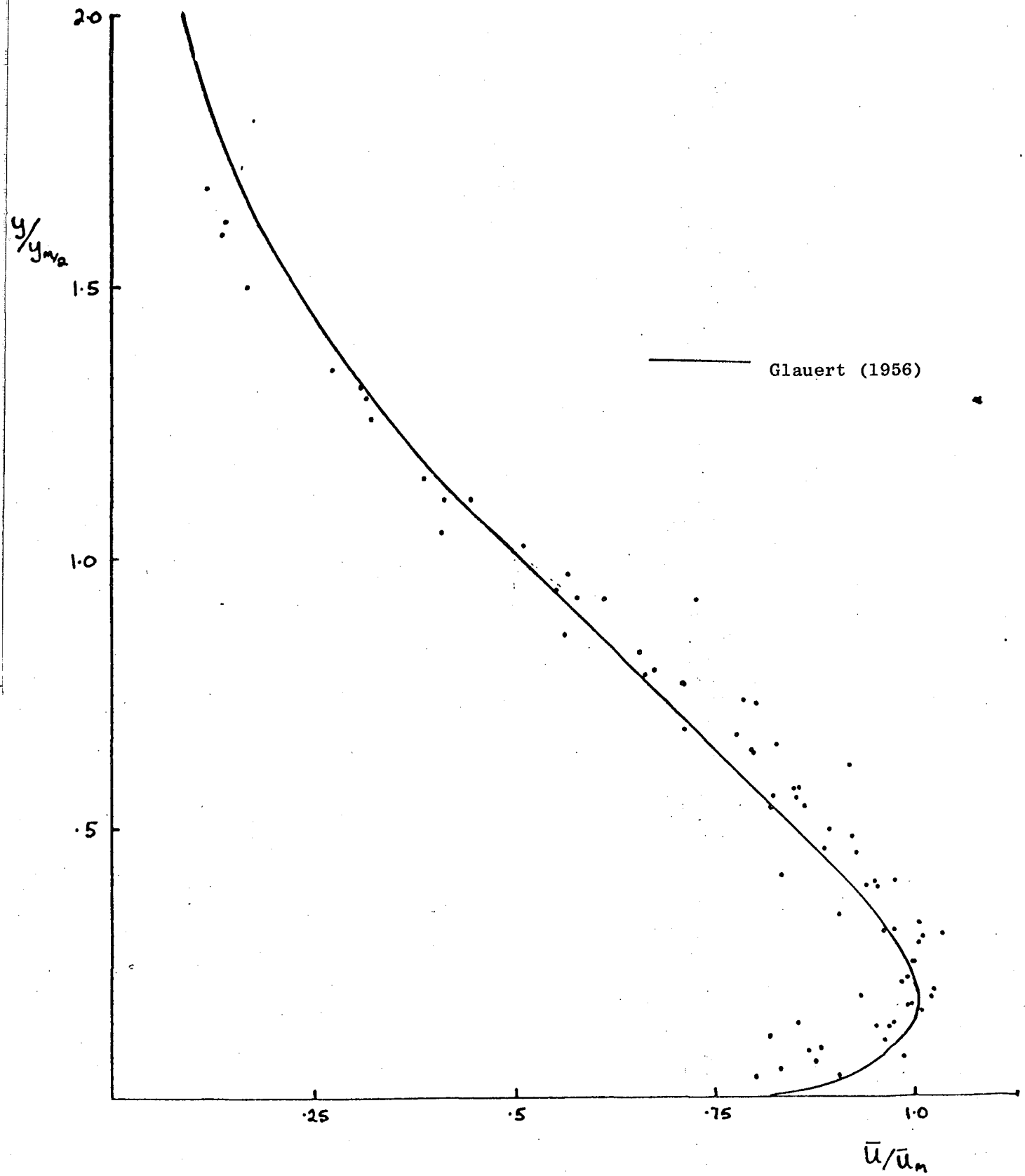


FIG. 5.23: Full Scale Tests: Non-dimensional $\sqrt{\bar{u}^2 + \bar{v}^2}$ v y

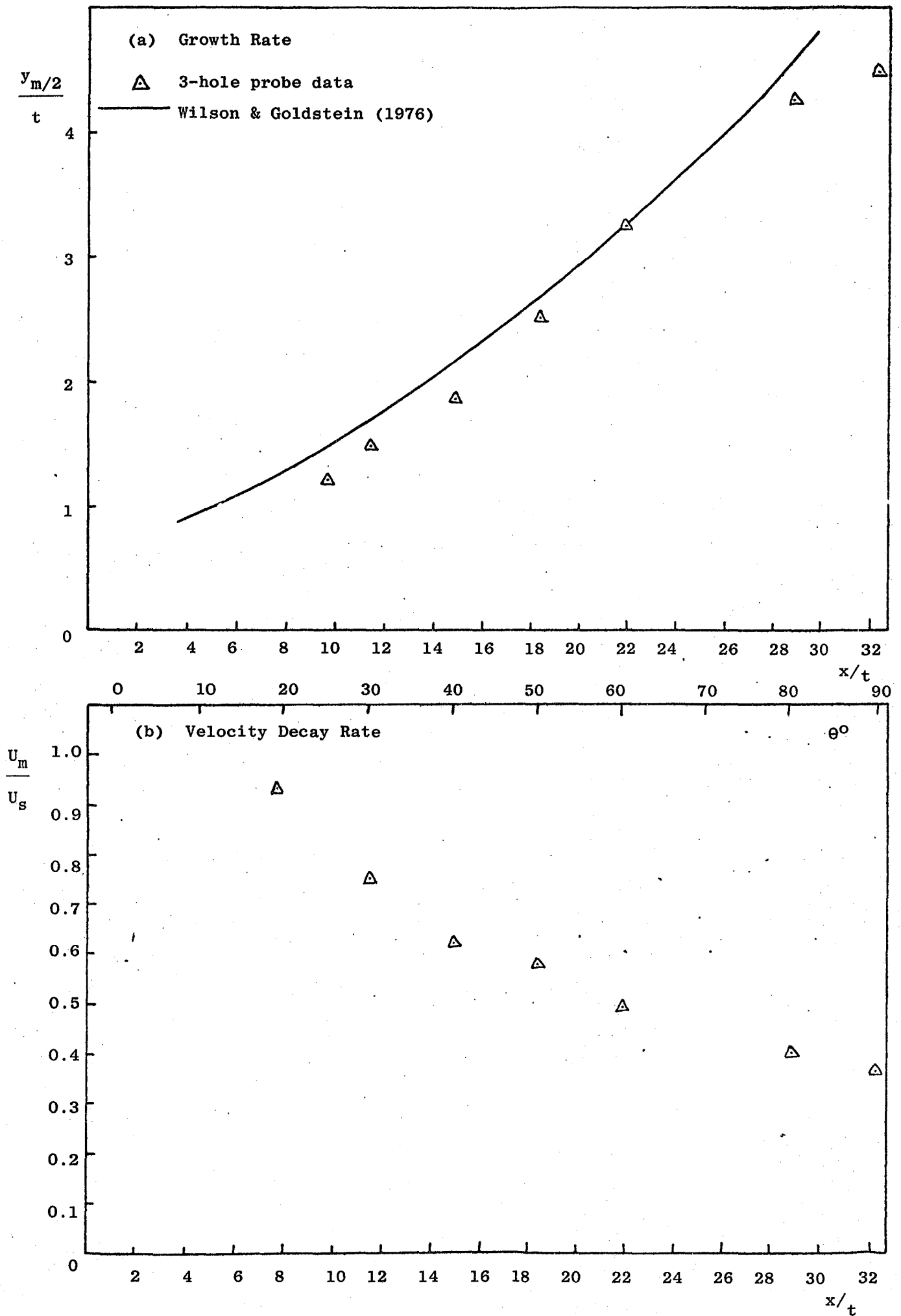


FIG 5.24 Full Scale Tests: Growth/Velocity Decay Rate

CHAPTER 6

CALCULATION METHOD

A qualitative outline of the structure of the flow around the Coanda flare was given in Chapter 1. Even though the mean flow is two dimensional (the turbulence is of course three dimensional) and simplified to exclude the effects of combustion, heat transfer, compressibility and a porous wall, the choice of calculation method for a complex flow of this type is an important decision. This chapter is concerned with the numerical procedure used to solve the equations of motion as distinct from the turbulence model used to effect closure.

6.1 REVIEW OF AVAILABLE METHODS

Nearly all calculation methods for turbulent boundary layers can be divided into two groups. The first are so called integral methods where ordinary differential equations are obtained as weighted integrals of the Navier-Stokes x-component equation. Alternatively the Navier-Stokes equations can be solved directly using a suitable numerical technique. These are differential methods. Kline et al (1969) provided a comprehensive comparison of calculation methods of both types up to 1968. Later methods have concentrated on the solution of the approximated Navier-Stokes equations because of the advent of fast computers which have made differential methods practicable. Bradshaw (1972) reviews methods of both types also.

6.1.1 Integral Methods

Integration of equation (2.30) for $0 < y < \delta$ when multiplied by 1, \bar{U} and y yields the momentum, energy and moment of momentum integral equations respectively. (Rotta (1962)). These equations are exact but require empirical input. The momentum integral

equation can be written as follows:

$$\frac{d\theta}{dx} + \frac{\theta}{U_{\infty}} (2 + H) \frac{dU_{\infty}}{dx} = \frac{C_f}{2} \quad \dots (6.1)$$

The shape factor H , which contains information about the mean velocity profile, and the skin-friction coefficient C_f , which contains information about the Reynolds shear stress, both have to be defined empirically, to a greater or lesser extent. One of the more successful integral methods by Head (1960) assumes that H is a function of a dimensionless entrainment velocity and uses the Ludwig and Tillman skin-friction formula. For a review of integral methods, the reader is referred to Cebeci and Smith (1974) and Bradshaw (1976a).

For simple flow cases such as a turbulent boundary layer on a smooth flat plate, integral methods can give accurate solutions even when calculated by hand. However, they cannot give solutions for each point in the flow field because an ordinary differential equation for integral quantities is solved. Different ways of describing the mean velocity profiles, skin-friction and shear stress profiles are required if extra effects such as surface roughness are to be included. Apart from the difficulties involved with the retention of the significant higher order terms in themselves, large curvature effects would cause even greater difficulties because of variation in these turbulence terms across the shear layer width. It is also important to note that Patel (1969a) found it necessary to redefine the usual integral parameters δ^* and θ , and that the flat-surface momentum integral equation broke down when used in calculations for flows with large cross-stream static pressure variations, i.e. with significant streamline curvature. Therefore, Patel incorporated extra terms in the momentum integral equation to account for the effects of cross-stream pressure gradient.

So (1975a) however, pointed out that both H and C_f have also to be modified in order to fully account for the effects of curvature.

An integral calculation method specifically developed for the Coanda flare (Titcombe (1980)) was tested with experimental data from the model flare tests. The momentum integral equation (6.1) is solved and a Coles-type velocity profile is assumed. The exact form of the velocity profile used is given in Spalding (1965). The skin friction formula used is consistent with the law of the wall and the entrainment rate is given by an empirical law derived by Escudier and Nicoll (1966) using data for a wall jet on a flat plate. The cross-stream static pressure gradient is assumed to be linear and the only other adjustment to the empirical input in order to account for the effects of stream-line curvature and divergence was that to the entrainment rate. The empirical expression developed by Kind (1967) is used to provide a correction to the entrainment rate. Some time was spent investigating this calculation procedure, but it failed to give good agreement for jet growth rate data. Integral methods were not considered further.

6.1.2 Differential Methods

The Navier-Stokes equations are in general second-order non-linear partial differential equations of the form:

$$a \frac{\partial^2 U}{\partial x^2} + b \frac{\partial^2 U}{\partial x \partial y} + c \frac{\partial^2 U}{\partial y^2} = e \quad \dots (6.2)$$

A characteristic is a line in the flow field along which the second order derivatives of U are indeterminate. Equation (6.2) therefore reduces to an ordinary differential equation and the gradients of the characteristic are given by a solution of (Chow (1979)):-

$$a \left(\frac{dy}{dx} \right)^2 - b \frac{dy}{dx} + c = 0 \quad \dots (6.3)$$

There are three possible results:

$b^2 - 4ac > 0$ there exist two real values for $\frac{dy}{dx}$ - hyperbolic type;

$b^2 - 4ac < 0$ solutions for $\frac{dy}{dx}$ are imaginary and characteristic lines do not exist - elliptic type;

$b^2 - 4ac = 0$ there is only one value of $\frac{dy}{dx}$ - parabolic type.

The above solutions are used to classify partial differential equations of the form of equation (6.2) and each type places certain restrictions on the type of flow to which they are applicable.

Disturbances in a compressible fluid are propagated at the speed of sound. If the flow is supersonic the disturbances cannot be passed upstream. Thus the region of influence in a supersonic flow is only downstream of the two characteristic lines (the Mach lines), and the corresponding equations of motion are hyperbolic. However, for subsonic compressible flow or for steady inviscid incompressible flow (in which the speed of sound is effectively infinite), the region of influence of the flow is unbounded, i.e. there are no characteristic lines and the Navier-Stokes equations are elliptic. However, for steady viscous incompressible flow, the equations of motion are (Potter (1977)):

$$U \frac{\partial U}{\partial x} + V \frac{\partial U}{\partial y} = - \frac{1}{\rho} \frac{\partial p}{\partial x} + \nu \left(\frac{\partial^2 U}{\partial x^2} + \frac{\partial^2 U}{\partial y^2} \right) \quad \dots (6.4)$$

$$U \frac{\partial V}{\partial x} + V \frac{\partial V}{\partial y} = - \frac{1}{\rho} \frac{\partial p}{\partial y} + \nu \left(\frac{\partial^2 V}{\partial x^2} + \frac{\partial^2 V}{\partial y^2} \right) \quad \dots (6.5)$$

neglecting body forces and together with the equation of continuity the flow is fully described.

$$\frac{\partial U}{\partial x} + \frac{\partial V}{\partial y} = 0 \quad \dots (6.6)$$

The Poisson equation for pressure can be obtained by differentiating equations (6.4) and (6.5) with respect to x and y and using continuity to rearrange:

$$\frac{1}{\rho} \left(\frac{\partial^2 p}{\partial x^2} + \frac{\partial^2 p}{\partial y^2} \right) = - \left(\left(\frac{\partial U}{\partial x} \right)^2 + 2 \frac{\partial U}{\partial y} \frac{\partial V}{\partial x} + \left(\frac{\partial V}{\partial y} \right)^2 \right) \quad \dots (6.7)$$

The terms of equations (6.4) and (6.5) can be grouped thus:

- (a) convection terms (e.g. $U \frac{\partial U}{\partial x}$) where fluid is transported downstream along streamlines
- (b) diffusion terms (e.g. $\nu \frac{\partial^2 U}{\partial x^2}$) where fluid is diffused by molecular viscosity in all directions
- (c) generation terms (e.g. $\frac{\partial p}{\partial x}$) where a change in static pressure in the fluid exerts influences in all directions.

The system of equations (6.4) to (6.7) is doubly elliptic in the sense that both the pressure field and viscous diffusion transmit disturbances in all directions. With the conditions that there is no recirculation and that the longitudinal diffusion of momentum

$$\left(\nu \frac{\partial^2 U}{\partial x^2} \right)$$

is negligible, the system is still elliptic because the Poisson equation is elliptic. Only when $\frac{\partial p}{\partial y} = 0$ with the pressure as a known function of x does the system become parabolic. The region of influence is then downstream of the characteristic line through the point of solution and the equations of motion can be solved directly by a marching procedure downstream through the flowfield.

The simplifications that there be no region of recirculating flow and that

$$\frac{\partial^2 u}{\partial x^2} = 0$$

$$\frac{\partial p}{\partial y} = 0, \quad \frac{dp}{dx} = f(x) \quad \dots (6.8)$$

are sufficient conditions for the Navier-Stokes equations to be parabolic, and they are the usual boundary layer assumptions. The incorporation of $\frac{\partial p}{\partial y} \neq 0$ in the calculation procedure is described in § 6.4.

Three calculation methods of finite difference form were studied for possible use. Bradshaw et al (1967) solved the differential equation for the shear stress simultaneously with the equations of mean motion. The form of the turbulence model makes the equations hyperbolic with the cross-stream pressure variation assumed negligible. The method relies on the definition of three non-dimensional empirical relations which would not in general be valid for wall jets. But the method has been extended to include the calculation of a cross-stream pressure gradient by Mahgoub and Bradshaw (1979), and even in its extended form the hyperbolic set of equations are solved by the method of characteristics. The Cebeci and Smith (1974) method was developed with particular reference to boundary layer flows. The equations of motion for plane or axisymmetric flow are transformed and a rectangular grid is used to obtain the finite difference equations. These are solved by Keller's box method. The scheme is unconditionally stable as the equations are highly implicit.

A popular and available calculation procedure is that of Patankar and Spalding (1970) (PS method). See also Spalding (1977) and Patankar and Spalding (1967). This method was selected as the basis of the present calculation procedure as it has been the subject of many years development and has been used successfully in widely differing flows by many workers

other than its authors, viz: Irwin and Smith (1975), Launder et al (1975), Rastogi and Whitelaw (1971), Ljuboja and Rodi (1980), Launder and Morse (1977) amongst others.

6.1.3 Outline of PS Method

This procedure possesses several numerical features which make it superior to the other two briefly described above. In its two-dimensional parabolic form the equation of motion is expressed in finite difference form by use of four nodes where the resulting equations are implicit. Therefore a method of solution such as Gauss elimination is required. Central differences are used in the cross-stream direction, whilst upwind differences are used in the streamwise direction. The important features of the method are listed below.

(a) The Transformation to $x \sim \omega$ co-ordinate system; for computational efficiency, the non-dimensional stream function ω , is used as the cross-stream independent variable. There is another important advantage. For an upwind difference scheme, (the most stable scheme at high Reynolds numbers) the use of a non-dimensional streamline co-ordinate axis reduces the truncation errors associated with the difference approximations used for the terms $\bar{U} \frac{\partial \bar{U}}{\partial x}$ and $\bar{V} \frac{\partial \bar{U}}{\partial y}$ in the x-component mean momentum equation (E.7).

This is even more important for highly curved shear layers where the truncation errors may be of the same order as the dominant Reynolds stress gradients when referred to shear layer axes. With the use of $x \sim \omega$ co-ordinates however, the $\bar{V} \frac{\partial \bar{U}}{\partial y}$ term disappears. For a fuller discussion see Bradshaw (1975, 1973) and Roache (1972).

(b) The process of marching integration; the flow field is divided into control volumes bounded by the upstream and downstream stations and the

half-way positions between nodes in the streamline co-ordinate system. See figure 6.2a. A solution is accomplished by a single sweep through the flow field where the finite difference equations are produced by integration of the x-component equation of motion in the cross-stream direction. This process ensures that continuity is satisfied in the finite difference equations. Also the non-linear terms in the equation of motion are linearised by using values of \bar{U} and \bar{V} prevailing at the upstream station. This allows the use of an efficient recurrence relation for solving the finite difference equations - the tri-diagonal matrix algorithm. See Spalding (1977) for further details.

(c) The allowance for high lateral convection; in some regions of flow, the lateral convection term can be larger than the lateral diffusion term e.g. in regions of high entrainment. Under these circumstances, mean cross-stream gradients are reduced and profiles tend to flatten out. The values of a general dependent variable ϕ at the cell boundaries tend to their 'upwind' value, e.g. for high entrainment there is high negative lateral convection and $\phi_{i+\frac{1}{2}} \rightarrow \phi_{i+1}$. This could lead to non-convergence or numerical instability if this phenomenon is not allowed for in the numerical procedure. Therefore if, in the cross-stream direction, the convective terms are less than the diffusive terms, central differences are used; but if the convective terms are larger than the diffusive terms, then the diffusive terms are neglected and the convective terms are expressed in upwind difference form. This combined scheme for simultaneous convective and diffusive processes was proposed by Spalding (1972) and examined by Runchal (1972).

The PS method was preferred for the reasons expressed above. For its use in the present calculation method, it was made more particular to

the case of a jet emerging from a plane or annular slot. Thus effects such as heat transfer, chemical reaction and surface porosity could be omitted. Also the geometry was made more specific. This considerably reduced the programming involved.

6.2 EQUATIONS OF MOTION

Some definition of terms is helpful. The flow is referred to as 'plane' where the axisymmetric radius of curvature R , tends to infinity; no statement concerning the streamline radius of curvature is intended. For a finite value of R , the flow is described as 'axisymmetric'.

6.2.1 Grid and Control Volume

The equations of motion are expressed using shear layer axes; the x-direction follows the I boundary (see figure 1.2) and therefore coincides approximately with the direction of flow. The y-direction is always orthogonal to the x-direction. For plane flow, the grid is obviously curved and rectangular and the control volume for flow/unit width is simply defined (Figure 6.1a). For the axisymmetric case, the control volume possesses both streamline and axisymmetric curvature. Therefore the control volume is as drawn in Figure 6.1b, from which the continuity equation (E.6) can be derived.

6.2.2 Momentum Equations

These are derived in appendix E. Equations (E.7) and (E.9) represent the rate of change of mean momentum through, and the force applied in, the control volume of figure 6.1b in the x- and y-directions respectively. They contain the same type of terms as the more general equations (6.2) and (6.3) as well as the streamline curvature terms denoted by r . The additional axisymmetric terms are produced if products of velocity and R are fully differentiated using the expressions for the rate of change of R shown in Figure 6.1a.

6.2.3 Order of Magnitude Analysis of Terms

This is necessary because for the parabolic procedure outlined above, not all the terms of equations (E.7) and (E.9) need be used. Also for the case of a highly curved shear layer where $x \simeq r$, the usual boundary layer approximations no longer apply. See § 2.3. Therefore, it is important to assess the relative sizes of terms in these equations so that consistent approximations can be made.

It is assumed that $r/x \ll 1$, $\bar{V} \ll \bar{U} \times \delta/x$ and that all the Reynolds stresses are of the same order. In general it may be supposed that gradients in the x - and y -directions will be of the same order of magnitude as the dependent variable divided by x and δ respectively. Also $h = 1 + y/r$ can be approximated to unity. Thus the individual terms of equation (E.7) are of the following order of magnitude:

$$\frac{\bar{U}}{\partial x} \frac{\partial \bar{U}}{\partial x} = O\left(\frac{\bar{U}^2}{x}\right)$$

$$h \bar{V} \frac{\partial \bar{U}}{\partial y} = O\left(\bar{U} \frac{\delta}{x} \cdot \frac{\bar{U}}{\delta}\right) = O\left(\frac{\bar{U}^2}{x}\right)$$

$$\frac{\bar{U}\bar{V}}{r} = O\left(\frac{\bar{U}^2}{x} \cdot \frac{\delta}{x}\right)$$

$$\frac{1}{R} \frac{\partial}{\partial y} (h \bar{u}\bar{v} R) = O\left(\frac{\bar{u}\bar{v}}{\delta}\right)$$

$$\frac{\partial \bar{u}^2}{\partial x} = O\left(\frac{\bar{u}\bar{v}}{\delta} \cdot \frac{\delta}{x}\right)$$

$$\frac{\bar{u}\bar{v}}{r} = O\left(\frac{\bar{u}\bar{v}}{\delta} \cdot \frac{\delta}{x}\right)$$

The same procedure is adopted for the y-component equation (E.9). However, in order to obtain consistent approximations for both equations, it is necessary to multiply orders of magnitudes of terms in the y-component equation by δ/x . Then the pressure gradients in both equations are approximated by $\frac{1}{\rho} \frac{\delta p}{\delta x}$ where $\delta y/\delta x = \delta/x$ as above. The orders of magnitude for the y-component equation (E.9) terms are:

$$\frac{\bar{U}}{\partial x} \frac{\partial \bar{V}}{\partial x} = O \left(\frac{\bar{U}^2}{x} \cdot \left(\frac{\delta}{x} \right)^2 \right)$$

$$h \frac{\bar{V}}{\partial y} \frac{\partial \bar{V}}{\partial y} = O \left(\frac{\bar{U}^2}{x} \cdot \left(\frac{\delta}{x} \right)^2 \right)$$

$$\frac{\bar{U}^2}{r} = O \left(\frac{\bar{U}^2}{x} \cdot \frac{\delta}{x} \right)$$

$$\frac{\partial(h\bar{v}^2)}{\partial y} = O \left(\frac{\bar{u}\bar{v}}{\delta} \cdot \frac{\delta}{x} \right)$$

$$\frac{\partial(\bar{u}\bar{v})}{\partial x} = O \left(\frac{\bar{u}\bar{v}}{\delta} \cdot \left(\frac{\delta}{x} \right)^2 \right)$$

$$\frac{\bar{u}^2}{r} = O \left(\frac{\bar{u}\bar{v}}{\delta} \cdot \left(\frac{\delta}{x} \right)^2 \right)$$

A typical ratio of Reynolds stress to mean maximum velocity in the jet flow is given by $\bar{u}\bar{v}/\bar{U}_m^2 = 0.05 - 0.15$. Therefore $\bar{u}\bar{v}$ can be considered to be of the same order as \bar{U} . Assuming that δ is one order of magnitude less than x and retaining terms up to order δ/x only, a consistent set of equations is:-

x-component equation

$$\frac{\bar{U}}{\partial x} \frac{\partial \bar{U}}{\partial x} + h \frac{\bar{V}}{\partial y} \frac{\partial \bar{U}}{\partial y} + \frac{\bar{U}\bar{V}}{r} = \frac{1}{\rho} \frac{\partial \bar{p}}{\partial x} - \frac{1}{R} \left(\right)$$

$$\frac{\partial(\bar{u}^2 R)}{\partial x} + \frac{\partial(h \bar{u} \bar{v} R)}{\partial y} + \frac{\bar{u} \bar{v} R}{r} + \frac{\nu}{R} \frac{\partial}{\partial y} \left(R h \frac{\partial \bar{U}}{\partial y} \right) \quad \dots (6.9)$$

y-component equation

$$-\frac{\bar{U}^2}{r} = -\frac{h}{\rho} \frac{\partial \bar{p}}{\partial y} - \frac{1}{R} \frac{\partial}{\partial y} (h \bar{v}^2 R) \quad \dots (6.10)$$

continuity

$$\frac{\partial(\bar{U} R)}{\partial x} + \frac{\partial(\bar{V} R h)}{\partial y} = 0 \quad \dots (6.11)$$

The plane flow form of these equations is recommended by Bradshaw (1973) in calculations of shear layers with significant streamline curvature. However, they can be further simplified in the case where $\frac{\partial \bar{p}}{\partial y}$ is assumed negligible in order to render the system of equations parabolic, allowing use of the PS marching integration procedure for a parabolic flow. Consistent with $\frac{\partial \bar{p}}{\partial y} = 0$ is the approximation $r \rightarrow \infty$. Under these conditions, equation (6.10) is unnecessary and terms of order δ/x can also be neglected in equation (6.9). This then reduces to:

$$\begin{aligned} \bar{U} \frac{\partial \bar{U}}{\partial x} + h \bar{V} \frac{\partial \bar{U}}{\partial y} &= -\frac{1}{\rho} \frac{d\bar{p}}{dx} - \frac{1}{R} \left(\frac{\partial}{\partial y} (h \bar{u} \bar{v} R) \right) \\ &+ \frac{\nu}{R} \frac{\partial}{\partial y} \left(R h \frac{\partial \bar{U}}{\partial y} \right) \quad \dots (6.12) \end{aligned}$$

where $\frac{d\bar{p}}{dx}$ is defined in an unconfined flow by the free stream pressure gradient and \bar{V} is available from the continuity equation (6.11). A convenient manipulative form of equation (6.12) is obtained by use of an effective viscosity, ν_{eff} , to represent the shear stress - $\bar{u} \bar{v}$.

(See § 7.1). Then the x-component equation becomes:

$$\bar{U} \frac{\partial \bar{U}}{\partial x} + h \bar{V} \frac{\partial \bar{U}}{\partial y} = - \frac{1}{\rho} \frac{d\bar{p}}{dx} + \frac{1}{R} \frac{\partial}{\partial y} \left(R h v_{\text{eff}} \frac{\partial \bar{U}}{\partial y} \right) \quad \dots (6.13)$$

This equation is used as the equation of motion in the PS method.

6.3 SOLUTION OF THE PARABOLIC EQUATIONS

The procedures described in § 6.1.3 are now stated mathematically. For a fuller treatment see Spalding (1977) and Patankar and Spalding (1970).

6.3.1 Definition of Stream Function and Mass Flow Rates

From figure 6.1a it can be seen that the mass flow rate across a line of constant x is:

$$\dot{m}_x = 2 \pi \rho \bar{U} R \delta y \quad \dots (6.14)$$

and that the mass flow rate across a line of constant y is:

$$\dot{m}_y = - 2 \pi \rho \bar{V} R h \delta x \quad \dots (6.15)$$

Therefore a suitable definition of stream function is given by:

$$\frac{\partial \psi}{\partial y} = \rho \bar{U} R^k \quad \frac{\partial \psi}{\partial x} = - \rho \bar{V} R^k h \quad \dots (6.16)$$

where k is a convenient index to distinguish plane and axisymmetric flow when k = 0 and 1 respectively. In addition, a non-dimensional stream function can be defined by:

$$\omega = \frac{\psi - \psi_I}{\psi_E - \psi_I} \quad \dots (6.17)$$

where subscripts denote values of stream function at the I and E boundaries. These are naturally functions of x only. From the

definition of stream function and ω , the mass flow rate across a line of constant x for axisymmetric flow may be rewritten:

$$\dot{m}_x = 2 \pi \delta \psi = 2 \pi (\psi_E - \psi_I) \delta \omega \quad \dots (6.18)$$

The mass flow rate across a line of constant ω may also be written:

$$\begin{aligned} \dot{m}_\omega &= \dot{m}_\omega' h \delta x \\ \dot{m}_\omega' &= \dot{m}_\omega'' 2 \pi R \\ &= 2 \pi \left((R\dot{m}'')_I + \omega \left((R\dot{m}'')_E - (R\dot{m}'')_I \right) \right) \end{aligned} \quad \dots (6.19)$$

$$\text{where } (R\dot{m}'')_E = - \frac{d\psi_E}{dx} \text{ and } (R\dot{m}'')_I = - \frac{d\psi_I}{dx} \quad \dots (6.20)$$

$$\text{For } a = - \frac{d\psi_I}{dx} / (\psi_E - \psi_I) \text{ and } b = - \frac{d(\psi_E - \psi_I)}{dx} / (\psi_E - \psi_I) \quad \dots (6.21)$$

$$\dot{m}_\omega' = 2 \pi (\psi_E - \psi_I)(a + b\omega) \quad \dots (6.22)$$

For plane flow $2\pi(\psi_E - \psi_I)$ is replaced by $(\psi_E - \psi_I)$.

6.3.2 Transformation to (x, ω) Co-Ordinates

For a general variable ϕ , the transformation of $\phi(x, y)$ to $\phi(x, \omega)$ is achieved by these equations:

$$\begin{aligned} \left(\frac{\partial \phi}{\partial x} \right)_y &= \left(\frac{\partial \phi}{\partial x} \right)_\omega + \left(\frac{\partial \phi}{\partial \omega} \right)_x \left(\frac{\partial \omega}{\partial x} \right)_y \\ \left(\frac{\partial \phi}{\partial y} \right)_x &= \left(\frac{\partial \phi}{\partial \omega} \right)_x \left(\frac{\partial \omega}{\partial y} \right)_x \end{aligned} \quad \dots (6.23)$$

Therefore the stream function definitions yield:

$$\left(\frac{\partial \omega}{\partial x} \right)_y = - \frac{1}{(\psi_E - \psi_I)} \frac{d\psi_I}{dx} - (\psi_E - \psi_I) \left(\frac{d\psi_I}{dx} + \omega \frac{d(\psi_E - \psi_I)}{dx} \right)$$

$$\left(\frac{\partial \omega}{\partial y} \right)_x = \frac{\rho \bar{U} R}{\psi_E - \psi_I} \quad \dots (6.24)$$

Then equation (6.13) transforms to:

$$\frac{\partial \bar{U}}{\partial x} + (a + b\omega) \frac{\partial \bar{U}}{\partial \omega} = \frac{\partial}{\partial \omega} \left(c \frac{\partial \bar{U}}{\partial \omega} \right) + d \quad \dots (6.25)$$

where a and b are given by equation (6.21) and

$$c = \frac{\rho \bar{U} R^2 h}{(\psi_E - \psi_I)} \mu_{\text{eff}} \quad \dots (6.26)$$

$$d = - \frac{1}{\rho \bar{U}} \frac{d\bar{p}}{dx} \quad \dots (6.27)$$

The definition of d is non-linear but is approximated by using the corresponding known upstream value for \bar{U} .

6.3.3 The Finite Difference Grid and Equations

Figure 6.2a shows how the control volumes are defined for the region between the upstream and downstream steps. Therefore, four nodes are used in the finite difference approximation of equation (6.25):

$$D_i \phi_{i,xpl} = A_i \phi_{i+1,xpl} + B_i \phi_{i-1,xpl} + C_i \quad \dots (6.28)$$

where C_i represents the sum of constant terms and the known upstream term $\phi_{i,x}$. The coefficients are derived by integration of equation (6.25) for $\omega_{i-\frac{1}{2}} \rightarrow \omega_{i+\frac{1}{2}}$ for which interval ϕ_i is considered constant. The form of the coefficients is given by Spalding (1977). Values of ϕ_1 and ϕ_N are known and form the boundary conditions for the tri-diagonal matrix algorithm.

No mention has been made here of how the grid is calculated, how the entrainment is controlled, nor the procedure adopted in wall regions. These items have been treated as by Spalding (1977).

6.4 EXTENSION OF METHOD TO FLOWS WITH SIGNIFICANT CROSS-STREAM PRESSURE GRADIENT - 'PARTIAL-PARABOLIC' PROCEDURE

A class of flow exists for which a full elliptic iterative solution of the Navier-Stokes equations is unnecessary whilst the assumption of a negligible cross-stream pressure gradient is too restrictive. These are flows where the assumptions of no recirculation and negligible streamwise diffusion of momentum is acceptable but where a significant degree of streamline curvature introduces a pressure field which affects the upstream flow as well as the downstream. The system of equations is not then, strictly speaking, parabolic. This type of flow has been called 'partially-parabolic' by Spalding (1976) who gives a useful summary of the flow types.

The question now arises if the system of equations can be solved directly as in a parabolic solution or whether an iterative technique is required as in an elliptic solution. A possible procedure could be to approximate $\frac{\partial \bar{p}}{\partial x}$ in equation (6.9) by

$$\left(\frac{\partial \bar{p}}{\partial x} \right)_y = \left(\frac{\partial \bar{p}}{\partial x} \right)_E + \frac{1}{r} \frac{\partial}{\partial x} \int_E^y \frac{\rho \bar{U}^2}{h} dy \quad \dots (6.29)$$

where $\left(\frac{\partial \bar{p}}{\partial x} \right)_y \cdot \Delta x_{\text{last}}$ is taken as the local pressure difference between two successive calculation stations in order to calculate the velocity distribution for the one following. Provided small enough forward steps are taken, a fairly accurate solution can be obtained in one iteration. However, the step size has to be small in order to prevent instability caused by attempting to march a system of equations that are

elliptic. Also the approximation of equation (6.29) is inconsistent with the order of magnitude analysis of § 6.2.3 although this would not be too important where the pressure gradient $\frac{\partial \bar{p}}{\partial y}$ dominates the stress gradient in equation (6.10). This type of procedure was adopted by Rastogi and Whitelaw (1971) and Gibson and Rodi (1981). The former used step sizes of 0.1% δ for the first fifty steps and thereafter gradually increased them to a maximum of 1% δ . The latter required 700 forward steps for grid independent solutions to a flow length of approximately 1300 mm.

Alternatively, an iterative procedure allows a much larger step length and can give more accurate results when a converged solution is obtained. The number of calculation stations actually calculated is also likely to be less and computing time therefore reduced. However, an initial guess to the pressure field $\bar{p}(x,y)$ has first to be made and the calculation is repeated until, say, the wall pressures are found to be within the required accuracy for convergence. In the method of Mahgoub and Bradshaw (1979), the pressure is calculated by integration of the y-component mean momentum equation across the shear layer width. $\frac{\partial \bar{p}}{\partial x}$ is evaluated using central differences in x of the pressure field that was calculated during the previous iteration. The method of calculating all the pressures of one sweep before using them in the next corresponds to a Gauss-Jacobi iteration which is stable. Use of the newly calculated pressures however, corresponds to a Gauss-Seidel iteration where the method would then suffer from the same problems of instability as the single-sweep methods outlined above and for the same reason.

The algorithm used by Patankar and Spalding (1972) is completely different in detail and relies on the uncoupling of the x- and y-momentum

equations so that an elliptic system of equations can still be solved by an essentially parabolic method. The uncoupling of equations (6.4) and (6.5) is achieved by specifying $\frac{\partial p}{\partial x}$ as the gradient of a bulk pressure which, for an unconfined shear layer, is defined by the free stream pressure. In effect then, the x-component momentum equation is solved by assuming $\frac{\partial p}{\partial y} = 0$, whilst the y-component equation is solved using the local values of pressure. At the end of the algorithm, when \bar{U} , \bar{V} and the Reynolds stresses are known, the pressure $p(x,y)$ is adjusted by corrections obtained from the solution of the Poisson equation (6.7). The equation is rendered parabolic by treating $\partial^2 p / \partial x^2$ as known. In any elliptic procedure which uses upwind differences, mean flow transport and pressure field effects are transmitted upstream at the rate of one step per sweep. Consistent with this procedure, the pressure corrections are applied at one grid location upstream from that from which they were obtained and so only the pressure influences upstream flow. This method has been successfully used for both two-dimensional (Singhal and Spalding (1976)) and three-dimensional flows. (Pratap and Spalding (1976), Patankar et al (1975)).

6.4.1 Equations to be Solved

Consistent equations for terms up to order δ/x are given by equations (6.9) (6.10) and (6.11). It should be noted that equation (6.10) does not actually contain \bar{V} (it is obtainable from the continuity equation) and therefore the full algorithm of Patankar and Spalding (1972) is not necessary. Also the equation (6.9) contains the additional terms of order δ/x which have yet to be put in finite difference form.

6.4.2 Algorithm Sequence

The sequence is:

- (a) The pressure field $p(x,y)$ is first guessed. This is done

assuming $\frac{\partial \bar{p}}{\partial y} = 0$, that ambient pressure is acting across the slot exit and that thereafter the pressure is determined by the free stream pressure gradient.

(b) The solution for \bar{U} and y is available from the previous step. For the first step, \bar{U} is calculated from inviscid nozzle theory.

(c) The Reynolds Shear stress is calculated via the turbulence model. See § 7.3. Normal stresses are represented by empirical relations with the shear stress.

(d) Equation (6.10) is integrated inwards from the free stream boundary to the I boundary to give the cross-stream pressure distribution. See figure 6.3.

(e) Substitution of the continuity equation in equation (6.9) via $\frac{\partial \bar{U}}{\partial x}$ yields an ordinary differential equation in \bar{V} . This can be solved by use of the tri-diagonal matrix algorithm.

(f) The pressures at one grid location upstream from the present are adjusted by the difference between the newly calculated pressures and those from the previous iteration.

(g) The x-component momentum equation (6.9) is solved as described in § 6.3 but incorporating the additional terms. The step to the next downstream station is therefore completed.

Steps (b) to (g) are repeated until the flow domain has been covered. A convergence criterion is then applied; if further iterations are necessary, the sweep is repeated. The additional parts of the algorithm

necessary for the partially-parabolic procedure can be incorporated in a single subroutine into the program. This makes it easy to use the program for both parabolic and partially-parabolic flows. It is important to note that the streamwise pressure gradient used in (g) is that defined by the free stream conditions, whereas the solution for \bar{V} in (e) uses the local pressure gradient. The equations (6.9) and (6.10) are therefore uncoupled.

6.4.3 Initial Conditions

Values for \bar{U} and ρ for the first step of the first iteration are available using inviscid nozzle theory for unchoked flow:

$$\frac{\bar{U}_1^2}{2} = \frac{\gamma R_a T_{\text{sup}}}{\gamma - 1} \left(1 - \left(\frac{P_{\text{atmos}}}{P_{\text{sup}}} \right)^{\frac{\gamma-1}{\gamma}} \right)$$

$$\rho_1 = \frac{P_{\text{sup}}}{R_a T_{\text{sup}}} \left(\frac{P_{\text{atmos}}}{P_{\text{sup}}} \right)^{1/\gamma} \quad \dots (6.30)$$

where the supply and ambient conditions are input data to the program. γ is an effective value of the ratio of specific heats for the fluid mixture. For subsequent iterations, the drop in pressure at the slot exit produces an increased velocity and mass flow defined by:

$$\frac{\bar{U}_i^2}{2} = \frac{\gamma R_a T_{\text{sup}}}{\gamma - 1} \left(1 - \left(\frac{P_i}{P_{\text{sup}}} \right)^{\frac{\gamma-1}{\gamma}} \right)$$

$$(\psi_E - \psi_I) = \sum_{i=2}^{i=N-1} \rho_i \bar{U}_i R_i \delta y_i \quad \dots (6.31)$$

If $\frac{P_{\text{atmos}}}{P_{\text{sup}}}$ is less than the critical pressure ratio, the procedure is stopped at the end of the first iteration as the velocity at the nozzle exit will be sonic. For choked flow conditions, the mass flowrate and

density are calculated accordingly. If $\frac{P_i}{P_{sup}}$ is less than the critical pressure ratio at any time, a warning is printed. The density of the jet at any point is calculated so that it is consistent with the pressure calculated, viz:

$$\rho_i = (F_i \rho_{jet} + (1 - F_i) \rho_{ambient}) \left(\frac{P_i}{P_{ambient}} \right)^{1/\gamma} \quad \dots (6.32)$$

where F_i is the proportion of original to total mass of fluid.

6.4.4 Pressure Calculation

Integration of equation (6.10) gives:

$$\begin{aligned} \int_i^{i+1} \delta \bar{p}_{i+1} &= \frac{\rho}{rh} (\bar{U}^2 - \bar{v}^2) \bigg|_{i+\frac{1}{2}}^{i+1} \left[\delta y \right]_i^{i+1} - \rho_{i+\frac{1}{2}} \left[\bar{v}^2 \right]_i^{i+1} \\ &- \rho \frac{\bar{v}^2}{R} \bigg|_{i+\frac{1}{2}}^{i+1} \left[\delta y \right]_i^{i+1} \quad \dots (6.33) \end{aligned}$$

The control volume for the integration is shown in Figure 6.3. The free stream static pressure defines \bar{p}_E , thus the complete cross-stream pressure distribution is obtained.

6.4.5 Solution for \bar{V}

Removing the $\frac{\partial \bar{U}}{\partial x}$ term in the equations (6.9) and (6.10) gives the ordinary differential equation for \bar{V} in which \bar{U} , $\frac{\partial \bar{p}}{\partial x}$ and the Reynolds stresses are all known:

$$\left(h \frac{\partial \bar{U}}{\partial y} - \frac{\bar{U} h \cos \alpha}{R} \right) \bar{V} - \bar{U} h \frac{\partial \bar{V}}{\partial y} = \frac{\bar{U}^2 h \sin \alpha}{R} - \frac{1}{\rho} \frac{\partial \bar{p}}{\partial x}$$

$$- \frac{1}{R} \left(\frac{\partial(\bar{u}_R^2)}{\partial x} + \bar{uv} \frac{R}{r} \right) + \frac{1}{R} \left(\frac{\partial}{\partial y} (Rh\nu_{\text{eff}} \frac{\partial \bar{U}}{\partial y}) \right) \quad \dots (6.34)$$

This is solved by a second-order Runge - Kutta approximation. Thus for solution by the tri-diagonal matrix algorithm, A_i in equation (6.28) is zero, and $\bar{V} = 0$ at the I boundary. The remaining 'constant' terms are all easily represented by their values at the i th node. x-direction gradients of ϕ are represented by

$$\frac{\phi_{i,x} - \phi_{i,xml}}{\Delta x_{\text{last}}}$$

6.4.6 Extra Terms in the x-Component Mean Momentum Equation

Transformation of the complete x-component mean momentum equation (6.9) to (x, ω) co-ordinates gives:

$$\begin{aligned} \frac{\partial \bar{U}}{\partial x} + (a + b\omega) \frac{\partial \bar{U}}{\partial \omega} &= d + \frac{\partial}{\partial \omega} (C \frac{\partial \bar{U}}{\partial \omega}) \\ - \frac{1}{\bar{U}} \left(\frac{\bar{uv}}{r} + \frac{\bar{UV}}{r} + \frac{\bar{u}^2 h \sin \alpha}{R} + \frac{\partial \bar{u}^2}{\partial x} + \frac{\partial \bar{u}^2}{\partial \omega} \left((a + b\omega) - \frac{\rho \bar{V} Rh}{\psi_E - \psi_I} \right) \right) \end{aligned} \quad \dots (6.35)$$

The last term of the right hand side represents those terms still to be put in finite difference form. With reference to figure 6.3, and following the procedure adopted for those terms already in finite difference form, integration across the x-component control volume gives:

$$- \frac{1}{\bar{U}_{i,x}} \left(\left. \frac{\bar{uv}}{r} \right|_{i,x} + \left. \frac{\bar{UV}}{r} \right|_{i,x} + \left. \frac{\bar{u}^2 h \sin \alpha}{R} \right|_{i,x} + \frac{\bar{u}^2|_{i,x} - \bar{u}^2|_{i,xml}}{\Delta x_{\text{last}}} \right)$$

$$\begin{aligned}
 & + \bar{u}^2 \Big|_{i,x} \left(\frac{(\psi_E - \psi_I)_{xpl} - (\psi_E - \psi_I)_x}{\Delta x (\psi_E - \psi_I)_x} \right) (\omega_{i+\frac{1}{2}} - \omega_{i-\frac{1}{2}}) \\
 & - \frac{1}{\bar{U}_{i,x}} \left(\frac{\dot{m} \bar{u}^2 \Big|_{i+\frac{1}{2},x} - \dot{m} \bar{u}^2 \Big|_{i-\frac{1}{2},x}}{2 \pi (\psi_E - \psi_I)_x} \right. \\
 & \left. - \frac{\rho V R h \Big|_{i,x}}{(\psi_E - \psi_I)_x} \left(\bar{u}^2 \Big|_{i+\frac{1}{2},x} - \bar{u}^2 \Big|_{i-\frac{1}{2},x} \right) \right) \dots (6.36)
 \end{aligned}$$

Linearization of the terms is achieved by using values at i, x for the control volume. Therefore the sum of these terms is added onto C_i in equation (6.28). Also terms such as $\frac{\partial \bar{u}^2}{\partial x}$ are treated as $\frac{\bar{u}^2 \Big|_{i,x} - \bar{u}^2 \Big|_{i,xml}}{\Delta x_{last}}$ so that they have known values.

6.4.7 Convergence Criterion and Stability

The solution is converged if, on successive iterations, all the corresponding wall pressures change by less than 0.2%. An alternative form of convergence criterion could be a negligible change in mass flow at the slot exit. An upper limit of ten iterations was set, above which the procedure is unlikely to converge if it has not already done so. Use of an implicit finite difference formulation for the solution of a forward step makes the procedure unconditionally stable. The uncoupling of streamwise and cross-stream pressure gradients in the two mean momentum equations ensures that an elliptic system of equations can be 'marched', provided that the condition $\partial^2 U / \partial x^2 = 0$ is satisfied. This is expected for nearly all shear layers.

6.5 ADDITIONAL FEATURES

6.5.1 Geometry and Boundary Conditions

The E boundary is always free whilst the I boundary can be specified either as a wall or an axis of symmetry but not both. This is true for both plane and axisymmetric flows. When the I boundary is an axis of symmetry no curvature can be induced without body forces which are not included in the momentum equations. For these cases then, $r \rightarrow \infty$. For the case of a wall at the I boundary and axisymmetric flow, two geometries are available; $\alpha = 90^\circ$ at $x = 0$ and r is finite, or α has a constant value and $r \rightarrow \infty$. These two geometries allow a complete description of the flare profile as the former is allowed to change to the latter at a pre-determined angle.

The boundary conditions used are:

- (a) wall at I boundary, $\bar{U}(1) = 0$, $\bar{V}(1) = 0$;
- (b) axis of symmetry at I boundary, $\bar{U}(1) = \bar{U}(2)$, $\bar{V}(1) = 0$;
- (c) at the E boundary (free), $\bar{U}(N) = 0$, $\bar{V}(N) = \dot{m}''_E / \rho$

For the solution to \bar{U} , two boundary conditions are required. For the \bar{V} solution only one is required, $V(1) = 0$.

6.5.2 Modified Law of the Wall

The near-wall grid and wall shear stress are calculated by use of the law of the wall in a modified form (Townsend (1961)) to include the effects of an adverse streamwise pressure gradient $\left(\frac{\partial \bar{p}}{\partial x} + \text{ve}\right)$. It is necessary in the present calculation method because of the large negative wall static pressure near the slot which increases to ambient further downstream.

For

$$\begin{aligned} U_+ &= U/(\tau_w \rho)^{\frac{1}{2}} \\ Y_+ &= Y(\tau_w \rho)^{\frac{1}{2}}/\mu \\ \text{and } p_+ &= \frac{\mu}{\rho} \frac{dp}{dx} / (\tau_w^3 \rho)^{\frac{1}{2}} \end{aligned} \quad \dots (6.37)$$

it can be stated as follows:

$$U_+ = \frac{1}{K} \left(2 \left((1 + p_+ Y_+)^{\frac{1}{2}} - 1 \right) + \ln \left(\frac{4 E Y_+}{2 + p_+ Y_+ + 2(1 + p_+ Y_+)^{\frac{1}{2}}} \right) \right) \quad \dots (6.38)$$

where E is the constant from the unmodified law of the wall. Integration of equation (6.38) between the wall and the adjacent node, which is positioned in the fully turbulent region of the flow, gives the value of a dimensionless stream function coefficient used for grid calculations. The log-law relation is therefore assumed to be valid for the whole of the inner layer. Bradshaw (1973) concludes that the use of the law of the wall in curved wall jets is satisfactory.

6.5.3 Determination of \bar{U}_m and $y_m/2$

An additional subroutine was used to interpolate values of \bar{U}_m and $y_m/2$. Newton's divided difference interpolating polynomial was used for the three nearest nodes to $y_m/2$ and \bar{U}_m .

6.6 SUMMARY

The calculation method described above is suitable for predictions of shear-layer flows with significant cross-stream pressure gradients where $r/x \approx 1$. All the significant Reynolds stress gradients are included in the mean momentum equations and the effects of variable pressure in the flow field are allowed for. The procedure can be extended to include the effects of combustion and scalar transport. It can also

be adapted for use with different types of turbulence model and is capable of use with a Reynolds stress closure in which transport equations for the Reynolds stresses are solved simultaneously with those for the mean flow.

$$C_i = D_i + E_i \theta_{i,x}$$

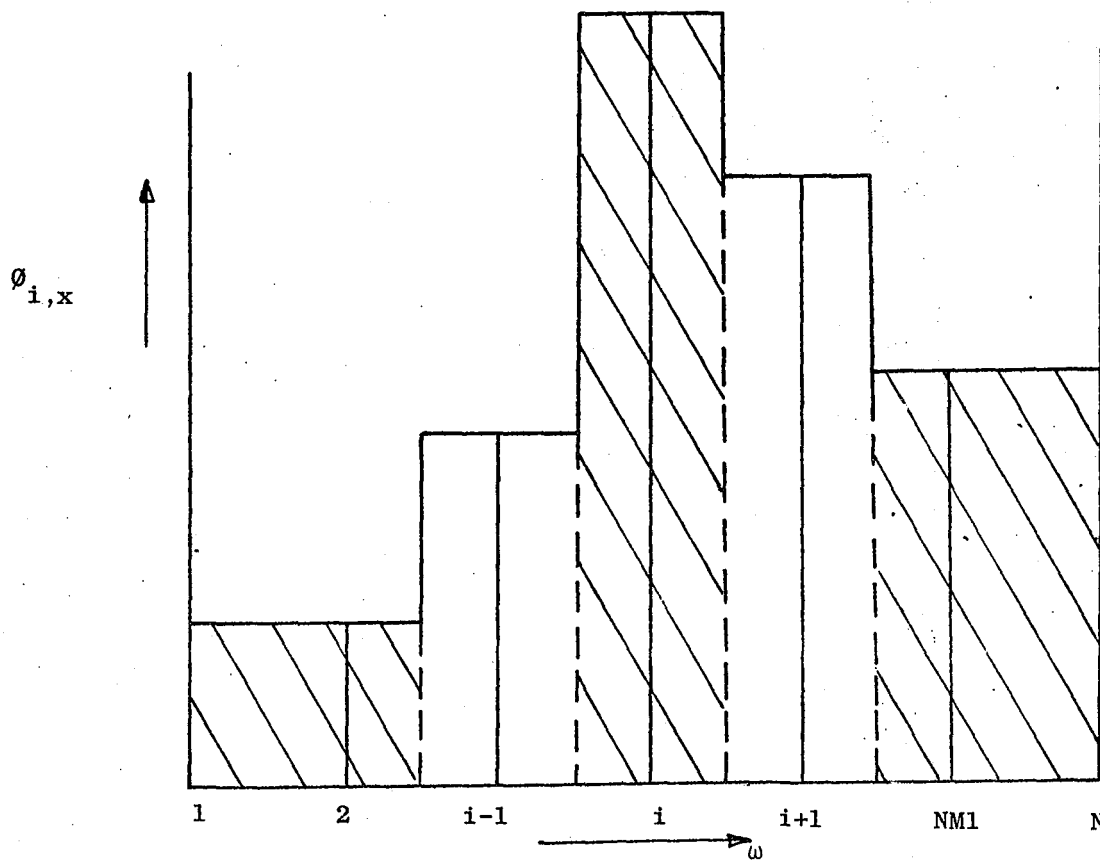


FIG. 6.2 Finite Difference Grid

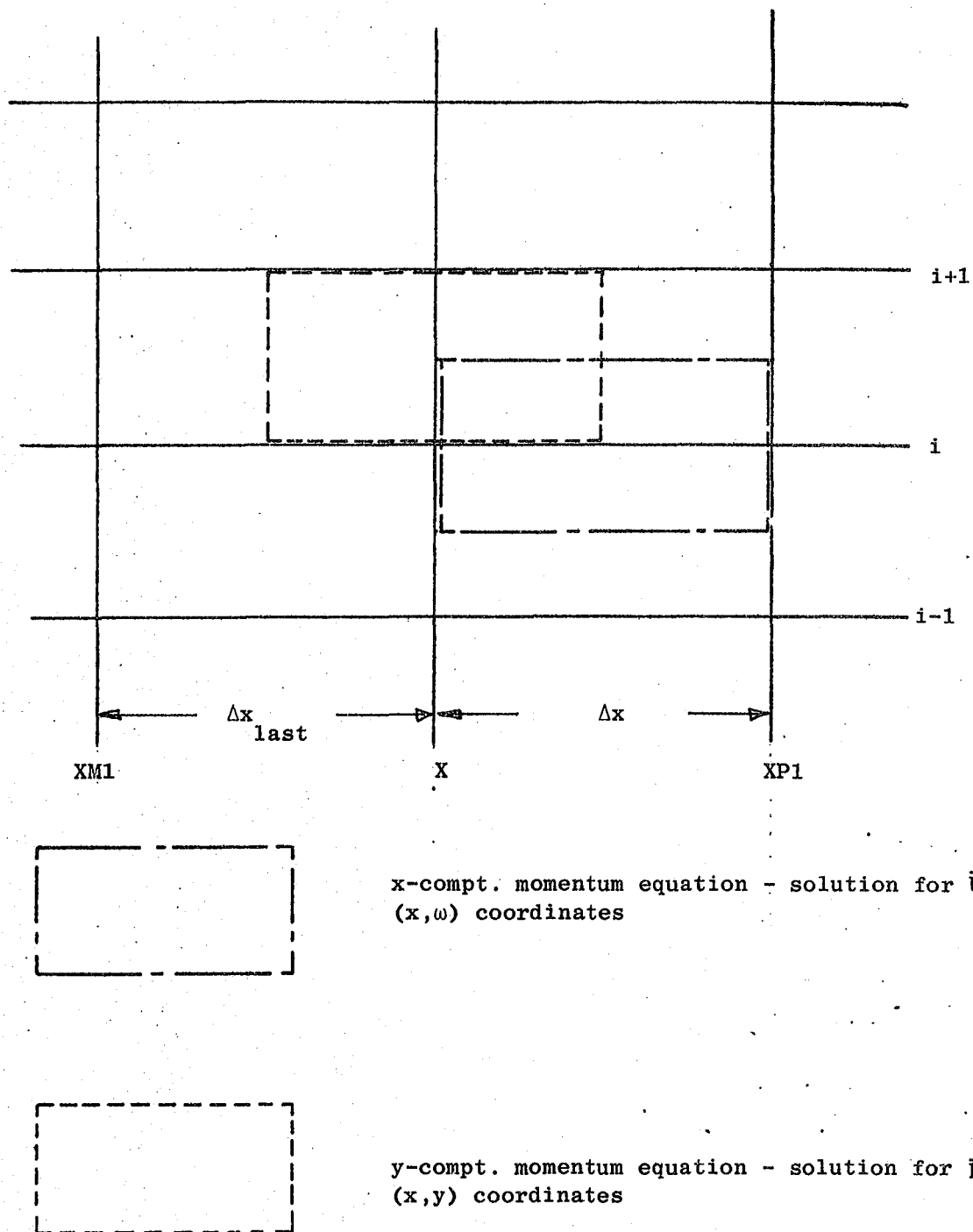


FIG. 6.3 Control Volumes for Partial-Parabolic Procedure

CHAPTER 7

TURBULENCE MODELLING

The problem of closure was introduced in Chapter 2. The subject of this chapter is the selection of an appropriate method of estimating the Reynolds stresses appearing in the equations of motion in such a way as to account for the effects of curvature and divergence. It is apparent from the order of magnitude analysis in § 6.2.3 that the pre-dominant stress gradient is $\frac{\partial(\overline{uv})}{\partial y}$. This is to be expected, for in order for a stress to affect the mean flow, it must change appreciably over a short distance. Examination of equation (F.7), the transport equation for \overline{uv} , shows that the shear stress is unlikely to change rapidly in the mean flow direction. Then the predominant stress gradient will be more or less perpendicular to the mean streamlines. The shear stress \overline{uv} therefore, is the most important stress in two-dimensional shear layers and is the major concern of turbulence modelling.

The order of closure reflects the degree of sophistication and complexity that is acceptable in the calculation procedure. Equation (6.13) assumed the use of Boussinesq's eddy viscosity defined by:-

$$\nu_T = - \frac{\overline{uv}}{\partial \bar{U} / \partial y} \quad \dots (7.1)$$

where $\nu_{eff} = \nu_T + \nu$ and in which it was tacitly assumed that the closure to be used is of first order. However, the calculation method could solve all or some of the Reynolds stress transport equations (Appendix F) and additional turbulence quantities simultaneously with the mean momentum equations. ν_{eff} would then not be required and closure would be of second order.

7.1 REVIEW OF AVAILABLE TURBULENCE MODELS

Table III summarizes models up to the second order that are currently available. Third order closures have not yet been developed, not only because of the complexity of using them in a calculation procedure, but also because of the difficulty of obtaining the required empirical information to a satisfactory accuracy. For a review of turbulence models see Launder and Spalding (1972), Mellor and Herring (1973) and Reynolds (1976).

The dimensions of ν_T are velocity x length. First order models can be sub-divided into groups where the velocity and length scale of ν_T are expressed either algebraically or by using a differential equation. In either case, the concept of an eddy viscosity is erroneous as it is based on physically unrealistic arguments. By analogy with molecular viscosity, it assumes that the mean free path between eddies is small compared with the flow dimensions and that eddies transfer momentum by a series of discrete collisions. This in no way represents the vortex interactions that occur nor the energy cascade which is completely described by the turbulent energy transport equation (2.25). Bradshaw (1972) discusses the validity of the use of eddy viscosity formulae in more detail.

7.1.1 Algebraic Specifications of Eddy Viscosity

The concept of mixing length is analogous to that of the eddy viscosity. The mixing length theorem was proposed by Prandtl and in it the mean free path between collisions is designated as the mixing length. Therefore the relation between eddy viscosity and mixing length can be written:

$$\nu_T = \ell_0^2 \left| \frac{\partial \bar{U}}{\partial y} \right| \quad \dots (7.2)$$

<p>Use of Eddy Viscosity</p> <p>$\tau = -\rho \overline{uv}$</p> <p>$= \mu_T \frac{\partial \overline{U}}{\partial y}$</p> <p>$v_T = \mu_T / \rho$</p> <p>= velocity scale</p> <p>x length scale</p>	<p><u>Algebraic Definition of μ_T</u></p> <p>$\mu_T = \rho \ell_0^2 \left \frac{\partial \overline{U}}{\partial y} \right$ Prandtl (1925); $\ell_0 \propto \left \frac{\frac{\partial \overline{U}}{\partial y}}{\frac{\partial^2 \overline{U}}{\partial y^2}} \right$; $v_T = \rho \overline{U}_o y_o f(y/\delta)$</p> <p>$\ell_0$ related to flow dimensions Von Karman (1930)</p>		<p>No. of p.d.e.'s</p> <p>0</p>
	<p>Prandtl/ Kolmogorov</p> <p>Eddy Viscosity Formula</p> <p>$\mu_T = C_\mu \rho k^{\frac{1}{2}} \ell$</p>	<p><u>One-Equation Models</u></p> <p>Differential equation for tubulent kinetic energy k. Length scale ℓ, prescribed algebraically.</p>	<p>1</p>
		<p><u>Two-Equation Models</u></p> <p>Differential equation for k and ℓ; ℓ prescribed by any turbulence quantity with a dimension of ℓ^n.</p> <p>e.g. Rodi & Spalding (1970): ℓ from $\frac{D(k\ell)}{Dt}$</p> <p>Harlow & Nakayama (1968): ℓ from $\frac{D\varepsilon}{Dt}$</p>	<p>2</p>
<p><u>Reynolds Stress Transport Equations</u></p> <p>Daly & Harlow (1970): $\frac{D(\overline{u_i u_j})}{Dt}, \frac{D\varepsilon}{Dt}$ Mean strain rate not in pressure-strain term Turbulent diffusion approximated by a gradient diffusion model.</p> <p>Launder et al (1975): $\frac{D(\overline{u_i u_j})}{Dt}, \frac{D\varepsilon}{Dt}$ Mean strain rate in pressure-strain term Turbulent diffusion approximated by a gradient diffusion model</p> <p>Lumley (1978): Rational closure scheme by method of invariant modelling</p>			<p>2+</p>

Table III : Classification of Turbulence Models

The mixing length is an easier concept to use and Prandtl related it to the dimensions of the flow considered. Von Karman attempted to generalize the formulation of the mixing length by use of the similarity hypothesis:

$$\ell_0 \propto \left| \frac{\partial \bar{U}}{\partial y} / \frac{\partial^2 \bar{U}}{\partial y^2} \right| \quad \dots (7.3)$$

Direct algebraic specifications of the eddy viscosity also exist where a typical velocity and length scale of the flow are treated as functions of y/δ .

7.1.2 Specification of Eddy Viscosity by Differential Equations

Later, Prandtl suggested that the velocity scale for v_T be replaced by the square root of the turbulent kinetic energy:

$$\mu_T = C_\mu \rho k^{1/2} \ell \quad \dots (7.4)$$

where k and/or ℓ could be specified by a transport equation. ℓ represents a length scale proportional to that of energy-containing eddies. Kolmogorov also used the turbulent kinetic energy for the velocity scale, but for the length scale used $\ell = k^{1/2}/f$ where f is the typical frequency of the energy containing motions. Nee and Kovaszny (1969) proposed a differential equation for $v_{eff} = v_T + v$ directly without use of equation (7.4). However most one and two-equation models use the Prandtl/Kolmogorov formula for μ_T above and these are now briefly described.

(a) One-Equation Models

The individual terms of the transport equation for kinetic energy, equation (2.25), have to be expressed in terms of known quantities, i.e. mean flow variables and constants, and the kinetic energy, before a

solution can be obtained. A possible model for a boundary layer is given by Launder and Spalding (1972) derived, for high Reynolds number flows, along the lines suggested by Prandtl and Kolmogorov. Two constants are required in the equation:

$$\bar{U} \frac{\partial k}{\partial x} + \bar{V} \frac{\partial k}{\partial y} = \frac{\partial}{\partial y} \left(\frac{\nu_t}{C_{k,1}} \frac{\partial k}{\partial y} \right) + \nu_t \left(\frac{\partial \bar{U}}{\partial y} \right)^2 - \epsilon$$

. . . (7.5)

where

$$\epsilon = C_{k,2} \frac{k^{3/2}}{\ell}$$

. . . (7.6)

A solution of this model equation together with a simple relation between ℓ and the flow dimensions gives a solution for μ_T . One equation models offer few advantages over the mixing length hypothesis because ℓ is still specified algebraically. Therefore more use has been made of two equation models.

(b) Two-Equation Models

The drawbacks of the one-equation models are overcome by the use of a transport equation to represent ℓ . This can be done in a number of ways leading to several different models of this type. The problem lies in the choice of length scale and it is likely that more than one would be required particularly for complex flows (Bradshaw (1972)). Another difficulty is that transport equations for length scales tend to be more complicated than that for the turbulent kinetic energy. Rotta (1951) suggested use of exact equations for turbulence length scales related to the integral scales whilst later workers (Daly and Harlow (1970), Hanjalic and Launder (1972)) implied a length scale by use of a transport equation for the dissipation rate ϵ , equation (2.26).

This is a popular definition of a length scale as ϵ appears explicitly in the k transport equation (2.25). At high Reynolds numbers, the modelled transport equation for ϵ can be written in boundary layer form as:

$$\bar{U} \frac{\partial \epsilon}{\partial x} + \bar{V} \frac{\partial \epsilon}{\partial y} = C_{\epsilon} \frac{\partial}{\partial y} \left(\nu_t \frac{\partial \epsilon}{\partial y} \right) + C_{\epsilon,1} \nu_T \frac{\epsilon}{k} \left(\frac{\partial \bar{U}}{\partial y} \right)^2 - C_{\epsilon,2} \frac{\epsilon^2}{k} \quad \dots (7.7)$$

where C_{ϵ} , $C_{\epsilon,1}$ and $C_{\epsilon,2}$ are empirical constants. Solution of this equation with equation (7.5) is known as the $k \sim \epsilon$ model. Other length scales that have been proposed are those associated with the product of k and ℓ (Rodi and Spalding (1970)) and the mean square of the frequency of the energy-containing eddies. Launder and Spalding (1974) review these last three models and prefer the use of the $k \sim \epsilon$ model which is tested with experimental data from several different types of flow, including those with recirculation. The use of a differential equation to specify the length scale in addition to the velocity scale in a turbulence model significantly improves the range of use and accuracy of a calculation procedure. However, the limitations imposed by the use of an eddy viscosity are only removed by direct modelling of the terms in transport equations for the Reynolds stresses.

7.1.3 Reynolds Stress Models

The term by term approximation of the Reynolds stress transport equations was first suggested by Chou (1945) and Rotta (1951). This brief review is intended only to highlight the major points of what is now an extensive subject. Two of the most important Reynolds stress closures are those of Launder et al (1975) (LRR) and Daly and Harlow (1970) (DH); both draw substantially on the work done previously by Chou and Rotta.

As in the two-equation models above, a length scale transport equation is also necessary. Both the DH and LRR models provide closure approximations for $\overline{u_i u_j}$ and use the ϵ transport equation (2.26) as the length scale equation. They are therefore suitable for comparison.

Equation (2.24) is the transport equation for the Reynolds stress $\overline{u_i u_j}$ in which only the convection term and the production term, P_{ij} are explicitly defined in terms of known quantities, i.e. second order correlations or mean velocities. The remaining terms are approximated. For high Reynolds number flows LRR uses the following approximations.

(a) Diffusion by Velocity Fluctuations

By simplification of the exact transport equation for third order correlations:

$$-\overline{u_i u_j u_k} = \beta \frac{k}{\epsilon} \left(\overline{u_i u_\ell} \frac{\partial \overline{u_j u_k}}{\partial x_\ell} + \overline{u_j u_\ell} \frac{\partial \overline{u_k u_i}}{\partial x_\ell} + \overline{u_k u_\ell} \frac{\partial \overline{u_i u_j}}{\partial x_\ell} \right) \dots (7.8)$$

DH, however uses:

$$-\overline{u_i u_j u_k} = \beta' \frac{k}{\epsilon} \left(\overline{u_k u_\ell} \frac{\partial \overline{u_i u_j}}{\partial x_\ell} \right) \dots (7.9)$$

where β and β' are constants.

(b) Diffusion by Pressure Fluctuations

LRR ignores these terms whilst DH uses a gradient diffusion model where $\overline{p' u_i}$ is proportional to $k \frac{\partial \overline{u_i u_\ell}}{\partial x_\ell}$

(c) Dissipation

For a high turbulent Reynolds number, the small scale motions may be considered isotropic. Then following Rotta (1951):

$$2 \nu \frac{\partial u_i}{\partial x_k} \frac{\partial u_j}{\partial x_k} = \frac{2}{3} \epsilon \delta_{ij} \quad \dots (7.10)$$

Both models use this approximation.

(d) Pressure-Strain/Redistribution

Chou (1945) showed that away from a wall, the term $\frac{p'}{\rho} \frac{\partial u_i}{\partial x_j}$ could be expressed in terms of the interaction of fluctuating velocities and the interaction of the mean and fluctuating flow. LRR label these two contributions as $(\phi_{ij,1} + \phi_{ji,1})$ and $(\phi_{ij,2} + \phi_{ji,2})$ respectively. Rotta (1951) proposed:

$$(\phi_{ij,1} + \phi_{ji,1}) = -\alpha \epsilon \frac{(\overline{u_i u_j})}{k} - \frac{2}{3} \delta_{ij} k \quad \dots (7.11)$$

where α is a constant. The right hand side of equation (7.11) represents the degree of anisotropy of the turbulence and shows a linear "return to isotropy". Since in an homogeneous flow, where the mean rate of strain is negligible, the statistically more probable state is one of isotropy, Rotta proposed that pressure fluctuations would act to equalise the normal stresses and to diminish the shear stresses. Naot et al (1970) proposed the model for the mean velocity gradient contribution to the redistribution term as:

$$(\phi_{ij,2} + \phi_{ji,2}) = -\alpha' (P_{ij} - \frac{2}{3} \delta_{ij} P) \quad \dots (7.12)$$

where P = production of turbulence energy. The model is exact for isotropic and homogeneous turbulence. This contribution to the redistribution term is proportional to the anisotropy of the production of turbulence. The DH model recognises the contribution of the mean rate of strain to the redistribution term but assumes that it is negligible. The LRR model uses a 'complete' and 'simplified' approximation for the

mean rate of strain contribution, where the simplified version is of the form of equation (7.12). It also uses a modified form of the complete pressure-strain model for near-wall turbulence.

LRR model the ϵ transport equation (2.26) as originally shown by Hanjalic and Launder (1972). The modelled equation is:

$$\frac{D\epsilon}{Dt} = -C_{\epsilon,1} \frac{\epsilon}{k} \overline{u_i u_k} \frac{\partial \overline{u_i}}{\partial x_k} - C_{\epsilon,2} \frac{\epsilon^2}{k} + C_{\epsilon} \frac{\partial}{\partial x_k} \left(\frac{k}{\epsilon} \overline{u_k u_l} \frac{\partial \epsilon}{\partial x_l} \right) \quad \dots (7.13)$$

which, after summation of indices, use of equations (7.1), (7.4) and (7.6) and application of boundary layer assumptions, reduces to equation (7.7), used in the $k \sim \epsilon$ model.

Bradshaw (1972) compares the LRR and DH models along with other similar Reynolds stress closures. Launder and Spalding (1972) compare predictions using the DH model with experimental data of a plane free jet. The $\overline{u^2}$ and $\overline{v^2}$ stresses are not predicted very well, which they ascribe to the modelling of the redistribution terms since k is predicted fairly well. However, this is a criticism of just one of the many assumptions required in a Reynolds stress closure. In order that a model may have the intended degree of universality, it has to be tested in a wide variety of flows. Only then can one model be said to be superior to another.

7.1.4 Additional Models

There are some models which do not fit into any of the categories of table III, and yet are important. The first of these is that of Bradshaw et al (1967) which is a one-equation model, but which does not

use the eddy viscosity concept. See § 6.1.2. The turbulent kinetic energy equation is converted into a differential equation for the turbulent shear stress by assuming $\tau \propto \rho k$ which holds for many types of boundary layers. The dissipation term in the kinetic energy equation is modelled by equation (7.6) where ℓ is prescribed algebraically. The model does have the advantage that the shear stress is not tied to the mean velocity gradient, but the model has no use in regions of negative shear stress where k is necessarily positive.

Another model which is not easily categorised is that of Rodi (1976) - an algebraic Reynolds stress model. The modelled stress transport equation is reduced to an algebraic form by the assumption:

$$\begin{aligned} \text{transport } (\overline{u_i u_j}) &= \frac{\overline{u_i u_j}}{k} \times \text{transport } (k) \\ &= \frac{\overline{u_i u_j}}{k} (P - \epsilon) \end{aligned}$$

Thus the convection and diffusion terms are approximated. In practice the model reduces to a $k \sim \epsilon$ model, where the constant of the Prandtl-Kolmogorov eddy viscosity equation (7.4) becomes a function of P , k and ϵ . This model was used by Ljuboja and Rodi (1981) in predictions of flat plate wall jet data.

7.2 ASSESSMENT OF MODELS

All of the models described above, with the exception of that of Bradshaw et al (1967), can, in principle be used in the calculation method described in Chapter 6. However, the simpler eddy viscosity/mixing length formulae lack the detail of prediction and universality of a full Reynolds stress closure, yet offer surprisingly good predictions when constants are adjusted for each flow type.

In general, the limitations of a model can be seen by inspection of the relevant transport equation at an order higher than that of the closure. Thus the limitations of the mixing length hypothesis are seen by inspection of the transport equation for turbulent kinetic energy when transport terms are neglected (§ 2.3.1). Irwin (1973) and Bradshaw and Gee (1962) both found that the position of zero shear stress in a flat plate wall jet was consistently closer to the wall than the velocity maximum. (§ 2.4.1) This phenomenon can be predicted by a Reynolds stress closure, but not by an eddy viscosity model which would predict $\overline{uv} = 0$ at the velocity maximum.

In complex shear layers where several gradients of components of the stress tensor $\overline{u_i u_j}$ may be significant in the mean momentum equation, the use of a scalar eddy viscosity, as in the Prandtl-Kolmogorov formula equation (7.4), may no longer be valid. ν_T is likely to be strongly sensitive to direction. Also, neglect of the modelled convection and diffusion terms in the \overline{uv} transport equation leads to retention of only the redistribution terms - there is no dissipation term. After retaining only the main redistribution terms and assuming $\overline{v^2}/k$ is constant the Prandtl-Kolmogorov formula is produced. Therefore this eddy viscosity formula inadequately represents convective and diffusive processes and implies that where a mean velocity gradient changes rapidly, that the Reynolds stress will respond immediately. Rodi (1975 b) assesses the constancy of C_μ in the Prandtl-Kolmogorov formula.

A Reynolds stress closure of the form of LRR, in which all the terms in the transport equation are separately modelled, is likely to be the only model, presently available, capable of giving satisfactory predictions of $\overline{u_i u_j}$ for a complex shear layer. At least one transport

equation for a length scale would also be necessary as $\frac{d\delta}{dx}$ is large for many complex shear layers. But the application of a Reynolds stress model to strongly curved flows is only just being developed (Gibson and Rodi (1981)). For purposes of the present work, a mixing length formula, modified to account for the effects of streamline curvature and divergence, is likely to give satisfactory predictions of the mean flow, relatively cheaply in terms of computer time and will serve as a good first approximation in a calculation method required to give predictions for only one flow type. The calculation method described in Chapter 6 is such that it could be extended to incorporate a full Reynolds stress closure at a future date.

7.3 REPRESENTATION OF MIXING LENGTH IN CALCULATION METHOD

For the two cases where the I boundary is either an axis of symmetry or a wall, the jet profile is divided into 'mixing regions', to the widths of which the mixing length is proportional. This is the procedure followed in the PS method.

Figure 7.1.a shows the positions of these 'mixing regions' for a wall jet in which the following mixing length representations are used:

$$\begin{aligned} l_{0,12} &= \lambda(y_2 - y_1) \\ l_{0,34} &= \lambda(y_4 - y_3) \\ l_{0,56} &= \lambda(y_6 - y_5) \\ l_{0,23} &= \frac{1}{2}(l_{0,12} + l_{0,34}) \\ l_{0,45} &= \frac{1}{2}(l_{0,34} + l_{0,56}) \end{aligned} \quad \dots (7.14)$$

Values of l_0 near the wall are subject to the law of the wall:

$$l_0 \propto K y \quad \dots (7.15)$$

where $K = 0.41$. The correction developed by van Driest (1956) for the

effect of damping of turbulent motion near a wall, viz:

$$\ell_0 = K y (1 - \exp(-y \frac{\tau_w^{1/2} \rho^{1/2}}{A\mu})) \quad \dots (7.16)$$

was not used ($A = 26.0$) as it was not considered necessary.

For the parts of the profile in which $\frac{\partial \bar{U}}{\partial y}$ is small, ℓ_0 is specified as the average of those values in the two adjacent 'mixing regions'. The possibility of $\ell_0 \rightarrow 0$ as $\frac{\partial \bar{U}}{\partial y} \rightarrow 0$ is therefore avoided. This procedure is consistent with the physical processes involved because in regions where the value of $\frac{\partial \bar{U}}{\partial y}$ is small, production of $\bar{u}\bar{v}$ is small and transport terms dominate. Since the mixing length hypothesis neglects transport processes, it is meaningless in these regions. Accordingly, the value of $\ell_0 \left| \frac{\partial \bar{U}}{\partial y} \right|$ was not allowed to fall below a certain minimum proportional to the local value of \bar{U} .

The representation of ℓ_0 in a jet with an axis of symmetry at the I boundary is shown in Figure 7.1 b, where the treatment is the same. The positions of $y_1 \rightarrow y_6$ are shown also for the initial top-hat profiles. These were defined so that consistency with the ℓ_0 representation for the downstream profiles was achieved.

The relative merits of different values of λ and K are discussed by Launder and Spalding (1972). They found that agreement between experimental data for wall jets and the PS calculation method could be optimised for different flow parameters by using different ratios of

K/λ . The values of K and λ used in the present calculation method are given in the table IV below.

JET TYPE	K	λ
Plane flat plate wall jet	0.41	0.09
Plane jet with axis of symmetry	0.41	0.115
Axisymmetric jet with axis of symmetry	0.41	0.075

TABLE IV: Values of K and λ in Jet flows without streamline curvature or divergence

7.4 MODELLING OF STREAMLINE CURVATURE EFFECTS

The effects of streamline curvature on a turbulent shear layer were reviewed in § 2.5. Curvature is likely to affect the higher order structural parameters of the turbulence, therefore implicitly changing the sizes of the terms in the Reynolds stress transport equations on top of the explicit changes in the production and transport terms. See Appendix F. Therefore, all of the turbulence models described in § 7.1 require empirical adjustment to account for the effects of streamline curvature.

7.4.1 Mixing Length Corrections For The Effects Of Streamline Curvature

The laminar shear stress term of equation (E.1) becomes after retention of only the significant terms (see § 6.2.3 for assumptions):

$$\tau = \mu \left(\frac{\partial \bar{U}}{\partial y} - \frac{\bar{U}}{rh} \right) \quad \dots (7.17)$$

Sawyer (1963), using Prandtl's 1929 mixing length arguments derived an expression for the turbulent shear stress:

$$\begin{aligned}
 -\overline{uv} &= \nu_T \left(\frac{\partial \bar{U}}{\partial y} - \frac{C \bar{U}}{rh} \right) \\
 &= \ell_o^2 \left| \frac{\partial \bar{U}}{\partial y} \right| \left(\frac{\partial \bar{U}}{\partial y} - \frac{C \bar{U}}{rh} \right)
 \end{aligned}
 \quad \dots (7.18)$$

where C is an empirical constant and ℓ_o is the mixing length in the equivalent flow without curvature. Equation (7.18) corresponds to the F-factor correction of Bradshaw (1973) applied to ℓ_o . See § 2.5. Sawyer found that in equation (7.18) $C = 5$ for a curved free jet for all ratios of jet thickness to radius of curvature of the jet centre-line. Giles et al (1969) used the same correction for the calculation of a turbulent wall jet on the logarithmic spiral. For the self-preserving jet, $C = 3$ gave a best fit to the measured profile shape.

The fact that $C \neq 1$ in equation (7.18) illustrates the fact that the turbulent shear stress has no direct analogy with its laminar counterpart. Also the expected variation of C in order to optimise agreement of predictions with different curved flow types highlights the approximations involved when using a mixing length modification. The variation of C accounts for not only the relative degree to which the production and dissipation terms in the turbulent kinetic energy equation (F.7) are affected, but also accounts for the failure of the local-equilibrium approximation where transport terms are significant to a different degree.

Using the analogy between the effect of buoyancy on a turbulent flow and that of curvature, Bradshaw (1969) made use of the original

idea of Prandtl. In buoyant flows the gradient Richardson number is defined as:

$$Ri = \frac{\text{buoyancy forces}}{\text{inertia forces}}$$

Bradshaw defines:

$$Ri_B = \frac{2S_B}{1 + S_B} \quad \dots (7.19)$$

$$\text{where } S_B = \frac{\bar{U}/r}{\partial \bar{U} / \partial y} \quad \dots (7.20)$$

S_B is equivalent to the flux Richardson number defined as the ratio of turbulent energy production by buoyancy forces to production by shearing forces, as shown by retention of only the main production terms in equation (F.7).

In unstably curved or buoyant flows, Ri_B is negative and in stable conditions it is positive. Bradshaw also proposed the use of a Monin-Oboukhov type formula, which was originally derived for modification of mixing length by small buoyancy effects, in order to compensate the mixing length in a curved flow. It is:

$$\ell_c / \ell_o = 1 - \beta Ri_B \quad \dots (7.21)$$

where ℓ_c denotes the corrected mixing length. For large r , S_B is small and equation (7.21) reduces to the curvature correction used in equation (7.18) for $C = 2\beta$. Equation (7.21) is therefore equivalent to the F-factor analysis used by Bradshaw (1973), who tests its use in the calculation method of Bradshaw et al (1967). The calculation method uses the thin-shear-layer approximation and the cross-stream pressure gradient is neglected. Meroney and Bradshaw (1975) report the comparison between predictions and experimental data for a stably and unstably curved boundary layer where $\pm \delta/r \sim 0.01 - 0.02$. Values of $\beta = 7$ and 4 were used for the convex and concave cases respectively, although for the latter, the presence of longitudinal vortices made the agreement less

good. Bradshaw (1973) also reports calculations made for curved wall jets using values of $\beta = 7$ and 4 in stabilised and destabilised regions respectively. No experimental data was available for comparison. However, the jet growth rate data of Giles et al (1966), suggested that optimum values for β were 4 in stabilised regions and 3 in destabilised regions, i.e. $C = 8$ and 6 respectively. The boundary layer data of So and Mellor (1972) was also used, but agreement was not so good. In this case, $\delta/r = 0.08$ on a convex surface and 0.13 on a concave surface. The linear correction of equation (7.21) is not expected to be adequate for large curvature effects.

7.4.2 Analysis For Mixing Length Correction Applicable To Flows With Large Curvature

The basis of the method is the approximation of each of the transport equations for the components of the Reynolds stress tensor $\overline{u_i u_j}$, modelling the remaining terms as outlined in § 7.1.3 and manipulating the remaining equations that are algebraic in $\overline{u_i u_j}$. This more rigorous approach gives a mixing length correction which is applicable to flows with large curvature.

Irwin and Smith (1975) assume that terms $\overline{u_i u_j}$ are of order $\left(\frac{y_m}{x}\right) \bar{U}^2$ and that the terms $\overline{u_i u_j u_k}$ are of order $\left(\frac{y_m}{x}\right)^2 \bar{U}^3$. They also assume that the redistribution terms are of the same order as the main production terms. Following these assumptions, equations (F.4) to (F.7) reduce to their local equilibrium form, i.e. transport and convection terms are neglected. The approximate $\overline{u^2}$, $\overline{v^2}$, $\overline{w^2}$, $\overline{q^2/2}$ and $-\overline{uv}$ transport equations are respectively:

$$- h \overline{uv} \frac{\partial \bar{U}}{\partial y} - \frac{\bar{U} \overline{uv}}{r} + \frac{\overline{p' \frac{\partial u}{\partial x}}}{\rho} - \frac{1}{3} \epsilon = 0 \quad \dots (7.22)$$

$$2 \frac{\bar{U} \overline{uv}}{r} + h \frac{\overline{p' \frac{\partial v}{\partial y}}}{\rho} - \frac{1}{3} \epsilon = 0 \quad \dots (7.23)$$

$$h \frac{\overline{p' \frac{\partial w}{\partial z}}}{\rho} - \frac{1}{3} \epsilon = 0 \quad \dots (7.24)$$

$$- h \overline{uv} \frac{\partial \bar{U}}{\partial y} + \frac{\bar{U} \overline{uv}}{r} - \epsilon = 0 \quad \dots (7.25)$$

$$h \overline{v^2} \frac{\partial \bar{U}}{\partial y} - (2 \overline{u^2} - \overline{v^2}) \frac{\bar{U}}{r} - h \frac{\overline{uv}}{R} (\bar{U} \sin \alpha + \bar{V} \cos \alpha)$$

$$- \frac{\overline{p'}}{\rho} \left(\frac{\partial v}{\partial x} + h \frac{\partial u}{\partial y} \right) = 0 \quad \dots (7.26)$$

Rearrangement of the approximated turbulent kinetic energy equation alone gives equation (7.18), viz:

$$- \overline{uv} = \ell_0^2 h^2 \left| \frac{\partial \bar{U}}{\partial y} \right| \left(\frac{\partial \bar{U}}{\partial y} \right) (1 - K)^2 \quad \dots (7.27)$$

where

$$K = \frac{\bar{U}/rh}{\partial \bar{U}/\partial y} \quad \dots (7.28)$$

The Richardson number is defined as:

$$Ri = \frac{2K(1 + K)}{(1 - K)^2} \quad \dots (7.29)$$

which for small curvature reduces to Ri_B . The only terms that require modelling in equations (7.22) to (7.26) are the pressure-strain terms

which are done so as in the LRR model, viz equations (7.11) and (7.12).

The modelled equations are therefore, in the same order:

$$\begin{aligned}
 h \frac{\overline{uv}}{\partial y} \frac{\partial \overline{U}}{\partial y} + \frac{\overline{U}}{r} \frac{\overline{uv}}{r} + C_1 \epsilon \left(\frac{\overline{u^2} - 1}{\overline{q^2}} - \frac{1}{3} \right) + C_2 \left(-\frac{2}{3} h \frac{\overline{uv}}{\partial y} \frac{\partial \overline{U}}{\partial y} - \frac{4}{3} \frac{\overline{uv}}{r} \frac{\overline{U}}{r} \right) \\
 + \frac{\epsilon}{3} = 0 \\
 \dots (7.30)
 \end{aligned}$$

$$\begin{aligned}
 2 \frac{\overline{U}}{r} \frac{\overline{uv}}{r} + C_1 \epsilon \left(\frac{\overline{v^2} - 1}{\overline{q^2}} - \frac{1}{3} \right) + C_2 \left(\frac{1}{3} h \frac{\overline{uv}}{\partial y} \frac{\partial \overline{U}}{\partial y} + \frac{5}{3} \frac{\overline{U}}{r} \frac{\overline{uv}}{r} \right) \\
 + \frac{\epsilon}{3} = 0 \\
 \dots (7.31)
 \end{aligned}$$

$$\begin{aligned}
 C_1 \epsilon \left(\frac{\overline{w^2} - 1}{\overline{q^2}} - \frac{1}{3} \right) + C_2 \left(\frac{1}{3} h \frac{\overline{uv}}{\partial y} \frac{\partial \overline{U}}{\partial y} - \frac{1}{3} \frac{\overline{U}}{r} \frac{\overline{uv}}{r} \right) \\
 + \frac{\epsilon}{3} = 0 \\
 \dots (7.32)
 \end{aligned}$$

$$\begin{aligned}
 h \frac{\overline{uv}}{\partial y} \frac{\partial \overline{U}}{\partial y} - \frac{\overline{uv}}{r} \frac{\overline{U}}{r} \\
 + \frac{\epsilon}{3} = 0 \\
 \dots (7.33)
 \end{aligned}$$

$$\begin{aligned}
 h \frac{\overline{v^2}}{\partial y} \frac{\partial \overline{U}}{\partial y} - (2\overline{u^2} - \overline{v^2}) \frac{\overline{U}}{r} + C_1 \frac{\epsilon}{k} \frac{\overline{uv}}{r} + C_2 \left(-h \frac{\overline{v^2}}{\partial y} \frac{\partial \overline{U}}{\partial y} + (2\overline{u^2} - \overline{v^2}) \frac{\overline{U}}{r} \right) \\
 - h \frac{\overline{uv}}{R} \left(\overline{U} \sin \alpha + \overline{V} \cos \alpha \right) = 0 \\
 \dots (7.34)
 \end{aligned}$$

LRR recommend $C_1 = 1.5$ and $C_2 = 0.4$. With the neglect of the divergence term in equation (7.34) (see § 7.5 and § 7.7) and the substitution for the dissipation rate using equation (7.6), expressions for \overline{uv} and the ratio $\overline{u^2}/\overline{v^2}$ can be obtained:

$$-\overline{uv} = \ell_0^2 (1 - \alpha_1 Ri - \alpha_2 Ri^2)^{3/2} (1 - k)^2 \left(\frac{\partial \overline{U}}{\partial y} \right)^2 \quad \dots (7.35)$$

$$\frac{\overline{u^2}}{\overline{v^2}} = 2 \frac{1 + \gamma_1 K/(1-K)}{1 - \gamma_2 K/(1-K)} \quad \dots (7.36)$$

These expressions were derived by So (1976) following the analysis of Irwin and Smith (1975). The constants are not universal as proposed however, for the reasons given in § 7.4.1. A similar procedure is adopted by So (1975) who obtained:

$$-\overline{uv} = \ell_0^2 (1 - \frac{\beta}{2} Ri)^{3/2} (1 - K)^2 \left(\frac{\partial \overline{U}}{\partial y} \right)^2 \quad \dots (7.37)$$

This expression was used by So (1978) for boundary layer predictions for the data of So and Mellor (1972, 1973 and 1975). Good agreement was found with the predictions of shear stress in cases of large curvature, $\delta/r \sim 0.01$.

Finally, it is worth noting that for small curvature, $Ri \rightarrow Ri_B$ and equation (7.35) reduces to equation (7.21) with $\beta = 3\alpha_1/4$. Also in the outer regions of a wall jet with streamline curvature, where there is destabilising curvature and Ri is negative, the mixing length is increased as expected in equation (7.35) for α_1 and α_2 positive.

The converse would be true for stabilising curvature. Equation (7.36) shows the reduction of the stress ratio for negative K (γ_1 and γ_2 are also positive) and incidentally for no curvature the ratio predicted is 2.0. Townsend (1976 p. 107) quotes \bar{u}^2/\bar{v}^2 as 1.37 and 1.45 for the outer layer of a boundary layer and a flat plate wall jet respectively.

7.5 MODELLING STREAMLINE DIVERGENCE EFFECTS

It was shown in § 2.7.1 that the effect of the extra rate of strain induced by lateral divergence can be represented by a simple formula, bearing in mind the restrictions mentioned in § 2.5.

Thus the mixing length in a flow with divergence of the mean flow streamlines can be represented by:

$$\ell_D = \ell_0 \left(1 - \gamma \left(\frac{\bar{U} \sin \alpha + \bar{V} \cos \alpha}{R \partial \bar{U} / \partial y} \right) \right) \quad \dots (7.38)$$

where γ is an empirical constant of order ten. Now differentiation of equation (6.14) with respect to x gives:

$$\frac{d\ell_D}{dx} = \rho \frac{\delta y}{R} \left(\frac{\bar{U}}{dx} \frac{dR}{dx} + R \frac{\partial \bar{U}}{\partial x} \right) \quad \dots (7.39)$$

where $dR/dx = 0$ and 1 for the plane and axisymmetric ($\alpha = 90^\circ$) cases respectively. For say, the case of a radial wall jet where $R = x$, assuming the value of x is sufficiently far downstream and that $\partial \bar{U} / \partial x = \bar{U} / x$, then the ratio of radial to plane wall jet entrainment rates reduces to two and therefore the ratio of shear stresses also. $\partial \bar{U} / \partial y$ is negative in the larger outer region of a wall jet, hence equation (7.38) gives the expected increase in mixing length for the axisymmetric case with divergence. It may be noted from equation (7.38)

that for a cylindrical wall jet where $\alpha = 0$, only divergence of the streamlines in the x-y plane with respect to cartesian coordinates occurs, whereas for $\alpha \neq 0$, divergence is three-dimensional, occurring in the x-z plane also.

For the present case $\delta/R = 1/6$ is a maximum estimate for transverse curvature. This value is less than the value at which Smits et al (1979 b) concluded that transverse curvature effects were negligible. No empirical correction is therefore made for transverse curvature.

7.6 ALLOWANCE FOR "HISTORY" EFFECTS

The only terms in the Reynolds stress transport equations that can change immediately the mean rate of strain changes are the production terms and those terms involving p' . The latter can change immediately because the mean strain rate appears in the Poisson equation for p' . Therefore the effect of a sudden application of an extra rate of strain is not immediately apparent on the shear stress. Castro and Bradshaw (1976) demonstrate this with data from a strongly curved mixing layer. The maximum principal stress has a lagged response to the extra rate of strain, i.e. the effect of mean transport on the Reynolds stress is apparent.

For the response of a shear layer subjected to a sudden extra rate of strain, e , Bradshaw (1973) proposed that an effective rate of strain could be calculated from the ordinary differential equation:

$$X \frac{d}{dx} (\alpha e)_{\text{eff}} = \alpha_0 e - (\alpha e)_{\text{eff}} \quad \dots (7.40)$$

X is a 'time constant' representing the memory of the stress-containing eddies which, using local equilibrium arguments, is approximately 10δ

for a boundary layer and 2δ for a jet or free mixing layer. Equation (7.40) therefore shows an exponential growth response to an applied extra rate of strain e . The time constant for the present study was considered not likely to be very long, and therefore the above equation was not used.

However, problems were encountered in the initial calculations of shear stress. These originated not only from the above considerations, which are even more pertinent when transport terms are neglected as in the mixing length hypothesis, but also from the idealized velocity profile at the slot exit in which $\partial \bar{U} / \partial y = 0$ except at either wall where very large gradients occurred. Therefore it was necessary to control the rate at which the shear stress $\bar{U} \bar{V}$ could grow, being crudely related to the mean velocity gradient. This was done by controlling the rate at which y_3 in Figure 7.1 a was allowed to move inwards to its position on the fully developed profile. In accordance ^{with} established rates of development of shear layers, the mixing length was initially allowed to increase at a rate proportional to the distance downstream from the slot exit where the constant of proportionality was 0.12. Reynolds (1974 p. 329) suggests a ratio of nominal shear layer width to development length of about 0.1. The constant of 0.12 was used here because the mixing length was determined from the narrower mixing regions as defined by equations (7.14). This process of controlling the growth of shear stress and mixing length linearly was used instead of equation (7.40).

Smits et al (1979 a) derive a second order ordinary differential equation in the perturbation of $\partial \bar{U} / \partial y$ from its pre-curvature value in order to assess the recovery of a shear layer from the removal of the

extra rate of strain. The equation represents a damped simple harmonic response, i.e. the variation of $\partial \bar{U} / \partial y$ and \bar{uv} is oscillatory as indicated by the experimental data. In the present work, no procedure was incorporated into the shear stress calculation to simulate this oscillatory response to the removal of curvature, nor indeed the response to the sudden change from laterally diverging to converging flow, as occurring at $\alpha = 0$ on an axisymmetric profile with streamline curvature.

7.7 MODELLING OF COMBINED STREAMLINE CURVATURE AND DIVERGENCE EFFECTS

A simple algebraic solution for \bar{uv} is not immediately available from equations (7.30) to (7.34) with the inclusion of the extra production term due to streamline divergence in equation (7.33). The curvature and divergence terms are therefore treated separately as above and it is assumed that their effects on the shear stress are additive, which is unlikely to be realistic except in cases of small extra rates of strain. In any case, with the use of a mixing length model, further sophistication is probably not justified. Thus any interaction between the effects of the two extra rates of strain present are not taken into account in the present shear stress model.

A discussion of the present turbulence model appears in Chapter 9 together with possible improvements to the modelling of streamline curvature and divergence effects.

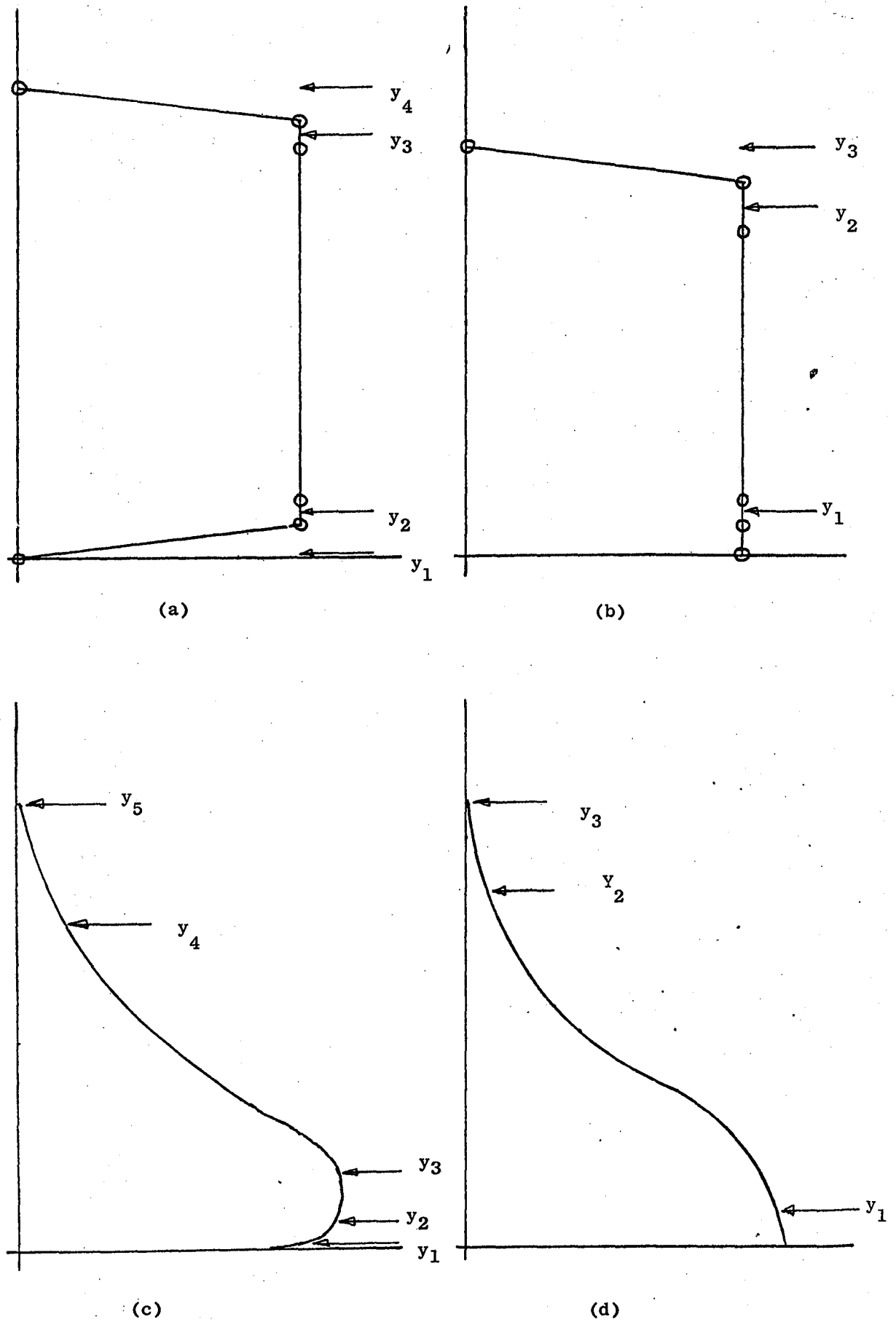


FIG. 7.1 Mixing Length Distributions:

(a) Initial wall jet
(c) typical wall jet

(b) initial axis of symmetry
(d) axis of symmetry

CHAPTER 8

COMPUTER PROGRAM RESULTS

The calculation method outlined in Chapter 6, with the approach for modelling the Reynolds shear stress described in the previous chapter was tested against established experimental data for five independent cases, all of differing geometries and constants, the program was then used to predict the data for the three sets of conditions used in the experimental work reported in Chapter 5. Thus eight separate flow cases were calculated and these are summarized in Table V below.

CASE	FLOW	t mm	U_s m/sec	N	NIT
I	Flat-plate wall jet: Wilson & Goldstein (1976)	6.09	34.34	20	1
II	Wall jet on a circular cylinder: Wilson & Goldstein (1976) $r/t = 16.5$	6.15	36.02	30	4
III	Radial wall jet: Baker (1967)	2.00	117.84	30	1
IV	Round free jet: Rodi (1975a)	6.45	100.13	20	1
V	Conical wall jet: Sharma (1981)	2.06	46.32	30	1
VI	Case A of experimental results: $r/t = 6.0$	5.00	67.01	30	4
VII	Case B of experimental results: $r/t = 15.0$	2.00	105.68	30	5
VIII	Case C of experimental results: $r/t = 19.9$	2.51	229.15	30	10

Table V: Test Cases for Calculation Method

All the cases in the table refer to an air jet in air, although the program does allow the physical properties of the primary fluid and entrained fluid to be changed. However, mixture properties are only obtained by mass average. The values of mixing length constants used are given in Table IV. The first pair of values are those used in all cases which specify a wall at the I boundary. Case IV is the only one in which the I boundary is an axis of symmetry. The values of slot exit velocity given in the table are, in the case of the iterative procedure, those calculated at the wall node for the converged solution. In all cases except the last, \bar{U}_s is below $M = 0.34$. With the exception of the node adjacent to the wall, the nodes were distributed according to a power law of 1.5 so that the nodes were closer together at the maximum of the mean velocity profile. This was necessary in order to reduce errors in $\partial \bar{U} / \partial y$ near the maximum. The node ($i = 2$) next to the wall was kept at a fixed dimensionless distance from the wall to ensure that it was always in the fully turbulent region. Where the number of iterations (NIT) is stated as one, the non-iterative procedure was used. Iterative procedures all used the wall-pressure convergence criterion of §6.4.6 and a relaxation factor of 0.3 for the adjustment of upstream static pressures. Step lengths were controlled so as to be no larger than either a preset multiple of the slot width, or a fixed angle increment, whichever was the smaller.

8.1 CASES I - V

The experimental data of case I was used to fix the entrainment constants using the two established values of mixing length constants specified in Table IV. Subsequently, the values of these entrainment constants were not changed. Predictions of growth/velocity decay rate, wall shear stress, mean velocity and shear stress profiles are presented in Figures 8.1 - 8.16.

For case I, the predictions of wall shear stress, figure 8.2, are slightly below, but on the same gradient as the wall shear stress measurements of Bradshaw and Gee (1962). The mean velocity profile \bar{U}/\bar{U}_m shows a typically thin velocity maximum and \bar{V}/\bar{U}_m is quite badly underestimated; most of the other mean velocity profiles in the other cases show similar defects. The shear stress profiles show good agreement except for $0.8 < \xi < 1.4$. This is due to the mis-placement of y_4 (figure 7.1) which controls the mixing length in this region. This fault can be traced to the relative scarcity of nodes in the outer parts of the profile and the consequential inaccuracies of $\partial\bar{U}/\partial y$ which was used as the criterion for positioning y_4 . Not surprisingly therefore, the values of $\bar{u}\bar{v}$ in this region show no degree of similarity as shown by the experimental data. Naturally, the position of zero shear stress coincides with the maximum in \bar{U} ; no diffusion of $\bar{u}\bar{v}$ can be accounted for with use of a mixing length model to give the expected reduction in the value of ξ at $\bar{u}\bar{v} = 0$ as the jet develops.

The same predictions for the case of a wall jet with streamline curvature are given in figures 8.5 - 8.8. The values of α_1 and α_2 used in equation (7.35) for the correction to mixing length to account for the effects of curvature are 3.26 and 3.09 respectively. These values were suggested by So (1976) whose values of $v_1 = 1.942$ and $v_2 = 3.865$ in equation (7.36) were also used for predictions of u^2/v^2 . Subsequently, the values of these constants were not changed for any of the other cases.

The prediction of jet growth rate agrees well with the experimental data, but the velocity decay rate is under-predicted. This is peculiar since one would assume that both ought to agree for conservation of

angular momentum to be enforced. Faulty interpolation for $y_{m/2}$ or \bar{U}_m appears not to be the reason. Predictions of wall shear stress appear to oscillate from step to step but show at least qualitatively, the trend of the data of Alcaraz et al (1977). The mean velocity profiles do not remain similar. \bar{U}/\bar{U}_m profiles show an over-sharp peak and therefore a slightly thicker profile for $\xi > 1.0$. \bar{V}/\bar{U}_m is underestimated by as much as 50%. The shear stress profiles show quite good agreement, except for $\theta = 90^\circ$ which is over-estimated for $\xi > 0.4$ and underestimated otherwise. Problems of over-large shear stress in the outer parts of the profiles apparent in the previous case are not so here, although the predictions show no steady increase as indicated by the experimental data.

The limit of the general axisymmetric geometry ($\alpha = 90^\circ$) with a flat wall produces a radial wall jet, figures 8.9 - 8.12. The value of $q = 9.0$ was used in equation (7.35) for the estimation of the effects of streamline divergence on the shear stress $\bar{u}\bar{v}$. Despite the lack of experimental data for comparison, the shear stresses in figure 8.12 are approximately twice those of figure 8.4 as expected. The wall shear stress appears to be slightly overestimated at large values of x/t (small values of $(Re)_{\max}$) and underestimated at low values of x/t . The mean velocity profiles show similar defects to those of the previous cases.

Values of the mixing length constants used in Case IV, figures 8.13 - 8.14, are shown in Table IV. The value of κ is of course irrelevant. It appears that a larger value of λ should have been used to optimise agreement with the experimental data - the shear stresses are underestimated by nearly 50%. However, the mean velocity profile is well predicted and does not show the defects common to all the previous cases.

Case V is a further test of the axisymmetric geometry where $\alpha = 54^\circ$. The profiles of \bar{U}/\bar{U}_m are similar to those for the preceeding wall-bounded cases. There are no experimental data for comparison with the velocity decay rate and shear stress predictions, but the growth rate prediction is satisfactory. The local maximum on the shear stress profile at $x/t = 42$, $\xi = 0.45$ is caused by a slight point of inflexion in the mean velocity profile.

8.2 CASES VI - VIII

Figures 8.17, 8.22 and 8.24 show the jet growth/velocity decay rates for the three sets of experimental data presented in Chapter 5. All three cases show underestimation of the velocity decay rate. The jet growth rates are predicted quite well, although at large x/t , where velocity maxima are not always well defined and where velocity gradients in the outer part of the jet are small, the experimental values of $y_{m/2}$ are subject to large errors. Therefore no specific comments can be made concerning the expected reduction in growth rate after the removal of streamwise curvature and the prediction of it. However for smaller values of x/t the agreement is least good for case VI. This is not surprising since the ratio $r/t = 6$ whereas it is 15 for case VII. With a larger slot width, the potential core of the jet extends further downstream, therefore making the simple assumptions concerning the shear stress modelling in the initial regions of the jet (§ 7.6) more critical. In fact, the positioning of the mixing region edge y_3 , is not determined by the usual criterion of $\partial\bar{U}/\partial y$ until $\theta = 70^\circ$ in case VI, whereas for case VII this is done so by $\theta = 30^\circ$. This leads to an underestimation of shear stress in the initial regions of the jet for case VI but not for case VII as shown by comparison of figures 8.21 and 8.23.

Figure 8.18 shows the wall shear stress predictions for case VI. There are two distinct gradients for the wall jet with and without streamline curvature, below and above the experimental laws respectively. The value of $(Re)_{\max}$ is least at $\theta = 90^\circ$. No adjustments were made to the values of the constants in the law of the wall either for the effects of streamline curvature, or the changes in surface curvature. The increase in wall shear stress up to $\theta = 90^\circ$ and the subsequent decrease is reflected in the profiles of figure 8.21.

The mean velocity profiles for case VI are shown in figures 8.19 and 8.20. Allowing for the profile at $\theta = 50^\circ$ which shows signs of not being fully developed, none of the \bar{U}/\bar{U}_m profiles show any distortion caused by the sudden change in surface curvature at $\theta = 100^\circ$, apparent in the experimental data (figures 5.10 and 5.11). The mean velocity profiles at $\theta = 100^\circ + 50$ mm overestimate both \bar{U}/\bar{U}_m and \bar{V}/\bar{U}_m . This is not likely to be caused by the sudden change in surface curvature at $\theta = 100^\circ$. The profiles of \bar{V}/\bar{U}_m collectively do not behave as expected from the experimental data.

The shear stress predictions of figure 8.21 (c.f. figure 5.18) show a steady increase up to $\theta = 90^\circ$ and a subsequent decrease, more sudden after $\theta = 100^\circ$. The non-monotonic response evident in the experimental data is naturally not apparent in the predictions since no programming was incorporated to model it. However, the maximum in shear stress at $\theta = 80^\circ$ rather than $\theta = 90^\circ$ or 100° can be interpreted as the effect of pressure on the upstream flow. Thus the mean flow and therefore the shear stresses can also anticipate the removal of curvature at $\theta = 100^\circ$. However, this is only because the shear stress is directly related to $\partial\bar{U}/\partial y$. The large values of $\bar{U}\bar{V}$ in the last profile

at $\theta = 100^\circ + 50$ mm are due to errors in $\partial \bar{U} / \partial y$ which are caused by the lack of nodes in the outer profile and the large jet width.

Figure 8.25 shows predictions for the entrainment rates plotted (a) for cases with streamline curvature and, (b) those cases without streamline curvature. Direct comparison of individual cases is not possible as each case has a different slot exit momentum. Cases I and II however, do have similar initial momenta and the effect of stream-wise curvature is apparent. Also of interest is the comparison of entrainment rates for the flare geometries (cases VI and VII) and that of case IV, the round free jet. Even though the exit momentum for the latter is three times those of the former, the entrainment rates for the flare cases are larger than that of case IV.

8.3 DISCUSSION OF CALCULATION METHOD

The foregoing results indicate certain shortcomings in the calculation method which could be improved and are not directly related to the turbulence modelling used.

8.3.1 Node Distribution

The distribution of nodes according to a power law of 1.5 on ω combined with the approximations used to calculate $y_N - y_{NMI}$ combine to give rather a sparse grid for $\xi > 1.0$. Consequently, the important positioning of y_3 and y_4 is not always sufficiently accurate, leading to bad estimates of $\bar{u}\bar{v}$ in this region. This could be remedied by increasing the number of nodes and therefore increasing the running time. A reduction in the power law exponent would displace nodes away from the velocity maximum outwards, thus causing the same problem for y_2 and y_3 .

8.3.2 Mean Velocity Profiles

With the exception of case IV, all the mean velocity profiles underestimate \bar{U}/\bar{U}_m near the velocity maximum, thereby giving a peak that is too sharp. Velocities for $\xi > 1.0$ are consequently overestimated. Consistent with this, the velocity decay rate is underestimated in all cases save case IV. (In this case, the growth rate is underestimated and as indicated above, correction of this would give a more accurate prediction of velocity decay rate than in any of the other cases). This trend in the profiles of \bar{U}/\bar{U}_m is naturally linked to those of \bar{V}/\bar{U}_m . Since $\partial\bar{U}/\partial x$ is underestimated, negative $\partial\bar{V}/\partial y$ is also; hence \bar{V}/\bar{U}_m is consistently predicted lower than the experimental data. This problem is not directly linked to the modeling of the shear stresses and therefore neither the mixing length calculation as the shear stress profiles are well predicted particularly in the region of the mean velocity maxima.

§ 6.1.3 refers to a high lateral convection modification in the calculation procedure, made necessary for reasons of stability under such circumstances, e.g. high entrainment. It depends on the relative sizes of the component terms (viz: diffusion and convection) of the A_1 and B_1 constants in the finite difference approximation to the x-momentum equation (6.28). For computational efficiency, the modification is approximated, in which case A_1 and B_1 are low estimates of their 'true' values, and generally the diffusion part of these constants is neglected. For strongly sheared flows such as a jet, neglect of this diffusion component causes a significant underestimation in velocity decay rate which would otherwise be greater due to the increased y-component momentum. Neglect of the diffusion component is particularly inaccurate near the wall where $\partial\bar{U}/\partial y$ is large and the node spacing small; case IV which has no wall, therefore fares better. Spalding (1977 p. 73) also

suggests another approximation for the high lateral convection modification which does not neglect the diffusion component but overestimates the 'true' values of A_1 and B_1 presumably with effects opposite to those described above. The 'true' values of A_1 and B_1 are exponential functions of the diffusion and convection rates. The end result therefore is a compromise between computation time and quality of prediction. However, the inaccuracies caused by the neglect of y-direction diffusion are bad enough for the 'true' values of A_1 and B_1 to be used.

8.3.3 The Pressure Calculation and Stability

Both the stability and convergence of the calculation method depend on the successful calculation of the static pressure. Figure 8.26 shows predictions of wall static pressure. Agreement with the experimental data, figure 5.3, is satisfactory except near the slot where predictions are rather high. These predictions of wall static pressure are indicative of the rest of the pressure field. For case VIII, the prediction oscillates from step to step and at $\theta = 20^\circ$ and 30° , these oscillations are too large to fit onto the plot. This calculation required ten iterations to converge and despite the use of upwind differences in the streamwise direction (unconditionally stable), nearly failed to converge within the required limits. The effects of pressure are allowed to propagate upstream at the rate of one step per sweep as in a fully elliptic procedure. Therefore it is not expected that instability is caused by inconsistencies in the solution algorithm. However, the y-component momentum equation (6.10) used in the calculation contains a normal stress term which under the conditions of these test cases is significant. But the normal stresses are only modelled by proportionality to the shear stresses, which do not always show a consistent trend. Thus the potential instability observed in case VIII

appears to be caused by the imprecise nature of the modelling of the normal stresses.

At the time of writing, the three major inadequacies of the calculation method had not been corrected. However, with more work, it can provide the basic numerical procedure required for advanced turbulence modelling in strongly distorted shear layers.

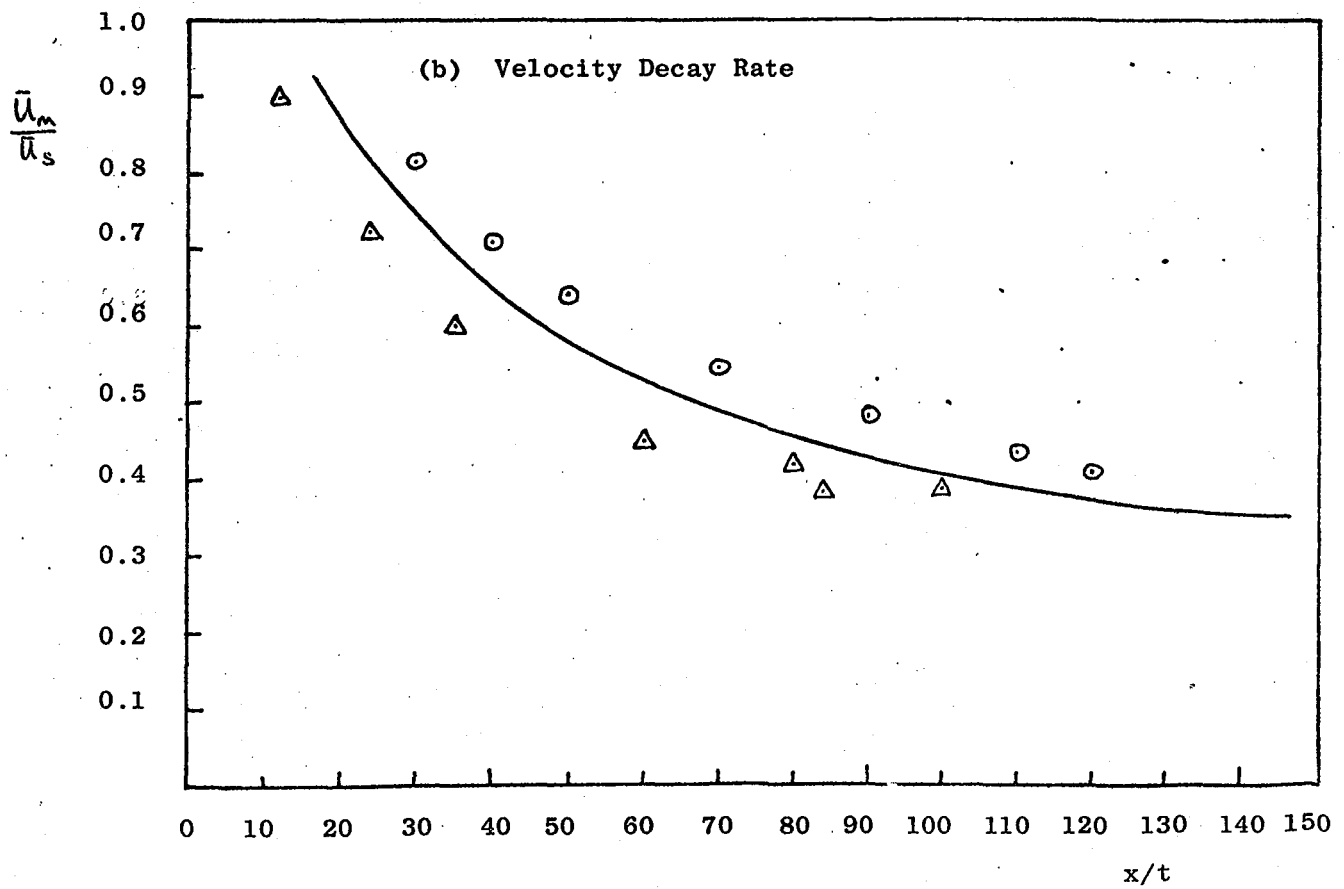
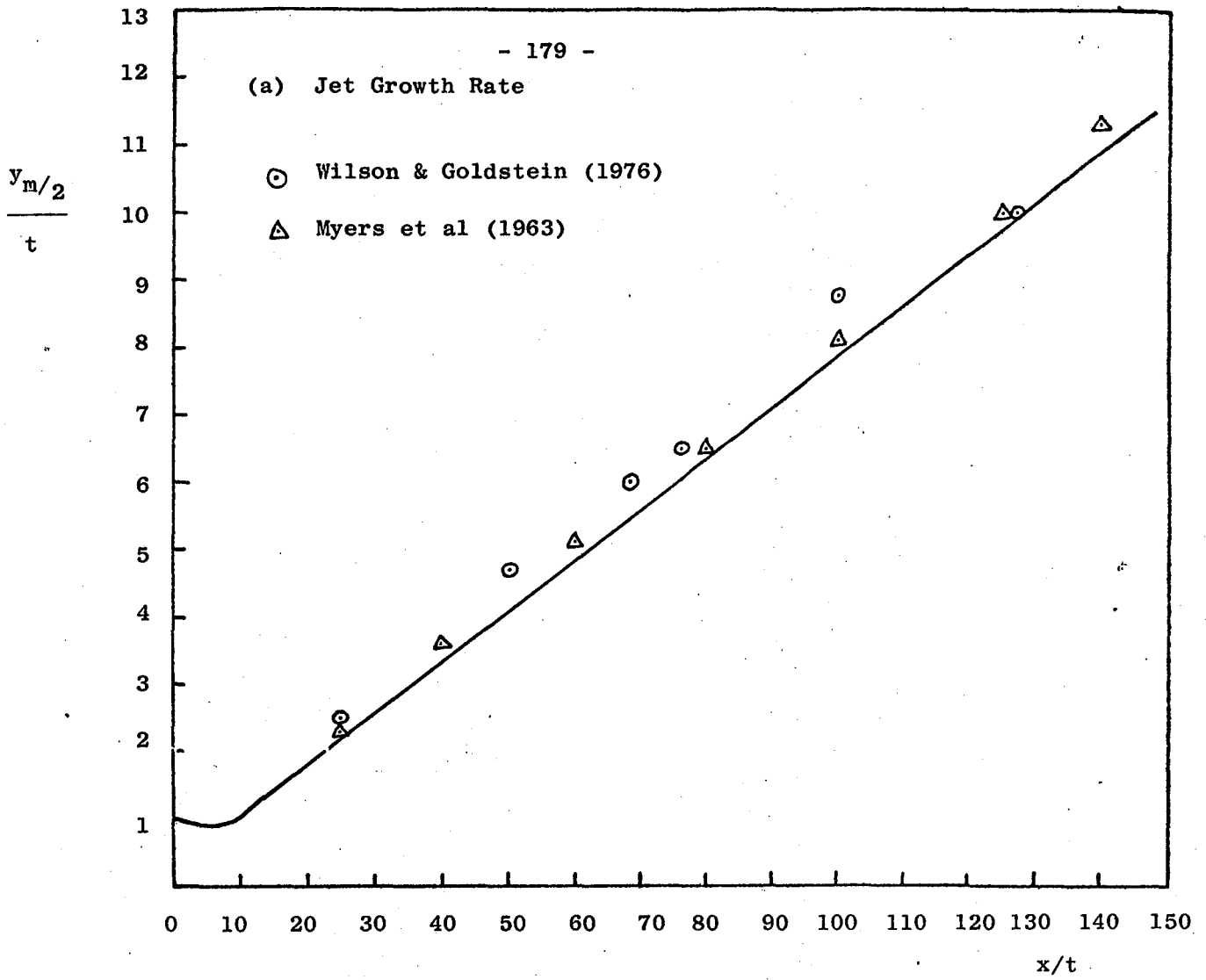


FIG. 8.1 Case I: Growth/Velocity Decay Rate

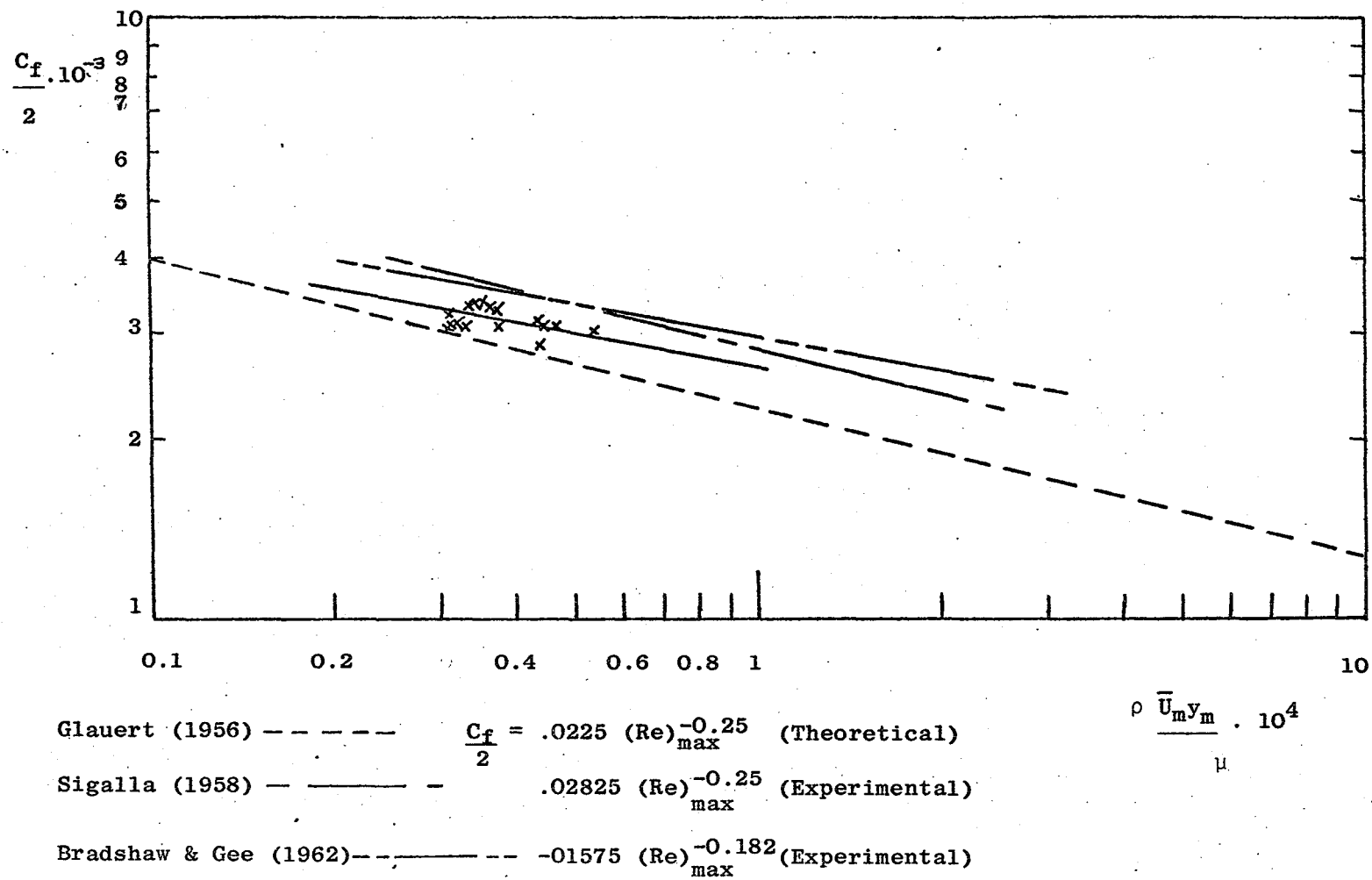


FIG. 8.2: CASE I: Wall Shear Stress

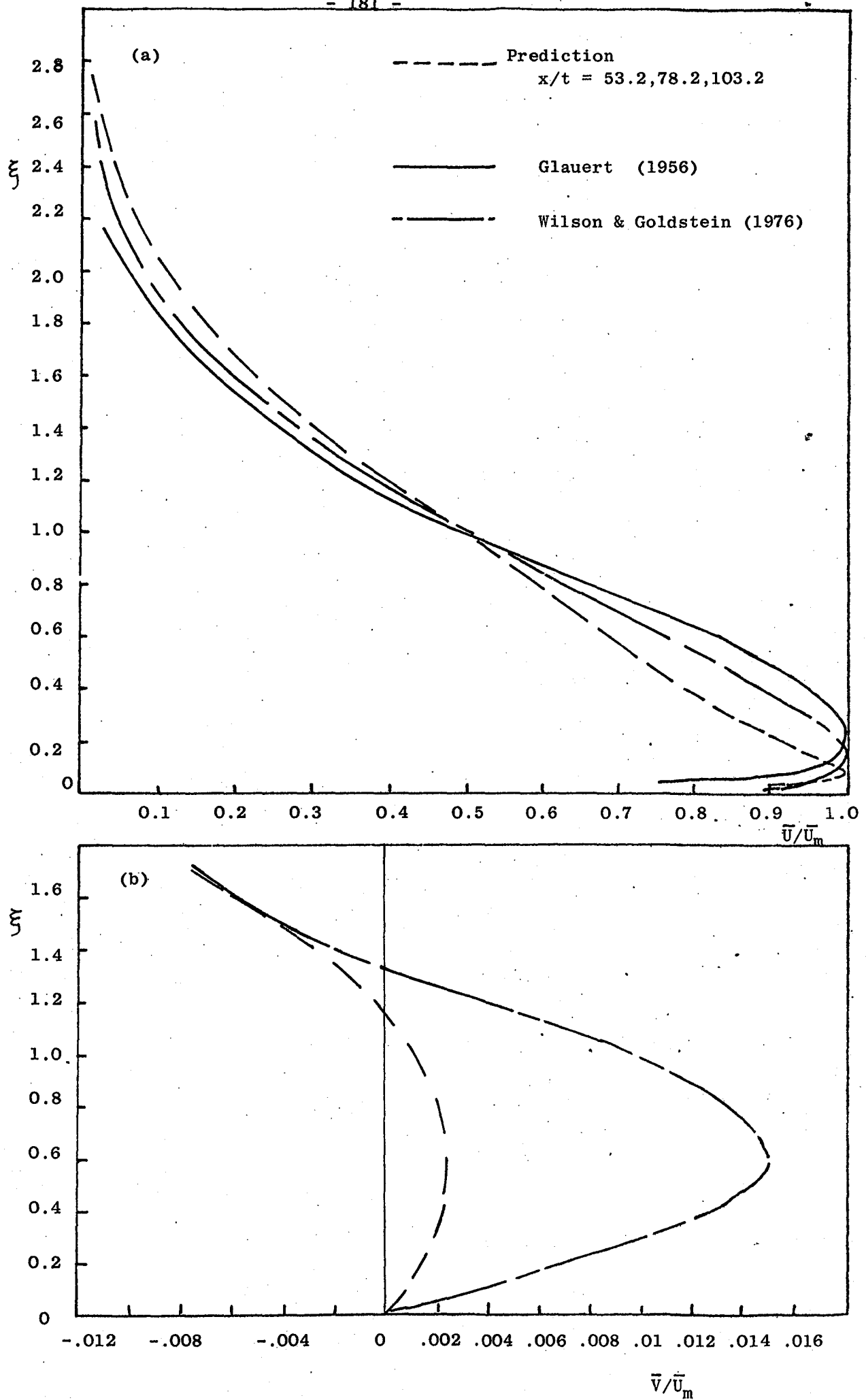


Fig. 8.3: CASE I: Mean Velocity Profiles

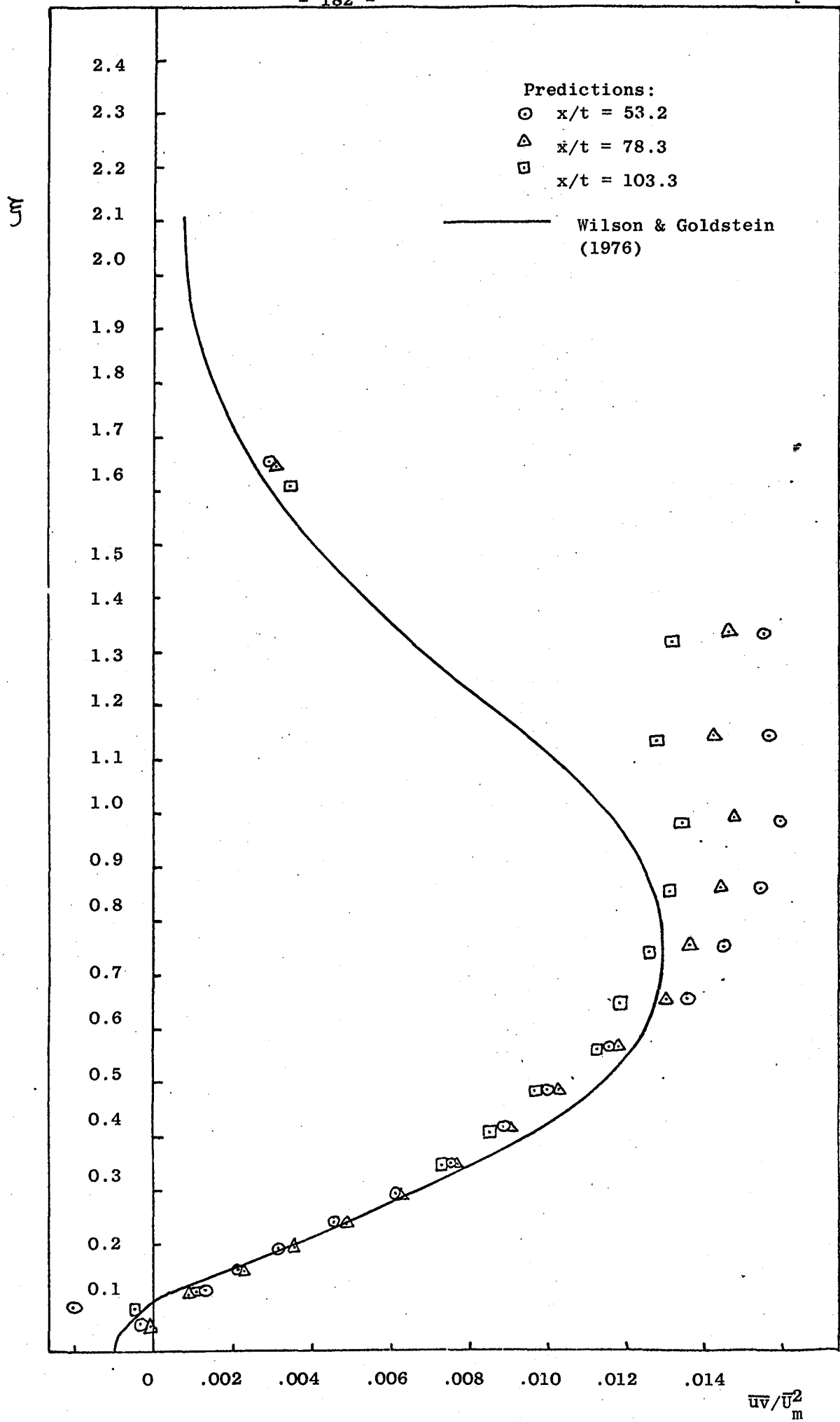


FIG. 8.4: CASE I: Shear Stress Profiles

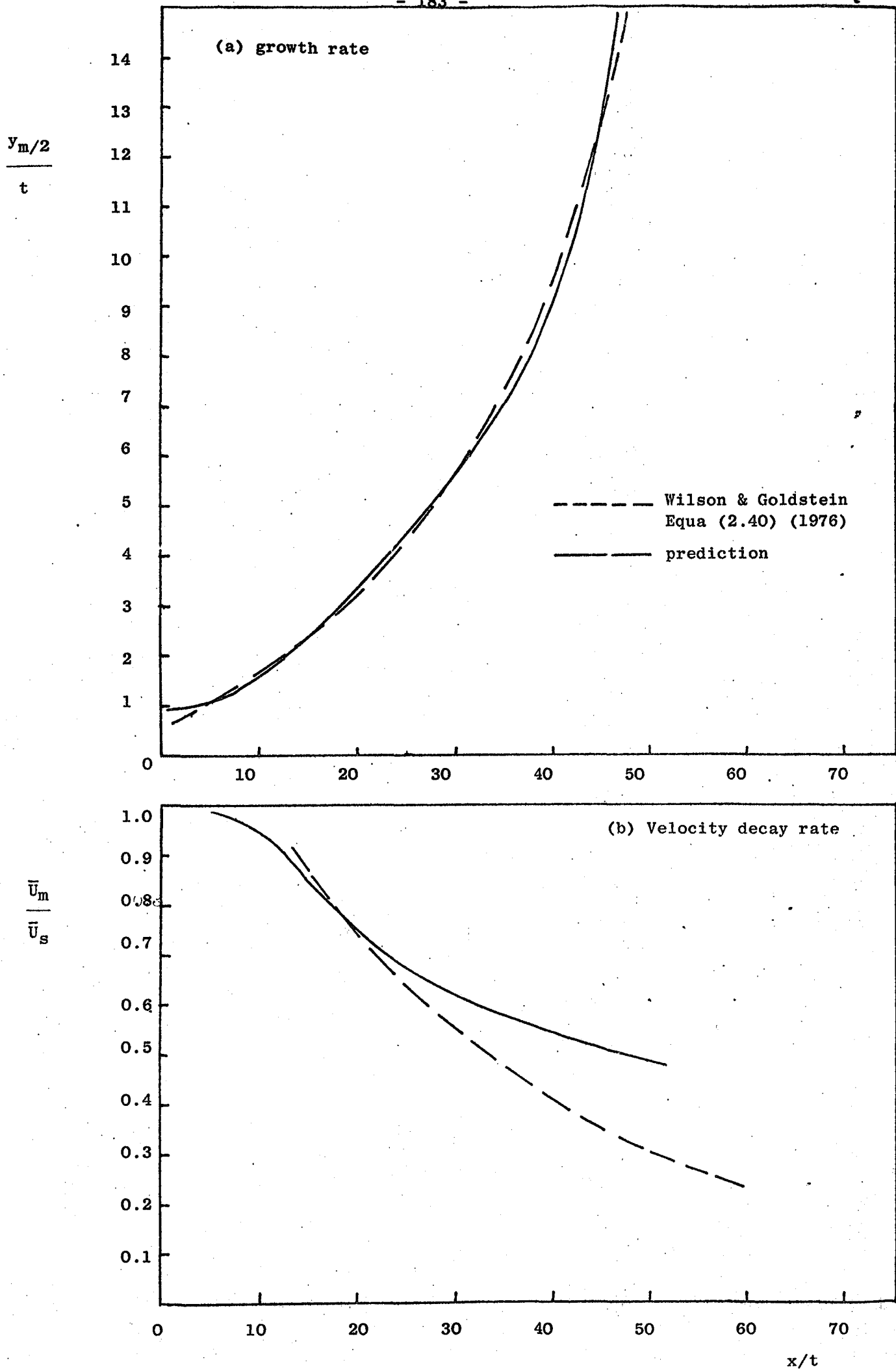


FIG. 8.5: CASE II: Growth/Velocity Decay Rate

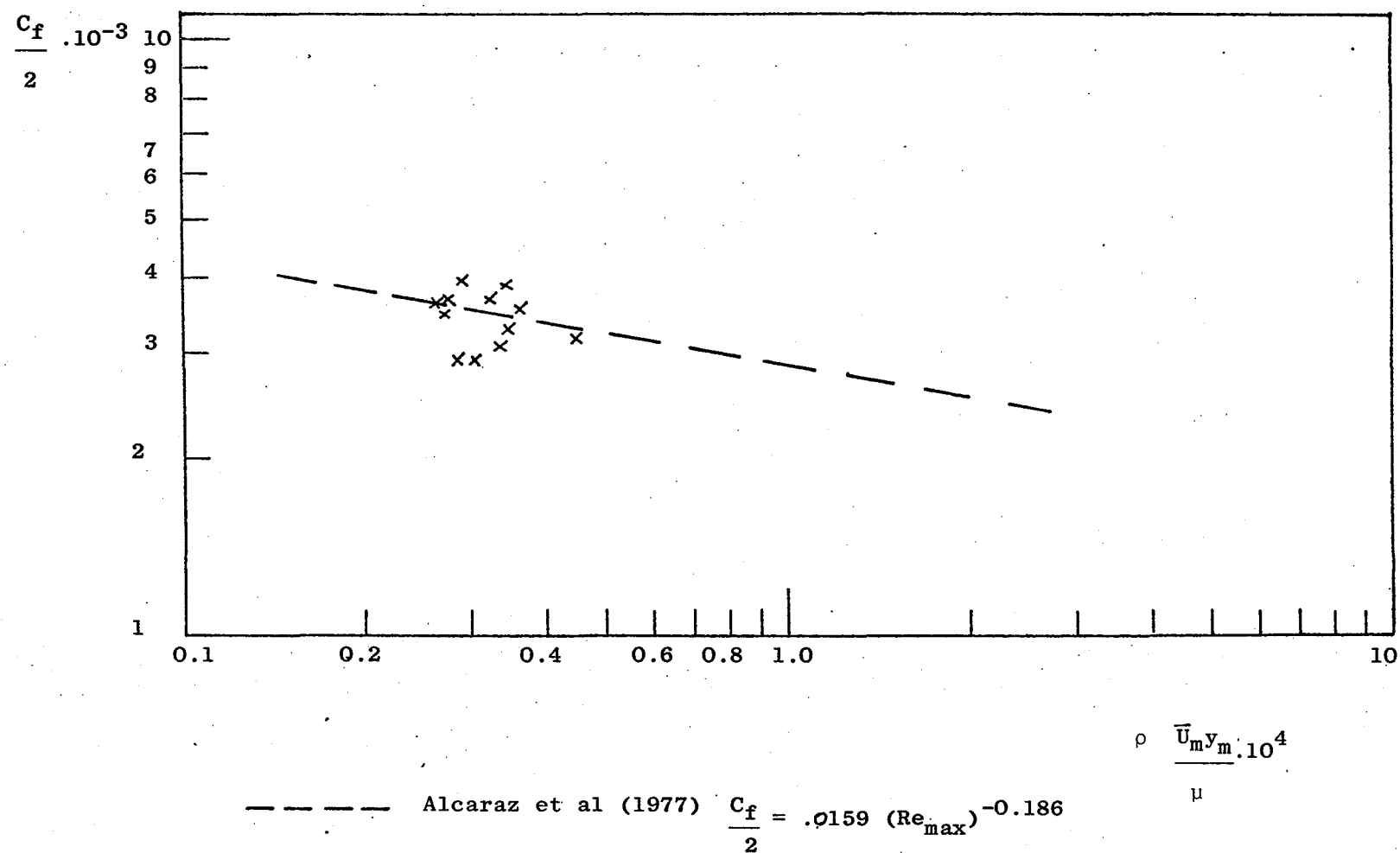


FIG. 8.6: CASE II: Wall Shear Stress

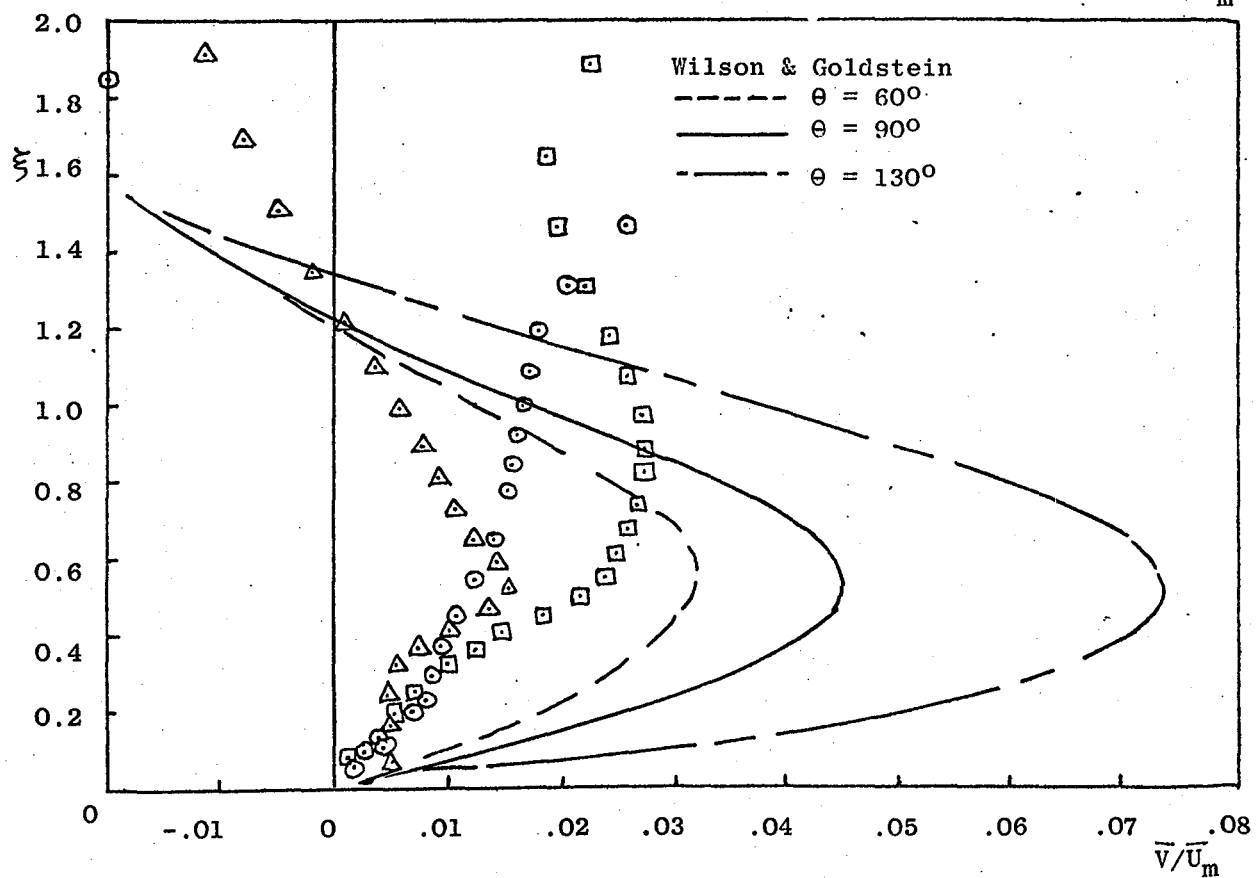
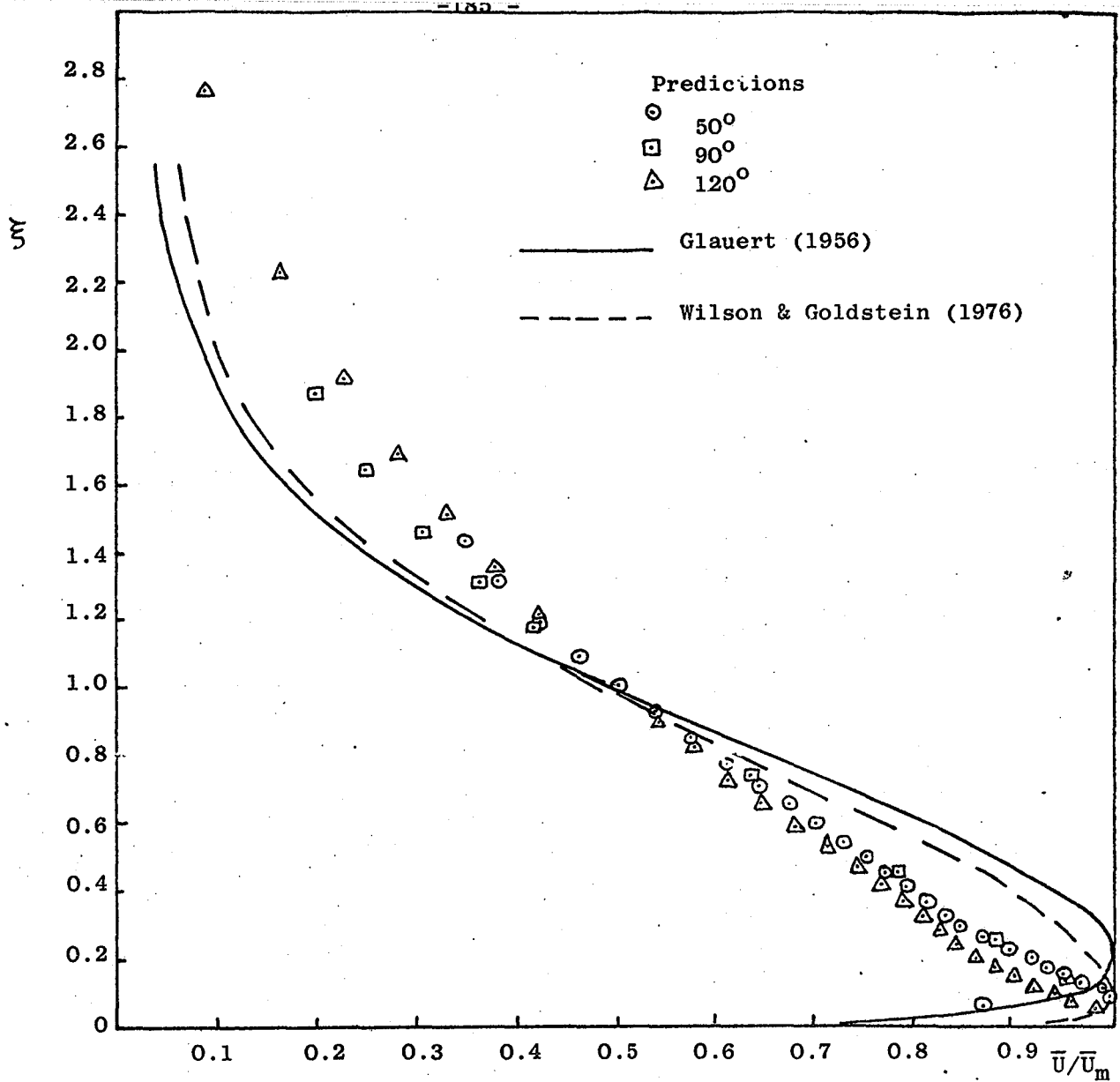


FIG. 8.7: CASE II: Mean Velocity Profiles

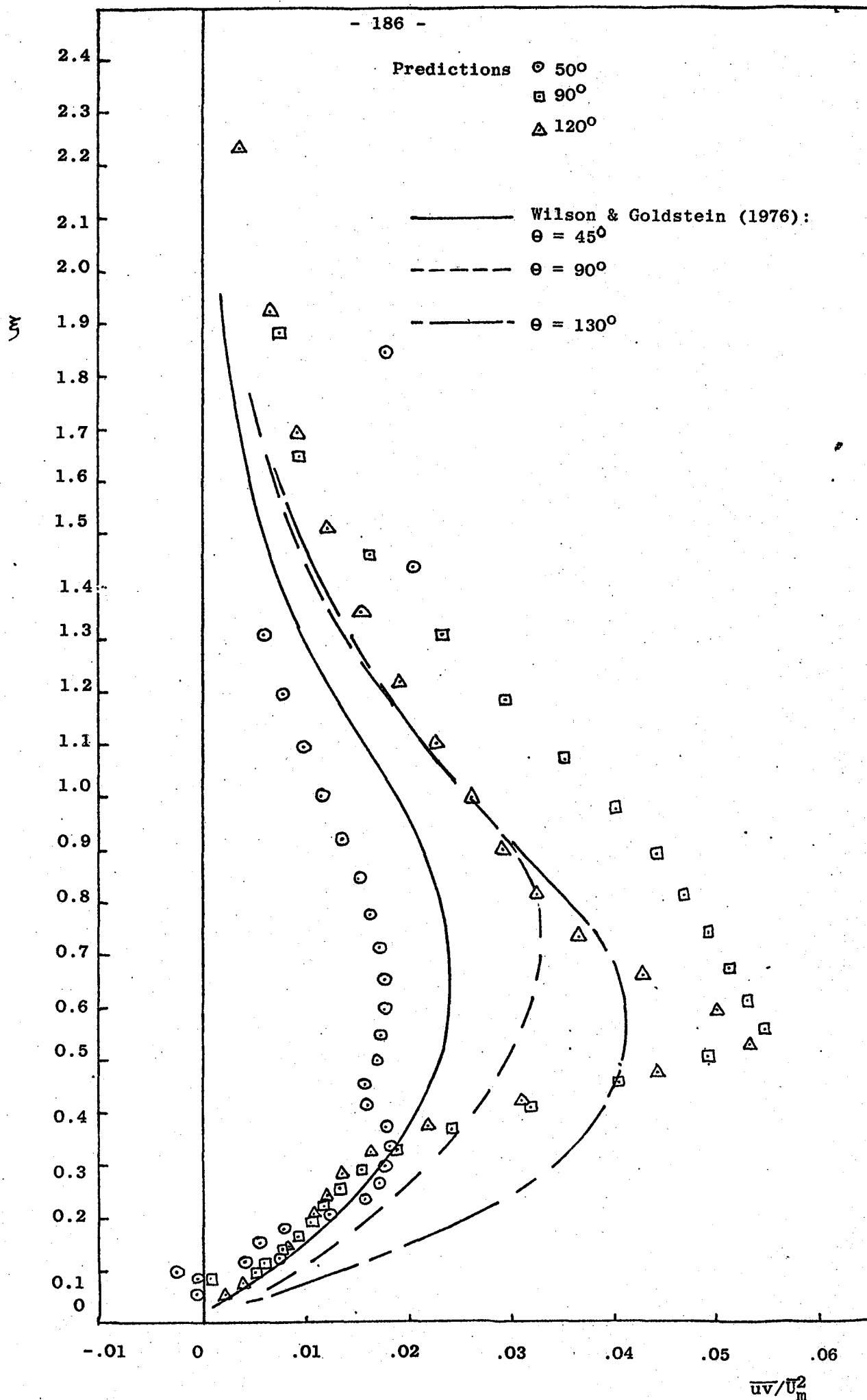


FIG. 8.8 CASE II: Shear Stress Profiles

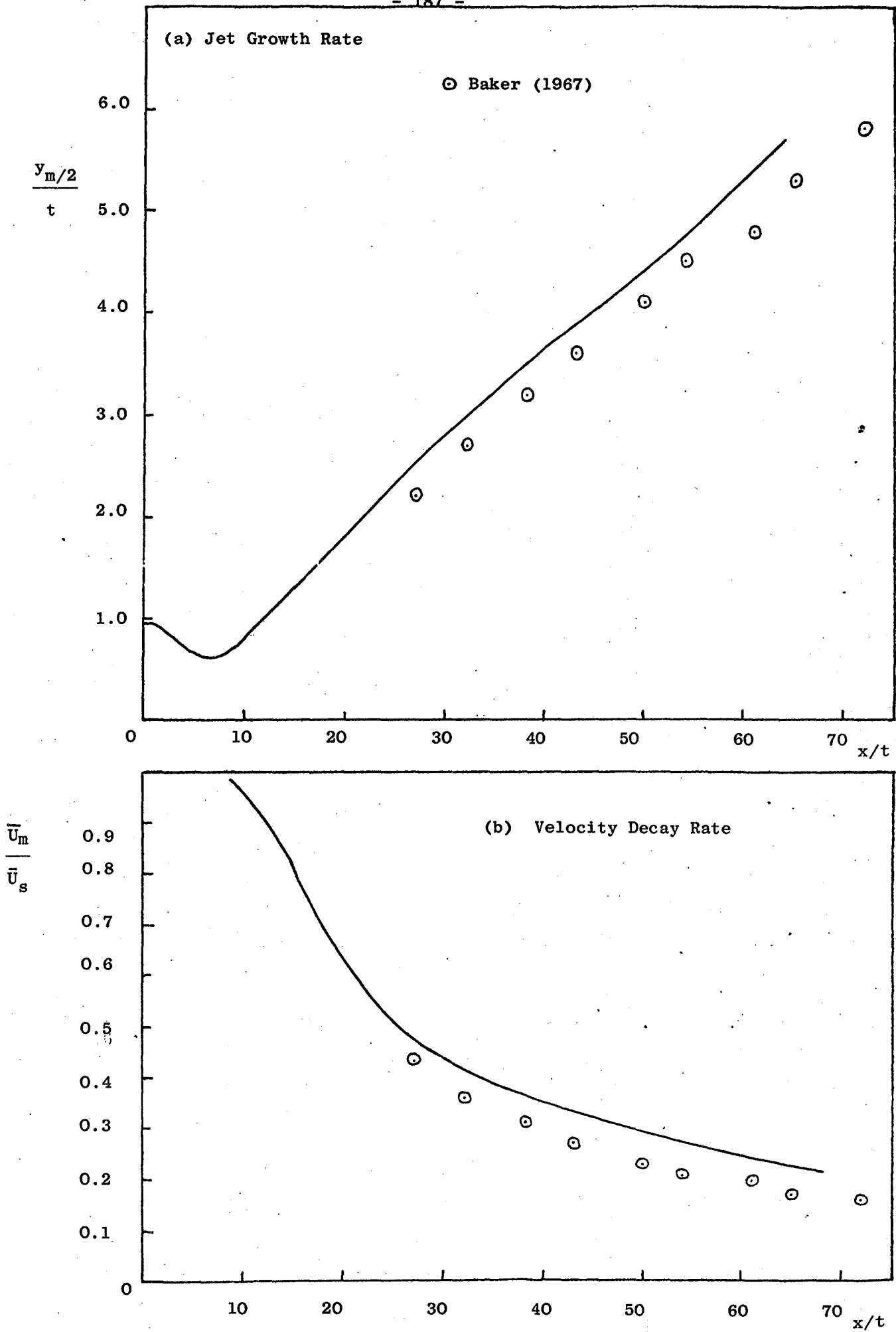


FIG. 8.9: CASE III: Growth/Velocity Decay Rate

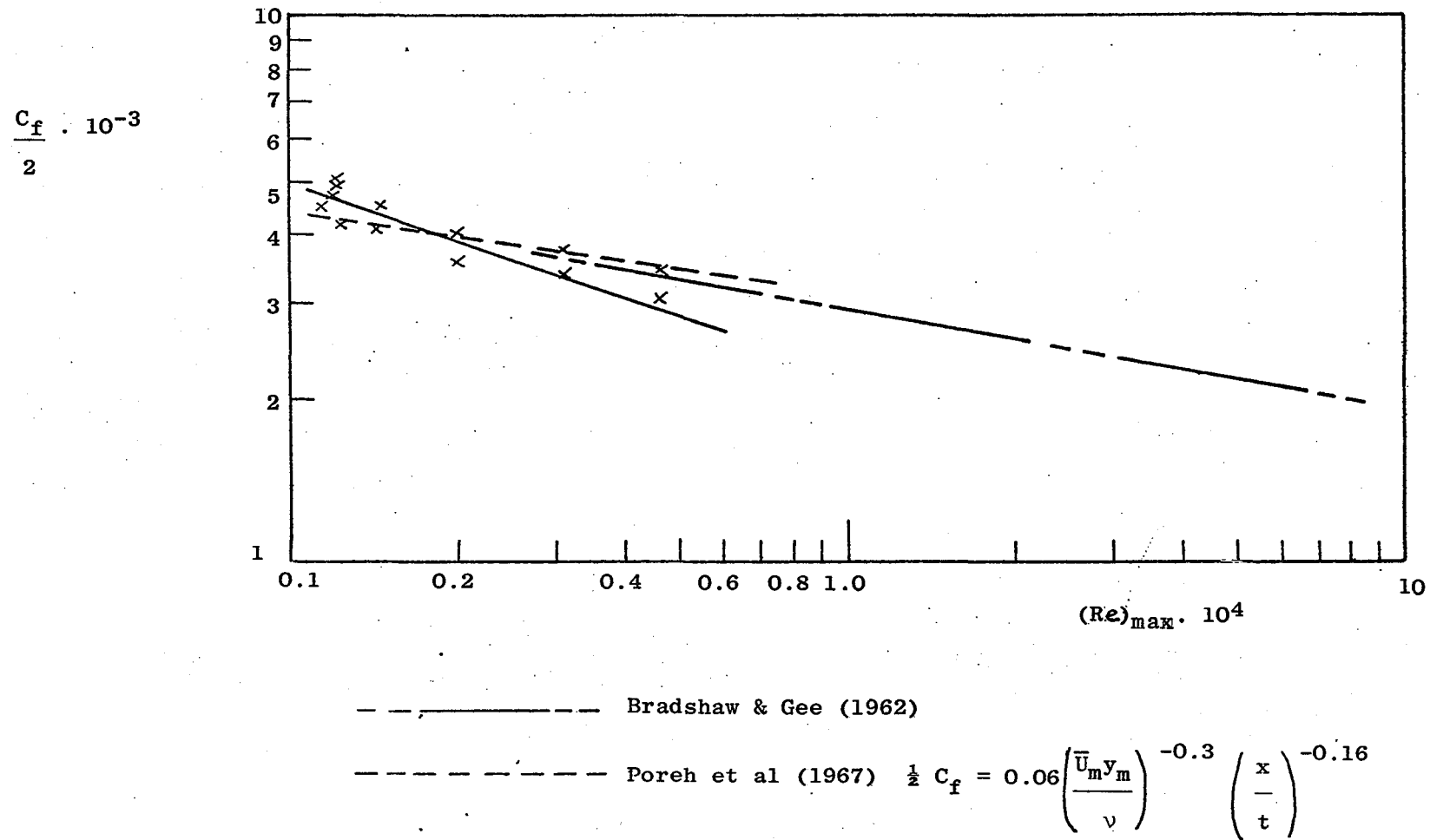


FIG. 8.10: CASE III: Wall Shear Stress

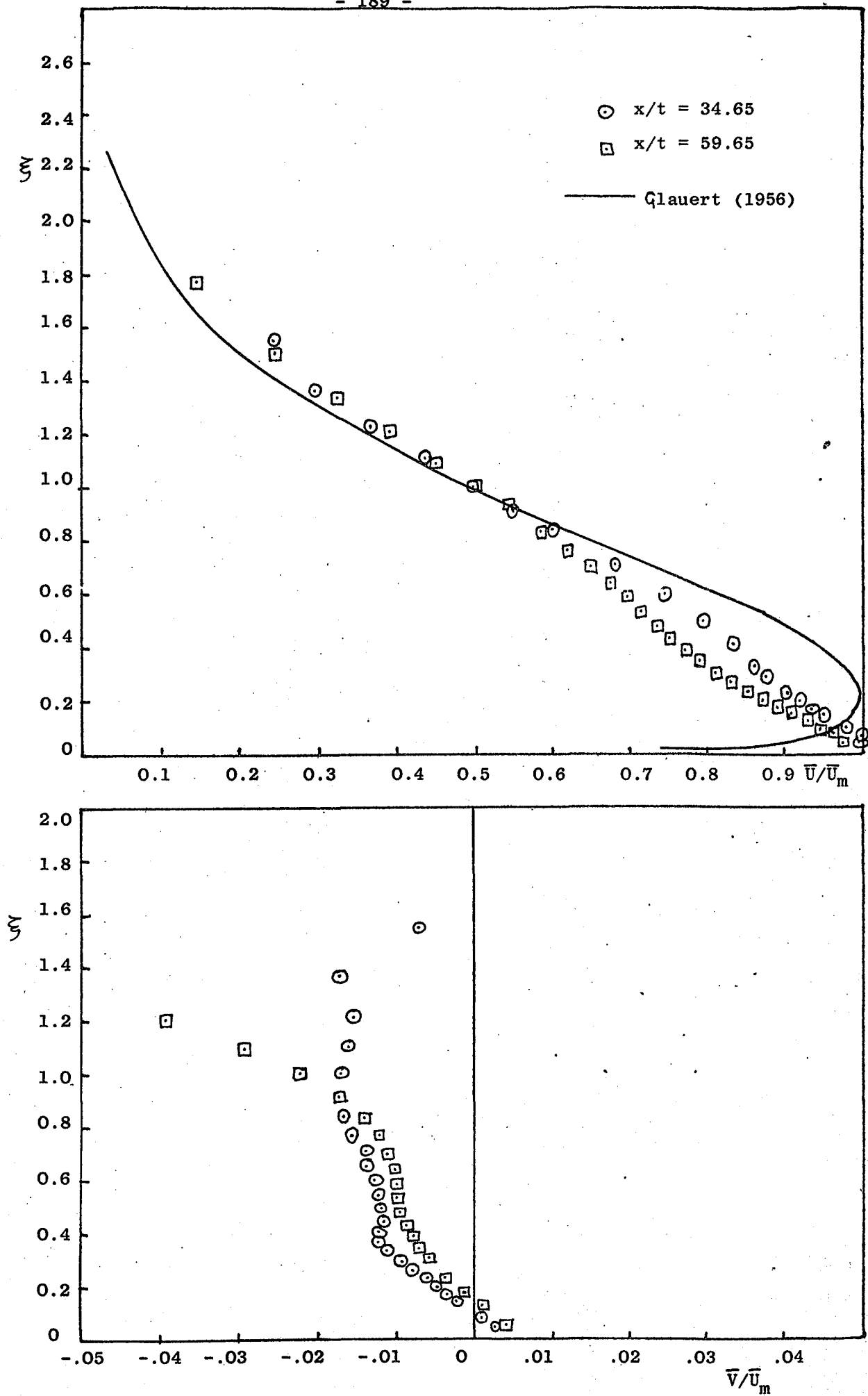


FIG. 8.11: CASE III: Mean Velocity Profiles

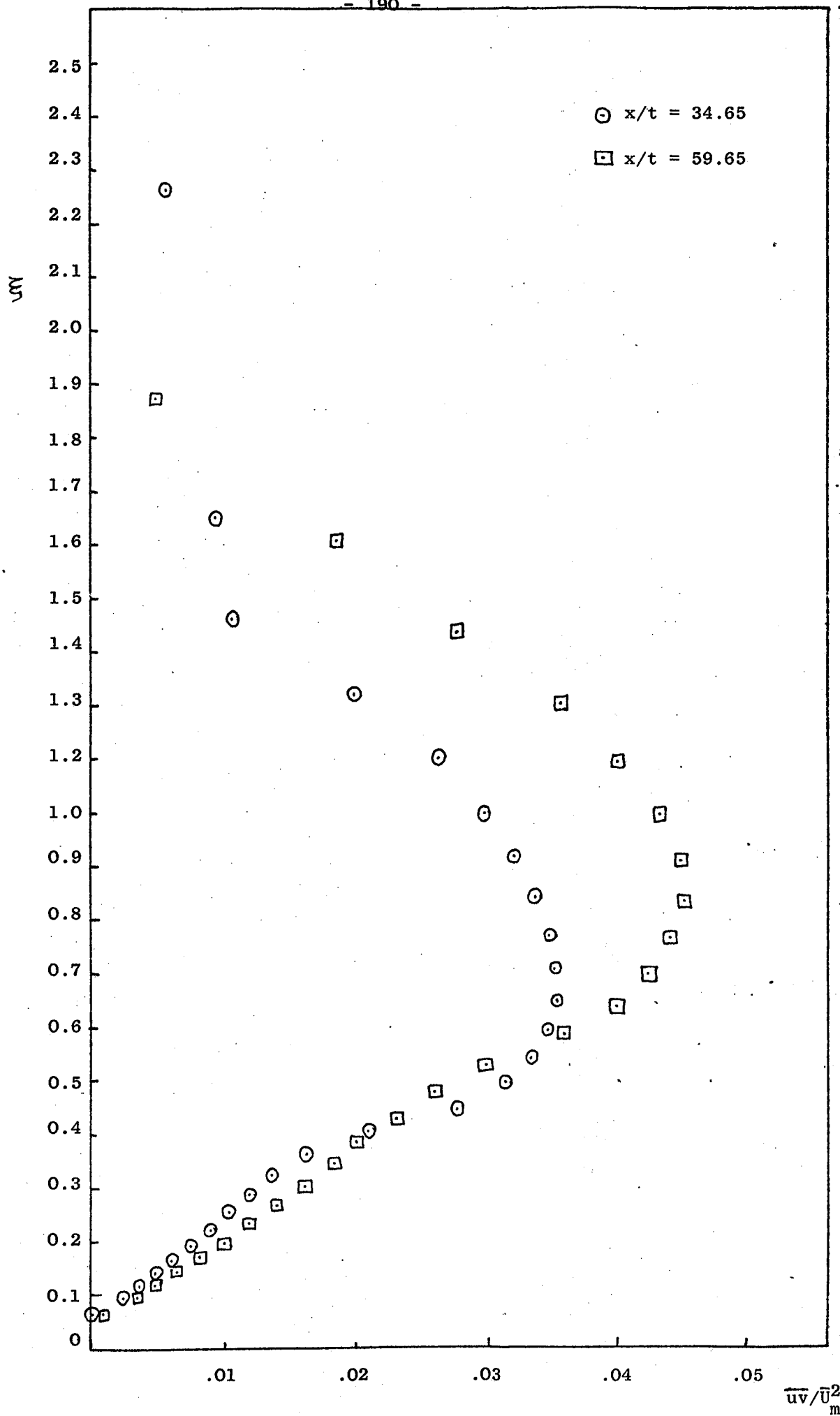


FIG. 8.12: CASE III: Shear Stress Profiles

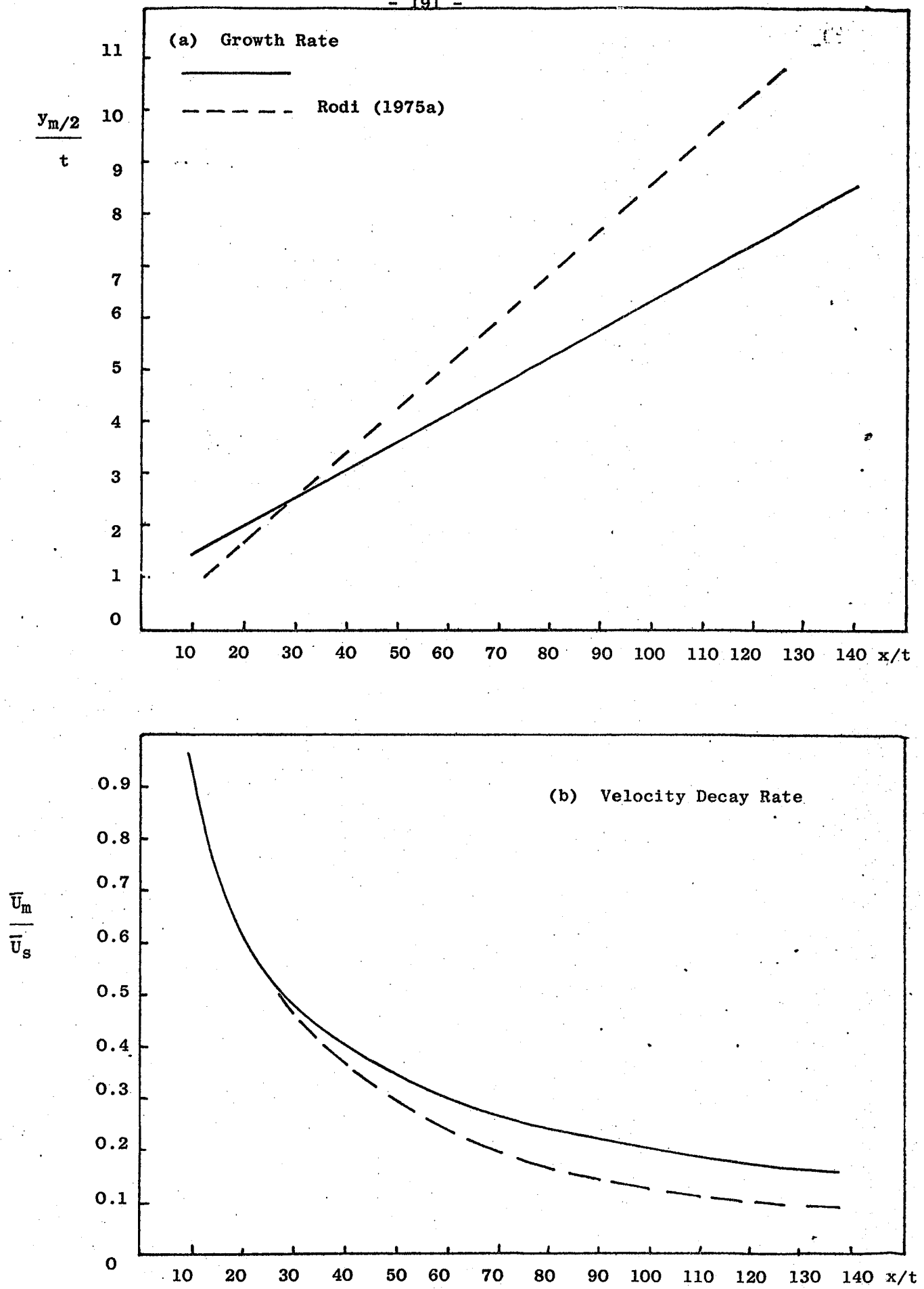


FIG. 8.13: CASE IV: Growth/Velocity Decay Rate

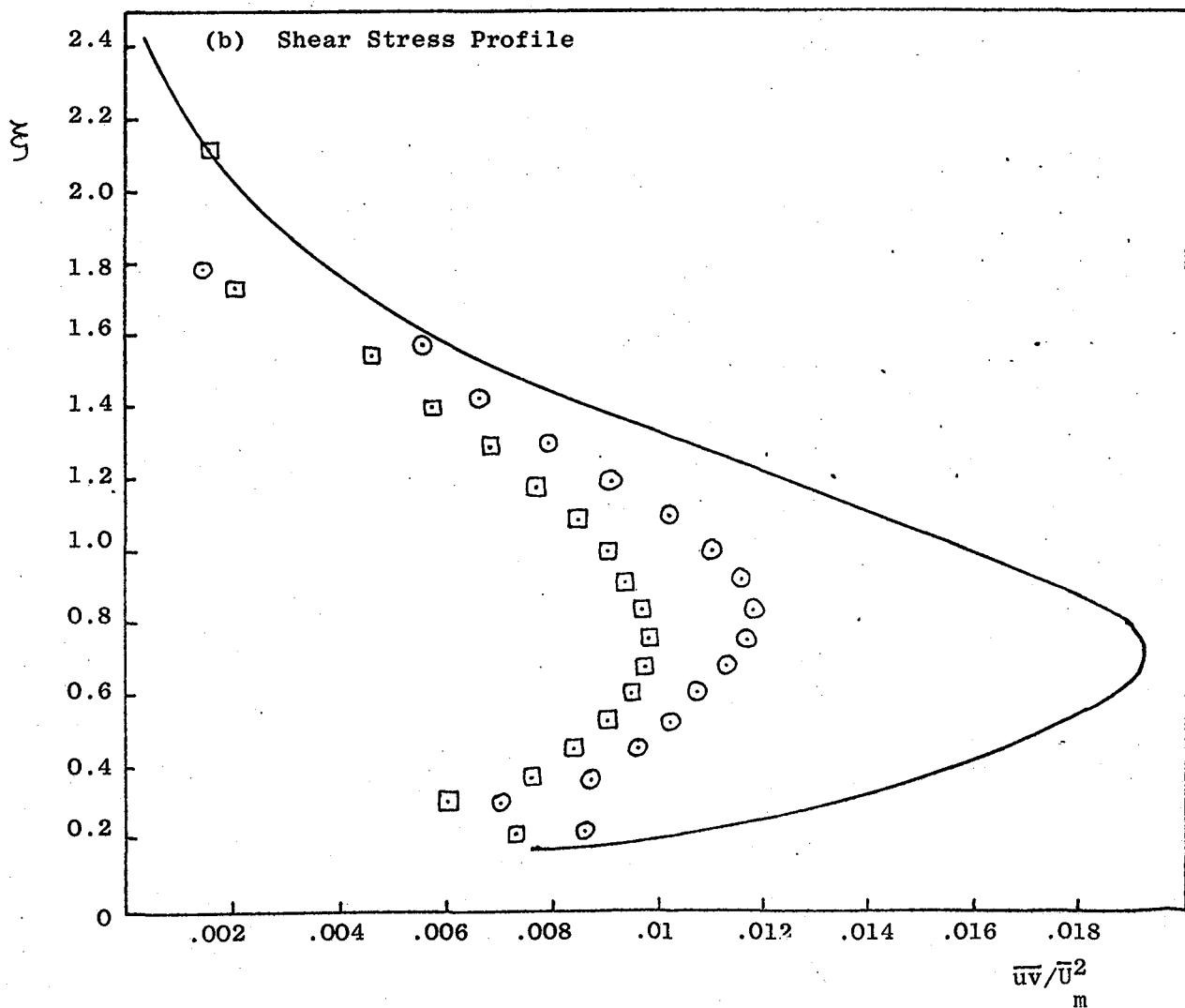
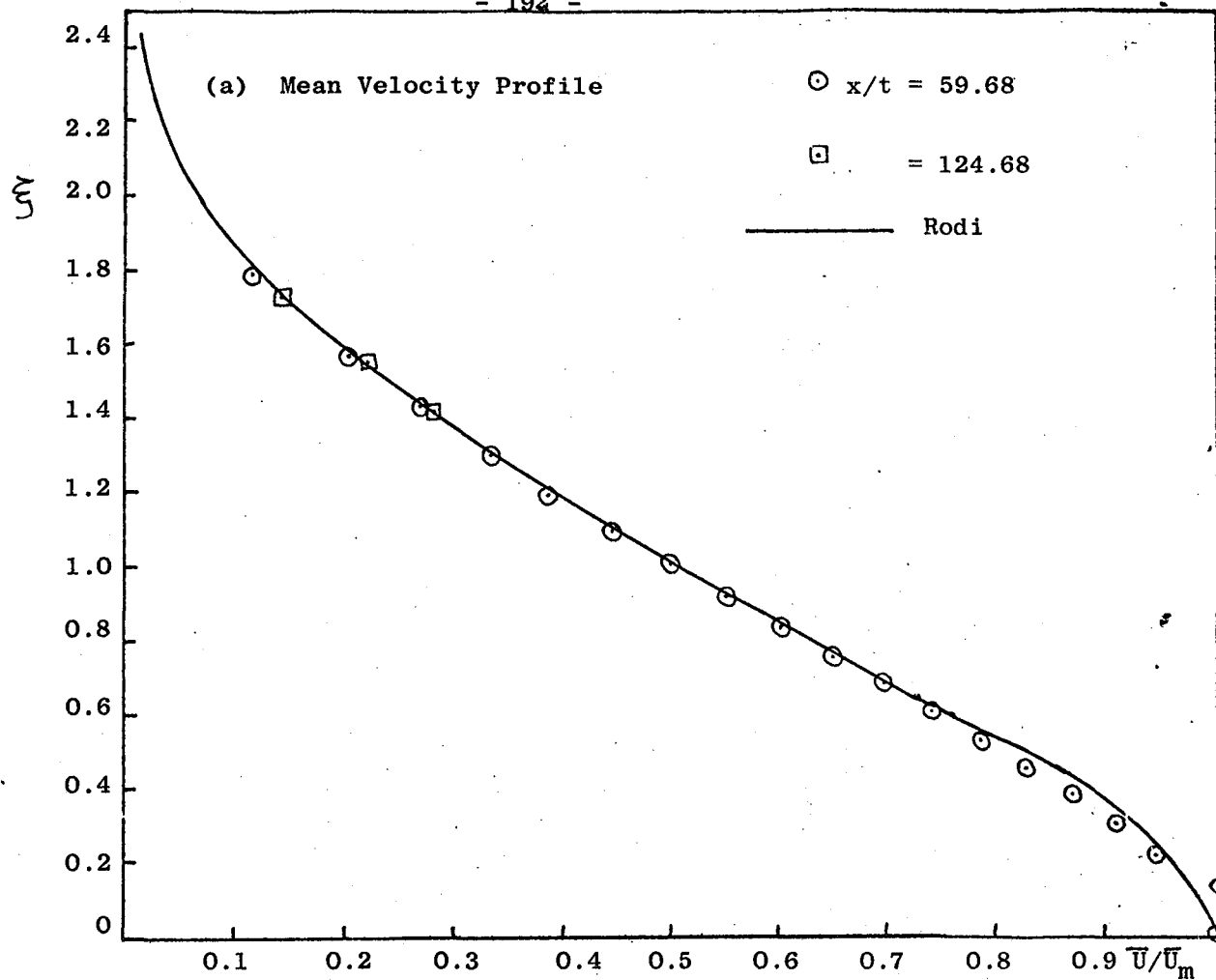


FIG. 8.14: Mean Velocity and Shear Stress Profiles

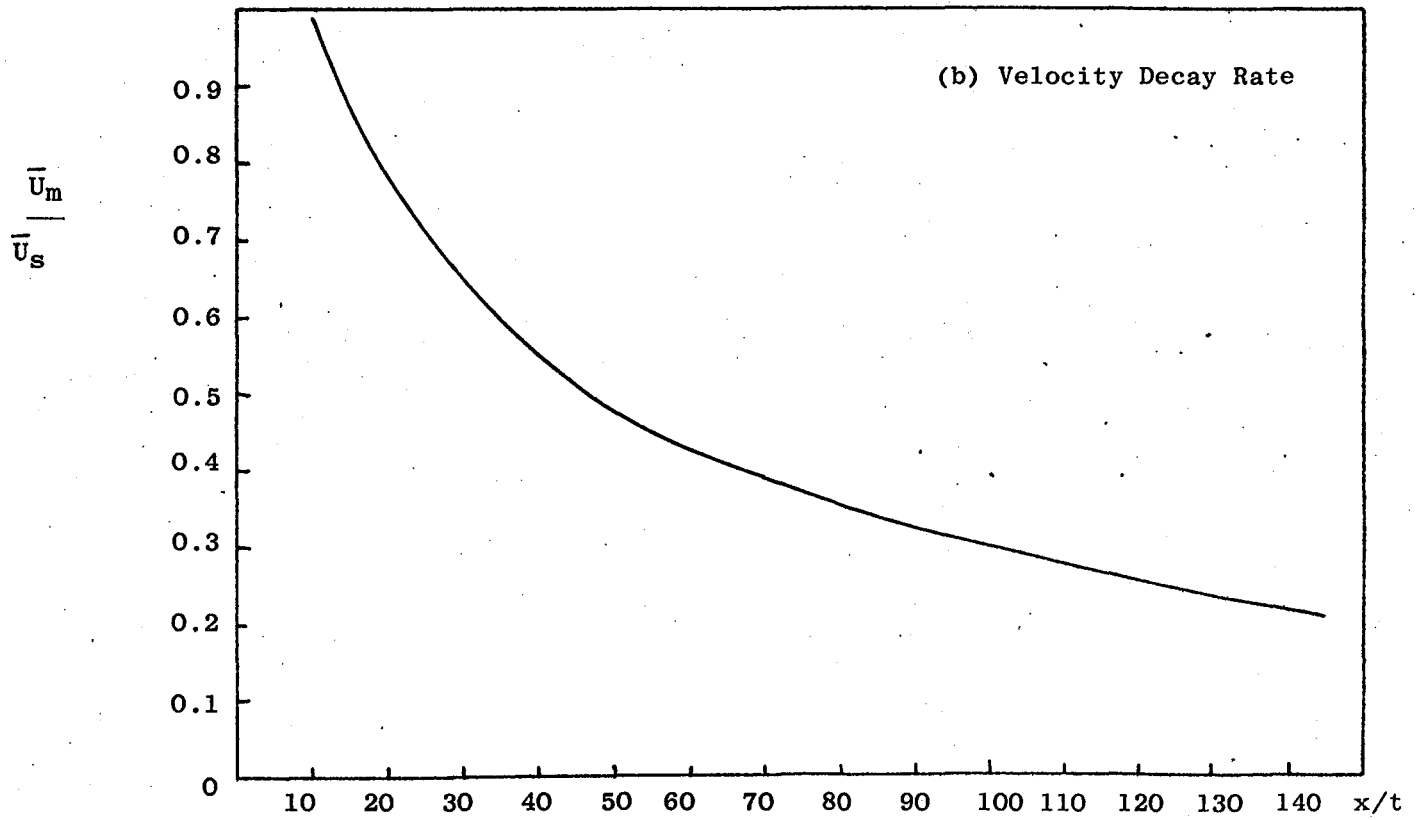
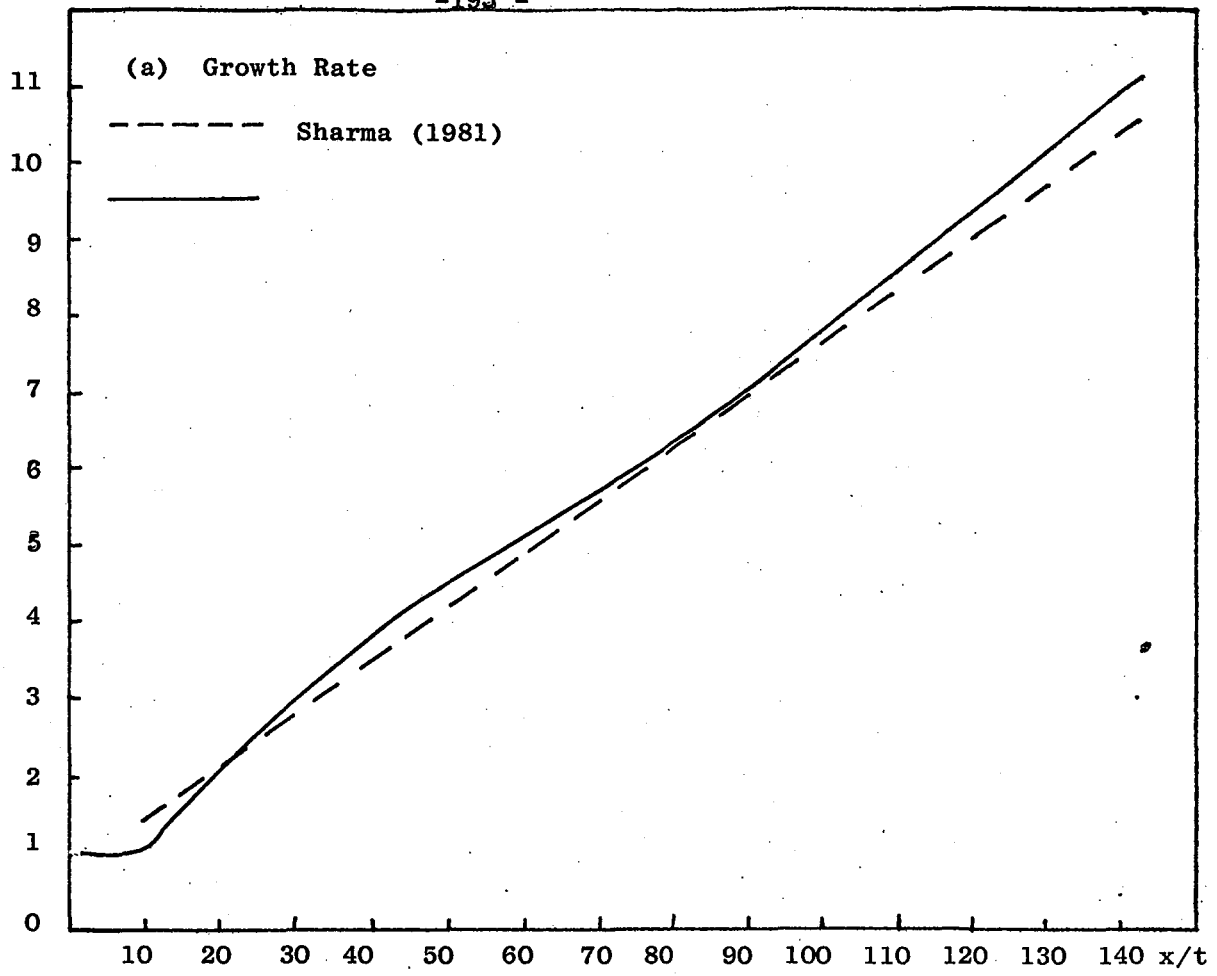


FIG. 8.15 CASE V: Growth/Velocity Decay Rate

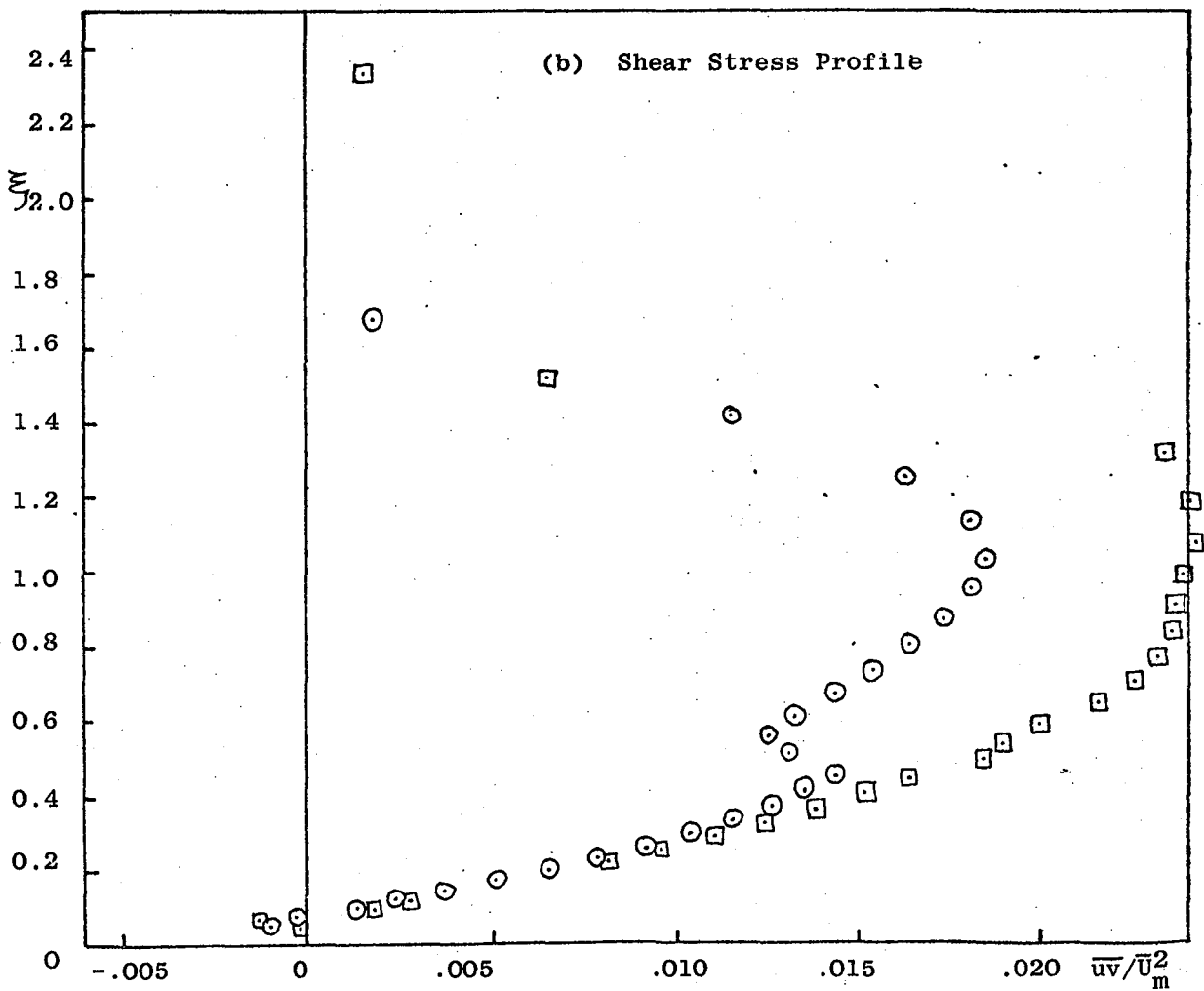
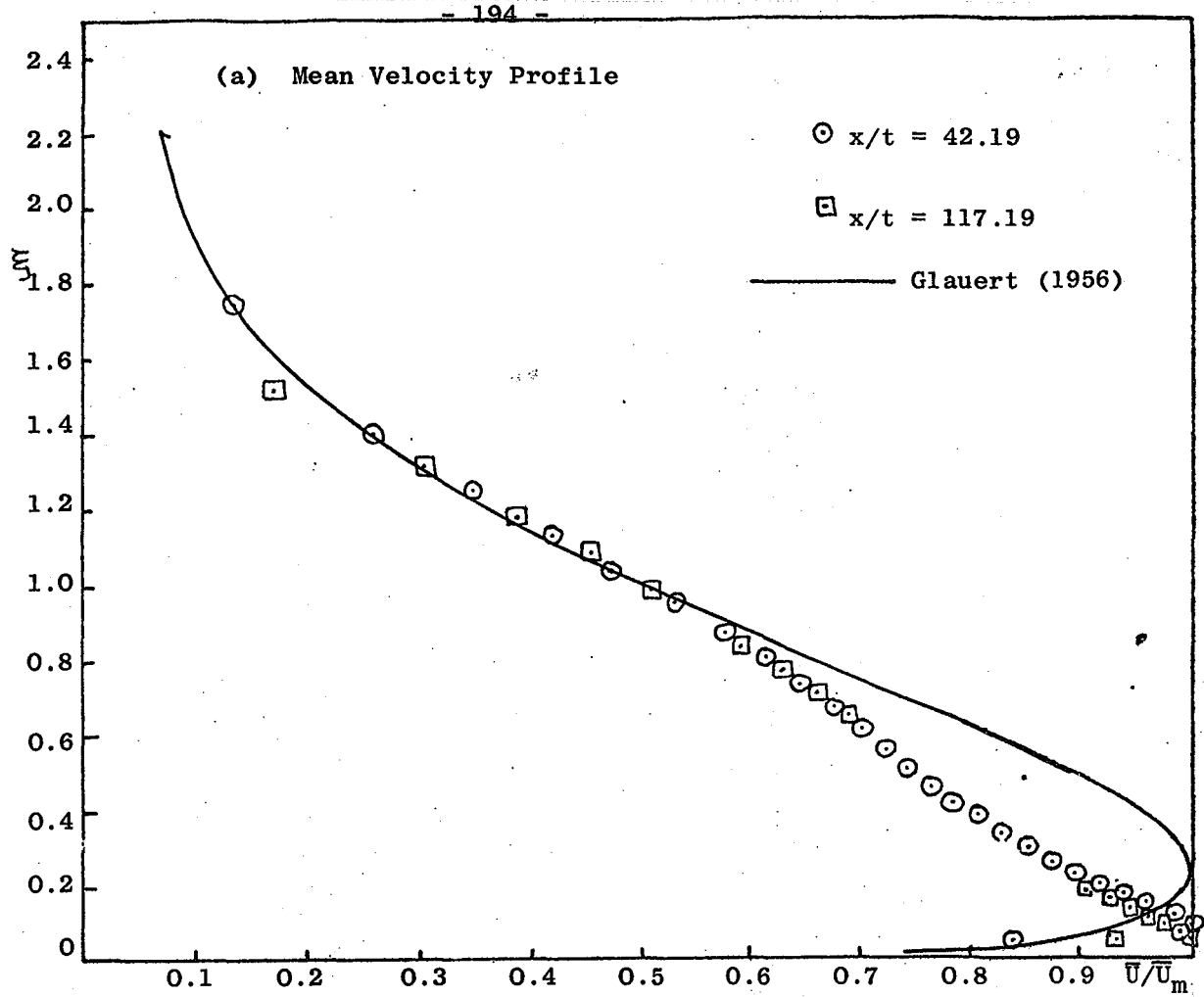


FIG. 8.16: CASE V: Mean Velocity/Shear Stress Profiles

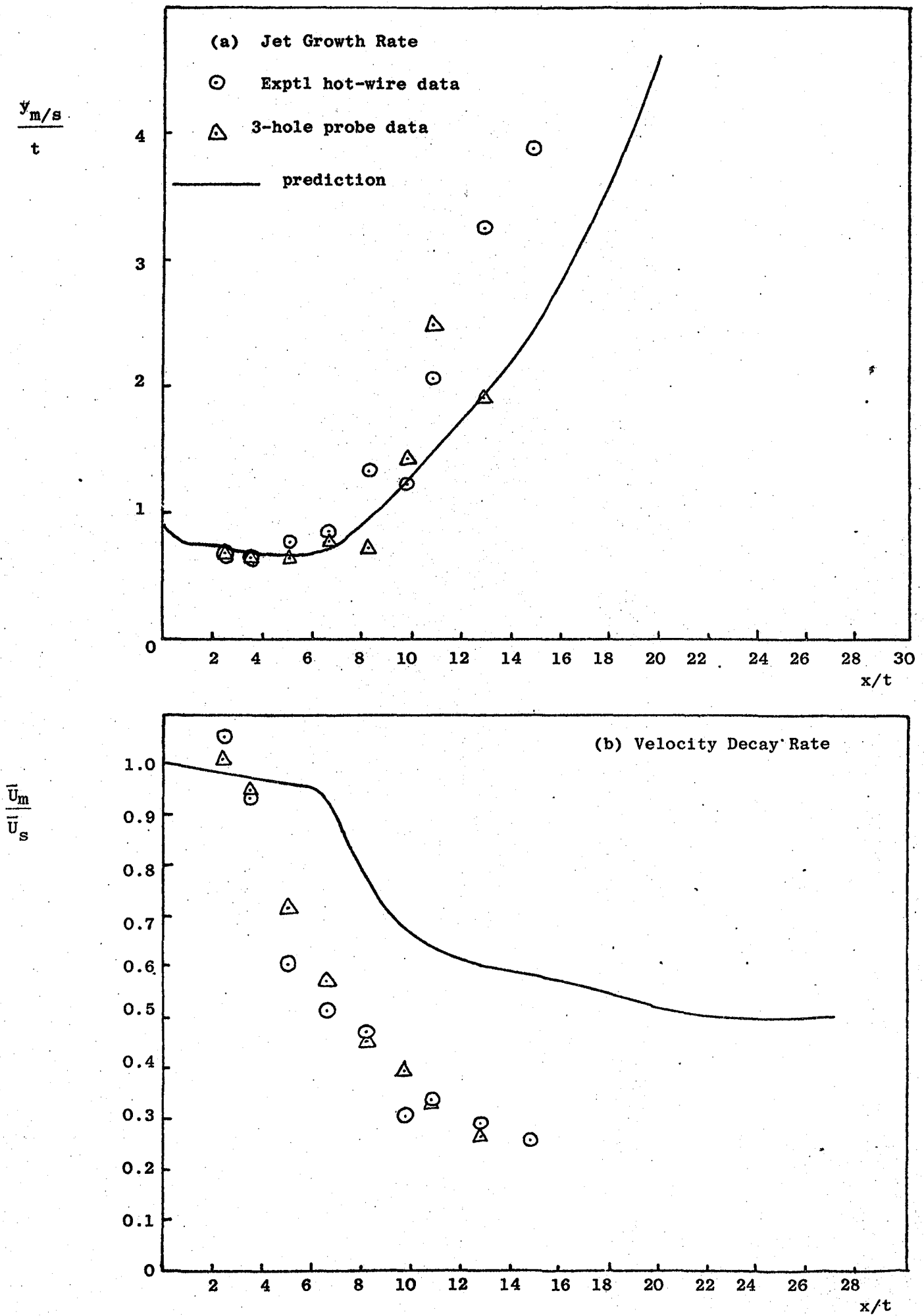
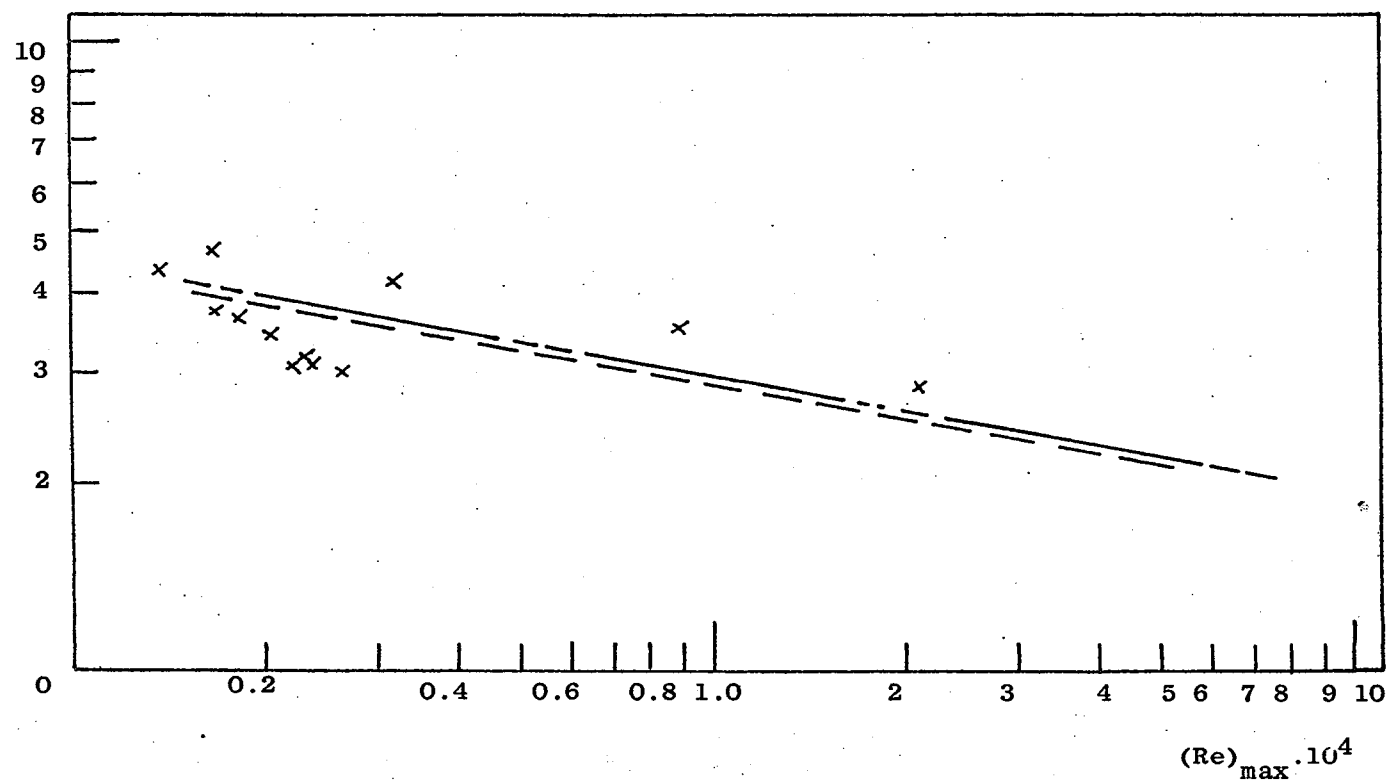


FIG. 8.17: CASE VI: Growth/Velocity Decay Rate

$$\frac{C_f}{2} \cdot 10^{-3}$$



----- Bradshaw & Gee (1960)

----- Alcaraz et al (1977)

FIG. 8.18: CASE VI: Wall Shear Stress

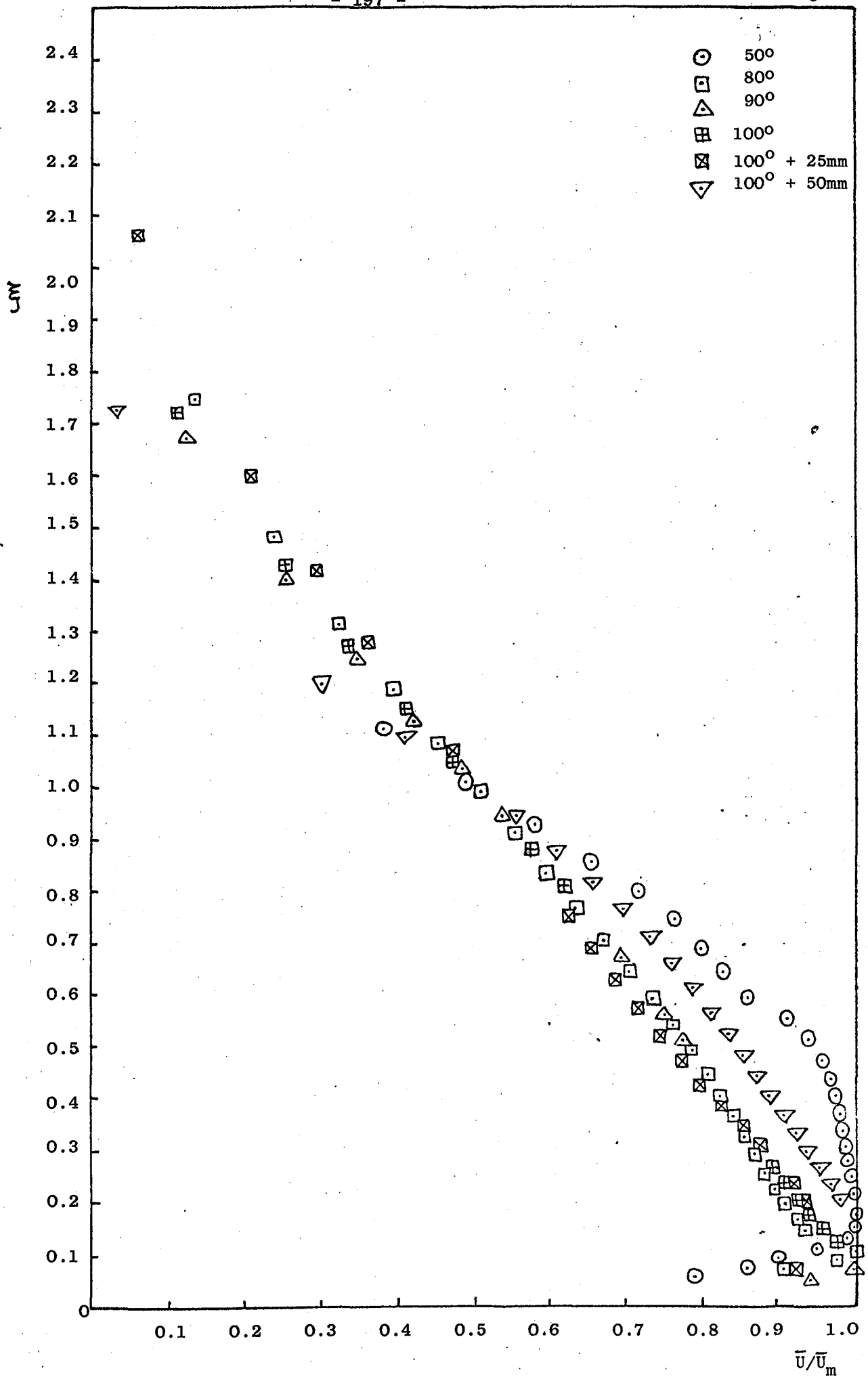


FIG. 8.19: CASE VI: Mean Velocity Profiles \bar{U}/\bar{U}_m

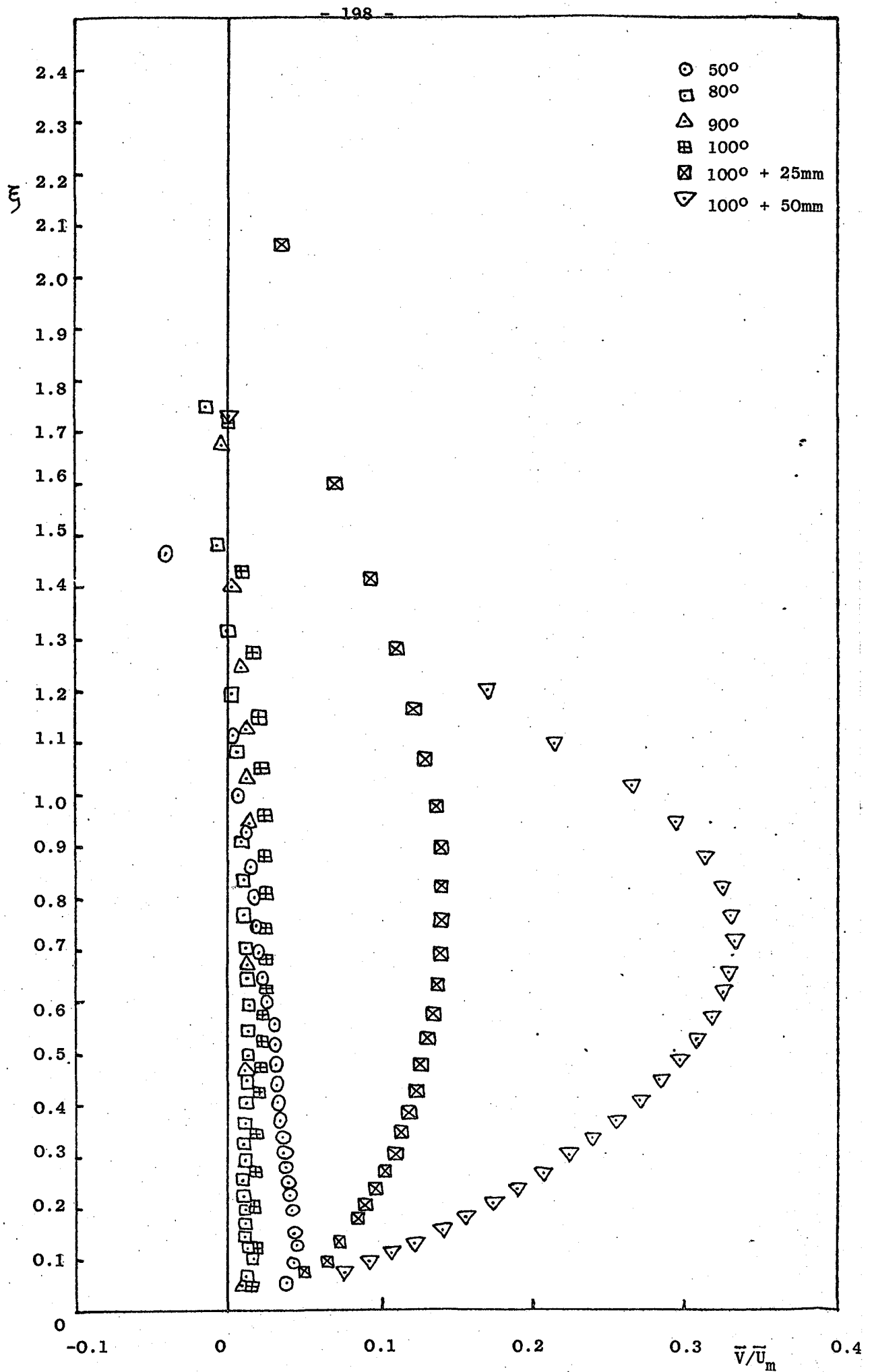


FIG. 8.20 CASE VI: Mean Velocity Profiles \bar{V}/\bar{U}_m

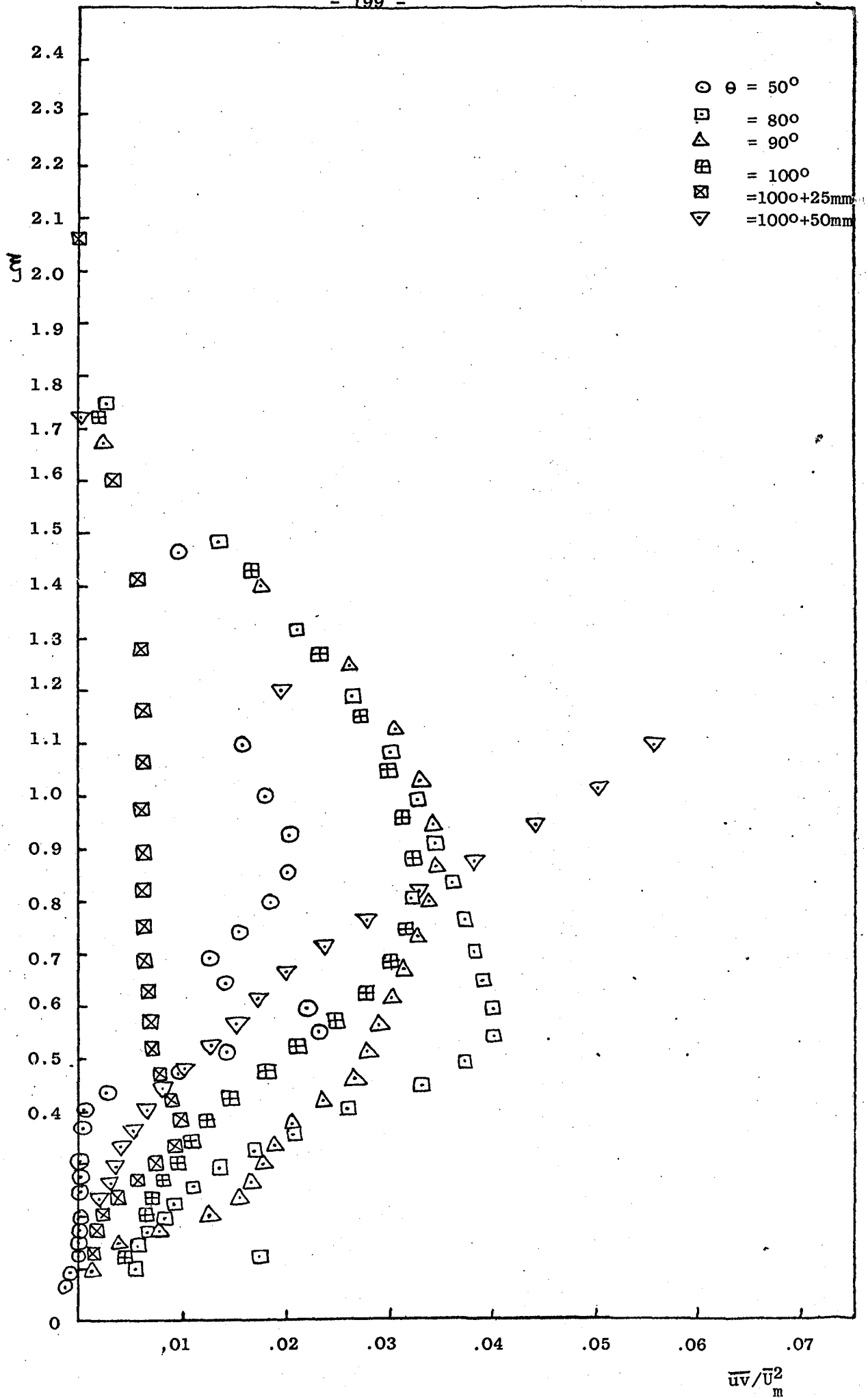


FIG. 8.21: CASE VI: Shear Stress Profiles

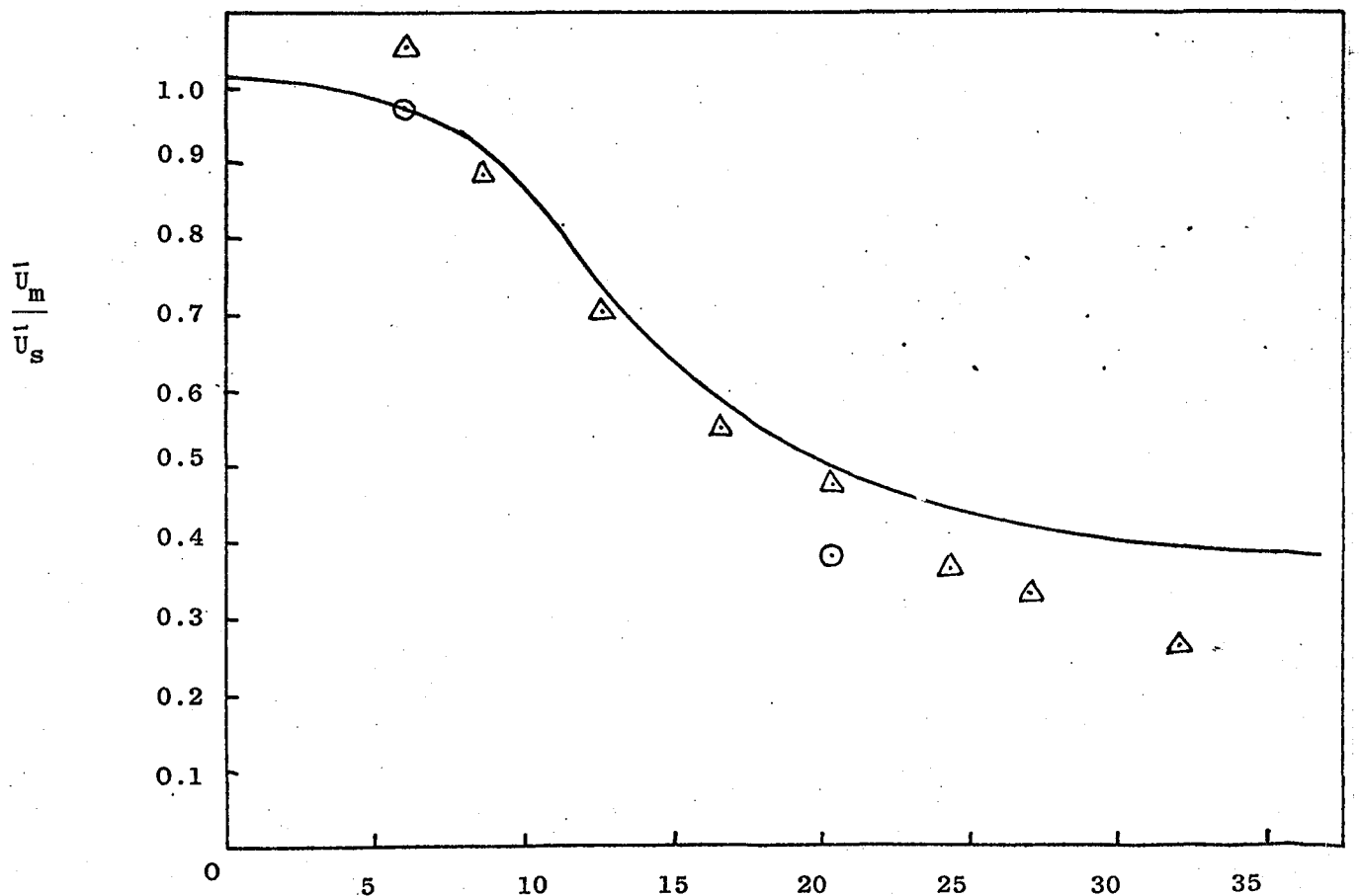
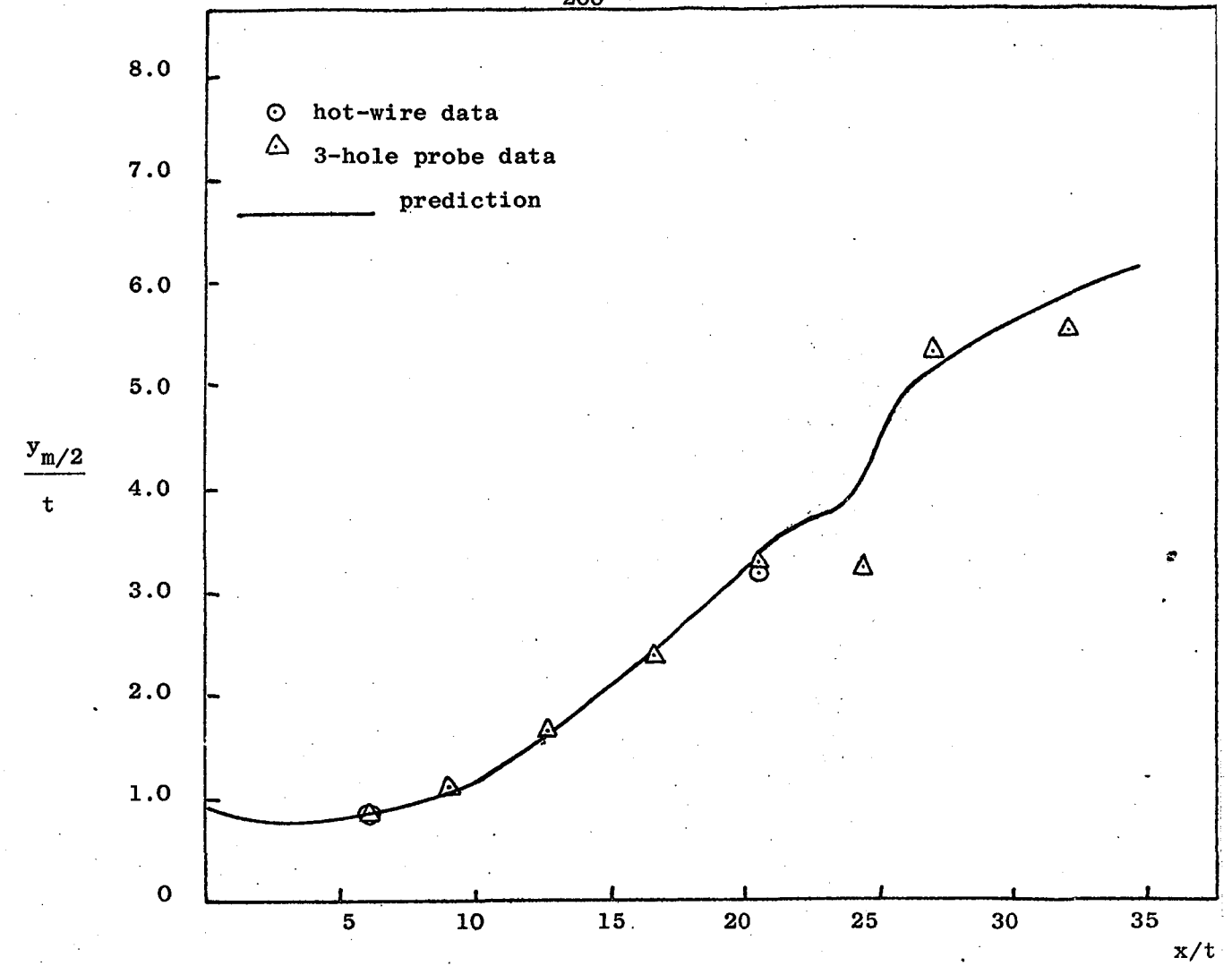


FIG. 8.22: CASE VII: Growth/Velocity Decay Rate

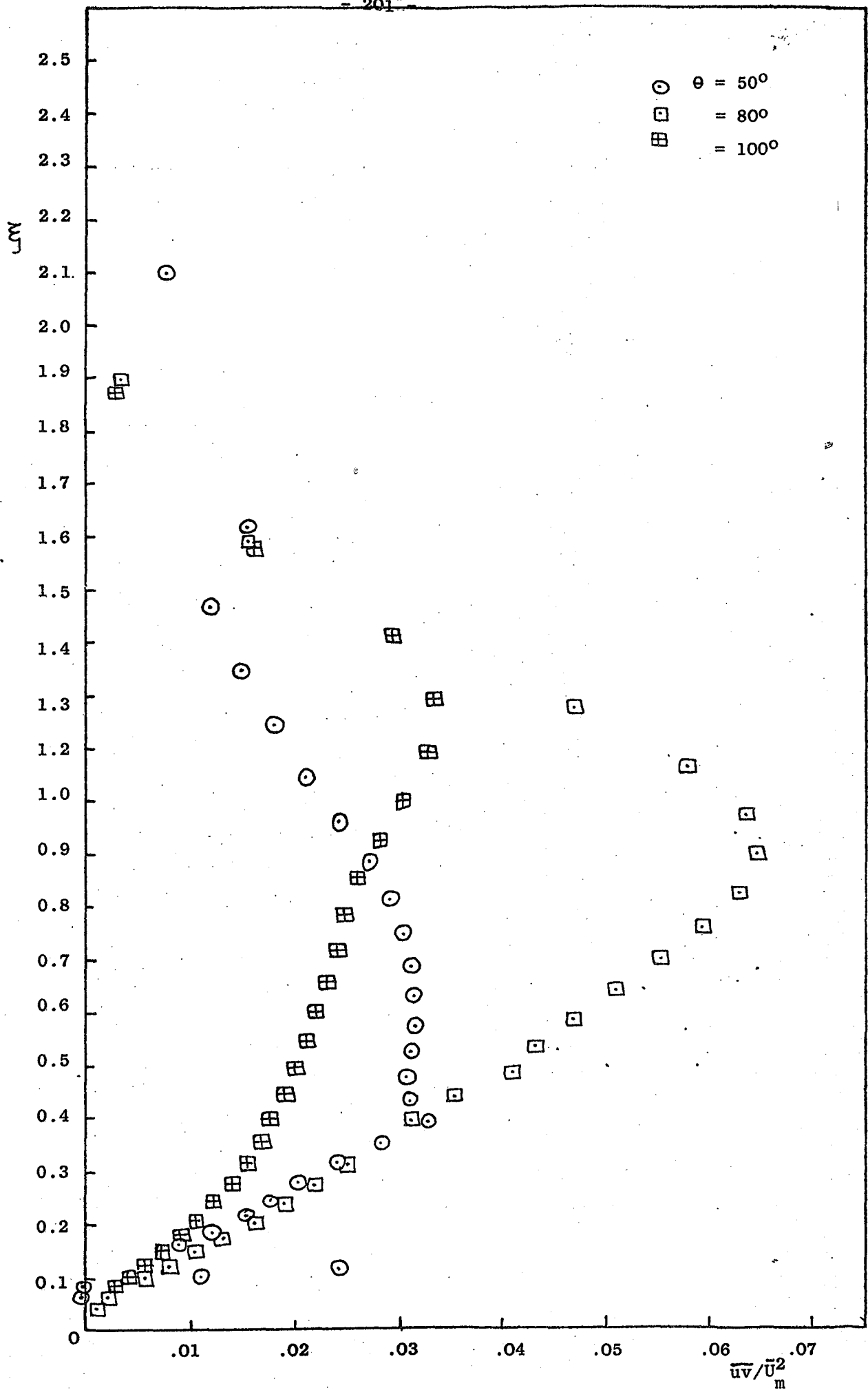


FIG. 8.23: CASE VII: Shear Stress Profiles

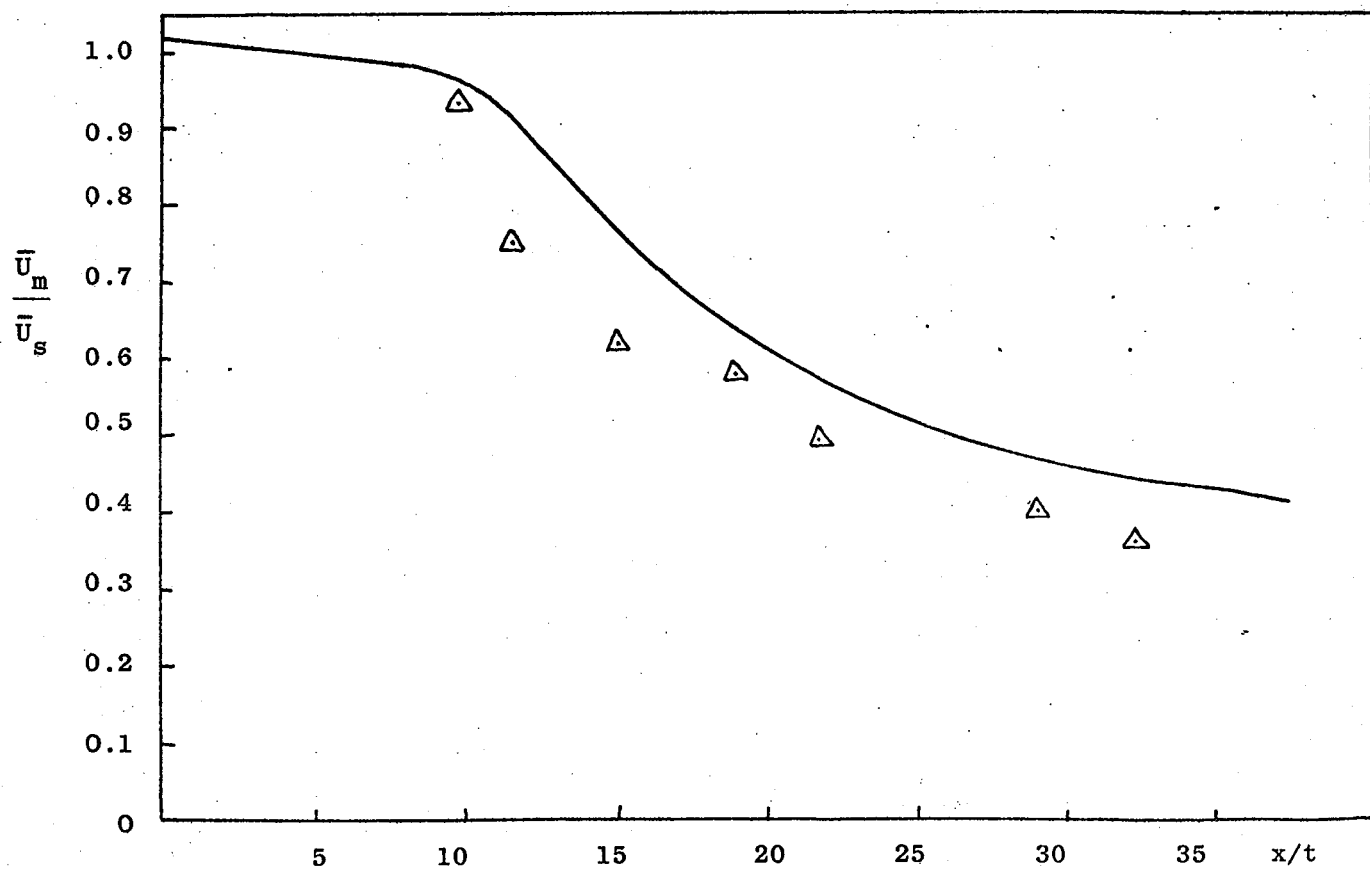
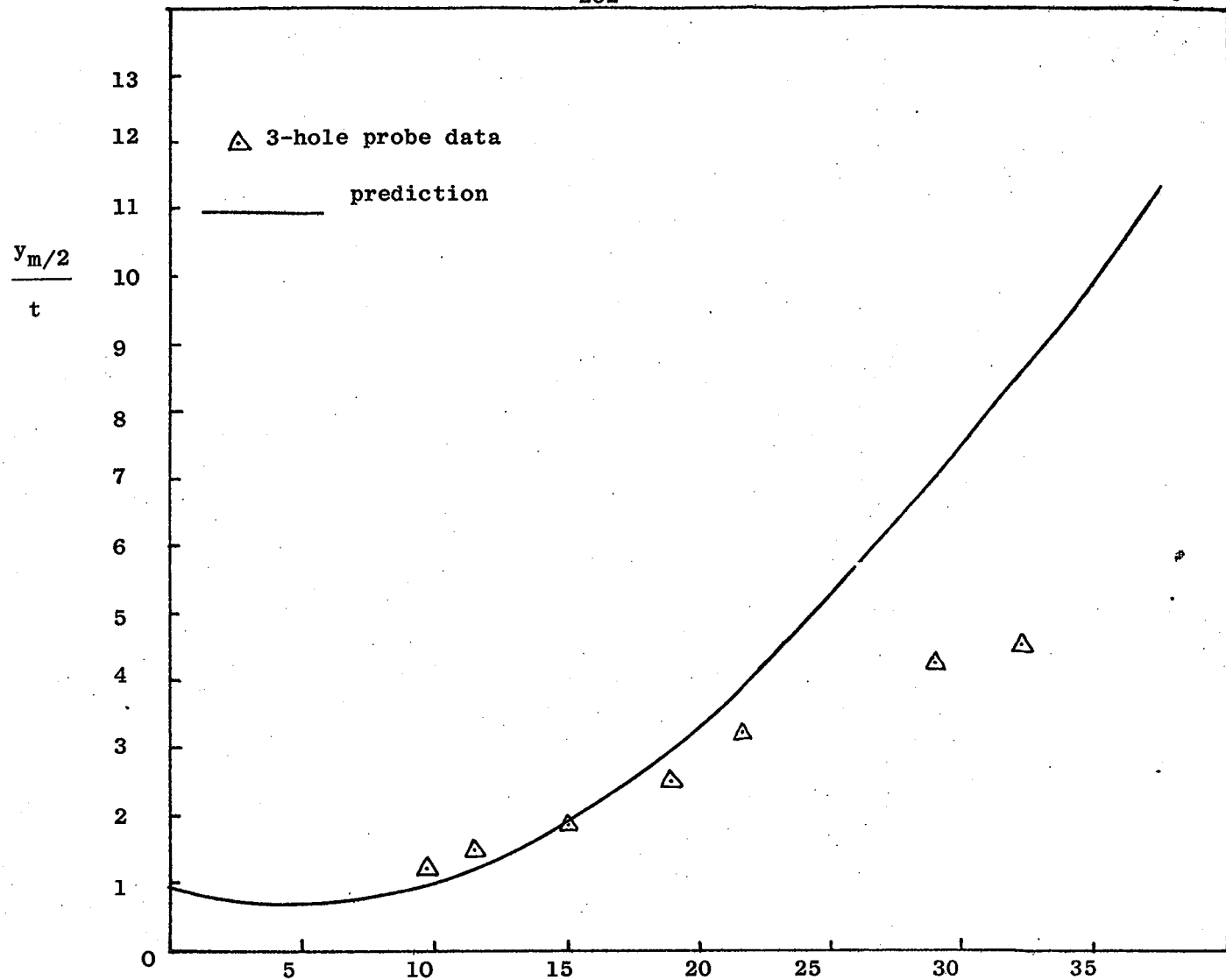
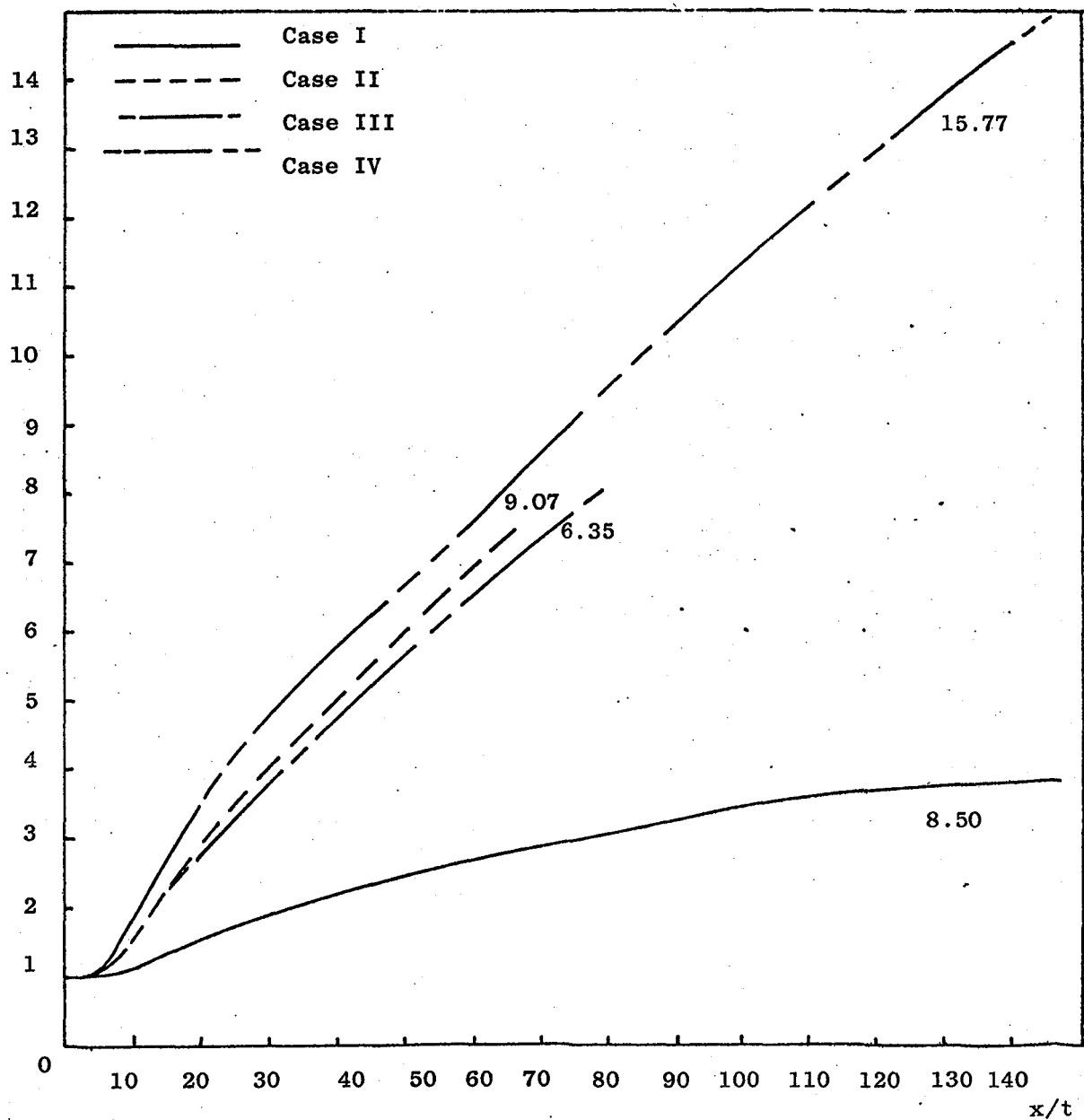
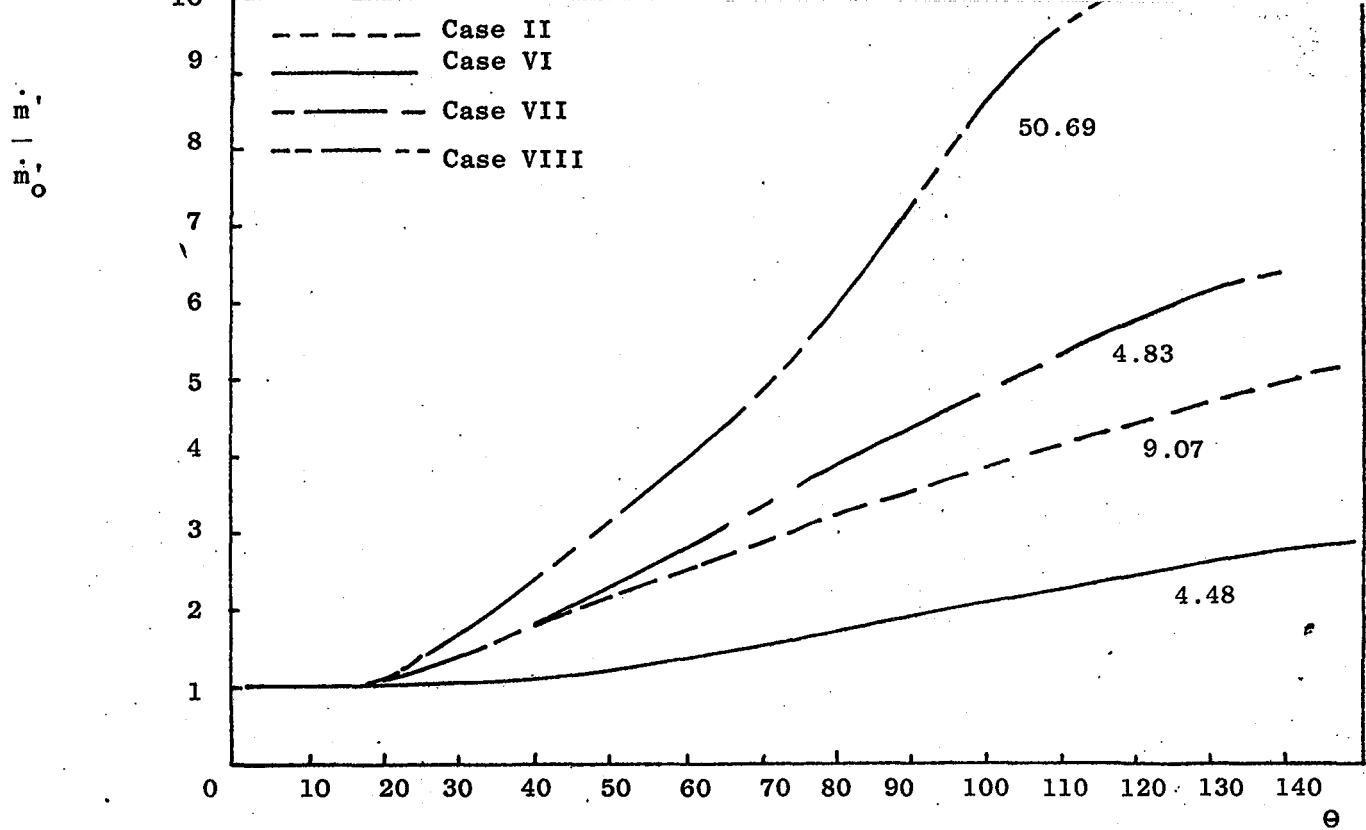


FIG. 8.24: CASE VIII: Growth/Velocity Decay Rate



(numbers refer to slot exit momenta (kg m sec^{-2}))

FIG. 8.25: Comparison of Entrainment Rates

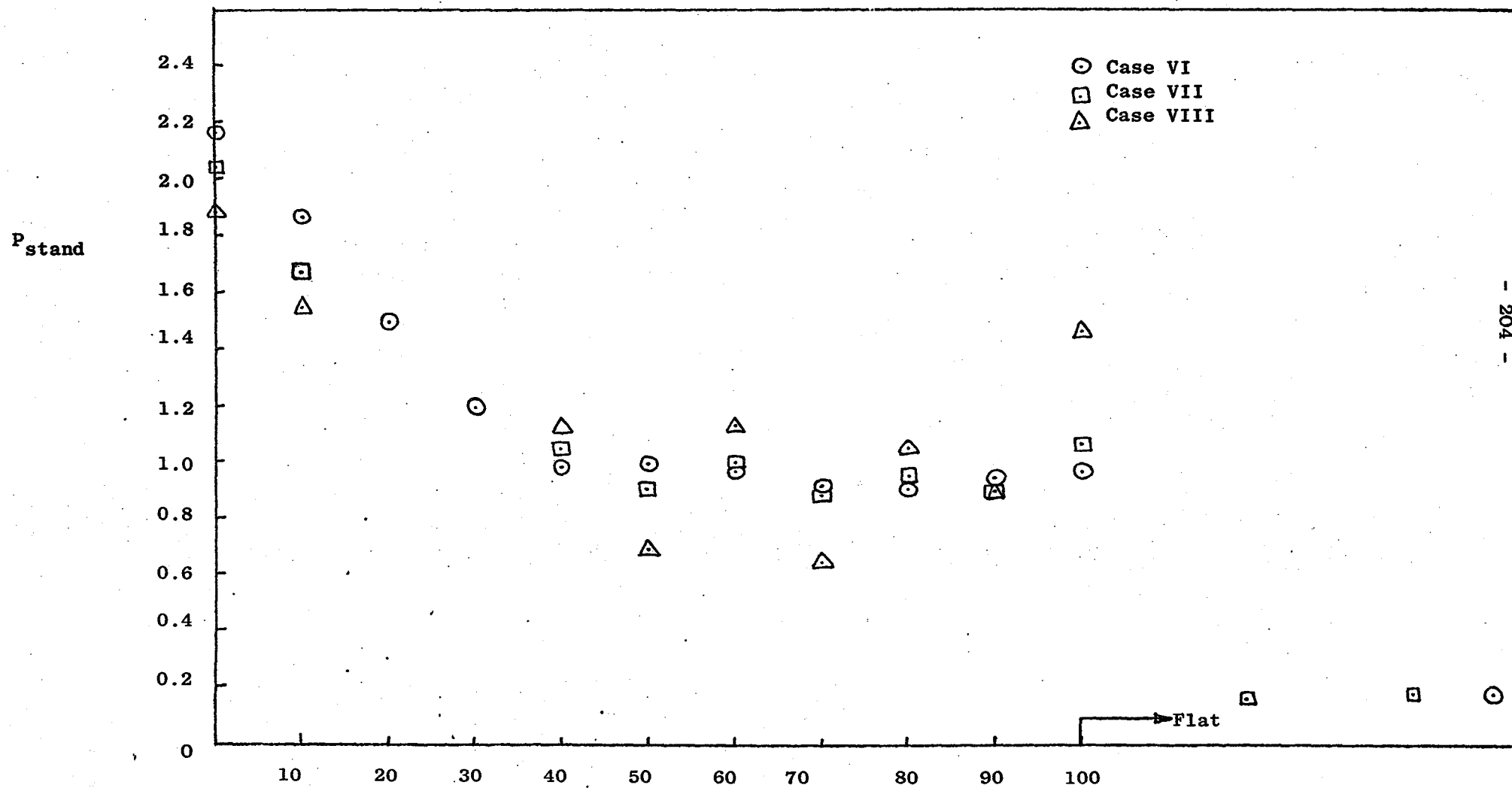


FIG. 8.26: Wall Pressure Predictions

CHAPTER 9

DISCUSSION

9.1 COMMENTS ON THE ACCURACY OF THE EXPERIMENTAL DATA

The conflicting design requirements for the test rig for both high and low pressure inevitably introduce an element of compromise into the design. The wish to measure discharge coefficients for the slot meant that the size of the rig was limited by the available air supply. Therefore, the low speed work suffered from three-dimensional effects which could have been reduced by use of a larger model. Construction of two separate rigs was not feasible.

On top of the usual restriction of incompressible flow, the maximum velocity was further restricted by the available linearizers whose range was limited to ensure that their response was sufficiently linear. This is of course a severe restriction for a strongly sheared flow. The use of a linearizer is in itself a potential source of inaccuracy at low velocities which predominate at the outer edges of the jet, particularly if the low-speed design requirements of the air supply are compromised by the need for higher supply pressures. This is illustrated in the linearization checks of figures 4.2. Without the velocity range restriction required with the use of a linearizer, a higher exit velocity could have been used, thereby removing the recirculation region shown in the data of case A (fig. 5.3). However, further surface pressure distributions (not presented in Chapter 5) for constant Re_p and varying r/t show that the recirculation region is neither a function of slot Reynolds number only, nor of the ratio r/t only. Indeed it seems likely that both the geometry of the slot lip and the slot Reynolds number affect the recirculation region.

The analogue signal analysis described in Chapter 4 is inherently inaccurate for two reasons. Firstly the third and fourth order correlations are not negligible and their necessary neglect to obtain an analysis of manageable proportions is dubious. This is discussed more fully below. Secondly, even if the retention of only up to second order correlations is reasonable, so many wire positions are required to give a solution that cumulative errors in the data are apparent. This is the cause of the scatter in the data of figures 5.15 - 5.18.

Conventional signal averaging at the intermittent jet/ambient fluid interface does not have any relevance to the physical situation. Moreover, the neglect of third order correlations in the analysis has already been shown to be questionable, since it implies a normal distribution of the probability density of the velocity fluctuations (see § 4.6.2). With such high intensities, flow reversal, which cannot be distinguished by the wire, is likely. This has the effect of 'folding' the probability density distribution about the point of zero velocity, causing an even larger departure from the assumption of zero skewness.

More specific comments on the reliability of the experimental data concern the hot-wire analysis and how it is affected by three-dimensionality. At an early stage in the work, binomial expansions of the equations of the effective cooling velocities in the xz-plane were used to provide the two extra solution equations required. This solution often failed to converge because of the original assumptions of two-dimensionality used, viz: $\bar{W} = \overline{uW} = 0$. Without these, a factor of $(k_1^2 - 1)(\bar{UW} + \overline{uW})\sin 2\alpha$ would be added to equation (B.5). However, convergence was obtained by expanding equations for wires in the xy-plane for which, without the assumptions of two-dimensionality, a term of $k_2^2 \overline{W^2}$ would be added to

equation (B.7). Noting that $k_1 \simeq 0.0$ and $k_2 \simeq 1.0$, this would imply that whilst three-dimensionality of the mean flow had been effectively removed, the shear stress $\bar{u}w$ in the principal traverses carried out at the flare centre-line was significantly non-zero. A logical extension of these arguments leads to the supposition that quasi-steady (i.e. "steady" as defined by Bradshaw (1973 p. 40) - see § 2.6.1) longitudinal vortices are present, generated by non-uniformity of the slot or of the flow in the plenum chamber, augmented by the unstable curvature and constrained sufficiently by the base-plate to give a periodic variation of $\bar{u}w$ in the circumferential direction. However, the wavelength of such a vortex system would be rather ill-defined since it would have to be an integer multiple of the layer thickness which varies rapidly with streamwise extent. Therefore it would seem likely that the longitudinal vortices are not steady enough to contribute to the mean motion, and therefore not detectable by any spanwise variations in wall pressure (figure 5.3).

9.2 STREAMWISE CURVATURE AND DIVERGENCE EFFECTS

Discussion of these effects is somewhat restricted by the available experimental data, limited to mean flow and Reynolds stress measurements outside the log-law region of the wall layer. The data, so far, has therefore been discussed by reference to the production terms of the Reynolds stress transport equations. Further inferences concerning the flow structure are possible and comparison with data of a wall jet on a circular cylinder are particularly useful. However, any conclusions attributing observed effects to either of the extra rates of strain present, or to the changes in extra rates of strain can be tentative only since their effects are certainly not additive. Furthermore, when the wall jet structure is regarded as the limit of the interaction between a mixing layer and boundary layer of similar thickness, the picture

becomes even more complicated. Comparison of the energy balances for a flat-plate wall jet and that of a cylindrically-curved wall jet (viz; Irwin (1973) and Alcaraz et al (1977)) show that the production term is more or less the same. But the dissipation is reduced for the curved case in mid-layer and the difference offset by an increase in turbulent diffusion. Thus transport and dissipation rates are also required to fully explain the present data.

Up to 75° , the normal and shear stresses are generally greater than those of a wall jet on a circular cylinder, c.f. Wilson and Goldstein (1976). This can be attributed to the effect of divergence on top of that of streamline curvature, and the higher order structural parameters are almost certainly affected too. A likely effect of divergence (Smits et al (1979b)) is to increase the fluctuating ~~radial~~^{circumferential} component of vorticity. The fluctuating rate of strain in the ~~radial~~^{circumferential} direction would therefore increase also, causing an increase in all three turbulence intensities without preference. The shear stress data of Smits et al revealed an outward going peak in the profiles as the downstream distance increased. However, the profiles of figure 5.18 are rather flat and no firm conclusions can be drawn. In fact, the large values of \overline{uv} are maintained right out to $\xi = 1.5$ and one may speculate as to whether this is a real effect or merely inaccuracies associated with the data analysis. Evidence for the interaction of an 'outer' and 'inner' layer is given by the position of zero shear stress which moves in towards the wall with increasing distance downstream. This also emphasises the unrealistic use of eddy viscosity models in complex flows of this nature.

The best comparison of the present data with other experimental data comes via the structural parameters in figures 5.19 - 5.21. Guitton (1970) and Wilson and Goldstein reported more or less constant values of

$R_{\overline{uv}} = 0.55$ with streamwise distance, decreasing near the wall. Alcaraz et al reported values of 0.45. In the present case, values of $R_{\overline{uv}}$ before the change in surface curvature are all about 0.45 also. Similarly a_1 in the present case is constant for much of the jet width at 0.13 in agreement with the data of Wilson and Goldstein. Therefore, since divergence affects these parameters very little, it does not preferentially change any one component of the stress tensor. This is true of the data for $\xi > 1.0$ also, even though the individual stress components are all increased in this region significantly more than the data in the region $\xi < 1.0$. The reason appears to be a valid effect of divergence which increases the velocity decay rate but not the jet growth rate. The maximum on the \overline{U} -profile is therefore wider in relation to the jet width producing a large region of small $\partial \overline{U} / \partial y$ and a relatively small region of large $\partial \overline{U} / \partial y$ in the outer region of the jet. Thus production of the shear stress and the $\overline{u^2}$ intensity is large here whilst it is smaller further in. This reasoning also explains the high values of $\overline{v^2} / \overline{u^2}$ at $\theta = 45^\circ$ and 60° produced not so much by the preferential effect of streamline curvature on $\overline{v^2}$, but by the divergence effect of reducing the production of $\overline{u^2}$. This effect is most noticeable at $\theta = 45^\circ$ and 60° since the jet has become wide enough for the reduced $\partial \overline{U} / \partial y$ to become apparent before increases in turbulent transport (third order products). $\overline{v^2} / \overline{u^2}$ peaks at 4.5 and 3.5 in the 45° and 60° positions in comparison to Guitton (1970) who recorded values of 0.37 and 0.7 at $y = y_{m/2}$ for the uncurved and curved cases respectively.

In the region where $dr/dx = \infty$ at $\theta = 100^\circ$, not only the individual stress components recover non-monotonically but also all of the structural parameters. This is in contrast to the data of Castro and Bradshaw (1976) and Smits et al (1979a) where a_1 returned monotonically to its equilibrium value. The recovery is slow in terms of the jet growth rate. Inspection

of figures 5.4, 5.10, 5.11 and 5.14 show that not only the turbulence structure, but the mean flow also is distorted by the sudden change in surface curvature. The mean velocity and static pressure profiles oscillate quite significantly in this region; this is best portrayed by the profiles of \bar{V}/\bar{U}_m . Thus the mean rates of strain $\partial\bar{U}/\partial y$ and $\partial\bar{V}/\partial x$ must oscillate also, directly affecting both the production and redistribution terms of the Reynolds stress transport equations. The fact that the streamwise variation of structural parameters is oscillatory also, and that they anticipate the removal of streamline curvature indicates very strong history effects on the shear layer, which die out very slowly relative to the shear layer growth rate.

The above comments have been made without any significant allowance for the effects of longitudinal vorticity on the flow in this case. The data are therefore subject to being interpreted in a qualitative rather than a quantitative fashion.

9.3 ASSESSMENT OF THE TURBULENCE MODELLING PROCEDURE

The modelling of the shear stress can be regarded as satisfactory, especially when bearing in mind the crudity of the initial assumptions and the complexity of the flow. The constants for the streamline curvature and divergence corrections have been tuned individually and the simple addition of their effects on the shear stress has proven to be an adequate first order approximation, although inaccuracies are masked by the simplicity of the model. Two factors have permitted a better agreement between prediction and experiment than might have been thought possible. Firstly, since a universal model was not required, the constants could be tuned to optimise agreement. Secondly, in cases where δ/r is large and pressure gradient effects are perhaps only an order of

magnitude less than extra rate of strain effects on the turbulence, the crudity of the closure assumptions is less critical.

The direct proportionality of $\overline{v^2}$ to \overline{uv} used to model $\overline{v^2}$ in the predictions of chapter eight, is clearly unsatisfactory. No correction has been applied for the preferential effect of the streamline curvature on the $\overline{v^2}$ intensity. This has repercussions on the stability of the calculation method as described in § 8.3.3. This inadequacy can not be improved upon without the introduction of more empiricism or the use of a higher grade model.

The values of the constants used in the correction for streamline curvature are those as suggested by So (1976) although with the simplicity of the assumptions it seems likely that a more suitable pair of constants could be found or another pair giving equally accurate predictions. The constant used for the divergence correction was the value suggested by Smits et al (1979b) and surprisingly, the simple addition of the two corrections to the mixing length gives adequate predictions.

9.4 SUGGESTIONS FOR FURTHER WORK

The unanswered questions concerning the analysis and interpretation of the experimental data give plenty of impetus to further low-speed experimental work. A much larger flare model would be required to reduce three-dimensional effects caused by any irregularities in the upstream turbulence^{*}/intensities and the means of signal analysis is obviously important - the present one is of limited scope. A digital data acquisition system would give the required versatility and also circumvent the necessity of approximating series expansions in analogue signal analyses.

Recommendations for the improvement of the modelling procedure can be made, although the validity of doing this in a flow that is likely to be subject to longitudinal vorticity is questionable. At the very least, a stress transport equation model is required. Some success has been obtained in the prediction of highly curved shear layers and wall jets (viz: Gibson and Rodi (1981), and Ljuboja and Rodi (1980)) using an algebraic stress model. Since these models will still predict coincidence of the point of zero shear stress and the mean velocity maximum, their use for particularly wall jets with streamline curvature may not be too successful. Turbulent transport of both shear stress and energy are particularly important in shear layers with destabilising curvature and is not likely to be simply related to second order products, nor the production and dissipation of turbulent energy. Thus a full Reynolds stress closure is required perhaps even using transport equations for triple products as suggested by Smits et al (1979a).

The incorporation of differential equations for the simulation of history effects on the extra rates of strain is probably not justifiable with the present model. However, such corrections could be included in the length scale calculation in a full Reynolds stress closure, and is likely to be necessary with such a model where the extra strain rates are large.

9.5 CONCLUSIONS

The wall jet with extra rates of strain induced by streamwise and axisymmetric curvature is a strongly perturbed shear layer in which the turbulence intensities are all very high and growth/velocity decay rates exceed those of a flat-plate wall jet.

The major effect of streamwise surface curvature is the preferential increase of the $\overline{v^2}$ intensity. The additional effect of divergence increases the three intensities without preference although for $\xi < 1.0$, the parameter $\overline{v^2}/\overline{u^2}$ is very large at $\theta = 45^\circ$ and 60° , due to small values of $\overline{u^2}$ as well as large values of $\overline{v^2}$. The former are caused by a relatively larger region of small $\partial\overline{U}/\partial y$ and hence relatively small production of $\overline{u^2}$. The other structural parameters a_1 and R_{uv} are unchanged over the region of constant streamwise curvature and their values do not show any preferential effect of divergence.

The whole layer shudders in the region of $\theta = 100^\circ$, caused by the sudden change in streamwise radius of curvature. Not only the individual components of the Reynolds stress tensor, but also the structural parameters and the mean flow oscillate after the removal of curvature; the oscillations are those of a damped second order system.

Discrepancies in the hot-wire data are caused by longitudinal vortices. Three-dimensional effects of the mean flow appear to have been removed indicating the longitudinal vortex system was sufficiently unsteady to contribute only to the Reynolds stresses.

The mean flow characteristics and predominant shear stress gradient have been adequately modelled using a partial-parabolic calculation method with a simple mixing length turbulence closure. The latter has been modified empirically to account for the effects of streamline curvature and divergence. To a first order, the straight-forward addition of these effects is satisfactory. Within the limits of the assumptions of this turbulence model, empirical corrections for any non-linear interaction between the two extra rates of strain, or for the lag of length scale

variation with change in extra rate of strain are probably not justifiable. However, for a higher order turbulence closure, these modifications would be necessary. Since turbulent transport is greatly affected by both streamwise curvature and divergence, a full Reynolds stress closure at the very least is required. Even then, no account would have been made for spanwise periodicity induced by longitudinal vortices.

Both the experimental data and the predictions of the calculation method are, strictly speaking, only relevant to the idealised case of a Coanda flare stated in Chapter One. The experimental data, however, form the preliminary part of an investigation of a strongly distorted shear layer and provide useful data for turbulence modelling. The idealisation of the flow was necessary to make measurements possible and interpretable. Computer predictions are available for subsonic flow without combustion although additional programming could be incorporated to permit compressible flow effects at the slot. The program can be used for design purposes in the flame-free region of flow, mainly in order to optimise the design of Coanda flares for a maximum entrainment rate using the simplest possible geometry.

REFERENCES

- ACRIVELELLIS, M. (1977a) Hot-wire measurements in flows of low and high turbulence intensity.
DISA Information 22 15.
- ACRIVELELLIS, M. (1977b) Finding the spatial flow field by means of hot-wire anemometry.
DISA Information 22 21.
- ACRIVELELLIS, M. (1978a) An improved method for determining the flow field of multi-dimensional flows of any turbulence intensity.
DISA Information 23 11.
- ACRIVELELLIS, M. (1978b) Flow field dependence on hot-wire probe cooling law and probe adjustment.
DISA Information 22 17.
- ALCARAZ, E., CHARNAY, G., and MATHIEU, J., (1977) Measurements in a wall jet over a convex surface.
Physics Fluids 20 203.
- BAKER, E. (1967) Influence of mass transfer on surface friction at a porous surface.
Ph.D. Thesis, University of London.
- BAKKE, P., (1957) An experimental investigation of a wall jet.
J. Fluid Mechs. 2 467.
- BARTENWERFER, M. (1979) Remarks on hot-wire anemometry using "Squared Signals".
DISA Information 24 4.
- BATCHELOR, G.K. (1953) The theory of homogeneous turbulence.
C.U.P. Cambridge.
- BRADSHAW, P., and GEE, M.T. (1960) Turbulent wall jets with and without an external stream.
A.R.C. R & M 3252.

BRADSHAW, P., FERRIS, D.H., and ATWELL, N.P. (1967) Calculation of boundary layer development using the turbulent energy equation. J. Fluid Mechs. 28 593.

BRADSHAW, P., and GOODMAN, D.G., (1968) The effect of turbulence on static-pressure tubes. A.R.C. R & M 3527.

BRADSHAW, P., (1969) The analogy between streamline curvature and buoyancy in turbulent shear flow. J. Fluid Mechs. 36 177.

BRADSHAW, P., (1971) An introduction to turbulence and its measurement. Pergamon Press.

BRADSHAW, P., (1972) The understanding and prediction of turbulent flow. Aero. J. 76 403.

BRADSHAW, P., (1973) Effects of streamline curvature on turbulent flow. Agard No. 169.

BRADSHAW, P., (1975) Review - complex turbulent flows. J. Fluids Engg. Trans. ASME 97 146.

BRADSHAW, P., (1976a) (Ed) Turbulence. Topics In Applied Physics 12 Springer- Verlag.

BRADSHAW, P., (1976b) Complex turbulent flows. Theoretical and Applied Methanics p. 103 (Ed. W.T. Koiter) North Holland.

BRADSHAW, P., and CEBECI, T., (1977) Momentum Transfer In Boundary Layers. McGraw Hill/Hemisphere, Washington.

BRADSHAW, P., (1978) Structure of turbulence in complex flows. Agard-LS-94 p.10.1.

- BRUNN, H. H., (1969) The performance of normal and yawed hot-wires.
ISVR Tech. Rep. No. 21, Univ. Southampton.
- BRUNN, H. H., (1971) Linearization and hot-wire anemometry.
J. Phys. E. 4 815.
- CATALANO, G.D., MORTON, J.B., and HUMPHRISS, R. R., (1977) An experimental investigation of a three-dimensional wall jet.
AIAA 15 1146.
- CASTRO, I.P., and BRADSHAW, P., (1976) The turbulence structure of a highly curved mixing layer.
J. Fluid Mechs. 73 265.
- CEBECI, T., and SMITH, A.M.O. (1974) Analysis of turbulent boundary layers.
Academic Press London.
- CEBECI, T., HIRSH, R. S., and WHITELAW, J.H., (1979) On the calculation of laminar and turbulent boundary layers on longitudinally curved surfaces.
AIAA J. 17 434.
- CHAMPAGNE, F. H., SLEICHER, C. A. and WEHRAMANN, O. H., (1967) Turbulence measurements with inclined hot wires. Part 1 - heat transfer experiments with inclined hot wire.
J. Fluid Mechs. 28 153.
- CHOU, P.Y., (1945) On the velocity correlations and the solution of the equations of turbulent fluctuation.
Q. Appl. Math. 3 38.
- CHOW, C., (1979) An Introduction To Computational Fluid Mechanics.
Wiley, New York.
- COLLIS, D.C., and WILLIAMS, M. J., (1959) Two-dimensional convection from heated wires at low Reynolds numbers.
J. FLuid Mechs. 6 357.

DALY, B.J., and HARLOW, F.H., (1970) Transport equations in turbulence
Physics Fluids 13 2634.

DURÃO, D., and WHITELOW, J.H., (1973) Turbulent mixing in the developing
region of coaxial jets.

J. Fluids Engg. Trans. ASME 95 467.

DURÃO, D., and WHITELOW, J.H., (1974) The evaluation of hot-wire signals
in highly turbulent flows.

Tecnica 420 253.

DURST, F., and WHITELOW, J.H., (1970) Evaluation of turbulence character-
istics from amplitude probability density measurements of hot-wire
anemometer output signals.

Dept. Mech. Eng., Rep. No. ET/TN/A/3 Imperial College.

DURST, F., (1971) The application of hot wire anemometers on low and
highly turbulent flows.

Tecnica 409 503.

DURST, F., and RODI, W., (1972) Evaluation of hot-wire signals in highly
turbulent flows.

Proceedings: DISA Conference on Fluid Dynamic Measurements In The
Industrial and Medical Environments p. 11.4-5.

Leicester Univ. Press.

DVORAK, K., and SYRED, N., (1972) The statistical analysis of hot-wire
anemometer signals in complex flow fields.

Proceedings: DISA Conference on Fluid Dynamic Measurements in the
Industrial and Medical Environments p 11.4.

Leicester Univ. Press.

ESCUDIER, M.P., and NICOLL, W.B., (1966) The entrainment function in
a turbulent boundary layer and wall jet calculations.

J. Fluid Mechs. 25 337.

FEKETE, G.I., (1963) Coanda flow of a two-dimensional wall jet on the
outside of a circular cylinder.

McGill Univ. MERL Rep. No. 63-11.

- GESSNER, F.B., and MOLLER, G.L., (1971) Response behaviour of hot wires in shear flow.
J. Fluid Mechs. 47 449.
- GIBSON, M.M., (1978) An algebraic stress and heat-flux model for turbulent shear flow with streamline curvature.
Int. J. Heat Mass Transfer 21 1609.
- GIBSON, M.M., and RODI, W., (1981) A Reynolds stress closure model of turbulence applied to the calculation of a highly curved mixing layer.
J. Fluid Mechs. 103 161.
- GILES, J.A., HAYS, A.P., and SAWYER, R.A., (1966) Turbulent wall jets on logarithmic spiral surfaces.
Aero. Quart. 17 201.
- GILLIS, J.C., JOHNSTON, J.P., KAYS, W.M., and MOFFAT, R.J., (1981) Turbulent boundary layer on a convex curved surface.
NASA CR 3391.
- GLAUERT, M.B., (1956) The Wall jet.
J. Fluid Mechs. 1 625.
- GOLDSTEIN, S., (1936) A note on the measurement of total head and static pressure in a turbulent stream.
Proc. Roy. Soc. Series A 155 570.
- GOLDSTEIN, S., (1965) Modern Developments In Fluid Mechanics.
Dover Publications Inc. New York.
- GORLIN, S.M., and SLEZINGER, I.I., (1966) Wind tunnels and their instrumentation.
Israel Prog. For Scientific Translations. Jerusalem.
- GREGORY-SMITH, D.G., and ROBINSON, C.J., (1982) The discharge from a thin slot over a surface of convex curvature.
Sub. to Int. J. of Heat Mass Transfer.

- GUITTON, D.E. (1964) Two-dimensional turbulent wall jets over curved surfaces.
McGill Univ. MERL Rep. No. 64-7.
- GUITTON, D.E. (1967) Corrigendum and addendum to report no. 64-7
McGill Univ. MERL Rep. No. 67-1.
- GUITTON, D.E. (1970) Some contributions to the study of equilibrium and non-equilibrium wall jets over curved surfaces.
Ph.D. Thesis, McGill Univ. Montreal.
- GUITTON, D.E. and NEWMAN, B.G. (1977) Self-preserving turbulent wall jets over convex surfaces.
J. Fluid Mechs. 81 155.
- HANJALIĆ, K., and LAUNDER, B.E. (1972) A Reynolds stress model of turbulence and its application to thin shear flows.
J. Fluid Mechs. 52 609.
- HARLOW, F.H., and NAKAYAMA, P., (1968) Transport of turbulence energy decay rate.
Univ. California Los Alamos Science Lab. Rep. LA-3854.
- HEAD, M.R. (1960) Entrainment in the turbulent boundary layer.
ARC R & M 3152.
- HINZE, J.O. (1975) Turbulence
McGraw-Hill 2nd Ed.
- HUNT, I.A. and JOUBERT, P.N. (1979) Effects of small streamline curvature on turbulent duct flow.
J. Fluid Mechs. 91 633.
- IRWIN, H.P.A. (1973) Measurements in a self-preserving plane wall jet in a positive pressure gradient.
J. Fluid Mechs 61 33.
- IRWIN, H.P.A., and SMITH, P.A. (1975) Prediction of the effect of streamline curvature on turbulence.
Physics Fluids 18 624.

JØRGENSEN, F.E. (1971) Directional sensitivity of wire and fiber-film probes.

DISA Information 11 31.

KACKER, S.C. and WHITELOW, J.H. (1968) Some properties of the two-dimensional turbulent wall jet in a moving stream.

J. Appl. Mech. Trans. ASME 35 641.

KACKER, S.C. and WHITELOW, J.H. (1971) The turbulence characteristics of two-dimensional wall jet and wall wake flows.

J. Appl. Mech. Trans ASME 38 239.

KIND, R.J. (1968) Calculation method for circulation control by tangential blowing around a bluff trailing edge.

Aero. Quart. 19 205.

KING, L.V. (1914) On the convection of heat from small cylinders in a stream of fluid.

Phil. Trans. Roy. Soc. 214A 373.

KINGHORN, F.C. (1970) The effects of turbulence and transverse velocity gradients on pitot-tube observations.

NEL Rep. No. 464.

KLATT, F. (1973) A study of systematic errors in measurement with the constant temperature anemometer in high turbulence flows with and without hot-wire signal linearization.

DISA Information 14 25.

KLINE, S.J., MORKOVIN, M.V., SOVRAN, G., and COCKRELL, D.G. (Eds.) (1969)

Proceedings: Computation of Turbulent Boundary Layers

1968 AFOSR-IFP-Stanford Conference Vol. 1.

Stanford Univ. Thermosciences Div.

LAUNDER, B.E. and SPALDING, D.B. (1972) Lectures in Mathematical Models of Turbulence.

Academic Press, London.

- LAUNDER, B.E., and SPALDING, D.B. (1974) The numerical computation of turbulent flows.
Comput. Methods Appl. Mech. & Engg. 3 269.
- LAUNDER, B.E., REECE, G., and RODI, W. (1975) Progress in the development of a Reynolds stress turbulence closure.
J. Fluid Mechs. 68 537.
- LAUNDER, B.E. & MORSE, A. (1977) Numerical prediction procedure for axisymmetric shear flows with a second order Reynolds stress closure. First Symposium on Turbulent Shear Flows. p.4C Penn. State Univ.
- LAUNDER, B.E., PRIDDIN, C.H., and SHARMA B.I. (1977) The calculation of turbulent boundary layers on spinning and curved surfaces.
J. Fluids Engg. Trans. ASME 99 231.
- LJUBOJA, M., and RODI, W. (1980) Calculation of turbulent wall jets with an algebraic Reynolds stress model.
J. Fluids Engg. Trans. ASME 102 350.
- LUMLEY, J.L., (1978) Computational modelling of turbulent flows.
Adv. Appl. Mech. 18 123.
- MAHGOUB, H.E.H., and BRADSHAW, P. (1979) Calculation of turbulent shear layers with large normal pressure gradients.
AIAA J. 17 1025.
- MARGOLIS, D.P., and LUMLEY, J.L. (1965) Curved turbulent mixing layer.
Physics Fluids, 8 1775.
- MASSEY, B.S. (1975) Mechanics of Fluids,
Van Nostrand, Canada.
- MELLOR, G.L., and HERRING, H.J. (1973) A survey of the mean turbulent field closure models.
AIAA J. 11 590.
- MERONEY R.N., and BRADSHAW, P. (1975) Turbulent boundary layer growth over a longitudinally curved surface.
AIAA J. 13 1448.

- MYERS, G.E., SCHAUER, J.J., and EUSTIS, R.H. (1963) Plane turbulent wall jet flow development and friction factor.
J. Basic Engg. Trans. ASME 85 47.
- NAOT, D., SHAVIT, A., and WOLFSHTEIN, M. (1970) Interactions between components of the turbulent velocity correlation tensor due to pressure fluctuations.
Israel J. Tech. 8 259.
- NEE, V.W., and KOVASZNAY, L.S.G. (1969) Simple phenomenological theory for turbulent shear flows.
Physics Fluids 12 473.
- NEWMAN, B.G. (1961) The deflection of plane jets by adjacent boundaries - Coanda Effect.
Boundary Layer Theory and Flow Control p. 232. Ed. Zachmann, G.V.
Pergamon Press.
- NEWMAN, B.G., (1969) The prediction of turbulent jets and wall jets.
Can. Aeronaut. J. 15 288.
- OKA, S., and KOSTIĆ, Z. (1972) Influence of wall proximity on hot-wire velocity measurements.
DISA Information 13 29.
- PARTHASARATHY, S.P., and TRITTON, D.J., (1963) Impossibility of linearizing a hot-wire anemometer for measurements in turbulent flows.
AIAA J. 1 1210.
- PATANKAR, S.V., and SPALDING, D.B. (1967) A finite difference procedure for solving the equations of the two dimensional boundary layer
Int. J. Heat Mass Transfer 10 1389.
- PATANKAR, S.V., and SPALDING, D.B., (1970) Heat and Mass Transfer In Boundary Layers.
Intertext Books London 2nd Ed.

- PATANKAR, S.V., and SPALDING, D. B. (1972) A calculation procedure for heat, mass and momentum transfer in three-dimensional parabolic flows. Int. J. Heat Mass Transfer 15 1787.
- PATANKAR, S.V., RAFIINEJAD, D., and SPALDING, D.B. (1975) Calculation of the three-dimensional boundary layer with solution of all three momentum equations. Comput. Methods Appl. Mech. & Engg. 3 283.
- PATEL, V.C. (1969a) The effects of curvature on the turbulent boundary layer. ARC R & M 3599.
- PATEL, V.C. (1969b) Measurements of secondary flow in the boundary layers of a 180 degree channel. ARC CP 1043.
- PATEL, V.C., NAKAYAMA, A., and DAMIAN, R. (1974) Measurements in the thick axisymmetric turbulent boundary layer near the tail of a body of revolution. J. Fluid Mechs. 63 345.
- POREH, M., TSUEI, Y.G., and CERMAK, J.E. (1967) Investigation of a turbulent radial wall jet. J. Appl. Mechs. Trans. ASME 34 457.
- POTTER, D. (1977) Computational Physics, Wiley, New York.
- PRATAP, V.S. and SPALDING, D.B., (1976) Fluid flow and heat transfer in three-dimensional duct flows. Int. J. Heat Mass Transfer 19 1183.
- RAMAPRIAN, B.R., and SHIVAPRASAD, B.G. (1978) The structure of turbulent boundary layers along mildly curved surfaces. J. Fluid Mechs. 85 273.
- RAPP, A.F., and MARGOLIS, D.P. (1967) Turbulent and pressure transport in a curved mixing layer. Physics Fluids 10 1347.

- RASTOGI, A., and WHITELOW, J.H. (1971) Procedure for predicting the influence of longitudinal curvature on boundary layer flows. ASME pp No. 71-WA/FE-37.
- RAYLEIGH (1916) On the dynamics of revolving fluids
Proc. Roy. Soc. Series A 113 148.
- REYNOLDS, A.J., (1974) Turbulent Flows In Engineering
Wiley.
- REYNOLDS, O. (1870) Suspension of a ball by a jet of fluid
Proc. Man. Lit. Phil. Soc. 9 114 & 133.
- REYNOLDS, W.C. (1976) Computation of turbulent flows.
Ann. Rev. Fluid Mech. 8 183.
- ROACHE, P.J. (1972) Computational Fluid Dynamics
Hermosa Publishers. Albuquerque.
- RODI, W., and SPALDING, D.B., (1970) A two-parameter model of turbulence and its application to free jets.
Wärme Und Stoffübertragung 3 85.
- RODI, W. (1975a) A new method of analysing hot-wire signals in highly turbulent flow and its evaluation in a round jet.
DISA Information 17 9.
- RODI, W. (1975b) A note on the empirical constant in the Kolmogorov-Prandtl eddy viscosity expression.
J. Fluids Engg. Trans ASME 97 386.
- RODI, W. (1976) A new algebraic relation for calculating the Reynolds stresses.
Z. angew. Math. Mech. 56 219.
- ROTTA, J. C. (1951 & 1953) Statische theorie nichthomogener turbulenz.
Z. angew. Math. Phys. 129 547 1951, 131 51 1953.
- ROTTA, J.C. (1962) Turbulent boundary layers in incompressible flow.
Progress In Aeronautical Sciences 2
Pergamon Press.

- RUNCHAL, A.K. (1972) Convergence and accuracy of three finite difference schemes for a two-dimensional conduction and convection problem.
Int. J. Numer. Meth. Engg. 4 451.
- SAWYER, R.A. (1963) Two-dimensional reattaching jet flows including the effects of curvature on entrainment.
J. Fluid Mechs. 17 481.
- SCHWARZ, W.H. and COSART, W.P. (1960) Two-dimensional turbulent wall jet.
J. Fluid Mechs. 10 481.
- SHARMA, R.N. (1981) Experimental investigation of conical wall jets.
AIAA J. 19 28.
- SIDALL, R.G. and DAVIES, T.W. (1972) An improved response equation for hot-wire anemometry.
Int. J. Heat Mass Transfer 15 367.
- SIGALLA, A. (1958) Experimental data on turbulent wall jets.
Aircraft Eng. 30 131.
- SINGHAL, A.K. and SPALDING, D. B. (1967) A two-dimensional partially-parabolic procedure for axial flow turbomachinery cascades.
Imperial College Dept. Mech. Eng. Rep. No. HTS/76/20.
- SMITS, A.J., YOUNG, S.T.B., and BRADSHAW, P. (1979a) The effect of short regions of high surface curvature on turbulent boundary layers.
J. Fluid Mechs. 94 209.
- SMITS, A.J., EATON, J.A., and BRADSHAW, P. (1979b) The response of a turbulent boundary layer to lateral divergence.
J. FLuid Mechs. 94 243.
- SO, R.M.C., and MELLOR, G.L. (1972) An experimental investigation of turbulent boundary layers along curved surfaces.
NASA C.R. 1940.

- SO, R.M.C., and MELLOR, G.L. (1973) Experiment on convex curvature effects in turbulent boundary layers.
J. FLuid Mechs. 60 43.
- SO, R.M.C., and MELLOR, G.L. (1975) Experiment on turbulent boundary layers on a concave wall.
Aero. Quart. 26 25.
- SO, R.M.C. (1975a) Momentum integral for curved shear layers.
J. Fluids Engg. Trans. ASME 97 253.
- SO, R.M.C. (1975b) A turbulence velocity scale for curved shear flows.
J. Fluid Mechs. 70 37.
- SO, R.M.C. (1976) Note: Turbulent wall jets with cylindrical streamwise surface curvature.
By Wilson, D.J., and Goldstein, R.J.
J. FLuids Engg. Trans. ASME 98 780.
- SO, R.M.C. (1978) Turbulent boundary layers with large streamline curvature effects.
Z. angew. Math. Phys. 29 54.
- SPALDING, D.B. (1964) A unified theory of friction, heat and mass transfer in the turbulent boundary layer and wall jet.
ARC CP 829.
- SPALDING, D.B. (1972) A novel finite difference formulation for differential expressions involving both first and second derivatives.
Int. J. Numer. Meth. Engg. 4 551.
- SPALDING, D.B. (1976) Numerical computations of steady boundary layers - a survey.
Computational Methods and Problems In Aeronautical Fluid Dynamics
Academic Press.
- SPALDING, D.B. (1977) Genmix - a general computer program for two-dimensional parabolic phenomena.
Science and Applications of Heat and Mass Transfer Vol. I. Pergamon Press.

- STARR, J.B., and SPARROW, E.M. (1967) Experiments on a turbulent cylindrical wall jet.
J. FLuid Mechs. 29 495.
- TANAKA, T., and TANAKA, E. (1976 & 1977) Experimental study of a radial turbulent jet.
Japan Soc. Mech. Engg. Bull. 19 792 1976, 20 209 1977.
- TANI, I. (1962) Production of longitudinal vortices in the boundary layer along a concave wall.
J. Geophys. Res. 67 3075.
- TITCOMBE, C.G. (1980) Mathematical model of Coanda flares.
Unpublished report. B.P. Research Centre,
Sunbury-on-Thames.
- TOWNSEND, A.A. (1961) Equilibrium layers and wall turbulence
J. FLuid Mechs. 11 97.
- TOWNSEND, A.A. (1976) The Structure of Turbulent Shear Flow.
Cam. Univ. Press. 2nd Ed.
- VAN DRIEST, E.R. (1956) On turbulent flow near a wall,
J. Aeronaut. Sci. 23 1007.
- WILKINS, J., WITHERIDGE, R.E., DESTY, D.H., MASON, J.T.M., and NEWBY, N.
(1977) The design, development and performance of Indair and Mardair
Flares
Offshore Technology Conference, Houston Texas, OTC 2822.
- WILLE, R., and FERNHOLZ, H. (1956) Report on the first European
mechanics colloquium on the Coanda effect.
J. Fluid Mechs. 23 801.
- WILSON, D.J., and GOLDSTEIN, R.J. (1976) Turbulent wall jets with
cylindrical streamwise surface curvature.
J. Fluids Engg. Trans ASME 98 550.

WYNGAARD, J.C., TENNEKES, H., LUMLEY, J.L., and MARGOLIS, D.P. (1968)

Structure of turbulence in a highly curved mixing layer.

Physics Fluids 11 1251.

YOUNG, T. (1800) Outlines of experiments and inquiries respecting sound and light, Lecture to the Royal Society.

J. Roy. Aero. Soc. 61 157 1957.

ZARIĆ, Z. (1969) Statistical interpretation of the velocity measurements in high intensity turbulence.

International Summer School, Herceg-Novi, Yugoslavia.

A P P E N D I X A

THREE-HOLE PROBE CALIBRATION AND CORRECTIONS

The following assumptions were made in the calibration of the three-hole probes shown in Figure 3.4a:

- (a) P_2 measures the total pressure for the range of mean-flow angles encountered in the flare flow.
- (b) $(P_1 + P_3)/2$ is a function of mean velocity only.
- (c) $(P_1 - P_3)$ is a function of mean velocity and pitch angle θ

(a) was checked and a negligible deviation from total pressure was observed for $\theta \leq \pm 7^\circ$. Therefore the calibration used was:

$$(1) \quad P_2 - (P_1 + P_3)/2 = f\left(\frac{1}{2}\rho \bar{U}_{\text{meas}}^2\right) \quad \dots (A.1)$$

$$(2) \quad \frac{P_1 - P_3}{P_2 - (P_1 + P_3)/2} = f(\theta) \quad \dots (A.2)$$

With the use of assumption (a) above, the static pressure in the jet could be obtained. The velocity calibration was performed at $\theta = 0^\circ$; the pitch calibration, for the smaller probe, was done at $U_{\text{meas}} = 60 \text{ m/s}$. These calibrations are shown in Figure 3.5. Temperature variation between calibration and measurement was assumed negligible.

A.1 Correction for Mach Number Effects

The effect of compressibility on the pitot tube used to calibrate the three-hole probes can be allowed for by the formula (Massey (1975 p.353)):

$$\frac{1}{2}\rho \bar{U}_{\text{act}}^2 = \frac{\frac{1}{2}\rho \bar{U}_{\text{meas}}^2}{(1 + M^2/4 + M^4/40 \dots)} \quad \dots (A.3)$$

assuming $\gamma = 1.4$ and $M < 1$. This correction was particularly important for the larger probe whose calibration went up to $M = 0.62$. This probe was used in the large scale tests described in § 3.2.

A.2 Correction for Transverse Velocity Gradient

Young and Maas (1937) obtained the empirical relationship:

$$\frac{\delta y}{d} = \frac{0.131 + 0.082 d}{D} \quad \dots (A.4)$$

for the displacement δy , of the effective centre of a total pressure tube in a transverse velocity gradient. d and D are the inner and outer diameters of the tube which had a square-cut nose. However, the validity of equation (A.4) was only tested for a range of positive dynamic head gradients. Kinghorn (1970) investigated several transverse velocity gradient correction formulae but none were suitable to the present geometry. The use of equation (A.4) was considered but it was felt that it would not give an improvement in accuracy. δy was estimated at 0.045 mm for the smaller probe, but this correction was not applied.

A.3 Correction for Turbulence

Velocity data from the above calibration were corrected on analysis by the following formula:

$$P_{\text{total}} = P_{\text{static}} + \frac{1}{2}\rho (\overline{U}^2 + \overline{V}^2 + \overline{u}^2 + \overline{v}^2 + \overline{w}^2) \quad \dots (A.5)$$

in order to allow for the effects of averaging by the three-hole probe.

The values of \overline{u}^2 , \overline{v}^2 and \overline{w}^2 were available from the hot-wire data.

This formula was originally proposed by Goldstein (1936) and examined by Kinghorn (1970) and Bradshaw and Goodman (1968).

A P P E N D I X B

HOT-WIRE ANALYSIS - FOUR PROBE ORIENTATIONS

The effective cooling velocity for each wire position (Figure 4.3) can be described by:-

$$U_{\text{eff}}^2 = U_N^2 + k_2^2 U_B^2 + k_1^2 U_T^2 \quad \dots (B.1)$$

B.1 Single Wire Probe 55P14

$$U_{\text{eff}}^2(o)_{xz} = (\bar{U} + u)^2 + k_2^2 (\bar{V} + v)^2 + k_1^2 w^2 \quad \dots (B.2)$$

on averaging:-

$$\overline{U_{\text{eff}}^2(o)_{xz}} = (\bar{U}^2 + \overline{u^2}) + k_2^2 (\bar{V}^2 + \overline{v^2}) + k_1^2 \bar{w}^2 \quad \dots (B.3)$$

B.2 Cross Wire Probe 55P54

$$\begin{aligned} U_{\text{eff}}^2(o)_{yz} = & ((\bar{U} + u) \cos \alpha - w \sin \alpha)^2 + k_1^2 ((\bar{U} + u) \sin \alpha + w \cos \alpha)^2 \\ & + k_2^2 (\bar{V} + v)^2 \quad \dots (B.4) \end{aligned}$$

on expanding and averaging:-

$$\begin{aligned} \overline{U_{\text{eff}}^2(\alpha)_{yz}} = & ((\bar{U}^2 + \overline{u^2}) (\cos^2 \alpha + k_1^2 \sin^2 \alpha) + k_2^2 (\bar{V}^2 + \overline{v^2}) \\ & + \bar{w}^2 (\sin^2 \alpha + k_1^2 \cos^2 \alpha) \quad \dots (B.5) \end{aligned}$$

where $\alpha = + 45^\circ$

B.3 Cross Wire Probe 55P53

$$\begin{aligned} U_{\text{eff}}^2(\alpha)_{xy} = & ((\bar{U} + u) \cos \alpha + (\bar{V} + v) \sin \alpha)^2 + k_2^2 w^2 \\ & + k_1^2 ((\bar{U} + u) \sin \alpha - (\bar{V} + v) \cos \alpha)^2 \quad \dots (B.6) \end{aligned}$$

on expanding and averaging:-

$$\begin{aligned} \overline{U_{\text{eff}}^2}(\alpha)_{xy} &= (\overline{U^2} + \overline{u^2}) (\cos^2 \alpha + k_1^2 \sin^2 \alpha) + (\overline{V^2} + \overline{v^2})(k_1^2 \cos^2 \alpha + \sin^2 \alpha) \\ &\quad + k_2^2 \overline{w^2} + (\overline{UV} + \overline{uv}) \sin 2\alpha (1 - k_1^2) \quad \dots (B.7) \end{aligned}$$

for $\alpha = \pm 45^\circ$.

A P P E N D I X C

FULL SOLUTION OF SIX HOT-WIRE RESPONSE EQUATIONS

Rearrangement of equations (B.3), (B.5), and (B.7) in matrix form gives:

$$\begin{bmatrix} \overline{U_{\text{eff}}^2} (0)_{xz} \\ \overline{U_{\text{eff}}^2} (\alpha)_{xz} \\ \overline{U_{\text{eff}}^2} (\alpha)_{xy} \\ \overline{U_{\text{eff}}^2} (\alpha)_{xy} \end{bmatrix} = \begin{bmatrix} 1 & k_2^2 & k_1^2 & 0 \\ \cos^2 \alpha + k_1^2 \sin^2 \alpha & k_2^2 & \sin^2 \alpha + k_1^2 \cos^2 \alpha & 0 \\ \cos^2 \alpha + k_1^2 \sin^2 \alpha & k_1^2 \cos^2 \alpha + \sin^2 \alpha & k_2^2 & (1-k_1^2) \sin 2\alpha \\ \cos^2 \alpha + k_1^2 \sin^2 \alpha & k_1^2 \cos^2 \alpha + \sin^2 \alpha & k_2^2 & (1-k_1^2) \sin 2\alpha \end{bmatrix} \times$$

$$\begin{bmatrix} \overline{U^2} + \overline{u^2} \\ \overline{V^2} + \overline{v^2} \\ \overline{w^2} \\ \overline{UV} + \overline{uv} \end{bmatrix}$$

(C.1)

Where values of k_1 , k_2 and α are dependent on the wire.

For $\bar{U}_{\text{eff}}(\alpha)_{xy}$, expansion of equation (B.6) yields after averaging:-

$$\begin{aligned} \bar{U}_{\text{eff}}(\alpha)_{xy} = & \bar{U}(\cos^2 \alpha + k_1^2 \sin^2 \alpha)^{\frac{1}{2}} \left(1 + \theta_1 \frac{\bar{v}}{\bar{U}} + \theta_2 \left(\frac{\bar{v}^2}{\bar{U}^2} + \frac{\bar{v}^2}{\bar{U}^2} + \frac{\bar{v}^2}{\bar{U}^2} \frac{\bar{u}^2}{\bar{U}^2} \right) \right. \\ & + \theta_3 \frac{\bar{v}}{\bar{U}} \frac{\bar{uv}}{\bar{U}^2} + \theta_4 \frac{\bar{w}^2}{\bar{U}^2} + \theta_5 \frac{\bar{v}^2}{\bar{U}^2} \frac{\bar{v}^2}{\bar{U}^2} + \theta_6 \frac{\bar{v}^2}{\bar{U}^2} \frac{\bar{w}^2}{\bar{U}^2} \\ & \left. + \theta_7 \frac{\bar{v}}{\bar{U}} \frac{\bar{v}^2}{\bar{U}^2} + \theta_8 \frac{\bar{v}}{\bar{U}} \frac{\bar{w}^2}{\bar{U}^2} + \theta_9 \frac{\bar{v}^2}{\bar{U}^2} \frac{\bar{uv}}{\bar{U}^2} \right) \end{aligned} \quad \dots (C.2)$$

where

$$\theta_1 = \mu/2$$

$$\theta_2 = \nu/2 - \mu^2/8$$

$$\theta_3 = -\nu + \frac{1}{4}\mu^2$$

$$\theta_4 = \frac{k_2^2}{2(\cos^2 \alpha + k_1^2 \sin^2 \alpha)}$$

$$\theta_5 = \nu \left(-\frac{3}{4}\nu + \frac{9}{8}\mu^2 \right)$$

$$\theta_6 = \frac{k_2^2}{\cos^2 \alpha + k_1^2 \sin^2 \alpha} \left(-\frac{1}{4}\nu + \frac{3}{16}\mu^2 \right)$$

$$\theta_7 = -\frac{3}{4}\nu \sin 2\alpha (1 - k_1^2) + \frac{3}{16}\mu^3$$

$$\theta_8 = -\frac{1}{4}k_2^2 \mu$$

$$\theta_9 = \sin(2\alpha (1 - k_1^2)) \left(\frac{3}{2}\nu - \frac{3}{8}\mu^2 \right)$$

$$\text{and } \mu = \frac{\sin 2\alpha (1 - k_1^2)}{\cos^2 \alpha + k_1^2 \sin^2 \alpha}$$

$$\nu = \frac{k_1^2 \cos^2 \alpha + \sin^2 \alpha}{\cos^2 \alpha + k_1^2 \sin^2 \alpha}$$

Substitution for $\bar{U}^2 + \bar{u}^2$, $\bar{v}^2 + \bar{v}^2$, $\bar{U}\bar{v} + \bar{uv}$ and \bar{w}^2 in equation (C.2)

yields two equations for $\alpha = \pm 45^\circ$ of form:

$$a_1 \bar{U}^3 + a_2 \bar{U}^2 + a_3 \bar{U}\bar{v} + a_4 \bar{U}^2 \bar{v}^2 + a_5 \bar{U}^3 \bar{v} + a_6 \bar{U}\bar{v}^3 + a_7 \bar{v}^2 + a_8 \bar{v}^4 = 0$$

... (C.3)

A P P E N D I X D

SIMPLIFIED HOT-WIRE ANALYSIS FOR NEAR-WALL REGION

Equations (B.3) and (B.5) are used together with binomial expansions of equations (B.2) and (B.4) up to second order terms and assuming $V = 0$.

Hence:-

$$\overline{U}_{\text{eff}}^2(0)_{xz} = \overline{U}^2 + \overline{u}^2 + k_2^2 \overline{v}^2 + k_1^2 \overline{w}^2 \quad \dots (D.1)$$

$$\overline{U}_{\text{eff}}^2(\alpha)_{xz} = (\overline{U}^2 + \overline{u}^2)(\cos^2 \alpha + k_1^2 \sin^2 \alpha) + k_2^2 \overline{v}^2 + \overline{w}^2(\sin^2 \alpha + k_1^2 \cos^2 \alpha) \quad \dots (D.2)$$

$$\overline{U}_{\text{eff}}(0)_{xz} = \overline{U} \left(1 + \frac{k_2^2 \overline{v}^2}{2 \overline{U}} + \frac{k_1^2 \overline{w}^2}{2 \overline{U}} \right) \quad \dots (D.3)$$

$$\begin{aligned} \overline{U}_{\text{eff}}(\alpha)_{xz} = \overline{U} \left(1 + \frac{k_1^2}{2} \tan^2 \alpha \right) \cos \alpha + \frac{k_2^2}{2 \cos \alpha} \frac{\overline{v}^2}{\overline{U}} \\ + \frac{k_1^2}{2} (1 + 2 \tan^2 \alpha + \tan^4 \alpha) \cos \alpha \cdot \frac{\overline{w}^2}{\overline{U}} \quad \dots (D.4) \end{aligned}$$

By successive substitution these equations reduce to a quadratic:

$$a \overline{U}^2 + b \overline{U} + c = 0 \quad \dots (D.5)$$

A P P E N D I X E

EQUATIONS OF MOTION

Rather than deriving the full Navier- Stokes equations for incompressible flow with streamline and axisymmetric curvature from first principles, the following approach is adopted. Goldstein (1965) gives the x- and y-component Navier-Stokes equations for flow with streamline curvature as:-

$$\begin{aligned} \frac{\partial U}{\partial t} + \frac{1}{h} U \frac{\partial U}{\partial x} + V \frac{\partial U}{\partial y} + \frac{UV}{rh} = - \frac{1}{\rho h} \frac{\partial p}{\partial x} + \\ v \left(\frac{1}{h^2} \frac{\partial^2 U}{\partial x^2} + \frac{\partial^2 U}{\partial y^2} - \frac{y}{h^3} \frac{\partial(1/r)}{\partial x} \frac{\partial U}{\partial x} + \frac{1}{rh} \frac{\partial U}{\partial y} - \frac{U}{r^2 h^2} + \right. \\ \left. \frac{1}{h^3} \frac{\partial(1/r)V}{\partial x} + \frac{2}{rh^2} \frac{\partial V}{\partial x} \right) \end{aligned} \quad \dots (E.1)$$

$$\begin{aligned} \frac{\partial V}{\partial t} + \frac{U}{h} \frac{\partial V}{\partial x} + \frac{V}{\partial y} - \frac{U^2}{rh} = - \frac{1}{\rho} \frac{\partial p}{\partial y} + \\ v \left(\frac{1}{h^2} \frac{\partial^2 V}{\partial x^2} + \frac{\partial^2 V}{\partial y^2} - \frac{y}{h^3} \frac{\partial(1/r)}{\partial x} \frac{\partial V}{\partial x} + \frac{1}{rh} \frac{\partial V}{\partial y} - \frac{V}{r^2 h^2} - \right. \\ \left. \frac{1}{h^3} \frac{\partial(1/r)}{\partial x} U - \frac{2}{rh^2} \frac{\partial U}{\partial x} \right) \end{aligned} \quad \dots (E.2)$$

Similarly the continuity equation is written as:-

$$\frac{1}{h} \frac{\partial U}{\partial x} + \frac{\partial V}{\partial y} + \frac{V}{rh} = 0 \quad \dots (E.3)$$

E.1 Simplification of the Viscous Terms

For a turbulent jet flow, the ratio of turbulent to laminar shear stress is likely to be of order 10^{-5} . Therefore the viscous terms can be greatly simplified without compromising accuracy except in the viscous sub-layer where the laminar shear stress predominates. Applying the order of magnitude assumptions of § 6.2.3 and retaining terms $O(U/\delta)$ only, the viscous term of equation (E.1) reduces to:-

$$\nu \frac{\partial^2 U}{\partial y^2}$$

and the viscous term of equation (E.2) can be neglected.

E.2 Development of Equations in Axisymmetric Form

Following Bradshaw (1973), the axisymmetric equivalent of equations (E.1), (E.2) and (E.3) can be obtained by placing them in their divergence form and multiplying all velocity products and pressure gradients by the axisymmetric radius of curvature R to the point. Thus addition of equation (E.3) $\times U$ to (E.1) yields the divergence form of the latter, viz:-

$$\frac{\partial(U^2)}{\partial x} + \frac{\partial(UVh)}{\partial y} + \frac{UV}{r} = - \frac{1}{\rho} \frac{\partial p}{\partial x} + \nu \frac{\partial^2 U}{\partial y^2} \quad \dots (E.4)$$

and the axisymmetric equivalent becomes:-

$$\frac{\partial(U^2 R)}{\partial x} + \frac{\partial(UVRh)}{\partial y} + \frac{UVR}{r} = - \frac{R}{\rho} \frac{\partial p}{\partial x} + R \nu \frac{\partial^2 U}{\partial y^2} \quad \dots (E.5)$$

The corresponding equation of continuity is:-

$$\frac{\partial(UR)}{\partial x} + \frac{\partial(VRh)}{\partial y} = 0 \quad \dots (E.6)$$

putting $U = \bar{U} + u$

$V = \bar{V} + v$

and $p = \bar{p} + p'$

in equation (E.5) yields, after averaging, subtracting $U \times$ equation (E.6) and rearranging:-

$$\begin{aligned} \bar{U} \frac{\partial \bar{U}}{\partial x} + h \bar{V} \frac{\partial \bar{U}}{\partial y} + \frac{\bar{U}\bar{V}}{r} = - \frac{1}{\rho} \frac{\partial \bar{p}}{\partial x} - \\ \frac{1}{R} \left(\frac{\partial (\bar{u}^2 R)}{\partial x} + \frac{\partial (h \bar{u} \bar{v} R)}{\partial y} + \frac{\bar{u} \bar{v} R}{r} \right) + \frac{v}{R} \frac{\partial}{\partial y} \left(R h \frac{\partial \bar{U}}{\partial y} \right) \end{aligned} \quad \dots (E.7)$$

Note that the viscous term has been rearranged slightly to include the higher order terms $\left(\frac{1}{r} + \frac{h \cos \alpha}{R} \right) \frac{\partial \bar{U}}{\partial y}$. This ensures that the laminar and turbulent shear stress terms are of the same form.

In the same way, an equation of instantaneous momentum in the y direction can be derived:

$$\frac{\partial (UVR)}{\partial x} + \frac{\partial (hV^2 R)}{\partial y} - \frac{U^2 R}{r} = - h R \frac{\partial p}{\rho \partial y} \quad \dots (E.8)$$

and the equation for mean momentum:

$$\begin{aligned} \bar{U} \frac{\partial \bar{V}}{\partial x} + h \bar{V} \frac{\partial \bar{V}}{\partial y} - \frac{\bar{U}^2}{r} = h \frac{\partial \bar{p}}{\rho \partial y} - \\ \frac{1}{R} \left(\frac{\partial (\bar{u} \bar{v} R)}{\partial x} + \frac{\partial (\bar{v}^2 R h)}{\partial y} - \frac{\bar{u}^2 R}{r} \right) \end{aligned} \quad \dots (E.9)$$

The equation of continuity for the mean flow is:-

$$\frac{\partial (\bar{U} R)}{\partial x} + \frac{\partial (\bar{V} R h)}{\partial y} = 0 \quad \dots (E.10)$$

Equations (E.5), (E.7), (E.8) and (E.9) are all exact except for the viscous terms which are approximate.

A P P E N D I X F

REYNOLDS STRESS TRANSPORT EQUATIONS

The transport equations for the four Reynolds stresses \overline{uv} , $\overline{u^2}$, $\overline{v^2}$, $\overline{w^2}$ and the equation of turbulent kinetic energy are derived for two-dimensional axisymmetric flow with streamline curvature. The starting point is the instantaneous equation of momentum, viz:

x-component

$$\overline{U \frac{\partial U}{\partial x}} + \overline{h V \frac{\partial U}{\partial y}} + \overline{\frac{UV}{r}} = - \frac{1}{\rho} \frac{\partial p}{\partial x} \quad . . . (F.1)$$

y-component

$$\overline{U \frac{\partial V}{\partial x}} + \overline{h V \frac{\partial V}{\partial y}} - \overline{\frac{U^2}{r}} = - \frac{h}{\rho} \frac{\partial p}{\partial y} \quad . . . (F.2)$$

z-component

$$\overline{U \frac{\partial w}{\partial x}} + \overline{h V \frac{\partial w}{\partial y}} = - \frac{h}{\rho} \frac{\partial p}{\partial z} \quad . . . (F.3)$$

The transport equation for the stress $U_i U_j$ is obtained by addition of the products of the i-component equation and U_j , and the j-component equation and U_i . After substitution of $U_i = \overline{U}_i + u_i$ and averaging the following equations are obtained:

$$\frac{D(\frac{1}{2} \overline{u^2})}{Dt} = - \overline{u^2} \frac{\partial \overline{U}}{\partial x} - \overline{h u v} \frac{\partial \overline{U}}{\partial y} - \left(\frac{\overline{u^2 v} + \overline{u v u}}{r} \right) \quad \text{PRODUCTION}$$

$$+ \frac{\overline{p' \frac{\partial u}{\partial x}}}{\rho} \quad \text{REDISTRIBUTION}$$

$$-\frac{1}{\rho} \frac{\partial(\overline{p'u})}{\partial x} - \frac{3}{2} \frac{\overline{u^2 v}}{r} - \frac{1}{2R} \left(\frac{\partial(\overline{u^3 R})}{\partial x} + h \frac{\partial(\overline{u^2 v R})}{\partial y} \right) \text{TRANSPORT}$$

$$-\frac{1}{3} \epsilon$$

DESTRUCTION

. . . (F.4)

$$\frac{D(\frac{1}{2}\overline{v^2})}{Dt} = -\overline{uv} \frac{\partial \overline{v}}{\partial x} - h \overline{v^2} \frac{\partial \overline{v}}{\partial y} + 2\overline{u} \frac{\overline{uv}}{r}$$

PRODUCTION

$$+ h \frac{\overline{p' \partial v}}{\rho \partial y}$$

REDISTRIBUTION

$$-\frac{h}{\rho} \frac{\partial(\overline{p'v})}{\partial y} + \frac{\overline{u^2 v}}{r} - \frac{\overline{v^3}}{2r} - \frac{1}{2R} \left(\frac{\partial(\overline{uv^2 R})}{\partial x} + h \frac{\partial(\overline{v^3 R})}{\partial y} \right) \text{TRANSPORT}$$

$$-\frac{1}{3} \epsilon$$

DESTRUCTION

. . . (F.5)

$$\frac{D(\frac{1}{2}\overline{w^2})}{Dt} = h \frac{\overline{p' \partial w}}{\rho \partial z}$$

REDISTRIBUTION

$$-\frac{\overline{vw^2}}{2r} - \frac{1}{2R} \left(\frac{\partial(\overline{uw^2 R})}{\partial x} + h \frac{\partial(\overline{vw^2 R})}{\partial y} \right)$$

TRANSPORT

$$-\frac{1}{3} \epsilon$$

DESTRUCTION

. . . (F.6)

Addition of the three normal stress transport equations yields the transport equation for turbulent kinetic energy.

$$\frac{D(\frac{1}{2}\overline{q^2})}{Dt} = -\overline{u^2} \left(\frac{\partial \overline{u}}{\partial x} + \frac{\overline{v}}{r} \right) - h \overline{v^2} \frac{\partial \overline{v}}{\partial y} - \overline{uv} \left(h \frac{\partial \overline{u}}{\partial y} + \frac{\partial \overline{v}}{\partial x} - \frac{\overline{u}}{r} \right)$$

PRODUCTION

$$\left. \begin{aligned} & - \frac{1}{\rho} \frac{\partial}{\partial x} (\overline{p'u}) - \frac{1}{2R} \frac{\partial}{\partial x} (\overline{q^2 u R}) \\ & - \frac{h}{\rho} \frac{\partial}{\partial y} (\overline{p'v}) - \frac{1}{2R} \frac{\partial}{\partial y} (h \overline{q^2 v R}) \end{aligned} \right\} \begin{array}{l} \text{TRANSPORT} \\ \dots (F.7) \end{array}$$

DESTRUCTION

$- \epsilon$

The equation for the shear stress is:

$$\frac{D(-\overline{uv})}{Dt} = \overline{u^2} \left(\frac{\partial \overline{v}}{\partial x} - \frac{\overline{u}}{r} \right) + h \overline{v^2} \frac{\partial \overline{u}}{\partial y} - \overline{u} (\overline{u^2} - \overline{v^2}) - h \frac{\overline{uv}}{R} (\overline{u} \sin \alpha + \overline{v} \cos \alpha)$$

PRODUCTION

$$- \frac{\overline{p'}}{\rho} \left(\frac{\partial v}{\partial x} + h \frac{\partial u}{\partial y} \right)$$

REDISTRIBUTION

$$+ \frac{\partial}{\partial x} \frac{(\overline{p'v})}{\rho} + \frac{1}{R} \frac{\partial}{\partial x} (\overline{u^2 v R}) + h \frac{\partial}{\partial y} \frac{(\overline{p'u})}{\rho} + h \frac{\partial}{\partial y} \frac{(\overline{uv^2 R})}{R}$$

$$+ \frac{2(\overline{uv^2} - \overline{u^3})}{r}$$

TRANSPORT

$\dots (F.7)$

These equations are very nearly exact for two-dimensional flows where there is no mean transport in the z-direction. The only assumption made is that the Reynolds number is high enough for the small scale motions to be isotropic and transport by viscosity to be negligibly small. This is true for all regions of flow except in the viscous sub-layer where viscous transport would be significant. With these assumptions however, the turbulent energy dissipation rate ϵ is equally distributed in the three component directions and there are no viscous

terms in the $\frac{D(-\overline{uv})}{Dt}$ equation. Hence viscous terms in equations (F.1), (F.2) and (F.3) are not required for development of the stress transport equations.

A P P E N D I X G

C O A N D A F L A R E

PROGRAM-USERS GUIDE

by

J. F. MORRISON

SUMMARY

This is a brief description of the use of a FORTRAN program written for the prediction of jet flow around the Coanda Flare. This guide refers to the program version of 26th June, 1981.

1. INTRODUCTION

The program comprises a main routine and nine subroutines not all of which are called by the main routine. It can predict the mean flow parameters (two components of velocity and static pressure) and shear stress in a two-dimensional isothermal jet. The geometry is variable, but orientated towards that of the Coanda flare. It is nominally axisymmetric therefore, but in the limit handles plane flow geometry also. The term 'plane' refers here to a non-axisymmetric geometry. The exterior (E) boundary is free whilst the interior (I) boundary is a wall or also free and therefore an axis of symmetry. The program is iterative in nature, a necessary feature in order to handle flows with a significant cross-stream pressure gradient. For flows with negligible streamwise curvature, however, only a single sweep of the flow field is required. For further details and in particular the sequence of the main algorithm see chapter six of reference (1). The finite difference procedure used is that of reference (2).

2. SUBROUTINE DESCRIPTION

BDATA

Block data entry. Non-variable data entry including physical properties of jet and ambient fluid, entrainment rate constants, free stream pressure gradient control constants, and streamline curvature/divergence constants.

MAIN

Main routine. Contains all READ statements and all programming pertinent to the parabolic calculation method. It calculates:

initial velocity profile

entrainment rate

step length (first iteration only)

and sets up arrays for solution of the x-component momentum equation.
It also controls the step length according to the geometry requirements.

START

Two entries:

ENTRY INIT - initialises variables at beginning of program run

ENTRY RESET - initialises main flow variable for each iteration and calculates a consistent set of initial conditions; assigns boundary conditions according to flow type and tests for supersonic flow at slot exit in which case calculation method is invalid and procedure stops.

MIXLEN

Two entries:

MODEL1 - calculates effective viscosity and shear stress, according to mixing length hypothesis and use of 'mixing regions'.

MODEL2 - facility for use of different turbulence model. This is not used at present.

MODIFY

Multiple entry:

ENTRY CURVSL(CURV) - adjusts mixing lengths for streamline curvature.

Called from MODEL1.

ENTRY CURVDV - adjusts mixing lengths for streamline divergence/convergence.

Called from MODEL1.

CURVSL and CURVDV can be used simultaneously for geometries containing both streamwise and axisymmetric surface curvature.

ENTRY KIND4(DX,XDCHNG,ICALL) - changes main control switches for a geometry change from a curved to a flat wall. Called from MAIN three times for each iteration.

WALL (I1,OUT1,OUT2)

Calculates wall shear stress (OUT2) and wall function (OUT1) according to modified law of the wall.

SOLVE (N, ISW,PHI)

Solves a system of N-2 linear simultaneous equations of a general variable PHI by use of the tri-diagonal matrix algorithm. See ref.2. It is used for a solution to the two components of mean velocity.

GRID

Three entries:

ENTRY OMCALC calculates (first iteration only) functions of ω , the non-dimensional stream function used as the cross-stream independent variable.

ENTRY YCALC calculates the y-coordinate of the grid and equivalent values of R and h.

ENTRY INTERP interpolates for \bar{U}_m and $y_{m/2}$ using Newton's quadratic divided difference interpolating polynomial.

CMPUTE

Three entries; contains all extra computation relevant to the partially- parabolic procedure. See Chapter 6, reference 1.

ENTRY VCOMPT - calculates static pressure variation across layer. It then calculates the component of velocity perpendicular to the I-boundary using a ^{second-order Runge kutta} ~~one-step Euler~~ approximation and the appropriate boundary conditions. Finally, it updates the static pressure at the previous calculation station using a fraction of the difference between the pressure just calculated at the present station and the equivalent pressure from the previous iteration.

ENTRY UCOMPT - calculates extra terms in x-component mean momentum equation made non-negligible by large streamwise curvature.

ENTRY TEST - tests for convergence. The criterion is that the percentage change in wall pressure for all calculation stations from one iteration

to the next should change by no more than 0.2%. Maximum number of iterations equals ten.

OUTPUT

Two entries which contain all WRITE statements for ISW = \emptyset . OUT \emptyset called from main for writing out of geometry and initial flow conditions. OUT called from MAIN when convergence criterion is satisfied, or if number of iterations exceeds ten.

3. POSSIBLE GEOMETRIES

Plane Cases: wall jet (KIND = 1) procedure parabolic or partially-parabolic depending on degree of streamwise wall curvature. Figure 1 free jet (KIND = \emptyset) parabolic procedure Figure 2.

Axisymmetric Cases: Cylindrical/radial wall jet (KIND = 3) parabolic procedure. Figure 3 Coanda flare jet (KIND = 4) parabolic procedure or partially-parabolic procedure depending on degree of streamline curvature. Figure 4 free jet (KIND = 2) parabolic procedure Figure 5.

4. INPUT DATA

Three input devices are used and numbered 5, 7 and 8. Data attached to unit 5 is used for all runs. Data attached to units 7 and 8 are adjusted for the requirements of each geometry, unit 7 being used for plane cases and 8 for axisymmetric cases. Integer variables are in FORMAT (I1 \emptyset) whilst real variables are in FORMAT (F1 \emptyset .5).

Unit 5 Data

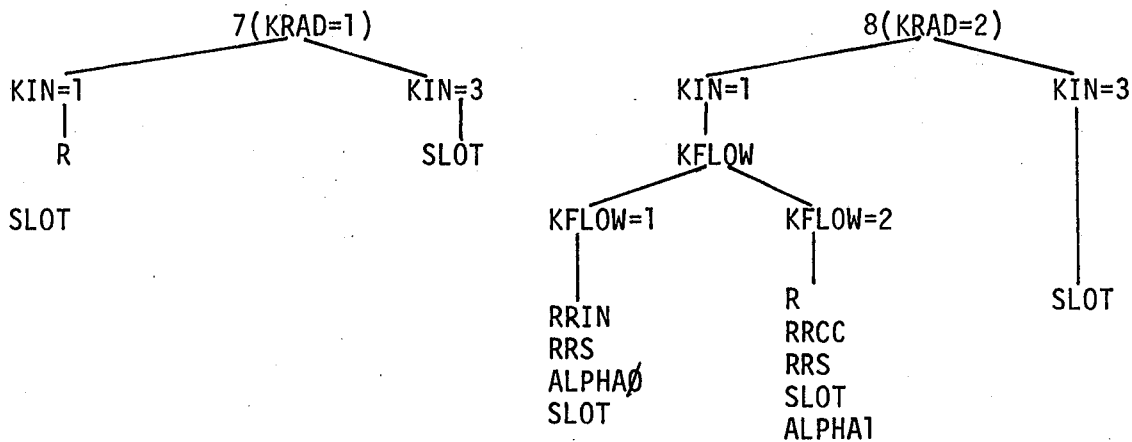
Variables

Function

KMODEL	= 1, MODEL1 called. =2, MODEL2 called.
KPARAB	= 1, parabolic. = 2, partial-parabolic (iterative) procedure
KRAD	= 1, plane geometry. = 2, axisymmetric geometry.
KIN	= 1, wall at I boundary. = 3, axis of symmetry at I boundary

LASTEP max. no. of steps.
 N no. of cross-stream nodes
 XDLAST max. distance downstream for solution.
 DCOEFF Coefficient of discharge
 PATMOS Atmospheric pressure
 TATMOS " temp.
 PSUP Supply pressure
 TSUP " temp.
 AK Mixing length constant $K : \ell_0 = Ky$
 ALMG " " " $\lambda : \ell_0 = \lambda (y_2 - y_1)$
 ISW = 1, additional output to that of OUTPUT
 = \emptyset , no additional output.

Data for units 7 and 8 (See figures for definition of variables)



5. OUTPUT DATA Units 6 and 11

Unit 6

ISW = \emptyset : Labelled output data layed out for each step of last iteration. See list of main flow variables for meanings. Note that pressure data refers to previous step owing to nature of program.

ISW = 1: not advisable unless substantial debugging required!

Additional output labelled only by subroutine. One has to be careful to distinguish which data refers to which step or iteration. Also some of the data is repeated, but this additional output can be useful as it follows sequence of control in program whereas output generated by OUTPUT does not.

Unit 11

Useful output for monitoring progress of calculation when iterative. Prints number of iteration, wall pressures of present and previous iteration and their difference. Recommended assignment to printer in batch use and V.D.U. in terminal use.

6. GENERAL NOTES AND HINTS

- (a) Regrettably some of the program contains non-standard FORTRAN statements which will have to be changed for use on machines other than the NUMAC computer. These are largely statements involving declaration of double-precision variables or double-precision library functions.
- (b) For use with the NUMAC computer, all input units must be assigned in the RUN command even if they are not actually used.
- (c) For cases involving significant streamwise curvature, it is advisable, if not necessary, to use 30 (maximum) number of cross-stream modes. This makes calculation of cross-stream mean-velocity gradients more accurate and eliminates a potential source of instability.
- (d) Typical run time is about 1 sec c.p.u. time per iteration for a 14-step 30-node calculation. Naturally, the input/output commands take the longest to execute and therefore use of ISW = 1 will greatly lengthen the execution time required.
- (e) Maximum size of arrays permitted is 30 for cross-stream variable. Press (30,50) is the only two-dimensional array where the maximum number of calculation stations is 50, i.e. 49 steps.

(f) A major source of potential instability is the crude relationship linking the shear stress to the mean velocity gradient $\partial \bar{U} / \partial y$. Therefore if the procedure fails to converge, adjusting the constants affecting the curvature and divergence corrections may be tried. Nearly all the problems that will be encountered will have a root source in MIXLEN and the calculation of the mixing lengths and shear stresses.

(g) Some predictions of static pressure are unsatisfactory. This is because of the normal stress term in the y-component momentum equation which is linked to the shear stress merely by a constant of proportionality. See Ref. (1) for further details.

References

1. J. F. Morrison (1982), Ph.D. Thesis
2. D. B. Spalding (1977), GENMIX - A general computer program for 2D parabolic phenomena. Science and Applications of heat and mass transfer Vol. I, Pergamon.
3. Listing and *FTNTIDY listing of source program. Latter is very useful for locating main flow variables.

List of Main Flow Variables

CON (30)	\dot{m}'_ω	ALPHA	α	} curvature correction
DIFU (30)	T_ω	BETA	β	
DUDY (30)	$\partial \bar{U} / \partial y$	BPE	ψ_E	$\bar{u}^2 / \bar{u} \bar{v}$ or $\bar{v}^2 / \bar{u} \bar{v}$
EL (30)	l_o	BPI	ψ_I	
EMU (30)	μ_{eff}	CUVMN	$d\bar{p}/dx$	
FLOW (30)	m'_x	DPDX	$\psi_E - \psi_I$	
H (30)	h	PEI	$(Rm'')_E$	divergence correction
OM (30)	ω	REM	τ_E	
RHO (30)	ρ	TAU	τ_I	
RR (30)	R	TAUI	σ	
U (30)	\bar{U}	SIGMA		
UVMN (30)	$\bar{u} \bar{v}$			
V (30)	\bar{V}			
Y (30)	y			
PRESS (30,50)	p			

Figure 1

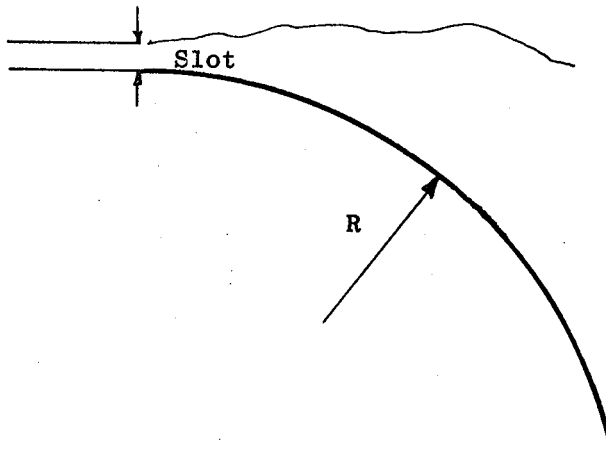


Figure 2

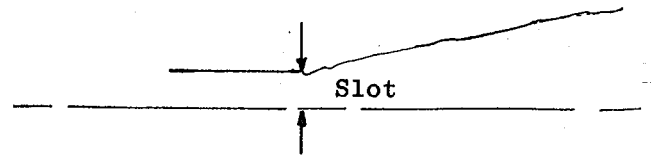


Figure 3

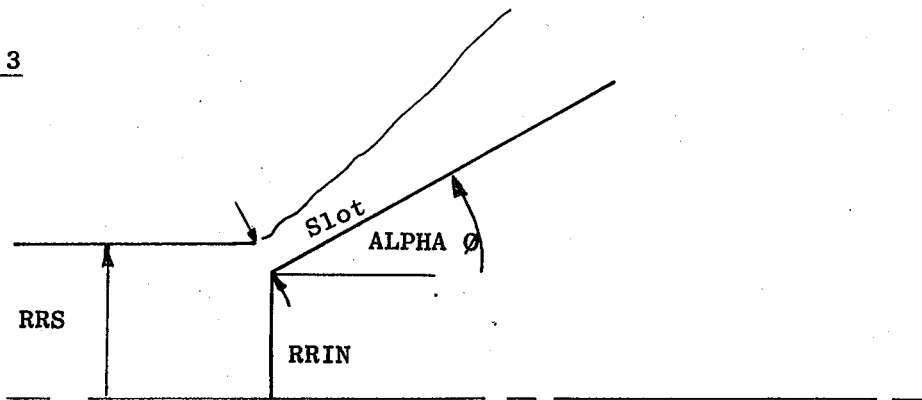


Figure 4

